RICE UNIVERSITY

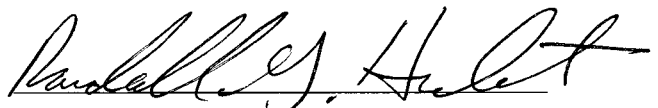# Transport Properties of a Bose-Einstein Condensate with Tunable Interactions in the Presence of a Disordered or Single Defect Potential
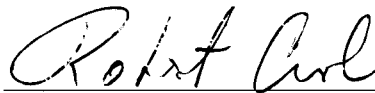
by

Daniel Franklin Dries

A THESIS SUBMITTED
IN PARTIAL FULFILLMENT OF THE
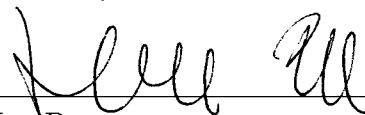REQUIREMENTS FOR THE DEGREE

Doctor of Philosophy
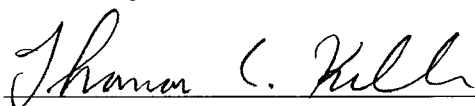
APPROVED, THESIS COMMITTEE:

Randall G. Hulet, Chairman
Fayez Sarofim Professor of Physics and
Astronomy

Robert F. Curl
University Professor Emeritus,
Pitzer-Schlumberger Professor of Natural
Sciences Emeritus, Professor of
Chemistry Emeritus

Han Pu
Assistant Professor of Physics and
Astronomy

Thomas C. Killian
Associate Professor of Physics and
Astronomy

HOUSTON, TEXAS
APRIL 2010

Abstract

Transport Properties of a Bose-Einstein Condensate with Tunable Interactions in the Presence of a Disordered or Single Defect Potential

by

Daniel Franklin Dries

Bose-Einstein condensates (BECs) have proven to be remarkable systems with which to study some of the foundational models of condensed matter physics. The observation of a critical velocity for the breakdown of superfluidity in a BEC and the superfluid to Mott insulator transition observed in a BEC trapped by an optical lattice are but two examples of the, by now, dozens of exciting results in this field, which combines theoretical tools from condensed matter physics with state-of-the-art experimental techniques from ultra-cold atomic physics. However, any real condensed matter system has to contend with the effects of disorder, a phenomena notably absent in the inherently clean BEC systems. We have developed and implemented a way to add well characterized disorder in a controlled way to the otherwise clean BEC system using the light field from a laser speckle pattern. Using this system, we have investigated the effects of disorder or a single Gaussian defect, on the collective dipole motion of a BEC of ^{7}Li in an optical trap. In addition, we perform transport

experiments on a weakly interacting BEC expanding in a disordered one-dimensional atom wave-guide. We have observed that in such a system, the wave nature of matter can lead to spectacular and counterintuitive phenomena. Specifically, we verify that this system exhibits Anderson localization, a phenomena fundamentally resulting from the interference of multiply scattered matter waves. In such a state, the localized gas behaves as an insulator in a regime where it is classically expected to be conducting.

We also present results of experiments regarding a repulsive BEC scattering from a semi-permeable, single defect potential. We investigate the transport properties of such a system with special emphasis on the velocity and defect strength dependent dissipation of the collective dipole motion of the BEC. Finally, we present the results of our experiments on the scattering properties of bright matter wave solitons. We have observed fragmentation of the soliton in a disordered potential as well as both splitting and recombination of a soliton after interacting with a single repulsive defect potential.

Bear in mind that the wonderful things you learn in your schools are the work of many generations, produced by enthusiastic effort and infinite labor in every country of the world. All this is put into your hands as your inheritance in order that you may receive it, honor it, add to it, and one day faithfully hand it to your children. Thus do we mortals achieve immortality in the permanent things which we create in common.

Albert Einstein

Chapter 1

Acknowledgments

My time in graduate school has been the most humbling experience in my life. I have had the opportunity to work with several people whose work ethic and intellectual prowess have left me astounded and honored to have shared in the work that they do. First and foremost on this list is Randy whose tireless efforts keep the lab at the forefront of the ever competitive world of AMO physics. His weeks spent traveling worldwide and countless hours slogging through proposal after proposal keeps the lab in the highest possible state. His ability to keep his enthusiasm for the wonders of AMO physics has inspired me when times were tough in the lab. Through his efforts alone have I had the opportunity to take part in world class research over the last several years, and his overall vision and expertise have served to inspire me on countless occasions.

I have also had the opportunity to work with, and learn from, several gifted students along the way. In the early years Mark Junker and I spent many late

nights troubleshooting the apparatus and collecting data. I learned everything I know about aligning optics from him. His agility in the lab always impressed me. On many occasions he would step in and align a laser system in a few minutes, that I had been struggling with for several hours. With these embarrassing moments, Mark taught me the importance of noticing the finer details of laser beam spots: what you might be missing might be the difference between success and failure. Kevin Strecker and Guthrie Partridge, while also serving as mentors to me in the lab, provided much appreciated friendship throughout their years here. It is much easier working long hours every day when one is among friends and I appreciate Kevin and Guthrie for keeping the atmosphere positive at the lab. Chris Welford also provided much needed assistance with the experiment. His passion for optics, lasers and hearty conversation made many a laser alignment session enjoyable. James Hitchcock was instrumental in building key parts of the apparatus in addition to working on the first iteration of the disorder experiment. Not just a bright student, James has the most impressive work ethic of anyone I have ever met. For several years James was the first in and the last to leave. I am proud to have helped him in the early stages of his grad school career and look forward to the great things he is going to accomplish in the future. Ramsey Kamar and I came to Rice the same year and began work on the same project, the imaging system. Ramsey is also a tireless worker, a deep thinker, and a great friend. I will never forget our late night conversations about politics, science, religion, war, peace....well, you get the picture. I wish Ramsey the best of

luck in the future and also look forward to what the future holds for him. Yean-an Liao has been a steady companion throughout the years. I could always count on "Vinnie" to have my back when I stirred up trouble on the basketball court.

I have thoroughly enjoyed getting to know and working with the new generation of students in the lab. I am proud of Pedro for taking up the lab Beer Bike responsibilities, when I clearly failed. Tobias never ceases to amaze me with his breadth of knowledge. He has helped me with many an electronics problem and always seems to have the right part number stowed away in memory just when I need it. I am particularly thankful to Tobias for introducing me to the musical masterpieces of metal. Evan has been a great friend to me in the short time we have known each other. Without his help toward the end, I never would have finished all my requirements in a timely fashion. He has been "baptized by fire" so to speak and survived! I look forward to the groundbreaking experiments he is going to do in phase two in the life of the apparatus.

The amazing post docs that have come through the lab have each left their mark on me as well. Michael Jack's theoretical and conceptual muscle flexing helped my mind unwind out of many a quantum mechanical conundrum. Wenhui Li provided much needed "on demand" AMO experience when I had any burning question about the interaction of light and matter. I also need to thank Ted Corcovilos and Sophie Rittner for their openness to answer any of my questions and their optimistic attitudes when times got tough. I especially need to thank Scott Pollack who pro-

vided essential support over the last two years on the experiment. Scott is perhaps the most capable and ingenious researcher I have worked with in my time here and without his help I certainly would not have accomplished any of my goals over the past two years. After only the second week of Scott being in the lab, I found myself struggling to keep up with his level of productivity and accomplishment. After the fourth week of trying to teach him a thing or two about AMO, I gave up and realized that it was he that was destined to teach me. His ability to do both computational and experimental work (sometimes at the same time) astounds me. His computer programing skills were invaluable in automating the experiment, allowing us to make a huge leap forward in our productivity. I still haven't found anything Scott can't do (except maybe dunk a basketball) and look forward with great anticipation what the future holds for him. I should also thank his wife, Karin(ita) and son Kallobee (aka Eagle Pilot) for helping me calm down the night before my defense. Without them I may have hopped in the car and skipped town, but they were able to bring me back "down to earth" during possibly one of the most stressful times of my life.

Perhaps the most valuable thing I have gained from my time at Rice is knowledge of a great group of extraordinary people from all over the world. In no other place but Rice could I have gained such a valuable friendships. Of course many thanks to the Captains who kept me sane through their hospitality and mentorship but also for being great friends to myself and, in particular, to Sara when I wasn't there as much as I needed to be. I also thank the Captains for all the have done for Rice and

the GSA. They will forever hold a special place in my heart.

To all of my friends who have given me support throughout this journey I say, "Thank you." To all my friends back home in California: JK, Jordan, Ty, Nate, Zach, Brandon, thanks for always encouraging me. Since we were kids, you and your families always put your faith in me to do great things and for this I will always be thankful. I thrived on your encouragements many times in grad. school even though none of you may know it. I have to thank my cousin Jon who taught me that it was OK to take stuff apart to learn how things worked, even if my parents didn't appreciate it. I will always cherish our days as kids doing experiments in our backyard laboratory, building up the insatiable curiosity that would later drive my passion for phsyics in grad school.

Of course I owe a huge debt of gratitude to my mother and father for teaching me that knowledge is power and that I could truly do anything I wished to do. They somehow instilled in me the importance of hard work, imagination, creativity, kindness, and education. I know that a great portion of their life was focused on helping me develop into the best human I could be and I am forever grateful for their unwavering love and nurturing support of all my interests, hobbies, and obsessions over the years. I am also thankful to Sara's family for taking me in as one of their own when they didn't have to. The day Sara came home talking about a "California boy" I'm sure got them very worried, but as far as I can tell they never flinched. I thank them for many great holidays and long weekends out at "the farm." I want

to thank Mark for always giving me work to do when I asked for it (and perhaps inventing jobs for me to do on one or two occasions just so I could drive the tractor). The work at the farm kept me sane and can't wait to have some time to help once again!

Finally, and most importantly, I would like to thank the love of my life, Sara. You are my inspiration and I can't wait for our future together. During my time in graduate school I have watched you devote your life to the betterment of others even in the face of adversity. I was proud to see you advance in your own educational and professional goals and am proud that we will soon be starting a family of our own. You will be an amazing mother and I know I will learn much from you. I only hope that I can display the kind of patience and kindness you have extended toward me over the last eight years, even if I didn't deserve it. You are an amazing woman and I look forward with great anticipation to the next chapter of our life together.

To baby Dylan: thanks for holding off on your entrance into the world for a few months so I could finish my thesis. I can't wait to meet you and to teach you about all the truly inspiring, wonderful, and amazing things there are in this world. You can be and do anything you put your mind to and I can't wait to find out what it is that inspires you. The thought of you has inspired me during these last few difficult months and you must get here soon so I can begin to repay you. Dr. Daddy loves you!

Contents

Illustrations

And, therefore, the problem is, how can we simulate quantum mechanics?...We can give up on our rule about what the computer [is], we can say: Let the computer itself be built of quantum mechanical elements which obey quantum mechanical laws...

Richard Feynman 1981

Chapter 2

Introduction

When I began my journey in graduate school, I was expecting to learn how to build a system for trapping and cooling atoms and then how to use said system simply for the sake of elucidating the nature of trapped and cooled atoms. However, no sooner after we finished our first experiment studying the fundamental physics of ultra-cold molecule formation [1], did we set out on a wholly different path. This path was to be more concerned with using ultra-cold atoms, particularly Bose-Einstein condensates to learn about the physics of systems completely outside the realm of ultra-cold atoms, particularly the realm of condensed matter physics.[1]

On some level, the atomic system we study forced this choice on us. As our measurements reported in Ch. 4 show, a BEC of ^{7}Li is a wonderfully versatile system. In fact, our system possesses many of the required characteristics that Feynman's

---

[1] I should disclaim that historically the BEC community had actively pushed this "crossover" idea long before I began working in the lab. However, I did not grasp the full implications of this concept until I became personally involved in the experiments.

quantum simulator would need. If one is to use any quantum system to study or simulate another, the components composing the simulator must first and foremost be versatile and programmable. Also of primary importance, is the necessity that the system be fully characterizable. Only after a fully characterized and versatile system is found can one then engineer the experiment in such a way as to directly mimic the environment of a more complex, less well understood quantum system in the hopes that the results of such experiments will shed some light on the more complicated system.

So even though as a young student I did not set out to do so, what we ended up implementing is, in fact, the nascent stages of an analog quantum simulator. What do I mean by an "analog simulator?" For example, in the classical world, one could set up an electronic circuit to study the nonlinear mechanical oscillator, thereby bypassing all of the technical difficulties associated with actually building a complicated mechanical oscillator system. These elements would be replaced with off the shelf electronic components that have far superior performance characteristics. The key is that the electronic system obeys exactly the same mathematical laws that the mechanical system obeys. Said another way, if one mathematical model serves to describe two systems one can choose to use either system to study the implication of those laws; and of course, the clever experimentalist will always choose the more controllable system with which to do his experiments. This thesis serves to chronicle the steps we have gone through to create a controllable and well characterized quan-

tum system that we then used to investigate the physics of a completely analogous system; in short, an analog quantum simulator.

Chapter 3 describes in detail the technical parts of the apparatus we built. To put it succinctly, we have designed and built an apparatus for trapping and cooling ^{7}Li to quantum degeneracy. This system was designed with versatility in mind: we have the ability to conduct experiments using a single or cross beam trap, at an arbitrary magnetic field (0–1000 G) and varying temperature. We can conduct experiments using 3D or 1D trapping geometries. In addition, the static (equilibrium) properties or dynamic (transport) properties can be investigated using this system. We can also add, in a controlled way, well characterized disorder to the system, in the form of a disordered optical dipole trap based on the phenomena of optical speckle. Finally, we have implemented a detailed diagnostic system that allows for the full characterization of the atomic sample, from the "hot" cloud in the magneto-optical trap (MOT) to the "ultra-cold" BEC in the optical trap.

Chapter 4 discusses our detailed measurements characterizing the magnetic field dependence of the interatomic interactions (the so-called Feshbach resonance). It is perhaps the existence of this phenomena that makes ultra-cold atomic systems so attractive as quantum simulators. For ^{7}Li in particular, we show that one can tune the interatomic interaction over an unprecedented range; the s-wave scattering length a can be tuned nearly 7 decades over a modest field range from 544 G to 737 G. We conclude the chapter by exploiting this tunability to more fully understand

interactions in ^{7}Li, demonstrating our ability to observe subtle effects due to the extremely weak magnetic dipole interaction between atoms. We also show that by tuning the interactions we can create a quasi-one dimensional (quasi-1D) system and an ideal gas. We prove this through measurements of the frequency of the collective quadrupole mode of the BEC as the interatomic interactions are tuned via the Feshbach resonance. For a BEC with weakly attractive interactions in the quasi-1D geometry, we demonstrate our ability to controllably create a single matter-wave soliton, a wave packet that propagates without dispersion (spreading).

In Chapter 5, we revisit perhaps the first phenomena where BEC was used to study a concept traditionally thought of as living solely in the realm of condensed matter: superfluid transport. We present our results on superfluid transport of a BEC with tunable interactions in a disordered harmonic trap. We also present our results regarding the transport properties of a BEC flowing through a single attractive or repulsive, semipermeable defect at the center of the harmonic trap. In this study, we demonstrate the ability to create dark solitons in a BEC with weak attractive interactions.

In Chapter 6, armed with with a fully characterized system in which we understand the basic transport phenomena, we attack a well known condensed matter transport phenomenon, Anderson localization. We present our observations of 1D Anderson localization in a BEC. These observations lay a foundation for more complex quantum simulations of disordered condensed matter systems using BEC in

more realistic geometries, hopefully opening the door for new discoveries to be made in the BEC field that have implications for the broader physics community.

Chapter 3

A Versatile Apparatus for Studying a Bose-Einstein Condensate of ^{7}Li

3.1 Introduction

Experimental atomic physicists have taken the notion of being "control freaks" and elevated it to an art form. It has, in fact, been the phenomenal degree of controllability in BEC experiments that have led to some of the most important results in the field. In order to fully exploit the inherent controllability in BEC systems, we have designed and built an extremely versatile apparatus for trapping and cooling atomic ^{7}Li with the primary goal of studying the Bose-Einstein condensed state of ^{7}Li.

Of central importance is the ability to control the effective interatomic interactions via the so-called magnetic Feshbach resonance. We have, therefore, implemented an external magnetic field control and stabilization system that produces stable magnetic fields up to $\sim 1000\,\mathrm{G}$ in addition to easy programmability of arbitrary field ramps. Another benefit of ultra-cold atom systems is the ability to tune the confinement geometry. To allow for this possibility, we have implemented a versatile optical dipole plus magnetic trap to produce a variety of trap aspect ratios. This dipole trap setup includes the option of using a cross beam or single beam configuration at the user's choosing.

Of course, the ability to exquisitely control the system parameters is useless

without the necessary diagnostics for actually making measurements on the system. To this end we have designed and built a tunable diode laser system for optical imaging of the trapped atomic cloud.

For a detailed overview of the complete apparatus, including the vacuum system, the interested reader is directed to the Ph.D. thesis of M. Junker [2]. Dr. Junker's thesis contains many of the "nuts and bolts" details of the apparatus, so I will not attempt to repeat all those details here. However, many changes have been made to the system since the writing of [2]. In what follows, we discuss the technical details of these changes with additional discussion of the various technical problems (and solutions!) we found along the way. We conclude by highlighting the existing limits of the system and propose possible options for future improvement.

3.2 Atom Cooling Primer

To aid in the following description of the apparatus, it is useful to begin by tracing the path of an atom in its journey to become one of the coldest atoms in the known universe. [1]

As shown in Fig. 3.1 the atoms begin in an oven with $T \sim 800\,\mathrm{K}$. They are collimated by a nozzle before entering the high vacuum ($P \sim 10^{-9}\,\mathrm{torr}$) source cube. This hot atomic beam then enters the first cooling stage of the apparatus, the Zeeman

---

[1]The lowest natural temperature ever recorded (indirectly, of course) is $\sim 1\,\mathrm{K}$, found in the Boomerang nebula, a protoplanetary nebula located 5,000 light-years away from Earth in the Centaurus constellation. We routinely create atomic clouds with temperatures in the 100's of nK, 10 million times colder.
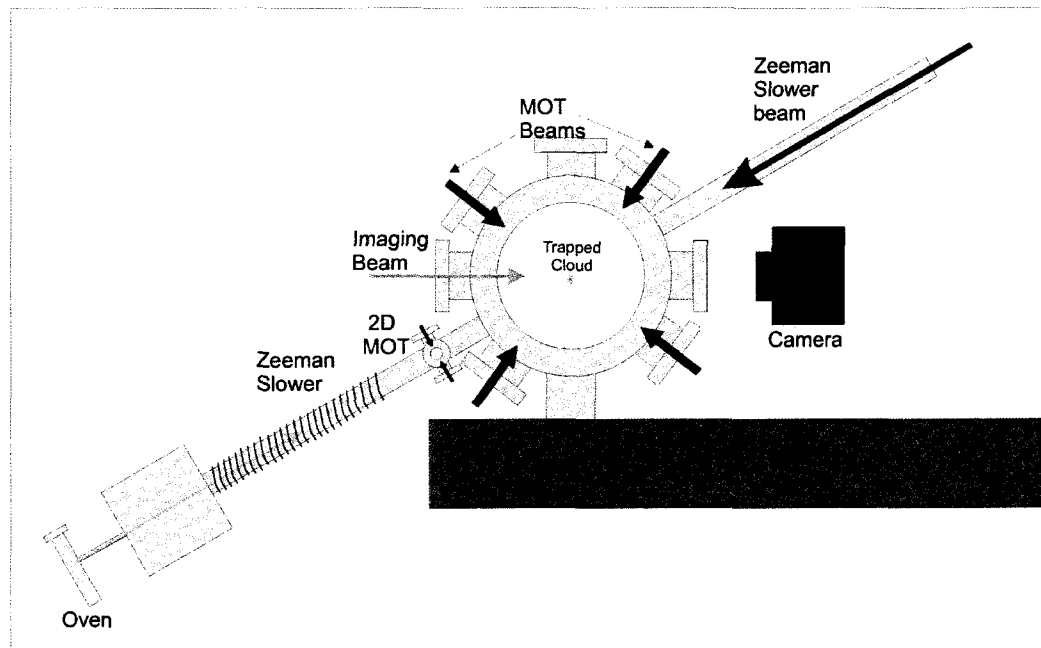
Figure 3.1 : Schematic diagram of our apparatus for trapping and cooling ^{7}Li.

slower [3, 4] where it is laser cooled to $\sim$1 mK as it travels through the length ($\sim$0.5 m) of the slower. As it leaves the slower, it is collimated and deflected toward the center of the ultra-high vacuum (UHV) chamber ($P < 10^{-11}$ torr) by a 2-D magneto-optical trap. Once in the UHV chamber, the pre-cooled atoms are trapped and cooled further in a six beam magneto-optical trap (MOT) [5] as shown in Fig. 3.2.

After a short cooling and compression sequence [6] we are left with roughly 10^8 atoms at $600\,\mu K$. This cloud of atoms is then magnetically polarized by optically pumping the atoms into the magnetically trappable $|F = 2, m_F = 2\rangle$ internal state.
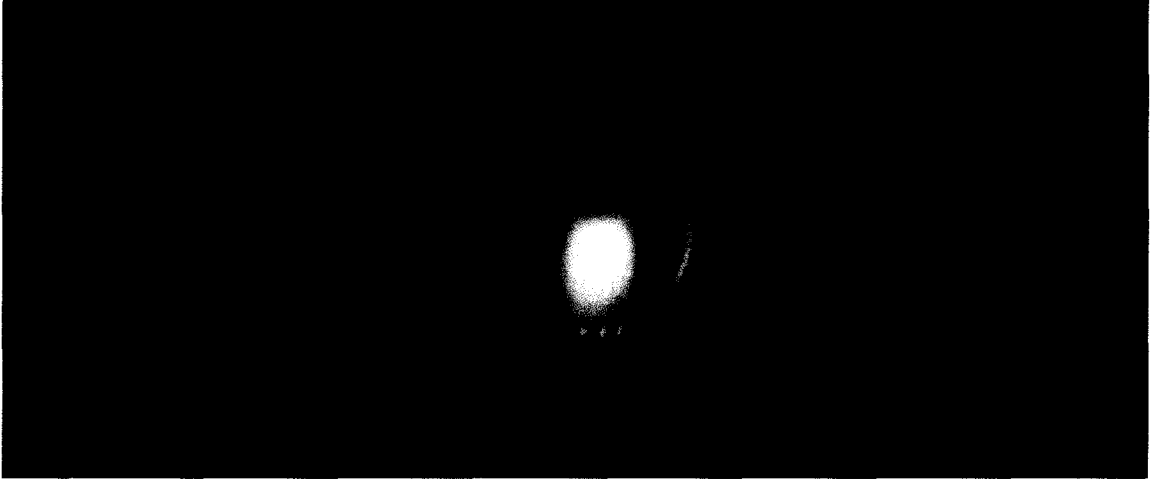
Figure 3.2 : "Naked eye" view of our ^{7}Li MOT.

The lasers are then switched off and a system of electromagnets is energized [7, 8]. Through the interaction of the atomic magnetic moment with the magnetic field, $U = -\vec{\mu} \cdot \vec{B}$, the field configuration created by the electromagnet forms the trapping potential landscape shown in Fig. 3.3.

Over the next 45 s, the gas is cooled further using an optimized forced evaporation technique [9], relying on the selective absorption of microwave photons by the hottest atoms, followed by the subsequent ejection of these hot atoms from the trap. The remaining atoms then rethermalize to a colder temperature. This process is repeated millions of times until we are left with a sample of $\sim 10^7$ atoms at a temperature of $\sim 20 \, \mu$K.

At this stage we shut off the magnetic trap and turn on an optical dipole trap consisting of a single 5 W focused IR laser beam with $\lambda = 1030$ nm (ELS Versadisk
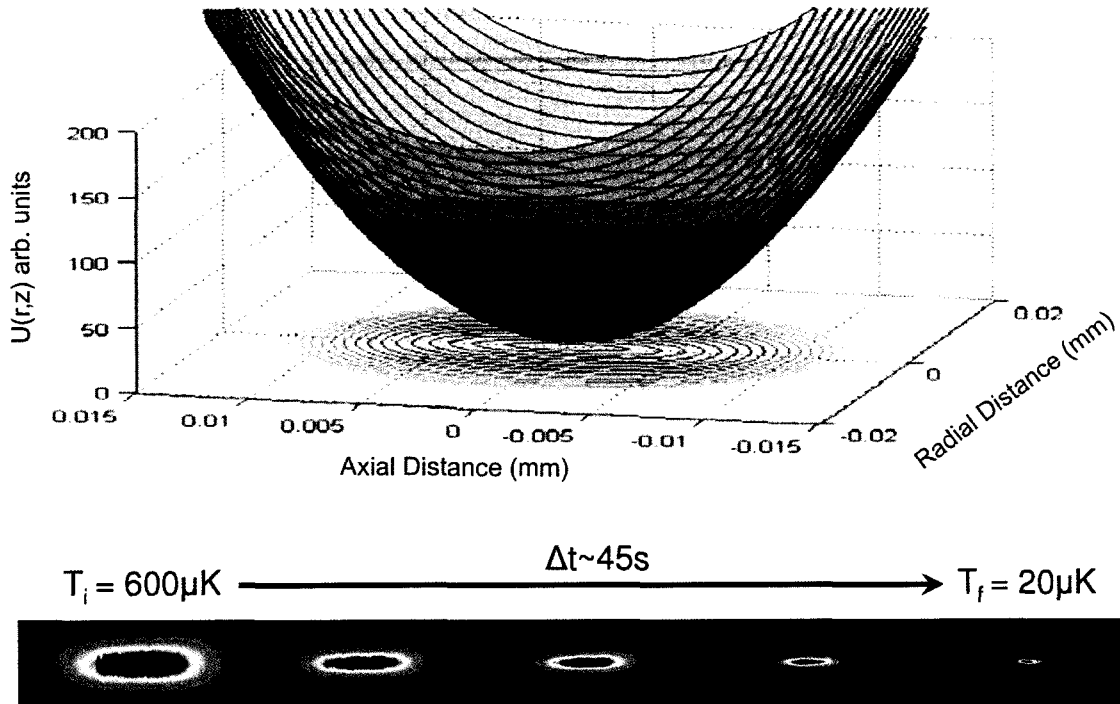
Figure 3.3 : Top panel shows the potential energy landscape due to the magnetic trap. Bottom panel shows fluorescence images of the magnetically trapped cloud at different times throughout the forced evaporation process. We use the size of the atom cloud to measure the temperature, just as one uses the size of a column of mercury as a measure of temperature in a thermometer.

Model VD 1030-50) and a focused beam waist of $24\,\mu$m.[2] A microwave sweep is then applied to transfer the atoms to the $|F = 1, m_F = 1\rangle$ internal state. In this state, the interactions between the atoms are widely tunable from attractive through non-interacting to repulsive by applying an external magnetic field created by energizing a set of Helmholtz coils. We then apply a 720 G bias field resulting in large enough interactions to allow for the rapid thermalization required for evaporative cooling in the optical trap. This evaporation takes place over $\sim 2\,$s as the depth of the trap

---

[2]We observe that the transfer efficiency from the magnetic trap to optical trap does not strongly depend on the optical trap beam waist over the range of $24\,\mu$m–$33\,\mu$m.
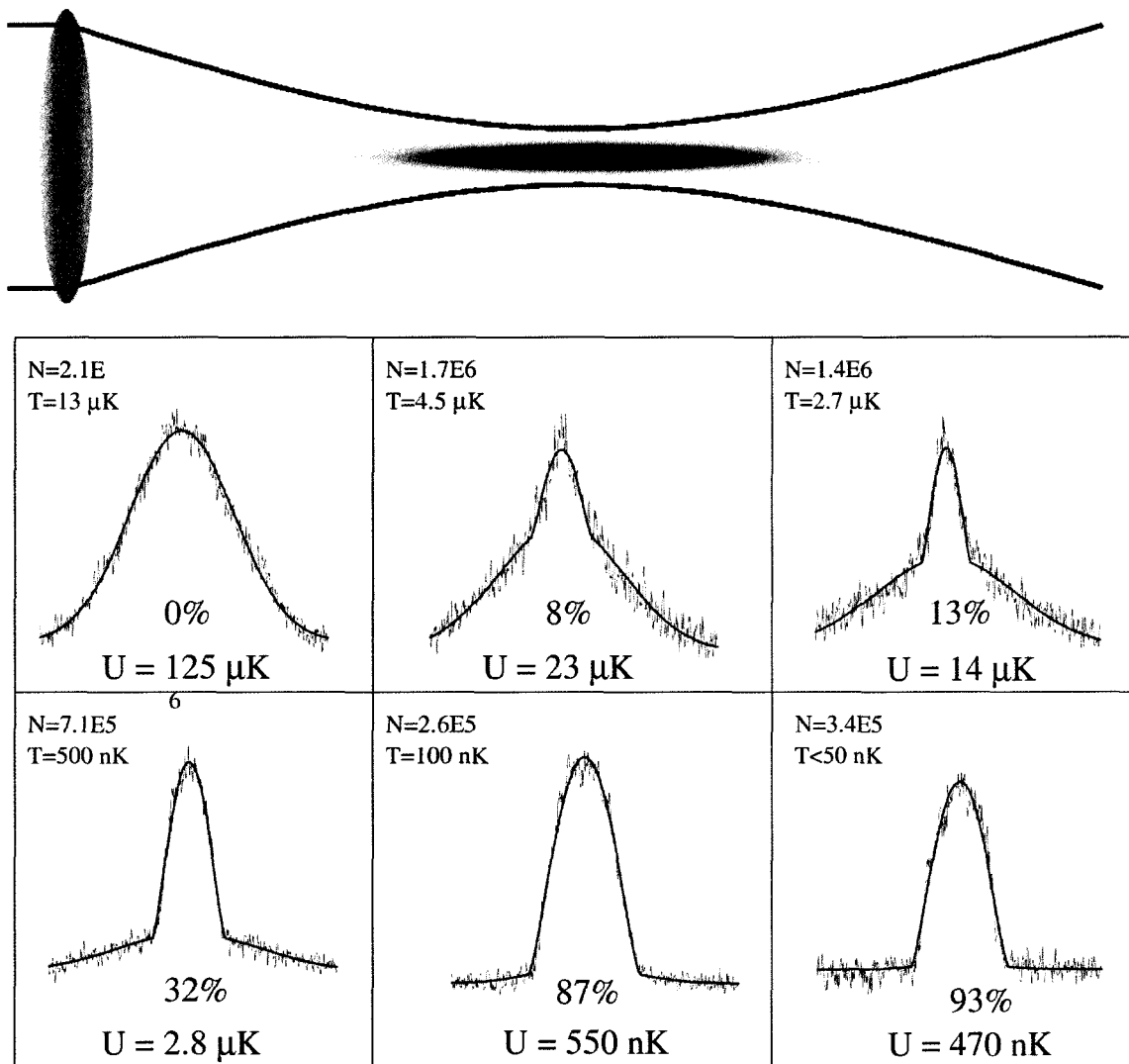
Figure 3.4 : Top panel: Schematic diagram of the single beam optical trap. We use a single lens to focus the beam down to a waist of 24 μm. Bottom panel: Axial cuts through the cloud at various times throughout the $\sim$2 s optical trap evaporation. Given for each sub-panel is the total atom number N, cloud temperature T, trap depth U and condensate fraction found from the bimodal fits. Figure adapted from [2].

is continuously reduced, thereby allowing the hottest atoms to escape. At the end

of this evaporation process we are left with about 3×10^5 atoms in a nearly pure

Bose-Einstein condensate, as shown in Fig. 3.4. Finally we are ready to *begin* the

experiment! [3]

3.3 The Red Diode Laser System

In order to accomplish the trapping and cooling scheme described above, we must

have a system that will generate the multiple frequencies needed for proper operation

of the MOT, Zeeman slower, optical pump, and imaging beams. This system has gone

through at least three main overhauls since our initial designs were implemented,

but the main design and functionality of the system remains unaltered from that

described within [6] and so will only briefly be outlined here. We have, however,

made several incremental improvements since the writing of [6] and these will be

described in detail below.

The laser system is designed to produce light that will drive both sub-lines of the

D2 transition in ^{7}Li: the $2\,^2S_{1/2}$ F $= 2 \rightarrow 2\,^2P_{3/2}$ F $= 3$ (trapping transition) and

the $2\,^2S_{1/2}$ F $= 1 \rightarrow 2\,^2P_{3/2}$ F $= 2$ (repump transition) as shown in Fig. 3.5. The

presence of both the trapping and repump light is necessary to avoid optical pumping

into the dark ground state hyperfine manifold resulting in catastrophic loss of atoms

from the MOT. Shown in Fig. 3.6 is a diagram of the diode laser system used to

---

[3]It should be noted that this extremely cold sample is still extremely dilute. The highest densities we work with are $\sim 10^{14}$ cm^{-3}, over 4 million times less dense than room temperature air. This is, in fact, why the BEC does not condense back into a solid form.

—
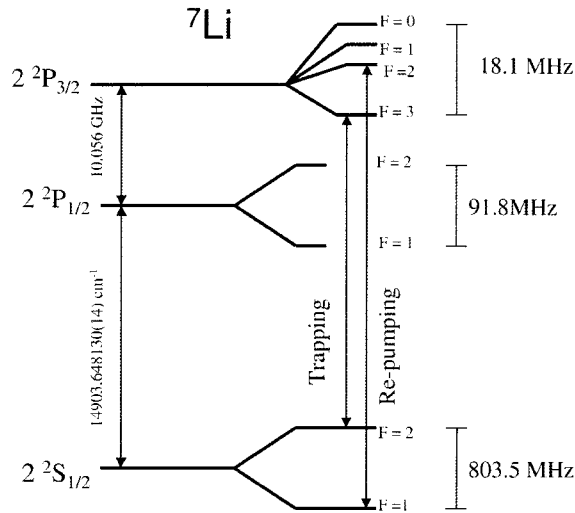
Figure 3.5 : Energy level structure for the D1 and D2 lines of ^{7}Li at zero field, including the hyperfine structure. The primary frequencies used in our experiment are the D2 lines which we designate as the "trapping" and "repump."

generate the red light used for the experiment. We derive all of the laser frequencies from a single external cavity diode laser (Master ECDL) in Littrow configuration. This laser is first locked to a Fabry-Perot cavity that is subsequently locked to a heat pipe via a modified Pound-Drever-Hall technique [10]. [4] The stabilized light from this laser is then split, beam-shaped, and frequency shifted to produce the beams that are necessary to injection lock the various amplification stages that produce the MOT, Zeeman, slower, and optical pump (m_F-pump) as is shown in the diagram.

---

[4] For a good pedagogical review of this technique refer to E. Black [11]. Our particular implementation is based on that described in C. A. Sackett's Ph.D. [12].
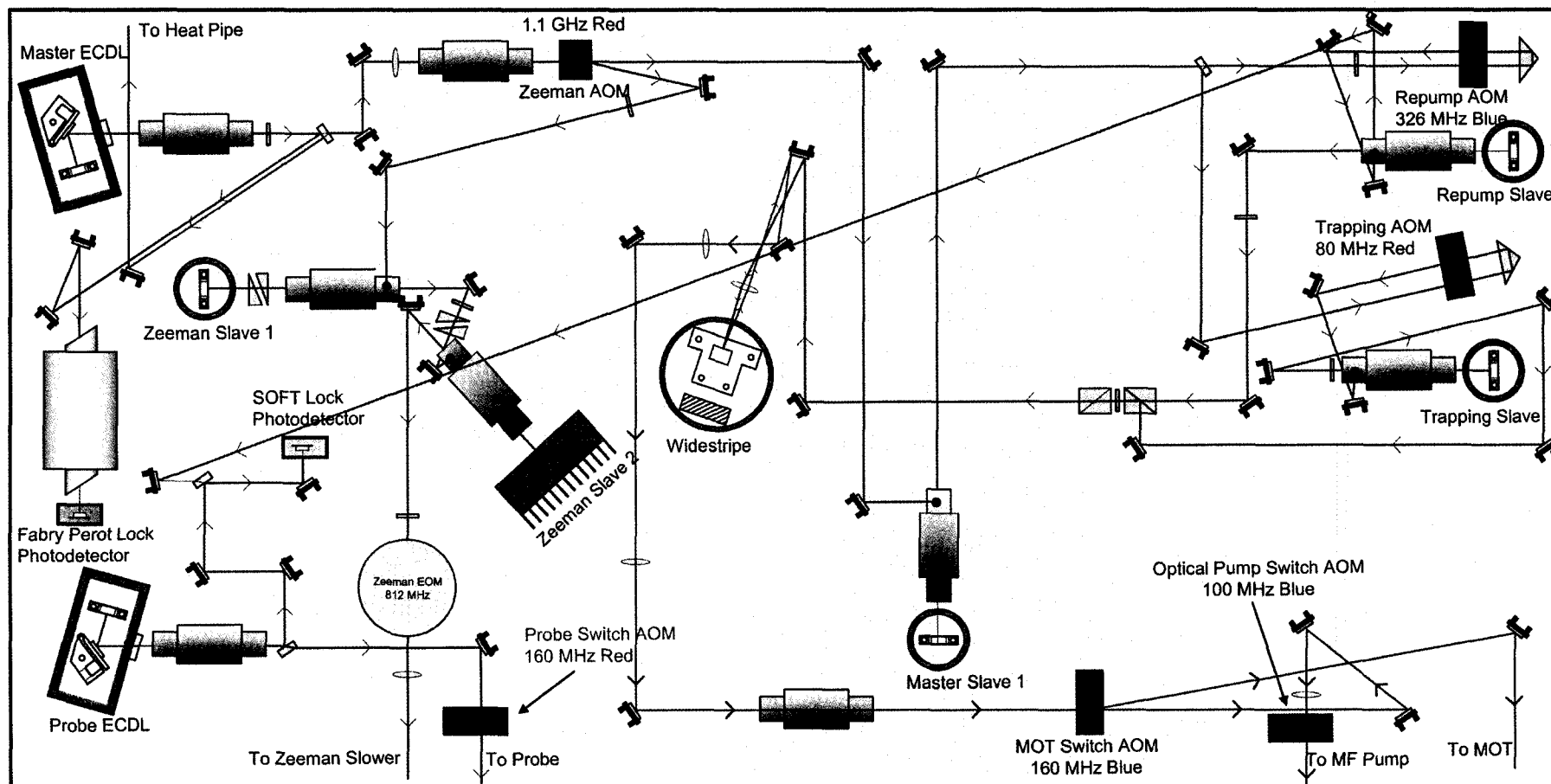
Figure 3.6 : The ^{7}Li diode laser system. For simplicity, AOM frequencies shown in the diagram will produce a MOT beam that is on resonance. During MOT operation, the repump and trapping double pass AOMs are set to give a net detuning of $\Delta \approx -6\,\Gamma$ where $\Gamma = (2\pi)\,5.9\,\mathrm{Mhz}$.

Consulting Fig. 3.6 we can trace the paths of each of these beams. Immediately

following the Master ECDL (Bluesky Research Circulaser, PN: PS110-00), the power

is split and a small fraction is sent to the Fabry-Perot lock and the heat pipe (not

shown). The remaining power is directed through the 1.1 GHz Zeeman AOM. The

first order diffracted (red) beam is then used to create the Zeeman slower beam by

first injecting low power Zeeman Slave 1 (Mitsubishi Laser, PN: ML101J8). The

output of Zeeman Slave 1 is then used to inject the high power Zeeman Slave 2

(Hitachi Laser, PN: HL6555G). The output from this laser is then sent though an

812 MHz EOM to generate a small repumping sideband. This beam is subsequently

beam shaped and sent to the chamber. The undiffracted order that passes through

the Zeeman AOM is then directed to the optical system used to generate the MOT

and optical pump beams. We first amplify this beam by injection locking high

power Master Slave 1 (Hitachi Laser, PN: HL6555G). The output of Master Slave

1 is then redirected to inject the Trapping (Mitsubishi Laser, PN: ML101J8) and

Repump Slaves (Roithner Laser, PN: RLT6720MG). These injection beams are first

sent through double pass AOMs to allow for independent tuning of the trapping and

repump frequencies. This functionality is absolutely essential for optimized MOT

cooling and compression, m_F pumping, and to allow for easy tuning of the imaging

laser. The output of the trapping and repump slaves is then combined and set to

a roughly 2:1 trapping to repump power balance using the 1/4-wave plate and two

polarizing beam splitting cubes. This beam is then amplified by injection locking
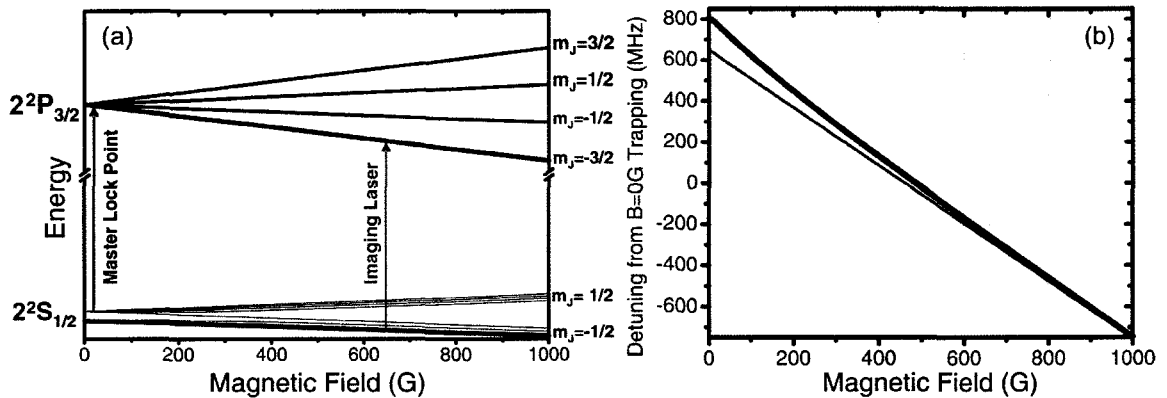
Figure 3.7 : (a) Zeeman structure of the $2\,^2S_{1/2}$ and $2\,^2P_{3/2}$ states of ^{7}Li. For all imaging done in this thesis, we probe the σ^- transition between the two sates shown in red. (b) Detuning of the imaging transition from the Master ECDL (which is locked to the trapping transition). We primarily image in the 500 G − 1000 G range, requiring a minimum of 700 MHz tunability of the probe laser. The thin red line is the high filed shift of $\mu_B = -1.41$ MHz/G for comparison. Data in these figures is the result of a numerical diagonalization of the Hamiltonian described in [13].

an AR coated widestripe. Finally this high power beam is directed to the MOT

Switch AOM and the first order (blue) diffracted beam is sent to the MOT fiber.

The m_F-pump is also fiber coupled (not shown) and is derived from the main MOT

beam. During m_F-pumping, the MOT Switch AOM is off and the Optical Pump

Switch AOM is on thereby directing all the MOT power to the optical pump fiber.

The leakage light from the injection port of the repump slave isolator is sent

across the table to provide a reference for the Probe ECDL frequency offset lock.

This versatile probe laser is designed to allow for imaging of the $|2, 2\rangle$ state in both

the magnetic trap and low field optical trap and for also imaging the $|1, 1\rangle$ state over

a large range of magnetic fields.

The Zeeman shifts for the σ^- transition used for probing is shown in Fig. 3.7.

The stabilization and tunability of the probe laser is accomplished through the use of

a frequency offset lock using a side-of-filter technique (SOFT lock) [14]. This locking technique uses the beat note between the probe and the Master laser created by overlapping the two beams on a high speed photodetector as shown in Fig. 3.6. A frequency dependent error signal is then electronically derived by mixing down this beat note to a frequency near the 3 dB point of an electronic high pass filter. The probe laser detuning is then varied by sweeping the local oscillator signal provided to the mixer. This technique has proved very robust with a large capture range and high bandwidth. The technical details of our implementation are detailed in Appendix B.

3.3.1 The IR Laser System for Optical Dipole Trapping

We have designed and implemented an optical trapping scheme based on a Yb:YAG thin disk laser manufactured by ELS (now serviced by Laser Nanotechnology). This system was derived from the free space system described in [2] but improvements have been made to improve versatility and stability. The existing optical setup is shown in Fig. 3.8. This system consists of a main beam with a beam waist $w_0 \approx 24\,\mu$m and a cross beam with a much larger beam waist of $w_0 \approx 250\,\mu$m. The main beam may be operated as single beam trap without the cross beam. Typical full trap depth characteristics of the main beam are $P = 5\,$W, $\omega_z = (2\pi)\,75\,$Hz, $\omega_r = (2\pi)\,7.8\,$kHz, and $U = 290\,\mu$K. At the end of the optical trap evaporation, typical characteristics are $P \sim 11\,$mW, $\omega_z = (2\pi)\,3.5\,$Hz, $\omega_r = (2\pi)\,360\,$Hz, and $U = 640\,$nK. The cross

beam can be added to turn the trap into a "dimple trap" where the radial confinement

of the cross beam serves to squeeze the trap axially at low trap depths.[5] Typical

radial trap frequency and depth of the cross beam are $\sim 60\,\mathrm{Hz}$ and $U \sim 2\,\mu K$ for

$P \sim 3\,\mathrm{W}$, allowing for the tuning of the aspect ratio of the combined trap from

$\sim$100:1 (no cross beam) to $\sim$6:1 (full cross beam). This system also allows for the

capability of studying 1D transport by abruptly switching off the cross beam after

the evaporation in the dimple trap, causing the cloud to expand in the single beam

trap.

---

[5]Recent studies have found that evaporation into tight dimple traps can be used to quickly and efficiently create large BECs. Such a technique could conceivably be implemented in our system in the future to enhance the efficiency of the magnetic trap evaporation [15]. A slightly more complicated transfer technique based on spatial mode matching has also produced impressive results [16].
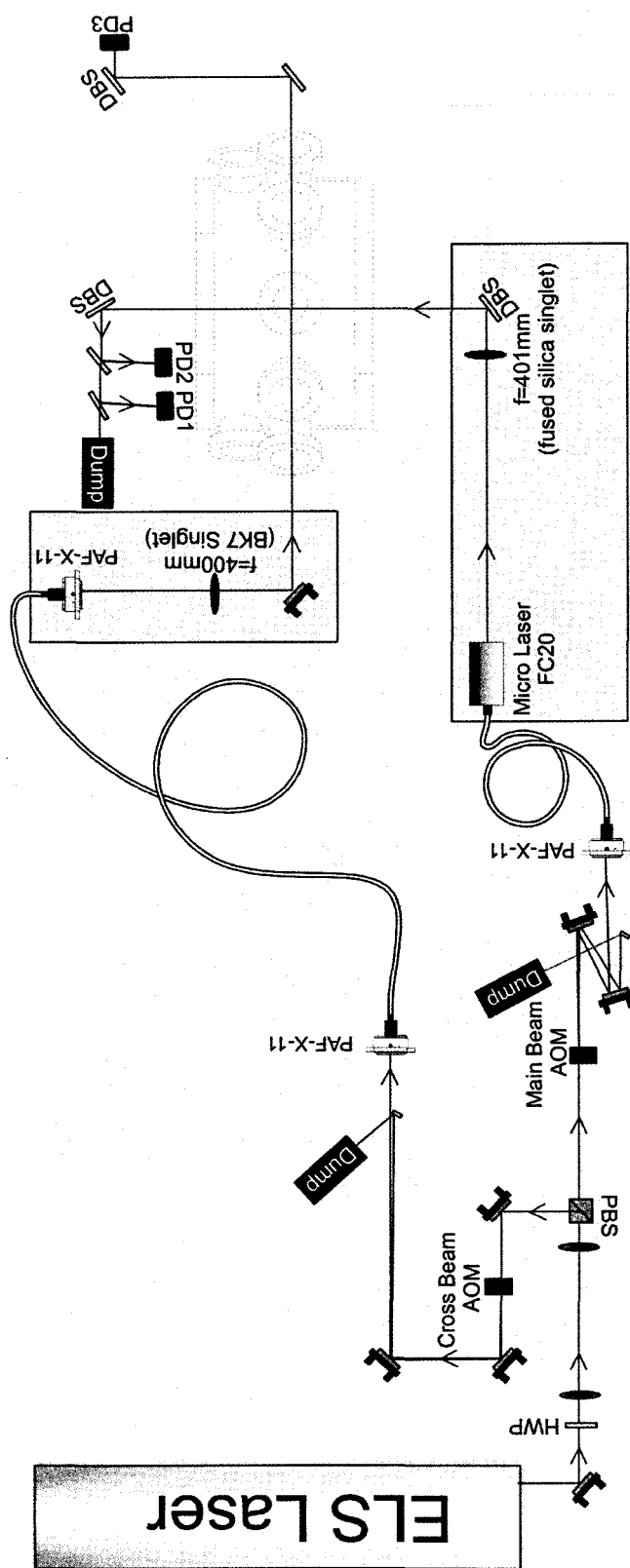
Figure 3.8 : The Optical Trap Laser System. This laser system consists of a fiber coupled cross beam optical dipole trap setup. The power balance between the main and cross beams can be adjusted arbitrarily through the rotation of the half-wave plate (HWP). Main and Cross Beam AOM's operate at 80 MHz and 90 MHz, respectively. To stabilize the output power from both fibers, the RF drive power to the two AOM's is modulated in order to keep the intensity at PD1 and PD3 constant. PD2 is used solely as an independent monitor of the intensity of the main beam.

One of the primary concerns this new setup, the fiber coupling in particular, was meant to address was any pointing instabilities and focal drift that were present in the original free space beam setup. Axial trap movement was particularly nefarious for our 1D expansion experiments as any change in the focal position of the trap would move the axial position of the trap during the expansion, giving the BEC a random "kick." In the single beam trap of $\omega_z \sim (2\pi)\,4\,\text{Hz}$, we would see as much as $100\,\mu\text{m}$ shot to shot variation in the central position of the condensate.

Of course, in any fiber coupled system, pointing instabilities are transformed into power instabilities due to the extremely sensitive dependence of the fiber coupling efficiency on the input beam position. We found that most of this problem is caused by thermal beam drift induced by the switching AOMs and would lead to a factor of two or more drift in the output power of the fibers on the time scale of several hundred ms after the AOM was switched on. At high trap depths, we solve this problem by an improved switching scheme that leaves the AOM's in the on state for most of the time. In the "off" configuration, rather than switching the RF power to the AO's off, we only quickly pulse the power off. During the short time the beam is off, the drive frequency of the AOM is swept a small amount and the power is switched back on. This deflected beam is then picked off and dumped as shown in Fig. 3.8.[6] This method can reduce the full trap depth drifts to under 10% but unfortunately does not help the thermal drifts after an optical trap evaporation,

[6]Care must be taken when using this technique to choose an "off" frequency that produces nearly the same VSWR as the "on" frequency, otherwise the AOM will slowly cool off as if the RF were off.

since the act of evaporating is practically the same as switching the AOM off. The subsequent cooling of the AOM crystal after evaporation leads to pointing drifts on the imput to the fiber as described above. To alleviate this problem, we have implemented an active AOM stabilizing system developed by S. E. Pollack. This system monitors the output power of the fiber with a photodetector (e.g. PD2 in Fig. 3.8) and compares the power to a set point derived from an analog out from the control computer. When the optical power drops below a user defined threshold power, the feedback circuit takes control and creates an error signal which is then fed back to the variable attenuator used to control the AOM RF drive power, thereby adjusting the input optical power to the fiber to keep the intensity at PD2 constant. A detailed schematic of this circuit along with more technical detail can be found in Appendix A.

Preliminary measurements showed that simple switching to a fiber coupled system did not significantly affect the shot to shot fluctuations in the central position of the BEC's. The redesign did, however, eliminate the free space setup as the source of the problem. Further tests revealed a drift in the focus of the optical trap in the low field, full trap configuration. The focal drift manifested as a drift in the axial position of the trapped thermal cloud vs. time. Examples of this drift are shown in Fig. 3.9. The majority of this drift appeared to be due to thermal effects in the focusing optics. In the original system, the fiber was initially collimated with a PAF-X-11 OFR fiber port with an output beam waist of $w_0 = 600\,\mu$m. This was immediately
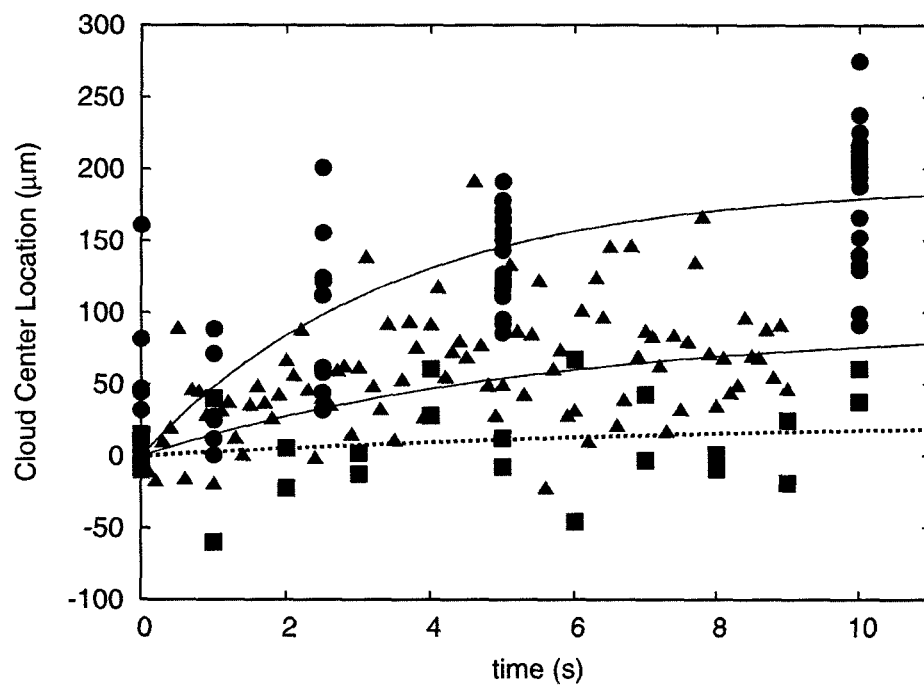
Figure 3.9 : Full trap depth focal drift. Red circles show the thermal focal drift in the original setup. Blue triangles show the drift with all lenses replaced with fused silica singlets. Black squares show the beam drift for the system shown in Fig. 3.8 (i.e. fused silica lenses and Micro Laser output coupler). The improvement in the focal drift is attributed to the improved optical components. Power drift over the course of these measurements was less than 10%. The large scatter reflects the uncertainty in the fitted centers of the large thermal clouds ($1/e$ radii of ~ 1.5 mm) due primarily to noise in the images.

followed by a 5:1 telescope using BK7 doublets of $f = 50\,\text{mm}$ and $f = 250\,\text{mm}$, respectively. Finally, the beam was focused onto the atoms using a BK7 doublet with $f = 400\,\text{mm}$. The drift in this system was significant: nearly $200\,\mu\text{m}$ in $10\,\text{s}$. Replacing all the doublets with fused silica singlets helped significantly, reducing the drift to $\sim 80\,\mu\text{m}$. Finally, we replaced the OFR fiber port with a large diameter, high numerical aperture, multi-element fiber collimator from MicroLaser. This collimator has an output beam waist of $5.3\,\text{mm}$, nearly 9 times larger than the OFR fiber port, resulting in nearly 80 times lower intensity on the collimating optics. This collimator also allowed us to remove all of the telescoping optics, greatly simplifying the system. This new optical system seemed to push the drift below our measurement accuracy. Unfortunately this accuracy is limited to $\pm 50\,\mu\text{m}$ for thermal clouds, due to our ability to resolve the center of the large clouds ($1/e$ radii of $\sim 1.5\,\text{mm}$) in the somewhat noisy images.

We have also characterized the beam in steady state at high ($6.2\,\text{W}$) and low ($30\,\text{mW}$) powers. Using a CCD camera, we measured the transmitted power through the final dichroic beam splitter used to reflect the beam into the chamber as shown in Fig. 3.8. Two cuts through the beam along orthogonal directions on the CCD are shown in in Fig. 3.10 and are horizontally offset on the graph for clarity. Comparing the high (red points) and low (blue points) power beam waist locations gives an average shift of $130(40)\,\mu\text{m}$. Since the system experiences a similar power change during an evaporative cooling cycle, this could indeed impart some axial motion to
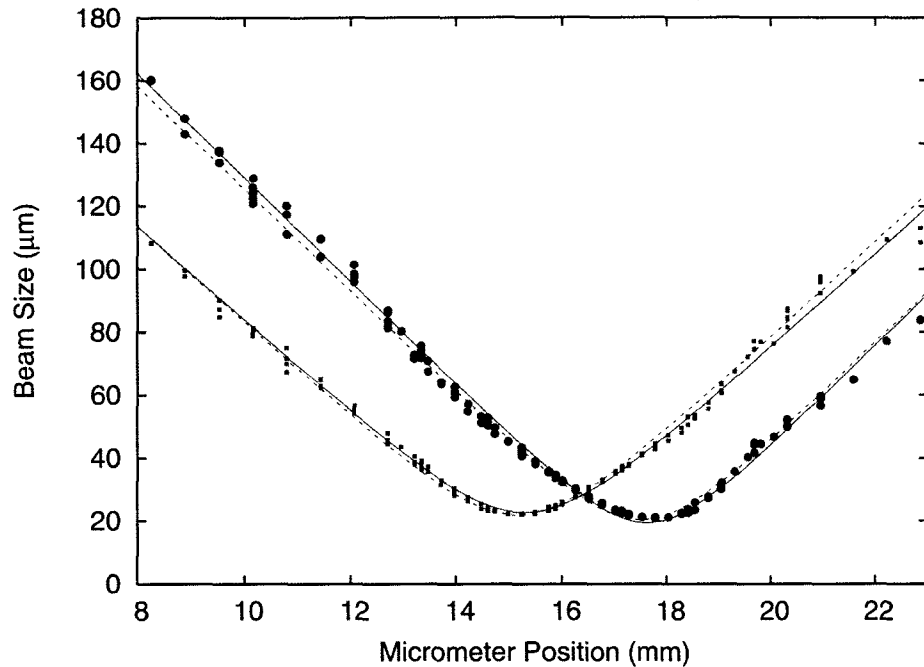
Figure 3.10 : Focal position of the optical trap at high and low power. Red data points are for 6.20 W and blue data points are for 30 mW. The two sets of curves are for two orthogonal directions imaged using a CCD camera (See text). A small focal shift is seen between the two different powers of $\sim$130(30) μm.

the BECs. Incidentally, since the final viewport was not present in the beam path during the above measurement, we can safely eliminate it as a source of the problem.

Fig. 3.11 shows the location of the center of the cloud as a function of time before, during and after the evaporation. The solid circles indicate that for short evaporations, the cloud does appear to drift nearly 150 μm, consistent with the CCD measurements. In the improved system, it is hard to imagine any thermal lensing due to the low intensity ($\sim$13 W/cm^2) on all of the optics. However, the large magnification in our system ($M = 6$) makes the focal position of the trap extremely sensitive to any changes in position of the front face of the fiber. It is straightforward to show
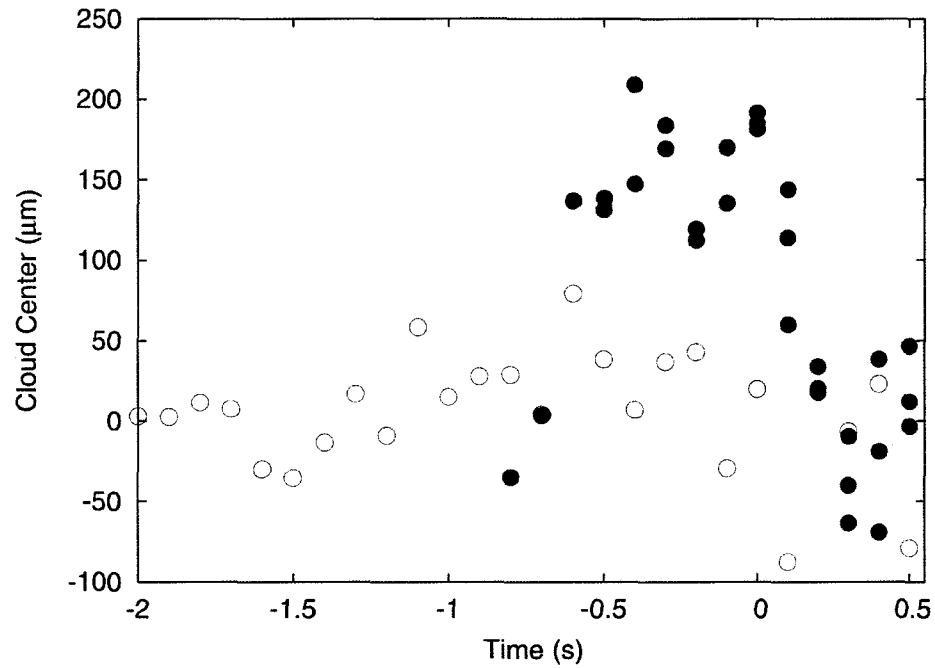
Figure 3.11 : Location of the cloud during optical trap evaporation. The end of the optical trap evaporation is defined to be $t = 0$, while the first points plotted occur at the start of the evaporation. For short evaporations (filled circles) the cloud appears to drift toward increasing coordinate as the power in the optical trap is reduced. After the evaporation, the cloud then appears to drift back towards its initial position. This drift is discussed in detail in Sec 3.4 below. For the slower evaporation, the cloud does not appear to drift significantly during the evaporation. Note also the 50 μm shot-to-shot fluctuation in the cloud. This is above our measurement error of 10 μm. This movement appears to be present in both the slow and fast evaporations.

that in our two lens system, any axial shift in the position of the fiber tip gets magnified by $M^2 = 36$ at the focal position of the trap. In order to explain the observed movement, a minuscule $3.25\,\mu m$ of fiber tip movement is all that is required over the full heating cycle. Visual inspection of the OZ fibers reveals approximately 4 mm of bare fiber cantilevered out of the FC/APC connector. Assuming the thermal expansion of ordinary glass of $9\,ppm/°C$, this requires a temperature increase of $\sim 100°C$ to produce the required $3.25\,\mu m$ of thermal expansion. Given that at full power, the intensity at the fiber tip is a hefty $24\,MW/cm^2$, this amount of heating does not seem out of the question. A possible design improvement that would minimize this effect would be to implement a large mode area photonic band gap fiber, such as the LMA-25 from NKT Photonics. Efforts to test this fiber are currently underway.

3.4 Magnetic Fields

This apparatus consists of many sets of electromagnetic coils: the MOT, 2D-MOT, bias, curves, quads, axial bias cage, push cage, and the x and y nulling cages. In the description that follows, we outline only the aspects of the system that have changed since the writing of [2] and [6]. In particular, we will discuss the added capability of energizing the curvature coils while in the high field, the feed forward system for the bias voltage set point, and the current control and stabilization scheme used for the push cage.

Figure 3.12 shows the coils responsible for generating both the magnetic trap and
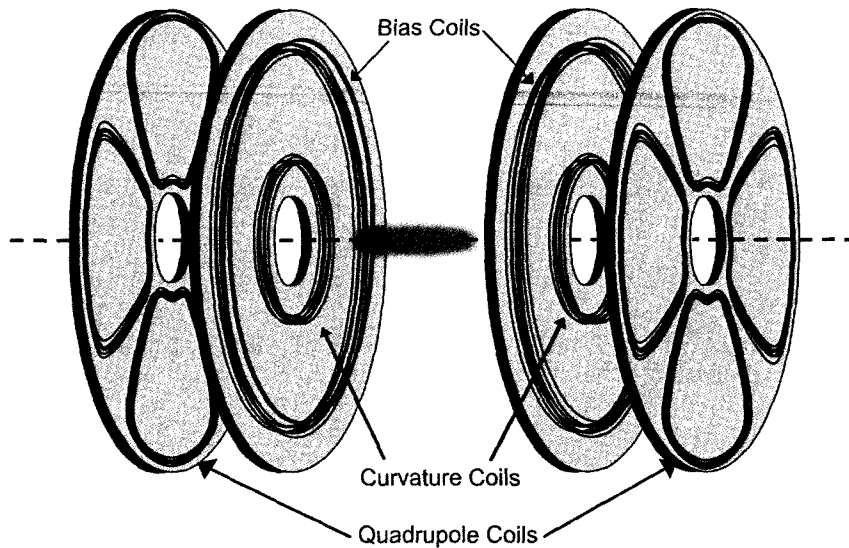
Figure 3.12 : Electromagnetic Trap Coils. In the magnetic trap configuration, all of the coils are energized. While in the optical trap, the bias coils provide a uniform bias field for tuning a via the Feshbach resonance. The curvature coils can also be independently energized while in the optical trap to add to or null out the axial confinement provided by the optical trap.

the high field. In magnetic trap configuration, all coils are energized: the curvature coils produce a harmonic axial confinement, the quadrupole coils produce a radial gradient that serves to confine the atoms along the radial direction, and the bias coils produce a uniform offset field that cancels the large bias field generated by the curvature coils. In the case of the high field optical trap, the bias coils are energized to produce the field necessary for tuning a via the Feshbach resonance. In addition, the curvature coils can be energized independently of the bias to produce additional axial confinement, or to null out the confinement due to the optical trap, if preferred.

Shown in Fig. 3.13 is a schematic diagram with the relevant coils and control electronics used during the magnetic trap and high field configurations. The interested
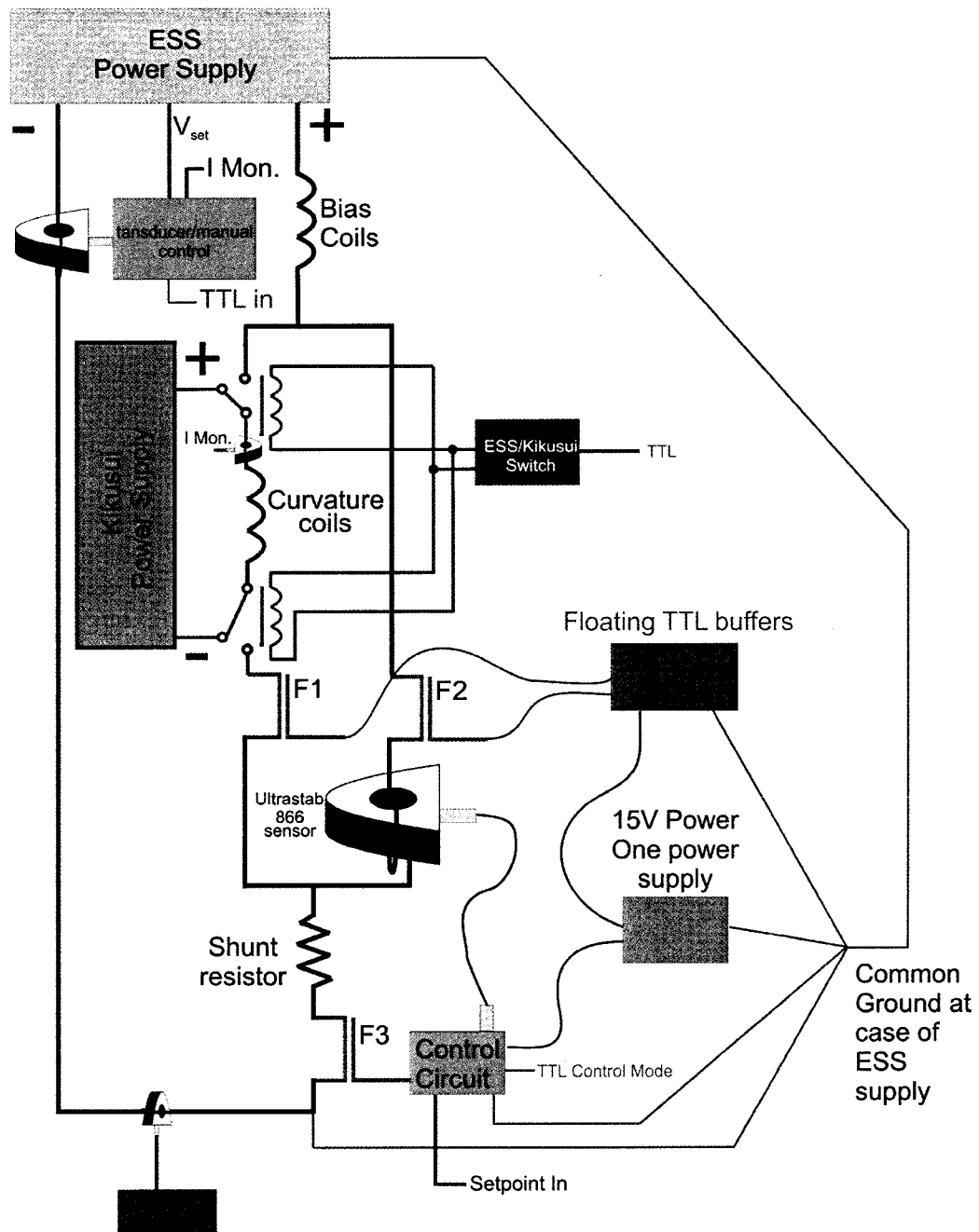
Figure 3.13 : Schematic diagram showing the control and diagnostic electronics for the electromagnetic coils used in the experiment

reader is directed to C. Welford's masters thesis [6] for detailed technical background. As described in [6] during the high field configuration, FET F1 is nonconducting and F2 is conducting. The current through the bias coils is then controlled by the modulation of FET F3 accomplished by the Control Circuit. This circuit compares the current measured by the Ultrastab 866 sensor with a set point provided by an arbitrary waveform generator (not shown). Shown in green is the circuitry used to energize the curvature coils while in the high field. Figure C.1 shows the circuitry used for switching the high current relays via TTL. This circuit allows for switching of the curvature coils out of the main (ESS supply) circuit and into a secondary circuit powered by a low current Kikusui power supply. The power supply is then controlled via an analog input from the control computer for ramping of the current in the curvature coils. Also note the many transducers in the system. These devices allow for the independent measurement of the current in the bias and curvature coils for diagnostic purposes.

One of the primary reasons for using F3 to control the current through the bias coils is to take full advantage of the ability to change the field using a preprogrammed arbitrary waveform. However, such arbitrary control is not possible without damaging the control FETs unless the voltage set point of the ESS power supply is set to move in tandem with the current through the coils. The reason for this is shown in Figure 3.14 that shows the dissipated power in F3 as a function of current through the coils, for a fixed voltage set point. The FETS must dissipate a power given by
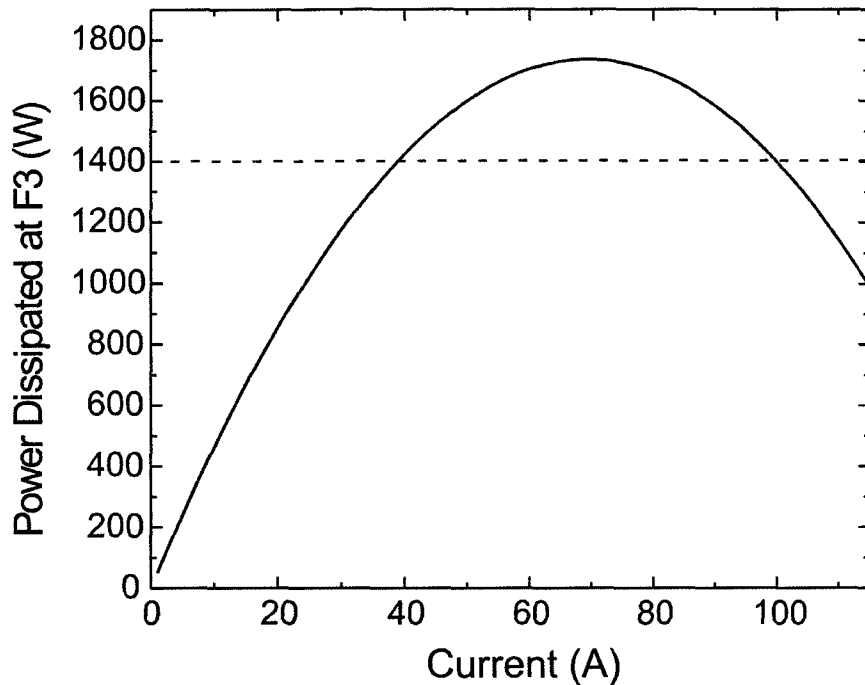
Figure 3.14 : Power dissipated in matched FET pair used as F3. The dashed line shows twice the power rating for a single FET, part number IXFN230N10.

$P = IV_{ESS} - I^2 R_{bias}$ where $R_{bias} = 360\,m\Omega$ is the resistance of the pair of bias coils and $V_{ESS} = 50\,V$ is the high field set point on the power supply. Currently, two matched high power FETs (PN: IXFN230N10), each having a power rating of 700 W are wired up in parallel, the pair functioning as F3. According to Fig. 3.14, the FETs will begin to fail if the current is ramped below 100A (∼630 G), consistent with our observations.[7] The design in Fig. 3.13 solves this problem by setting the voltage set point on the supply in two different ways. In the magnetic trap and initial high field configurations, the voltage is manually set by a pot on the front panel as described in

---

[7] One of the skills one acquires very early as an experimentalist is the uncanny ability to quickly distinguish the sweet smell of fried FET, burned resistor, or the always spectacular popped transient voltage suppressor.

[6]. However, shortly after the ramp to high field, the voltage control is switched over to "transducer control." In this configuration, a transducer is used to measure the current and to set the voltage of the ESS proportionally. This functionality is accomplished by the transducer/manual control circuit shown in Fig. 3.13 and described in the Appendix, Fig. C.2.

3.4.1 Non-ideality of the Bias Coils

The bias coils are not perfectly Helmholtz and consequently produce a small amount of magnetic curvature and gradient. The presence of this gradient and curvature makes evaporation in the optical trap impossible due to displacements of the trap center as a function of trap depth. Sometimes, the curvature induced by the bias coils may even be anti-trapping and this displacement will be accompanied by a severe loss of atoms out of the sides of the trap. The trapping frequency induced by a magnetic field curvature can be found from a simple energy consideration and is given by

$$\vec{\mu} \cdot \vec{B} = \frac{1}{2}m\omega^2 z^2 \tag{3.1}$$

$$\omega = \sqrt{\frac{2\mu B''}{m}} \tag{3.2}$$

For ^{7}Li atoms in the $|1,1\rangle$ state with a magnetic moment of $\sim \mu_B$, the trap frequency induced by a moderate magnetic curvature of $0.714\,\text{G/cm}^2$ produced by a

127 μm separation error in the bias coils is $\omega_{Bias} = (2\pi)\,3.8\,\mathrm{Hz}$. [8] Our measurements

show that the residual trap frequency from the curvature in the bias coils can vary

but is usually about 4 Hz or less if one wraps the coils properly. We often shim

the coils to "fine tune" this residual curvature. In addition, to compensate for the

curvature created by the bias coils, we can energize the curvature coils as described

above.

The stray gradient seen in the high field also varies from one coil build to another

but is typically anywhere from $0.5 - 1.0\,\mathrm{G/cm}$. The shift in trap position due to a

stray gradient can be found by using Eqn. 3.1 and completing the square, resulting

in

$$z_{shift} = \frac{\mu B'}{m\omega^2}. \tag{3.3}$$

Typical optical trap frequencies at the end of the evaporation in the single beam

trap are about 3 Hz (but can be as low a 1 Hz for the 1D transport experiments),

so we can see that without external compensation this effect would lead to 10's

of mm of axial movement during the evaporation. This effect always keeps us from

creating BECs without external compensation. To compensate for the stray gradient

we introduce an equal and opposite gradient by energizing a single coil. We call this

coil the push coil, because as proven above, altering the field gradient can have the

---

[8]This curvature was calculated using the Biot-Savart code written by A. Truscott.
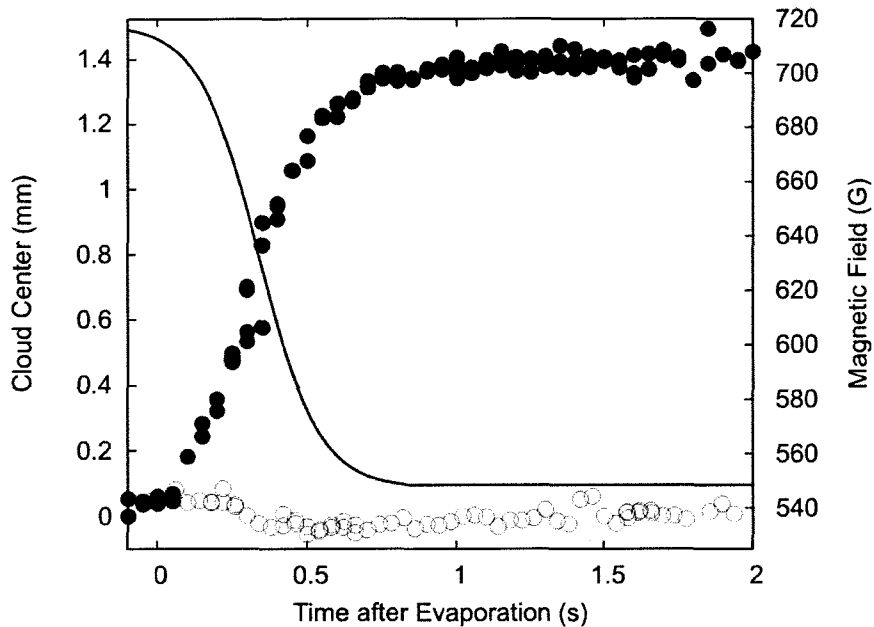
Figure 3.15 : Push coil correction for field ramp. Solid black line shows the magnetic field ramp. Filled blue circles show the center of the BEC during this ramp for a fixed push cage current. The open circles show the center of the cloud during the ramp using our push cage stabilization scheme. See text and Appendix C for details.

effect of "pushing" the cloud around.[9] As mentioned above, many of our experiments require the ability to sweep the field during a run in order to tune a using the Feshbach resonance. This ramp is another source of motion for the BEC. As the total current changes in the coils, the stray gradient and curvature change causing the center of the BEC to shift in position. To counteract this effect we must change the current in the push cage accordingly. The current in the push cage is controlled via feedback to a FET, similar to the high field control [6]. The set point is derived by measuring the current going through the bias coils using a transducer as shown in Fig. 3.13.

---

[9]The ability to push the cloud around is in fact very useful. For example, a quick "kick" from this coil made by briefly switching it off, can be used to drive the collective dipole mode of the BEC.
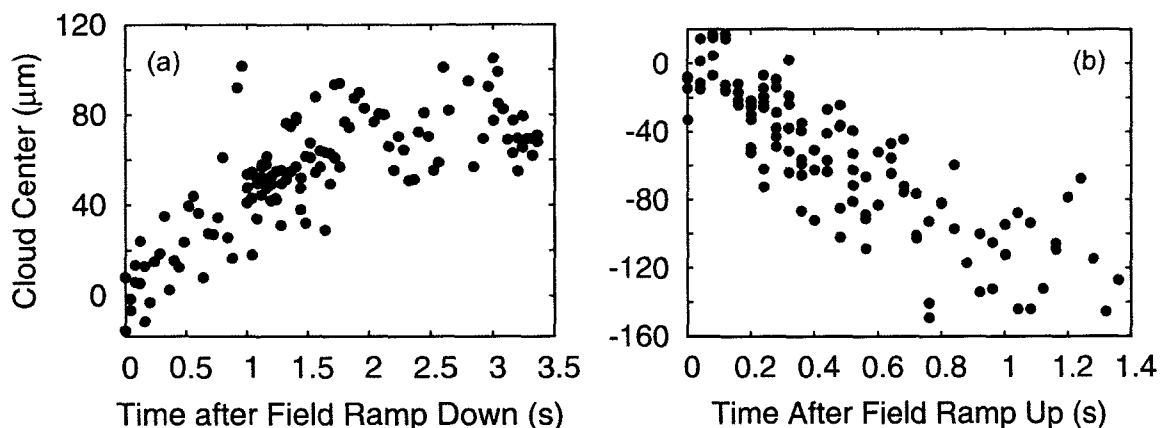
Figure 3.16 : Hysteretic drift the cloud position. (a) Central position of the cloud as a function of time after a bias ramp of ramp from 717 G to 545 G showing a *positive* drift. (b) Central position of the cloud as a function of time after a bias ramp of ramp from 545 G to 717 G showing a *negative* drift. Both data sets were taken using a fixed push coil current of 6.15 A.

The set point is therefore proportional to the bias field, resulting in a stable cloud position as illustrated in Fig. 3.15. A schematic showing the details of the push coil control circuit is shown in Fig. C.3.

Figure 3.15 shows that the push stabilization circuit does a reasonable job at eliminating the movement of the cloud induced by the field ramp. However, close inspection of the movement of both the corrected system and uncorrected system after the ramp down shows an additional slow drift, not directly caused by the ramp. Figure 3.16(a) shows a zoom-in of the stabilized data shown in Fig. 3.15 for times after the ramp down of the field. It can immediately be seen that the cloud drifts toward increasing position $\sim 80\mu$m over 2 s. Shown in Figure 3.16(b) is a similar measurement but this time, the center of the cloud is tracked after a ramp up of the field. Here we find that the cloud center drifts toward *decreasing* position. It

therefore appears that the direction of this long time drift depends on the initial value of the field, *before* the ramp. Such an effect could be explained by a slow drift in the push cage somehow induced by the ramp. However, we see the drift even for a constant push current (i.e. not ramping the push cage). For the particular trap parameters used here, the push cage current would have to drift by about 2% or nearly 120 mA. [10] It is unlikely that this drift is caused by the push since the stability specification for the power supply is $\pm 0.1\% + 1\,\text{mA}$. Even if the supply was not performing up to specification, it is hard to reason that any drift in the supply would be correlated with the sense of the bias field ramp, since in constant current mode, the push cage and bias field circuitry are completely decoupled.

Therefore, assuming that the gradient from the push cage is not the source of this drift, another possibility could be a slow drift of the trap frequency, however this interpretation is not consistent with our observations. During the optical trap evaporation, with $I = 6.15\,\text{A}$ on the push coil, the cloud moves less than $100\,\mu$m for a $\Delta\omega \sim 70\,\text{Hz}$. Equation 3.3 then tells us that we have canceled any external gradients to the .01 G/cm level. We measure the drift in trap frequency to be negligible after the evaporation so this possibility is ruled out. [11]

Due to the hysteretic nature of the drift (i.e. the direction of the drift depends

---

[10]The axial trap frequency was $\omega_z \approx (2\pi)\,5\,\text{Hz}$ for this data. For this trap we measure a shift of 0.9 mm/A of push current. The push current for this data was set to 6.15 A.

[11]For reference, we do observe a slight change in trap frequency vs. field of 2.5 mHz/G due to the non-Helmholtz nature of the bias coils. However, we have used RF spectroscopy to show that the field drifts by less than 200 mG over the duration reported in Fig. 3.16. Such a small drift therefore does not contribute significantly to the observed shift in center position of the cloud.

on the *historical* value of the field), one suspects a magnetization of the chamber due to the bias field as a possible explanation. If this magnetization resulted in a stray gradient on the order of 0.01 G/cm it could possibly explain the effect. While the chamber itself is made from non-magnetic 304 stainless steel, the Kovar seals on the reentrant windows could conceivably magnetize.

3.5 A Widely Tunable Probe Laser for Imaging Ultra-Cold Quantum Gases

3.5.1 Dispersive Imaging

Imaging ultra-cold quantum gases is by now a mature subject, with both absorption and phase contrast imaging techniques widely employed throughout the world. A particularly instructive discussion of the relevant physics can be found in the Ph.D. of Curtis Bradley [17]. In addition, the master's thesis of R. Kamar [18] has an extensive discussion of absorption imaging, a method frequently used to image ultra-cold quantum gases. The interested reader is also encouraged to consult the Proceedings of the Enrico Fermi School on BEC [19]. In the following section, I will briefly review the physics of dispersive imaging in ultra-cold gases with a focus on the details of our implementation of polarization phase contrast imaging (PPCI).

When a laser passes through a gas of ultracold atoms the result is just as one would expect: the beam gets both attenuated and phase shifted. By measuring both the absorption and phase shift due to the atomic cloud, a wealth of information
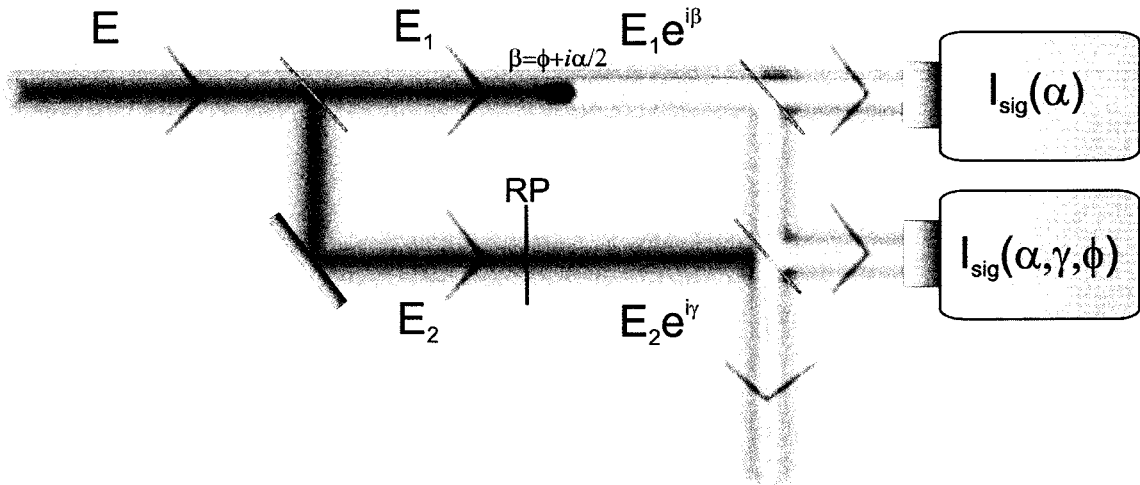
Figure 3.17 : Shown here is a cartoon of a generic system that would allow for the phase retardation and absorption properties of an object to be measured.

can be obtained about the gas. To concisely account for both the absorptive and retardation effects of an object on an electromagnetic (EM) wave it is convenient to introduce the idea of the complex phase $\beta = \phi + i\alpha/2$ where α is the absorption coefficient and ϕ is the induced phase shift. Figure 3.17 shows how one would design a simple system to measure both the absorption and induced phase shift of an object. The electromagnetic wave of amplitude $\vec{E_0}$ is split on the 50/50 beam splitter and the portion traveling along path 1 encounters the object and acquires a complex phase β. The resulting field is $\vec{E_1}e^{i\beta}$. The field from path 2 encounters a retardation plate that introduces an additional relative phase shift between the two beams of θ. The two fields are then recombined on the output beam splitter and imaged on the CCD detector. Assuming $\vec{E_1}$ and $\vec{E_2}$ are the same polarization, the resulting field

and intensity distributions are

$$\vec{E_{sig}} = \vec{E_1}e^{i\beta} + \vec{E_2}e^{i\gamma} \tag{3.4}$$

$$I_{sig} = \left|\vec{E_{sig}}\right|^2 = E_1^2 e^{-\alpha} + E_2^2 + 2E_1 E_2 e^{-\alpha/2}\cos(\phi - \gamma) \tag{3.5}$$

Equation 3.5 clearly shows that the field imaged on the lower CCD depends on both α and ϕ. It can also be clearly seen that if ϕ is small, as it is in most cases for our experiments, the sensitivity to ϕ in the final term is maximized when $\gamma = \pi/2$.

In the specific case of a gas of atoms with the laser tuned near an atomic transition, one can show that the complex phase is related to the column density $n_x(y, z) = \int n(x, y, z)dx$ with α and ϕ given by [20]:

$$\alpha = \frac{\sigma_0 n_x \Gamma^2}{4\Delta^2 + \Gamma^2 + 2\Omega^2} \tag{3.6}$$

$$\phi = -\Delta\alpha \tag{3.7}$$

with Γ being the natural linewidth of the transition and Δ the detuning of the laser from resonance. The cross section, σ_0 is given by

$$\sigma_o = \frac{3\lambda^2}{2\pi}(2j_u + 1)\sum_q |\hat{\varepsilon}_q \cdot \hat{\varepsilon}|^2 \begin{pmatrix} j_u & 1 & j_l \\ -m_u & q & m_l \end{pmatrix}^2 \tag{3.8}$$

where the subscripts u and l denote the upper and lower energy levels of the transition
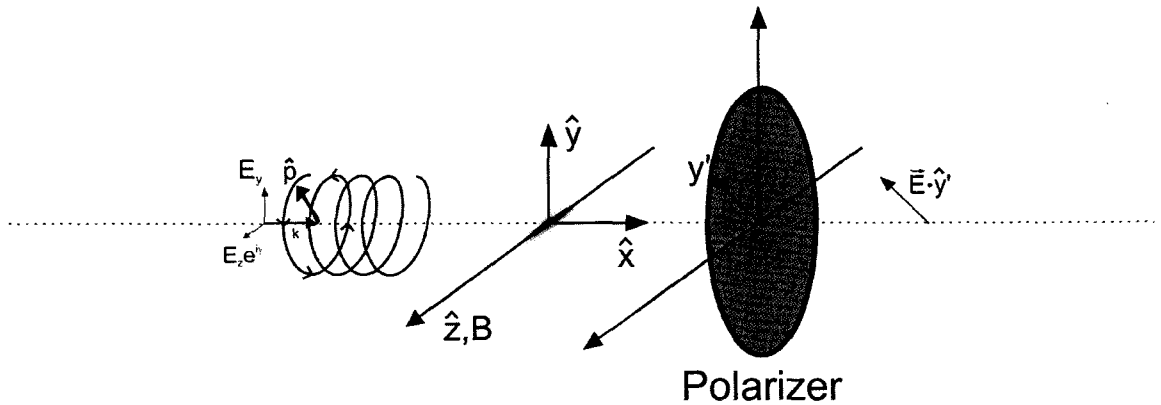
Figure 3.18 : Shown here is the specific PPCI set used for our experiment. We use circularly polarized light that propagates perpendicular to the magnetic field.

being driven, $\hat{\varepsilon}$ denotes the unit vector describing the polarization of the probe field, and the index q runs over all possible transition polarizations. It is important to note that the form of σ_0 leads to birefringence, with both ϕ and α strongly dependent on the polarization and the propagation direction of the probe field. In fact, in some cases one can find two orthogonal polarizations: one that interacts with the atoms and one that does not (called the bystander field). In our experiment we use this fact to our advantage and simplify the optical setup in 3.17. Rather than using a two leg interferometer, one can use a single elliptically polarized beam and treat the two orthogonal polarizations as independent beams. After this probe passes through the atoms, one polarization will have β encoded on it while the orthogonal polarization passes through unaffected. Subsequently, a polarizer is used to project the two components of the probe field onto the same polarization and observe the resulting interference on the CCD. The geometry of our imaging setup is shown in Fig. 3.18.

We choose our quantization axis to be the z-axis and also the direction of the applied magnetic field. The probe beam propagates along the +x direction and to start we will keep the polarization arbitrary describing it in terms of the real parameters a_1 and γ.

$$\vec{E}_0 = E_0 \hat{p} \tag{3.9}$$

$$\hat{p} = a_1 \hat{y} + \sqrt{1 - a_1^2} e^{i\gamma} \hat{z} \tag{3.10}$$

With $a_1 \in \{0, 1\}$ and $\gamma \in \{0, 2\pi\}$. With light propagating along x as we have, the y-component can couple to both σ_+ and σ_- transitions with equal strength. For all the data in this thesis, we drive the $2^2S_{1/2}\, m_I = 3/2, m_j = -1/2 \rightarrow 2^2P_{3/2}\, m_I = 3/2, m_j = -3/2$. This transition is considered σ_- since $\Delta m_j = -1$ and therefore due to the symmetry properties of the 3-j symbols, the only term in the sum over q in in Eq. 3.8 that survives is for $q = -1$. We then immediately see that the y-component of the probe couples to the atoms with a cross section of $3\lambda^2/(4\pi)$ and the z-component serves as the bystander light. The probe field after it passes through the atoms is then

$$\vec{E}(y, z) = E_0 a_1 e^{i\beta} \hat{y} + \sqrt{1 - a_1^2} e^{i\gamma} \hat{z} \tag{3.11}$$

The polarizer only passes light with polarization that is parallel to the y' axis described by the unit vector $\hat{y}'$. The final probe amplitude is then $E_{\text{sig}} = \vec{E}(y, z) \cdot \hat{y}'$

with given by

$$\vec{E}(y,z) \cdot \hat{y}' = \left(E_0 a_1 e^{i\beta} \sin(\theta) + E_0 \sqrt{1 - a_1^2} e^{i\gamma} \cos(\theta) \right) \qquad (3.12)$$

Substituting for β and taking the square gives the measured intensity

$$I_{\text{sig}} = E_0^2 a_1^2 \sin^2(\theta) e^{-\alpha} + E_0^2 (1 - a_1^2) \cos^2(\theta) + 2E_0^2 a_1 \sin(\theta) \sqrt{1 - a_1^2} \cos(\theta) e^{-\alpha/2} \cos(\phi + \gamma)$$

$$(3.13)$$

Comparison with Eq. 3.5 reveals the immediate similarity. As before, maximizing sensitivity to ϕ in the third term suggests $\gamma = \pi/2$ but now $a_1 = 1/\sqrt{2}$ is required to maximize the third term, i.e. circularly polarized light. In addition, the polarizer should be set to $45°$ to maximize the phase sensitive signal. Further inspection of Eq. 3.13 reveals that this method of imaging is quite versatile due to the fact that one can switch between purely absorptive imaging and polarization phase contrast imaging with a simple movement of the polarizer from $45°$ to $90°$. For the case of polarization phase contrast imaging one now has

$$I_{\text{sig}} = \frac{E_0^2}{4} e^{-\alpha} + \frac{E_0^2}{4} - \frac{E_0^2}{2} e^{-\alpha/2} \sin(\phi) \qquad (3.14)$$

In practice, to improve signal to noise, we take two pictures: one with atoms and

one without, then subtract the two and divide by the no atoms shot

$$S = \frac{I_{\text{atoms}} - I_{\text{noatoms}}}{I_{\text{noatoms}}} = -\frac{1}{2} + \frac{1}{2}e^{-\alpha} + e^{-\alpha/2}\sin(\phi) \qquad (3.15)$$

This equation is then solved numerically to get the column density n_z.

3.5.2 Non-destructive PPCI

For large detuning, i.e. $(\Delta/\Gamma)^2 \gg I/I_{\text{sat}}$, the off resonant scattering rate from the probe beam is negligible, and PPCI can be very useful for nondestructive *in situ* imaging. By operating the Andor camera in "fast kinetics" mode, multiple pictures may be taken of the same cloud in a *single* run for time steps as fast as $400\,\mu s$ (See Appendix D for details). This capability (multipic) is an extreme time saver for various diagnostic measurements. We find that at $10\,\Gamma$ detuning and $I/I_{\text{sat}} \sim 0.2$ we can take 10 pictures of the same cloud on a single run without significant loss of atoms, as shown in Fig. 3.20. For example, trap frequencies can now be made in a single 45 s run, whereas before it would have taken ten times that long. Multipic has also proved useful in diagnosing problems with residual movement of the cloud after evaporation. Whereas before we could only deduce that the cloud was in a different positions on every shot, multipic allowed us to know that the cloud was undergoing a random phase small amplitude dipole oscillation at the end of the evaporation. Examples of multipic results are shown in Fig. 3.19.

(a) **(b)** **(c)**
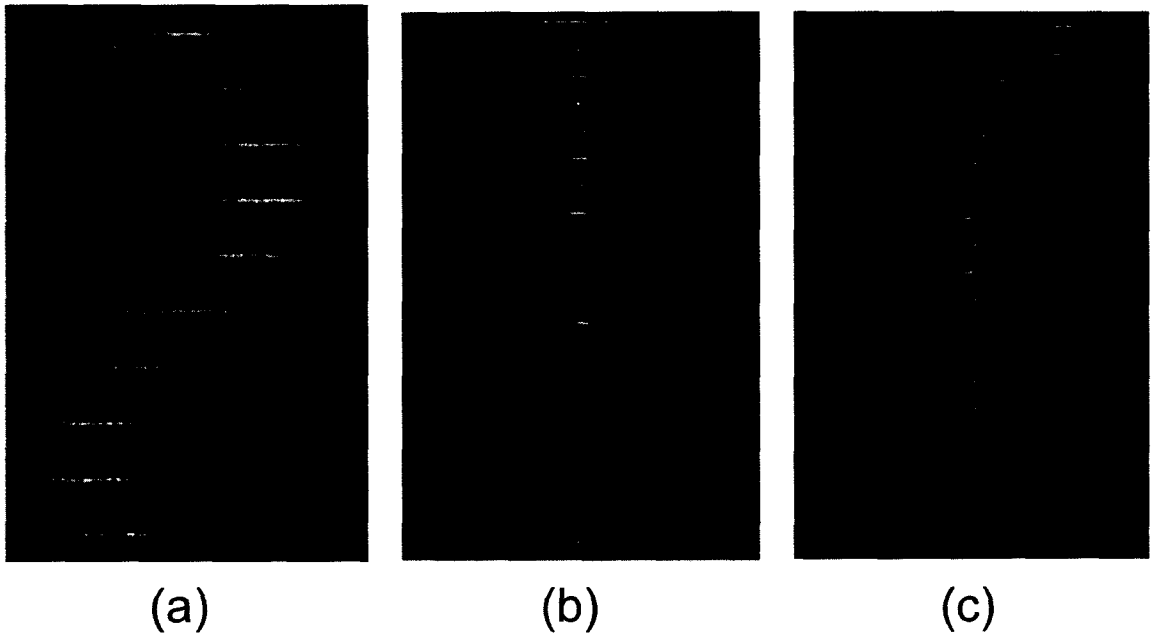
Figure 3.19 : (a) A trap frequency measurement, $\Delta t = 20\,\text{ms}$ per shot. (b) Movement of the cloud during the fast evaporation shown in Fig. 3.11, $\Delta t = 100\,\text{ms}$ per shot. (c) Evaporation from a displaced optical trap into a tight axially confining trap dominated by the curvature coils, $\Delta t = 100\,\text{ms}$ per shot.

3.6 External Potentials for the Study of Transport in BEC

3.6.1 Disordered Potential from Laser Speckle

Historically, the study of BEC has been limited to "ideal" potentials, e.g. harmonic traps and optical lattices. These traps are the work horses of the field and have been used to prove that BECs can be useful for studying some of the most fundamental concepts of condensed matter physics. Several of the paradigmatic results of condensed matter physics have been observed to date including: superfluidity and vortex lattices, the superfluid to Mott insulator transition, and Cooper pairing of fermions. In particular, there has been a recent push to use atomic BEC to emulate
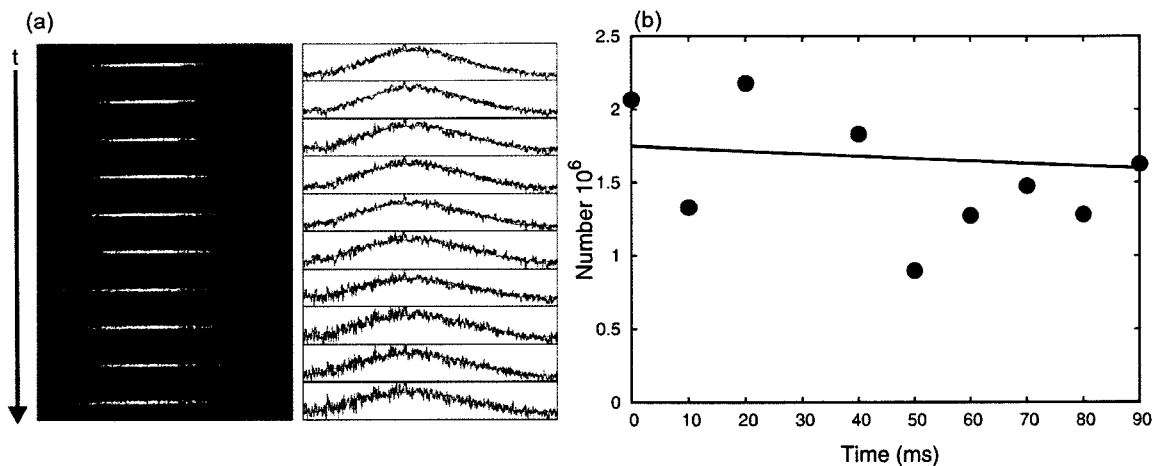
Figure 3.20 : (a) The result of 10 consecutive phase contrast images with $\Delta/\Gamma = 10$ and $I/I_{sat} = 0.2$. Separation between shots is $\Delta t = 10$ ms with a probe pulse duration of $5\,\mu s$ per shot. These shots were taken at full trap depth in the single beam optical trap at $a = 200\,a_0$ where the lifetime is dominated by three body loss with a $1/e$ decay time of $\tau \sim 1$ s. (b) Number of atoms in each shot in (a). The solid line is not a fit but rather a guide showing the expected $1/e$ lifetime of $\tau \sim 1\,s$ cloud in the trap. The excellent agreement with the data suggests that the imaging process does not contribute significantly to the loss.

real, less perfect condensed matter systems, i.e. systems with disorder. One of the most attractive aspects of atomic systems is that starting from the simple harmonically trapped BEC, one can *controllably* add disorder to the system thereby making it more like a "real" condensed matter system albeit with a *well characterized* disorder. What follows in this section are the technical details outlining how we create disordered potentials for atoms from optical speckle patterns.

When a diffusing surface is illuminated by a coherent, monochromatic source of radiation, what results from the scattered radiation is a grainy, noisy, spatially fluctuating intensity profile, a so-called speckle pattern. Physically, one can understand the formation of a speckle pattern as the result of the coherent superposition, in

Coherent Light

Diffusive Plate

Lens System
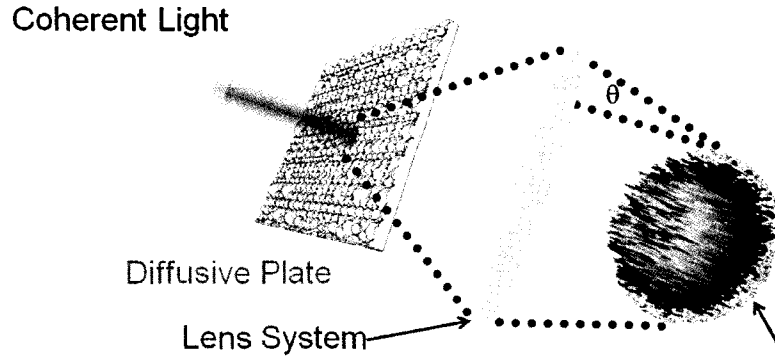
Figure 3.21 : A speckle pattern results from the transmission of coherent light through a rough surface. The correlation length of the speckle pattern is determined by the limiting numerical aperture $(\text{NA} = \sin(\theta))$ of the imaging system used to create the pattern.

the far field, of a large number of randomly phased point sources originating from the scattering plane. Mathematically one can understand the process of speckle formation by applying the Huygens-Fresnel principle in the far field approximation [21]

$$E_2(x,y) = \frac{e^{-i\frac{\pi}{\lambda z}(x^2+y^2)}}{\lambda z} \int dx_1 dy_1 E_1(x_1,y_1) e^{-i\frac{\pi}{\lambda z}(x_1^2+y_1^2)} e^{-i\frac{\pi}{\lambda z}(xx_1^2+yy_1^2)}, \qquad (3.16)$$

where $E_1(x,y)$ and $E_2(x,y)$ are the field amplitudes on the diffuser and at a distance z away, respectively. If one make the substitution

$$E_1' = E_1(x,y)e^{-i\frac{\pi}{\lambda z}(x^2+y^2)} \qquad (3.17)$$

$$E_2' = E_2(x,y)e^{-i\frac{\pi}{\lambda z}(x^2+y^2)}, \qquad (3.18)$$

one immediately sees that

$$E_2' = \mathscr{F}^{-1}(E_1'),$$ (3.19)

where $\mathscr{F}^{-1}(f(x,y))$ is the 2D inverse Fourier transform of $f(x,y)$. Adding the effect of an arbitrary aperture on the final distribution is then as simple as multiplying $E_1'(x,y)$ by a windowing function $W(x,y)$ describing the aperture before propagating the field via the Fourier transform. To theoretically construct the speckle pattern all one does is to let $E_1(x,y)$ consist of a set of phasors whose amplitude is determined by an aperture function $W(x,y)$ (for example a Gaussian or a rectangle function) and whose phases are uniformly distributed random numbers over the interval $[0, 2\pi]$.[12]

Armed with Eq. 3.16 one can derive the characteristic statistical properties of the speckle intensity pattern (i.e. the disordered potential) [21]. For example, the probability density for the intensity follows the decaying exponential:

$$P(I) = \frac{1}{\langle I \rangle} e^{-\frac{I}{\langle I \rangle}}.$$ (3.20)

From this knowledge one can immediately show that $\langle I \rangle = \Sigma_I$ where Σ_I is the standard deviation of the speckle. The "strength" of the disorder V_D is related to the average height of the intensity fluctuations and therefore $V_\mathrm{D} \propto \Sigma_I = \langle I \rangle$. In practice it is easier to measure $\langle I \rangle$ using a calibrated photodetector rather than

---

[12]The above equations then give a straightforward way to numerically generate speckle. First create $E_2'(x,y)$ by populating a 2D grid with random complex numbers of unit amplitude (e.g. the ordered pair $(\cos(2\pi x), i\sin(2\pi x))$ with the uniformly distributed random number $x \in [0,1]$.). Then Fourier transform back to $E_1'(x,y)$, apply the aperture function and then inverse Fourier transform to the final $E_2'(x,y)$.

imaging the speckle potential on each shot and calculating Σ_I. Specifically, the

average value of the speckle intensity $\langle I \rangle$ determines the disorder strength through

the relation $V_D = \hbar\Gamma^2 \langle I \rangle /(4 I_{sat} \Delta)$, where the transition linewidth $\Gamma = (2\pi) 5.9 \, \text{MHz}$,

the saturation intensity $I_{sat} = 5.1 \, \text{mW/cm}^2$, and the detuning from the $^7\text{Li} \, 2S \to 2P$

transition $\Delta = (2\pi) 300 \, \text{GHz}$ (blue). [13]

Another useful statistical property of the disorder potential is the autocorrelation

function, $c(\Delta z) = \langle I(z) I(z + \Delta z) \rangle$. This function, which is intimately related to the

Fourier transform of the aperture function $W(x, y)$[14] determines the minimum length

scale over which the speckle pattern has any spatial structure. Since the speckle

pattern originates from the scattering of light, the power spectrum (as well as the

autocorrelation) has finite support, determined by the diffraction limit of the optical

system used to create the speckle, that is to say the minimum spatial frequency found

in the signal is given by $\sigma_D \sim \lambda/(2\text{NA})$.[15] By engineering $W(x, y)$ one can affect

the functional form of $c(\Delta z)$. For example, for a non-apertured Gaussian beam, the

Fourier transform of $W(x, y)$ is simply the Gaussian envelope of the beam, leading

---

[13]For the strongest disorder used in these studies, off-resonant scattering from the disorder occurs at a rate of $\sim 0.1 \, \text{s}^{-1}$.

[14]By the Wiener-Khinchin theorem, the autocorrelation of a signal is the inverse Fourier transform of the power spectrum.

[15]One remarkable fact about fully developed speckle is that the cutoff in $c(\Delta z)$ is *always* given by the diffraction limit, even if the optical system used to generate the speckle introduces a large amount of aberration onto the wavefront. One way to understand this is that the diffuser already maximally aberrates the wavefront by completely randomizing the phase over a length scale on the order of the distance between scattering centers. Any additional aberrations induced on this already randomized wavefront are of little consequence. One can therefore measure the numerical aperture of a distant scatterer (i.e. the angular size of the source, say a star) by looking at the correlation length of the speckle potential scattered from the object regardless of the aberration picked up along the way from source to object! This is purely classical way of understanding the robustness of the Hanbury Brown-Twiss interferometer [22].
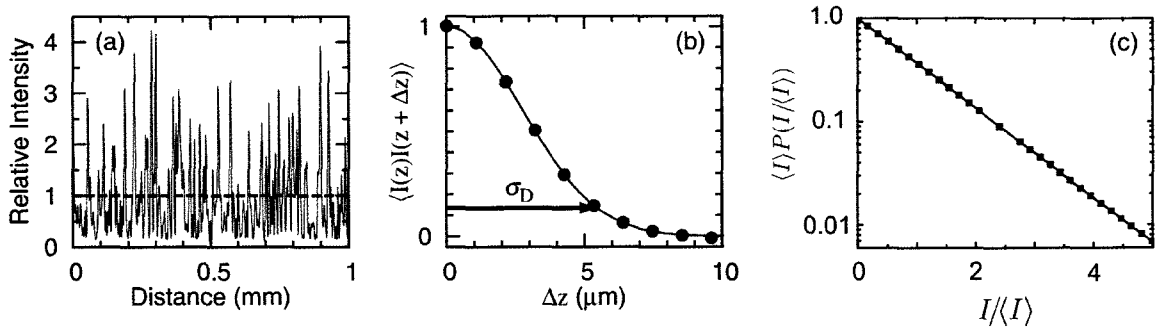
Figure 3.22 : Disordered potential created from laser speckle. (a) Cut through an image of the speckle potential. The disorder strength V_D is proportional to the average value of the intensity $\langle I \rangle$ (dashed line). (b) The autocorrelation of the intensity distribution is well fit by a Gaussian with $1/e^2$ radius $\sigma_D = 5.5\,\mu$m. (c) Measured intensity probability distribution $P(I)$ showing a negative exponential as expected for fully developed speckle.

to

$$c(\Delta z) \propto e^{-2\Delta z^2/\sigma_D^2}. \tag{3.21}$$

Much of the data in this thesis was taken using a disorder potential with a correlation function described by Eq. 3.21, as this resulted from the second generation optical setup described in J. M. Hitchcock's M.S. thesis [23]. A detailed characterization of this disorder is also shown in Fig. 5.1. This design was a compromise solution for obtaining both a high intensity at the atoms (i.e. minimize clipping of the beam on the optics) and a small correlation length. However, to avoid clipping of the beam, we did not take full advantage of the numerical aperture of the chamber leading to $\sigma_D = 5.5\,\mu$m, a value slightly larger than the fundamental limit corresponding to the chamber view port acting as the limiting aperture, $\sigma_D^{\min} = 3.0\,\mu$m. We have since implemented an improved system for taking full advantage of the numerical

aperture afforded to us at the expense of dumping some power by clipping some of the Gaussian beam. A schematic diagram of this new system is shown in Fig. 3.23.
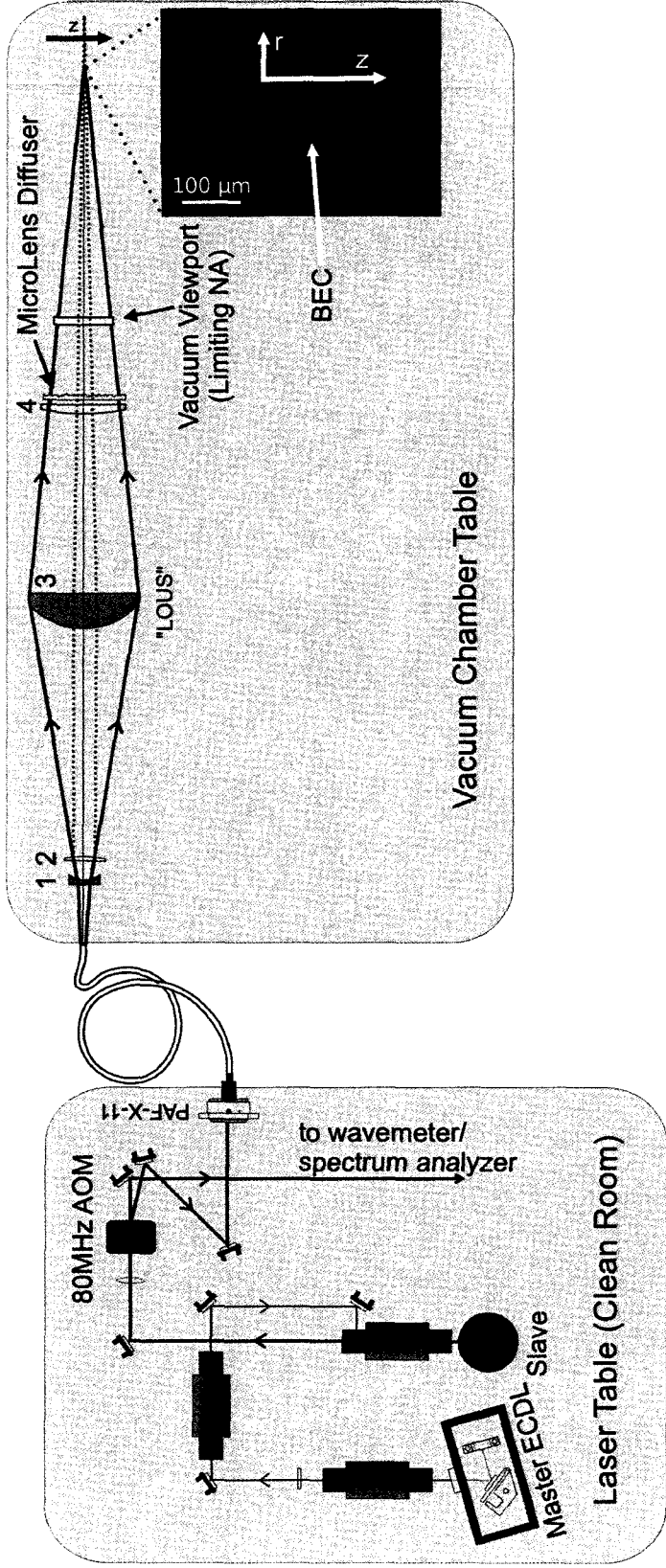
Figure 3.23 : The new system designed to take full advantage of the numerical aperture of the vacuum chamber. The master laser consists of a free running ECDL used to injection lock a high power diode laser model HL6555. This laser outputs ~45 mW that is sent to an AOM for switching and an optical fiber for mode cleaning and transport of the beam to the vacuum chamber. This setup allows for ~30 mW at the output of the fiber. A small fraction of this output is split from the main beam and monitored for diagnostics and intensity stabilization via the PI feedback scheme outlined in App. A. Also shown is a 2D image showing the disorder potential at the location of the atoms, obtained with a CCD camera before the system was installed on the chamber. Note the highly elongated nature of the speckle due to the highly elongated shape of the beam at the microlens diffuser. For the radial direction (path shown by blue dashed rays), lenses 1 (f=-15 mm, spherical), 2 (f=50 mm, cylindrical with axis along r) and 3 (f=200 mm, spherical) work in combination to make a beam waist of < 1 mm at the diffuser, while for the z-direction (path shown by red solid rays) lenses 1, and 3 blow the beam up to ~50 mm at the diffuser. The final cylindrical lens 4 (f=250 mm, cylindrical with axis along z) focuses the beam along a path that maximizes the NA in the z-direction.

There were two main changes in the design relative to that laid out in Ref. [23]. The first change was to increase the numerical aperture of the system. This was accomplished through the addition of the "Lens of Unusual Size" (LOUS).[16] In the old system it would have been the smaller cousin of this lens that would have been limiting the NA of the system, not the UHV view port. The new lens, as its name suggests, is comically large with a 3 in diameter. As mentioned earlier, in the previous design, due to our desire to have the maximum amount of light hitting the atoms, we were very careful not to clip the beam to within ~ 2 beam waists, anywhere in the system. This led to the old system not even taking full advantage of the NA available given the geometry of the chamber. The new system was designed with the prospect of investigating the localization of a BEC in a *weak* disorder, and as such, optical power was not our main design constraint. Rather, we wished to created as small of disorder as possible. To this end, we blew up the beam relative to the old design, with the result of clipping the beam at the LOUS at roughly 50% of the beamwaist. This ensured that it was indeed the vacuum viewport that was the limiting aperature not the Gaussian envelope of the beam. Because the beam on the limiting aperture is so big in the new system, the windowing function of the highly elongated beam at the diffuser approximates more of a rectangle. By Eq. 3.16, the envelope of the intensity distribution at the atoms is therefore a sinc^2 function. By the Wiener-Khinchin theorem this then makes the power spectrum of the disorder a

---

[16]It is alleged that this optic was manufactured in the bowels of the fire swamp by Prince Humperdinck and his menacing six-fingered assistant, Count Tyrone Rugen.
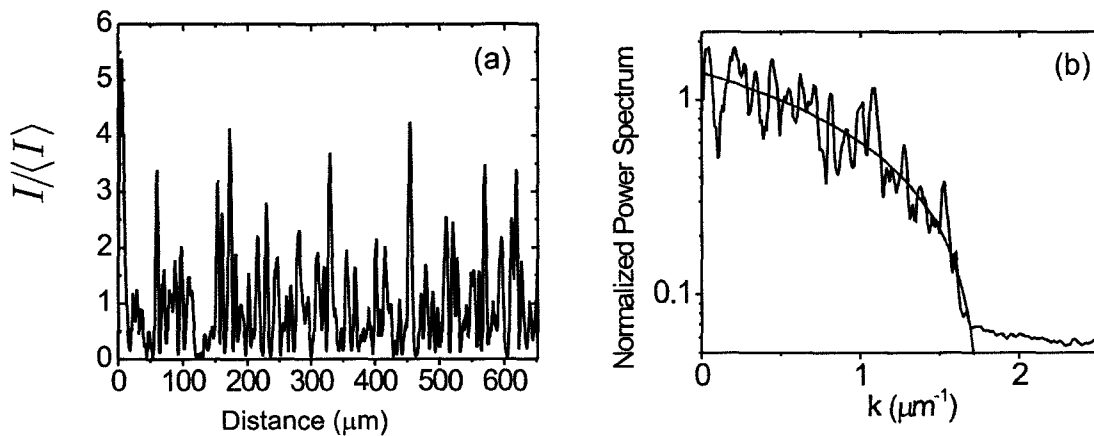
Figure 3.24 : (a) A 1D cut along the z-axis (long axis of the trap) of the disorder potential created by the setup shown in Fig. 3.23. (b) Average of 512 power spectra of 1D cuts like that shown in (a). Solid line is fit to the linear function $P(k) = 0.6\,(1.78\,\mu\mathrm{m}^{-1} - k)$.

triangle function. As shown in Fig. 3.24 this power spectrum fits well to the form:

$$
\hat{c}(k) = \begin{cases} 1 - kl_c/2 & \text{if } kl_c < 2, \\ \\ 0 & \text{otherwise.} \end{cases} \tag{3.22}
$$

with the correlation length $l_c \approx 1.1(2)\,\mu\mathrm{m}$. The normalized correlation function is then given by the inverse Fourier transform of Eq. 3.22

$$
c(\Delta x) = \frac{l_c}{\pi} \frac{\sin^2\left(\Delta x/l_c\right)}{\Delta x^2}. \tag{3.23}
$$

For ease of comparison with the previous disorder potential we fit the experimentally measured autocorrelation of many different cuts through the disorder to Eq. 3.21

rather than Eq. 3.23 with the result of $\sigma_D = 3.2(2)\,\mu$m. The error bar reflects the maximum deviation seen over measuring several hundred autocorrelations taken at different vertical positions in the disorder potential (covering a total vertical distance of $\sim 500\,\mu$m.). The new system therefore shows $\sim 40\%$ smaller disorder. Fitting the autocorrealtion functions to Eq. 3.23 simply inflates the size by $\sim 36\%$ so that $\sigma'_D = 4.4(4)\,\mu$m with the natural speckle size now taken to be the location of the first zero of the sinc^2, $\sigma'_D = \pi l_c$. This implies $l_c = 1.4(1)\,\mu$m, a value slightly larger than that obtained from the fit to the power spectrum. We take the average of these two measurements, $l_c = 1.3(2)\,\mu$m, for the remainder of this thesis. We will see later that the parameter l_c is extremely important for 1D transport in speckle potentials as it defines an effective mobility edge [24, 25].

Chapter 4

Physics Near a Feshbach Resonance

4.1 Introduction

Ever since the early days of atom trapping, characterization of the scattering proper-
ties of cold atomic gases has been of central importance. Particularly, knowledge of
the s-wave scattering length a is key. Remarkably, in low energy collisions, this single
parameter characterizes a wide range of physics. For example, the scattering length
determines the rate for both elastic and inelastic scattering processes within an ul-
tracold gas. In addition, the scattering length plays a pivotal role as the parameter
describing the strength of the effective interaction between atoms. For $a < 0$ atoms
behave as if they attract one another and for $a > 0$ effective repulsive interactions
are present. For a BEC, the strength and sign of these effective interactions can have
dramatic consequences. A high density BEC with attractive interactions, is unstable
to collapse, leading to the playfully termed "bose-nova" phenomena. In addition, for
BEC in a quasi-1D geometry attractive interactions allow for the creation of matter
wave solitons, atomic wave-packets that, due to the self focusing properties of the
attractive interactions, can propagate without dispersion. For a BEC with repulsive
interactions large stable condensates can be created. Such systems have proven ideal
for studying a variety of phenomena such as collective modes, sound propagation

and superfluidity in BEC.

In the case of ultracold Li, Nature has been particularly kind, providing us with broad Feshbach resonances at readily accessible magnetic fields. These resonances give us the ability to tune a over a huge range through the simple application of an external magnetic field. This chapter begins with a brief introduction to low energy scattering and the phenomena of Feshbach resonances in general. We then present our results characterizing the Feshbach resonance in the $|1, 1\rangle$ state of ^{7}Li. We then present results regarding soliton creation and the behavior of the quadrupole mode as a function of a.

4.2 Feshbach Basics

4.2.1 Introduction to Low Energy Scattering

In order to understand the physics of Feshbach resonances one must first understand the physics of low energy scattering. The quantum theory of scattering is a vast subject and has been treated exhaustively in countless articles, reviews and textbooks so I will only briefly review some of the fundamental results of the theory with special emphasis on those having relevance to the subject of Bose-Einstein condensation. [1]

In any low energy scattering problem, one typically begins by writing down the canonical form for the asymptotic wave function in the center of mass frame, describing the two particle scattering state as the sum of an incident plane wave and

---

[1] For a more detailed treatment focused on cold atoms see Pethick and Smith [26]. A very accessible introductory review can also be found in [27].

an outgoing scattered spherical wave:

$$\psi = e^{ikz} + \psi_{\text{scat}}(r) \tag{4.1}$$

For scattering from spherically symmetric potentials, ψ can be written as a superposition of Legendre polynomials $P_l(\cos\theta)$ (the so-called partial wave expansion)

$$\psi = \sum_{l=0}^{\infty} A_l P_l(\cos\theta) R_{kl}(r) \tag{4.2}$$

Plugging this function into the time independent Schrödinger equation (in the center of mass frame) and then applying separation of variables, one obtains for the radial portion

$$R_{kl}''(r) + \frac{2}{r} R_{kl}'(r) + \left(k^2 - \frac{l(l+1)}{r^2} - \frac{2\mu}{\hbar^2} U(r) \right) R_{kl}(r) = 0, \tag{4.3}$$

where μ is the reduced mass. Since we are considering only spherically symmetric potentials, $U(r)$ does not appear in the angular equation and Eq. 4.3 contains all the scattering physics. For the work in this thesis, we consider only very low energy scattering (the limit $k \to 0$) and therefore $l = 0$ is the only important term in the partial wave expansion.[2] To more clearly visualize the physics, it is convenient to

---

[2]The angular momentum of two colliding particles is given by dimensional arguments to be $|\vec{L}| = r_0 h/\lambda_{\text{T}}$ where r_0 is the length scale of the scattering potential ($\sim 30\, a_0$ for Li), λ_{T} is the thermal de Broglie wavelength, and $|\vec{L}| = \hbar\sqrt{l(l+1)}$. Taking $l = 1$ leads to $\lambda_{\text{T}} \sim 4\, r_0 = 120\, a_0$. Using $\lambda_{\text{T}} = h/\sqrt{2\pi m k T}$, one then finds $T_{l=1} \sim 3\,\text{mK}$. It is therefore reasonable to assume only s-wave scattering in our experiments since T is usually μK or even nK.

make a change of variables to $\chi(r) = rR(r)$ leading to the equation

$$\chi''(r) + \left(k^2 - \frac{2\mu}{\hbar^2} U(r) \right) \chi(r) = 0. \tag{4.4}$$

For $r \gg r_0$, where r_0 is the length scale associated with the interaction potential[3], $U(r) = 0$ and the solution to Eq. 4.4 takes the form of a plane wave

$$\chi(r) \propto \frac{1}{k} \sin(k(r-a)). \tag{4.5}$$

We therefore see that the result of the scattering process is simply a phase shift in the asymptotic scattering state, with the phase shift $\delta_0 = -ak$. One also immediately sees that for small k, a is simply the x-intercept of $\chi(r)$. For small r one must solve Eq. 4.4 to obtain $\chi(r)$. Examples of such wave functions characterized by three different values of a are shown in Fig. 4.1. The problem of low energy scattering thus reduces to problem of finding the scattering phase shift δ_0 or equivalently the scattering length a. From a theoretical perspective, once the potential is known, the scattering lengths can then be found by the calculation of the scattering wave functions $\chi(r)$. For attractive potentials, it can be shown that $a < 0$, while for repulsive potentials $a > 0$. This result, however, is only true if the potential does not support bound states. In general, the magnitude of a is extremely sensitive to

---

[3]For alkali atoms, the long range potential is dominated by the van der Waals interaction, with a length scale given by $R_{\mathrm{vdW}} = 1/2 \left(C_6 m/m_e \right)^{1/4} a_0$. For ^{7}Li, $C_6 = 1393$ A.U. resulting in $R_{\mathrm{vdW}} = 32.5\, a_0$ [26].

Distance (a_0)
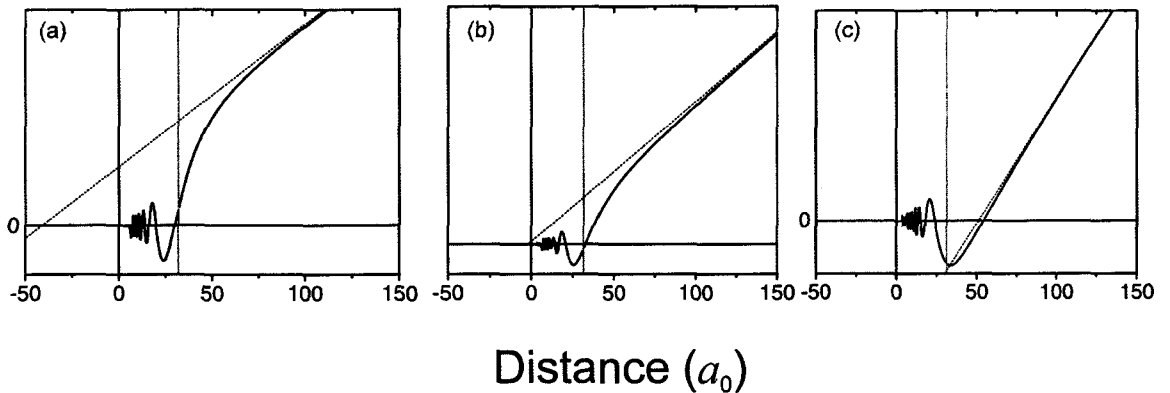
Figure 4.1 : Short range scattering wave functions for ^{7}Li in the $|1,1\rangle$ state at three three different interaction strengths. Panels (a), (b), and (c) are $a = -40\,a_0$, $a = 0\,a_0$, and $a = 50\,a_0$, respectively. These results were obtained via a numerical coupled channels calculation for three different magnetic fields near the Feshbach resonance at 737 G. (See detailed discussion below). They are shown here simply as examples of how the scattering length behaves like a virtual node in the asymptotic wave function. The solid green line denotes the van der Waals length.

the short range portion of the potential, and in particular the presence of bound

states (or virtual bound states) in the potential near the continuum can alter the

scattering length dramatically by way of near resonant threshold scattering. [4] This is

the essence of the tunability of the effective interactions in our system. By tuning the

location of a bound state relative to the continuum we can modify a (or equivalently

δ_0). As seen in Fig. 4.1 the asymptotic wave function then appears to have a node at

$r = a$. The consequence of this apparent node on the energetics of the gas is subtle

but of primary significance [27]. It can be most easily understood by likening the

behavior of the $r \to 0$ wave function to that of a pair of atoms trapped in a box of

width r_0. The energy of such a state is given by $E = \hbar^2\pi^2/(2\mu r_0^2)$. Changing the

---

[4]For example, the triplet scattering length of ^{6}Li is a whopping $-2160 \pm 250\,a_0$, nearly 70 times larger than the van der Waals length! This fact has been attributed to the presence of a near-threshold bound state in the scattering potential [28].
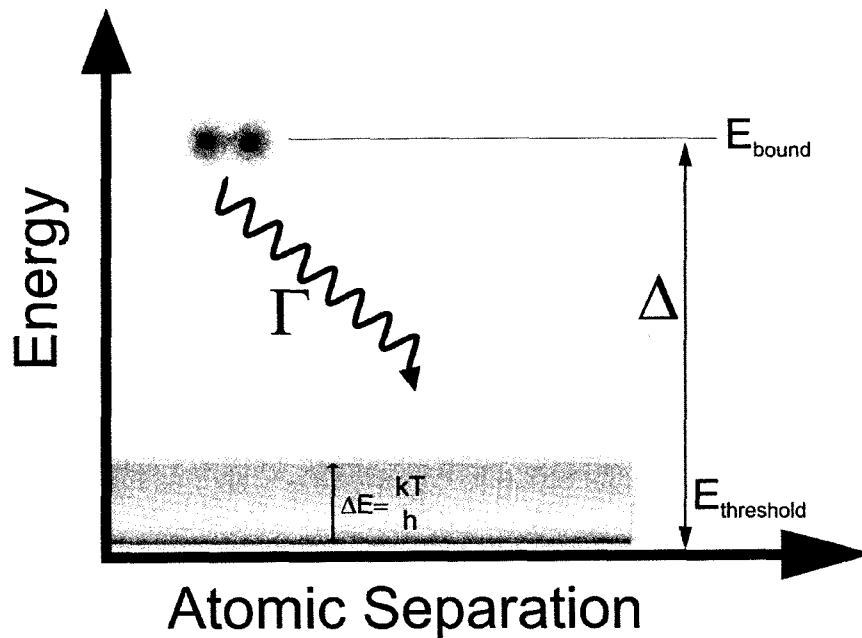
Figure 4.2 : Cartoon of the main aspects of threshold scattering. The scattering length a for free atoms in the continuum can be greatly modified by the presence of a bound state (blue circles) near threshold. In fact, a diverges when the bound state is tuned to resonance with the threshold ($\Delta = 0$).

position of the leftmost node, say by compressing the box a small amount a, raises the ground state energy of the pair with the new energy given by $E = \hbar^2\pi^2/(2\mu(r_0-a)^2)$. If $a \ll r_0$, then the shift in energy $\delta E \approx \hbar^2\pi^2 a/(2\mu r_0^3)$. A gas of N atoms will then experience a total shift $U \propto \hbar^2\pi^2 na/(2m)$ where $n = N/r_0^3$. Thus this simple toy model suggests that the energetics of the ground state are greatly influenced by the apparent position of the node of the scattering wave function, resulting in profound consequences for the BEC.

4.3 Feshbach Basics

Shown in Fig. 4.2 is a simplified diagram describing threshold scattering [27]. In the most general description of threshold scattering, the scattering properties of a pair of free atoms in the continuum are influenced by the presence of a bound state (either virtual or real) near the so-called threshold energy of the continuum. In principle, the coupling between the free and bound states can be provided by many different means. For example, in the case of an optical Feshabch resonance (OFR), the bound states are electronically excited state molecules and the coupling is provided by a laser. The energy difference between the continuum and bound state, known as the detuning Δ, can be tuned by adjusting the frequency of the laser, and the strength of the coupling can be tuned via the intensity of the laser. For OFR, the lifetime Γ of the excited state, profoundly influences the inelastic losses associated with the resonance. Another important aspect present in ultra-cold atomic physics experiments is that the thermal width of the atoms in the continuum is narrow (kT/h = 21 kHz/μK). This often makes threshold scattering experiments extremely accurate probes of scattering properties [29, 30, 27].

For the case of the magnetic Feshbach resonance [31] used in our experiments, the coupling between the continuum and the bound state is provided by the hyperfine interaction and the detuning is adjusted by an external magnetic field. Shown in Fig. 4.3 is the potential energy between two ^{7}Li atoms as a function of the interatomic distance for the interaction potentials responsible for the Feshbach resonance we

exploit in our experiments. Two atoms, each in the $|1,1\rangle$ state, collide along the shallow entrance channel potential (mainly triplet at high fields). It is the asymptotic energy of two atoms colliding along this potential that defines the threshold energy. The deeper closed channel (mostly singlet) potential results from the collision of two atoms, one with the spin of its valence electron flipped. Shown also in this diagram is the least bound vibrational level of the closed channel. It is this state that strongly effects the scattering properties of atoms near threshold. As a result of the differing magnetic moments of the two scattering states of $\delta\mu \approx 2\,\mu_B$, the detuning between the states can be adjusted via a magnetic field. The Feshbach resonance occurs at a field where the least bound state of the closed channel potential becomes resonant with the threshold energy of the entrance channel potential.[5]

4.4 BEC and the Scattering Length

The importance of the scattering length for ultra-cold atom experiments cannot be overestimated, particularly for experiments involving BEC. Often, the starting point for understanding the physics in any BEC experiment is the Gross-Pitaevskii equation

$$\mu\,\psi = -\frac{\hbar^2}{2m}\nabla^2\psi + V\psi + \frac{4\pi\hbar^2 a}{m}n(r)\psi \qquad (4.6)$$

---

[5]In ^{7}Li the hyperfine interaction of course mixes the singlet and triplet character of both of these potentials and a rigorous calculation must take this into account. We therefore prefer to use the terminology entrance channel and closed channel rather than singlet and triplet to avoid confusion. Interested readers should consult McAlexander's thesis [32] and citations therein.
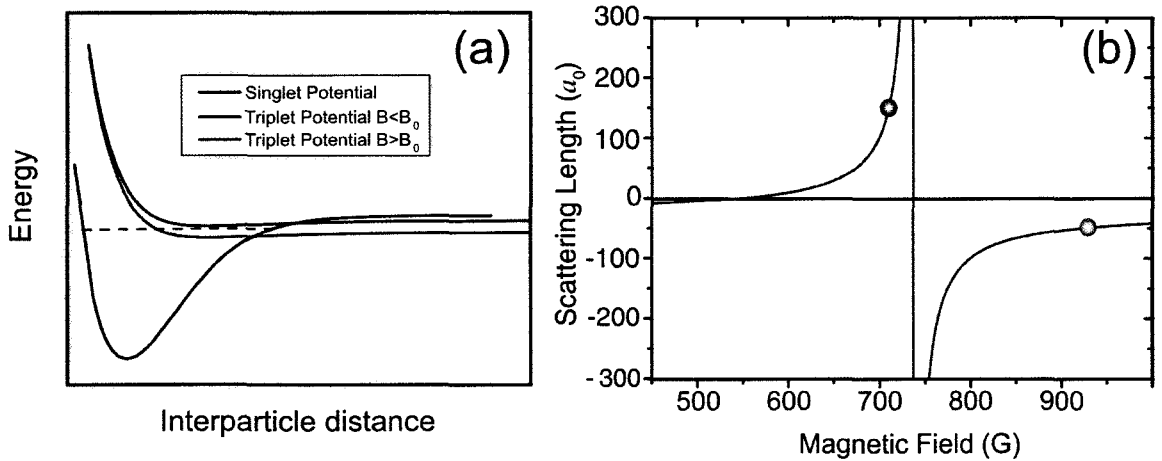
Figure 4.3 : Feshbach resonance as magnetically tuned threshold scattering. (a) Interaction potentials responsible for the creation of the Feshbach resonance. The energy of two free atoms colliding along the entrance channel potential (red and blue line). The energy of this potential is tuned via the magnetic field. Black line is the closed channel potential whose least bound molecular state is responsible for the resonance scattering behavior. (b) Divergence of a as the position of the the entrance channel threshold states are tuned through the closed channel bound state ($\Delta = 0$). This curve was produced from a numerical solution to a coupled channels calculation using the potentials shown in (a).

with $\int |\psi(r)|^2 dr = N$, and therefore $n(r) = |\psi(r)|^2$. In the Gross-Pitaevskii formalism, the atomic system is subject to a mean-field energy density defined by $U = 4\pi\hbar^2 an/m$. For $a > 0$ (repulsive effective interactions) the mean field energy is positive, whereas for $a < 0$ (attractive effective interactions) the mean field energy is negative. Therefore, relative to the noninteracting case the mean field leads to an expansion or contraction of the cloud. In addition to the s-wave contact interaction, alkali atoms also have a weak magnetic dipole interaction (MDI), due to the presence of the unpaired spin of the $2s^1$ electron. For ^{7}Li in the $|F = 1, m_F = 1\rangle$ state, the atomic magnetic moment is very weak with $\mu \sim \mu_B$. This interaction, like the

contact interaction can be treated as a mean field

$$\frac{\mu_0\mu^2}{4\pi} \int \frac{1 - 3\cos^2\theta}{|\mathbf{r} - \mathbf{r'}|^3} |\psi(\mathbf{r'})|^2 d\mathbf{r'}\psi \tag{4.7}$$

where $\mathbf{r}$ is the distance between the dipoles and θ is the angle between $\mathbf{r}$ and the direction (z) of the polarizing magnetic field. To get a feel for the relative strength between the contact and MDI interactions, it is useful to parameterize the MDI in a units of length using [33]

$$a_{\mathrm{MDI}} = \frac{\mu_0\mu^2 m}{12\pi\hbar^2} \tag{4.8}$$

For our system this yields $a_{\mathrm{MDI}} = 0.6\, a_0$, much weaker than other systems in which this effect has been observed, e.g. atomic Cr, where $a_{\mathrm{MDI}} = 15\, a_0$ [34]. Nevertheless, due to the presence of the shallow zero crossing in our system, the effects of MDI are observable as discussed later.

Equation 4.8 suggests that in order to obtain accurate scattering lengths down to values less than a_{MDI} using the size of the BEC as a proxy, we have to include the effect of MDI in Eq. E.13. The size of the cloud as a function of a can be found through solving Eq. E.13 using a variational method with 3D, cylindrically symmetric, trial wave functions of Gaussian shape. Minimizing the energy functional corresponding to Eq. E.13 produces the axial and radial sizes of the condensate as a function of a [35]. The results of such a calculation for the axial size of the condensate are shown in Fig. 4.4 (with and without MDI) along with the solution of Eq. E.13
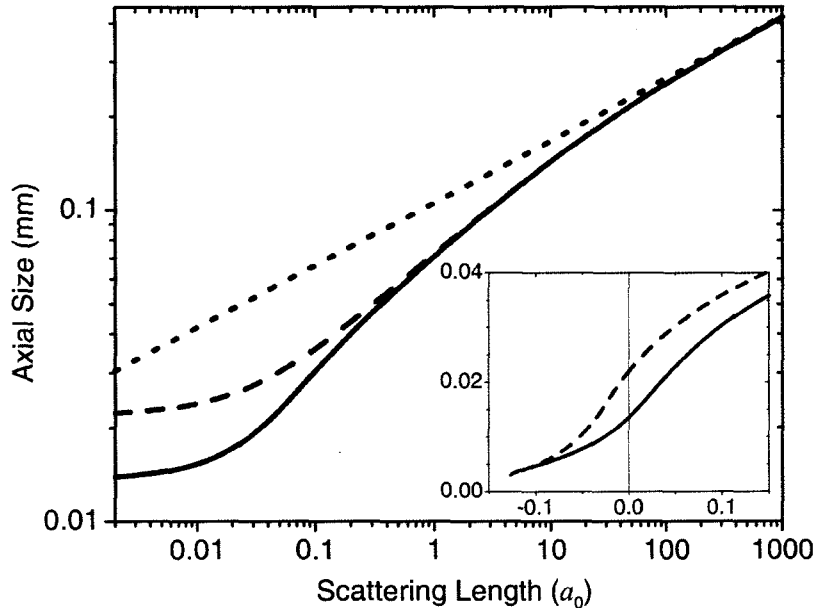
Figure 4.4 : Mapping functions of axial size to a using a Gaussian trial wave function in a variational solution to Eq. (E.13), including (solid) and neglecting (dashed) the MDI; also shown is the Thomas-Fermi approximation (dotted) for the axial size. These mappings were computed for $N = 3 \times 10^5$, $\omega_r/2\pi = 193\,\mathrm{Hz}$ and $\omega_z/2\pi = 3\,\mathrm{Hz}$. In practice, we compute the mapping individually for each imaged condensate to account for variations in N and a field dependent variation in ω_z. The mapping shows a smooth crossover between the Thomas-Fermi and Gaussian regimes. The Gaussian solution neglecting the MDI asymptotically approaches l_z at zero interactions, while their inclusion causes the solution to asymptotically approach a value smaller than l_z due to the attractive nature of the MDI in our geometry. The inset shows the zero-crossing in a on a linear scale.

obtained using the Thomas-Fermi approximation. As expected, the effects of MDI become evident for $a < 0.6\,a_0$. In our system, the BEC is spin polarized along the long axis of the trap, parallel to the prevailing magnetic field direction. Thus, individual atomic dipoles are approximately stacked end to end. In this configuration, the mean field from the MDI produces a weak saddle potential with the axial direction providing a slight attractive potential. This is particularly evident for $a = 0$ where

the effect of the MDI serves to reduce the size of the cloud to below the harmonic oscillator size $l_z = \sqrt{\hbar/m\omega_z}$ expected for a noninteracting gas. The opposite effect was used in the Cr experiments, where repulsive MDI in an oblate trap was used to stabilize an attractive condensate against collapse [33]. In cases where dipolar collapse has been observed, spectacular d-wave symmetric patterns emerge from the exploding density distributions [36].

4.5 Measuring the Scattering Length in a BEC

Atoms in the $|F = 1, m_F = 1\rangle$ state are confined in an optical trap formed from a single focused laser beam with wavelength of $1.03\,\mu m$. A bias magnetic field, directed along the trap axis, is used to tune a via the Feshbach resonance. We create condensates at a field where a is large to facilitate rapid rethermalization of the atoms during evaporation from the optical dipole trap. After a condensate is formed we slowly ($\sim 4\,s$) ramp the field to the desired value and determine the scattering length, as described below. There is no discernible thermal part to the density distributions and we estimate that $T/T_c < 0.5$, where T_c is the condensation temperature. The final trapping potential is a combination of the optical field and a residual axial magnetic curvature from the bias field. The trap is cylindrically symmetric with measured radial and axial trapping frequencies of $\omega_r/2\pi = 193\,\mathrm{Hz}$ and $\omega_z/2\pi = 3\,\mathrm{Hz}$, respectively. Due to the small residual curvature of the bias field, the axial frequency changes by $\sim 5\%$ over the relevant magnetic field range, which is

accounted for in the analysis.

We use *in situ* polarization phase-contrast imaging [37] to acquire the column density distribution of the condensate at the desired magnetic field. When the s-wave interactions are large and repulsive they inflate the size of the condensate well above the harmonic oscillator size. As the interactions decrease, the size of the condensate becomes smaller, approaching the harmonic oscillator ground state near zero interactions. Figure 4.5 shows representative images of condensates with various repulsive or attractive interaction strengths. Solitons form when $a < 0$, either a single one for a slow magnetic field ramp or multiple solitons for ramps fast compared to the axial trap period. Figure 4.5 shows 2D images of column densities for different values of the magnetic field and therefore different values of a. Full exploitation of the Feshbach resonance allows us to create cloud sizes ranging from a few mm down to a few 10's of μm, in addition to weak attractive condensates and matter wave solitons. As can be seen from the images, the axial size of the cloud is a very sensitive proxy for the measurement of a in a BEC.

Armed with the results from Fig. 4.4, we can map measured axial sizes to scattering lengths. Shown in Fig. 4.6 is the axial size of BECs as function of magnetic field for a region from $535\,G$–$737\,G$. Each point shows the average size obtained from approximately 10 independent runs. The average number of atoms per point is $N_0 = 3 \times 10^5$ atoms, with a shot-to-shot variation of 20%. The inset of Fig. 4.6 shows the axial size scaled by $(N/N_0)^{1/5}$. This scaling, accurate for the Thomas-
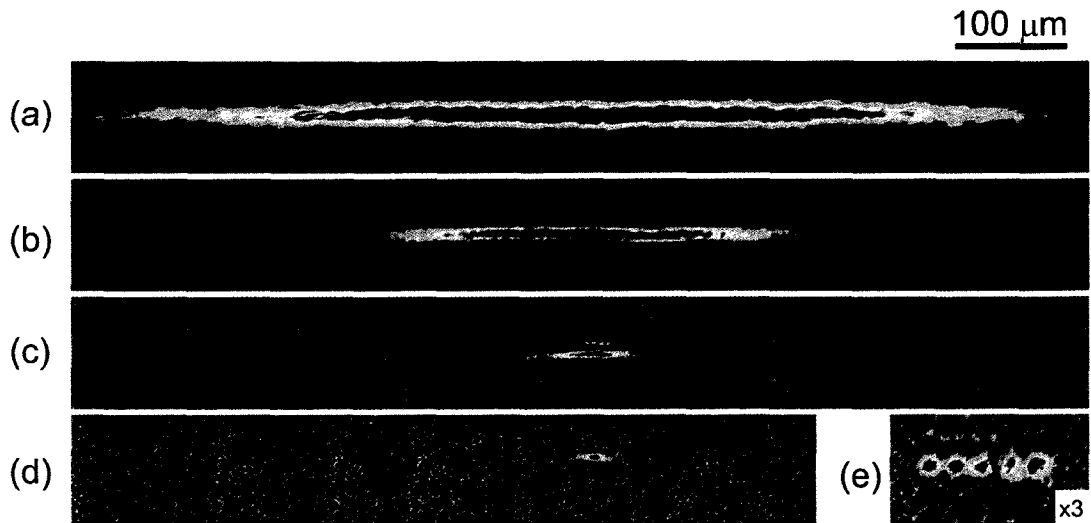
Figure 4.5 : Representative *in situ* polarization phase-contrast images of condensates with various interaction strengths. (a) $B = 719.1\,$G, $a = 396\,a_0$, $N = 1.7 \times 10^5$; (b) $B = 597.4\,$G, $a = 8\,a_0$, $N = 2.9 \times 10^5$; (c) $B = 544.7\,$G, $a = 0.1\,a_0$, $N = 2.0 \times 10^5$; (d) $B = 542.4\,$G, $a = -0.1\,a_0$, $N = 1.2 \times 10^5$; (e) similar to (d) but with a faster field ramp from $710\,$G to $542.4\,$G, resulting in multiple solitons with $N \approx 10^4$ per soliton. The probe laser detuning from resonance is adjusted to keep a nearly constant signal level, and varies between $20\,\gamma$ for large a to $150\,\gamma$ for small a, where $\gamma/2\pi \approx 5.9\,$MHz is the excited state linewidth. The color map is adjusted to maximize contrast for each image.

Fermi regime, removes the fluctuations in the size due to fluctuations in shot-to-shot number N.

Figure 4.7 shows the derived scattering lengths found by applying the mapping shown in Fig. 4.4 to the axial size data in Fig. 4.6. The general shape follows that
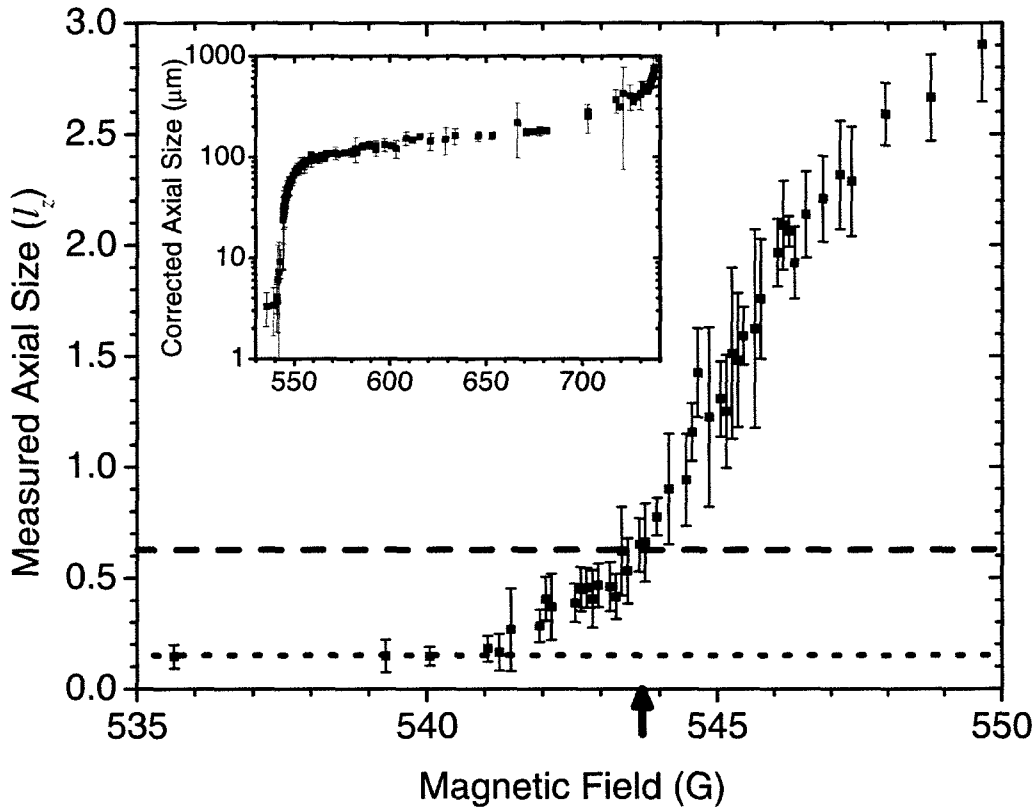
Figure 4.6 : Axial size of the condensate as a function of magnetic field. The axial size is defined as the $1/e$ point in the axial density profile and is scaled by the axial harmonic oscillator size $l_z = \sqrt{\hbar/m\omega_z} \approx 22\,\mu$m. The resolution of the optical imaging system is $\sim 3.3\,\mu$m (dotted line). The dashed line is the size of the condensate ($l_d \approx 0.62\,l_z$) found by solving Eq. (E.13) with $a = 0$. The zero-crossing in a occurs when the size of the condensate equals l_d and is found to be at 543.6(1) G (arrow) [38]. Neglecting dipolar effects results in a zero-crossing about 0.5 G higher, where the axial size equals l_z. Individual data points and error bars are the average and standard error of approximately 10 shots taken at each field. Systematic uncertainty in the axial size is $\sim 3\%$ from uncertainty in temperature and the uncertainty in magnification of our CCD. The systematic uncertainty in magnetic field due to calibration (via radio frequency transitions from the $|2,2\rangle$ to the $|1,1\rangle$ state) is ~ 0.1 G. We have binned our data into intervals of this size. The inset shows the axial size corrected for number variation as described in the text.
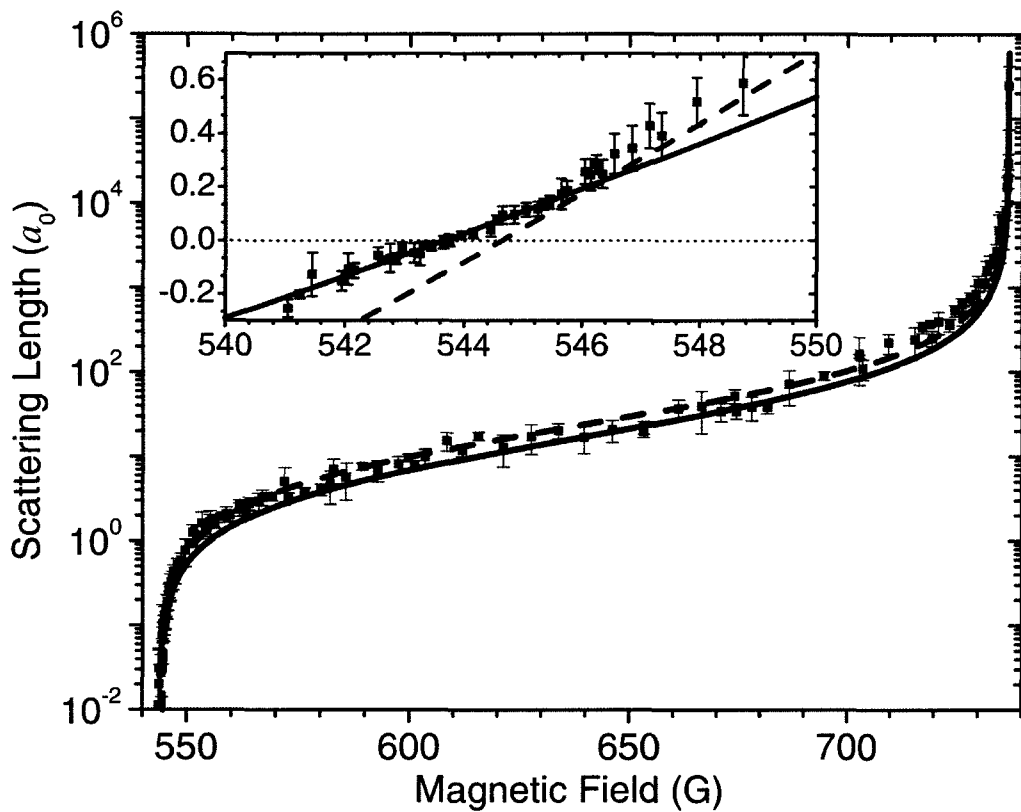
Figure 4.7 : Axial size data of Fig. 4.6 mapped onto a. Results of a coupled-channels calculation are shown by the solid line. The Feshbach resonance fit (dashed line), as described in the text, underestimates the data both above 700 G and below 570 G, and overestimates it slightly in between. The inset shows the extracted values of a near the zero-crossing. A linear fit in this regime, also described in the text, matches the coupled-channels calculation. The mean and standard error of approximately 10 shots taken at each field is shown. In addition, we estimate a systematic uncertainty of $\sim$20% in a as described in the text.

of a typical Feshbach resonance [6]

$$a = a_{BG}[1 + \Delta/(B - B_\infty)],$$ (4.9)

where $a_{BG} = -24.5^{+3.0}_{-0.2}\, a_0$, $\Delta = 192.3(3)$ G, and $B_\infty = 736.8(2)$ G. The uncertainties in these derived values are a result of the systematic uncertainty in field calibration of 0.1 G and a systematic uncertainty in a of $\sim 20\%$, primarily due to uncertainty in measuring the axial size and determination of ω_z. For a detailed accounting of these uncertainties please refer to Appendix E. A linear fit to the data for $B < 550$ G gives a slope of $0.08(1)\, a_0/$G and a zero-crossing at $B_0 = 543.6(1)$ G. The smallest mean positive scattering length of a collection of shots was $0.01(2)\, a_0$ at $543.6(1)$ G with $\sim 3 \times 10^5$ atoms. Under these conditions the peak density is $3 \times 10^{14}\,\mathrm{cm}^{-3}$ and the corresponding condensate healing length is comparable to the length of the condensate itself. The largest mean positive scattering length was $\sim 2 \times 10^5\, a_0$ at $736.9(1)$ G with $\sim 2 \times 10^4$ atoms. At this field, the BEC has a peak density of $n \approx 5 \times 10^{10}\,\mathrm{cm}^{-3}$ with $na^3 \sim 50$. The comparatively smaller number of atoms close to resonance is due to large inelastic collisional losses in this regime [39, 40]. The loss is dominated by three body recombination with $K_3 > 2 \times 10^{-20}\,\mathrm{cm}^6/$s. Although Eq. (E.13) assumes the mean field approximation, beyond mean field corrections are expected to be im-

---

[6]Remarkably, in regime of large scattering length, Eq. 4.9 *universally* describes the magnetic field dependence of the scattering length in any atomic system. The universal regime is defined to be $a \gg \bar{a}$ and $a \gg 4R^*$, where $\bar{a}$ is related to the van der Waals length scale by $\bar{a} = 0.955978...R_{\mathrm{vdW}}$ and $R^* = \bar{a}/s_{res}$ where s_{res} is a unitless paramter characterizing the strength of the Feshbach resonance [31]. For ^{7}Li $\bar{a} = 31.1\, a_o$ and $R^* = 40.6\, a_o$.

portant when $na^3 \gtrsim 1$ [41, 42, 43]. The leading order correction to the interaction

term in Eq. (E.13), the Lee-Huang-Yang parameter, is $\alpha = 32/(3\sqrt{\pi})\sqrt{na^3} \approx 40$

for the strongly interacting condensate described above. We have accounted for this

correction in extraction of a for data where $\alpha < 1$, but exclude the four data points

with $\alpha > 1$ in the Feshbach resonance fit.[7]

Figure 4.7 also shows a comparison between a coupled-channels calculation and

the experimentally extracted values of a. The coupled-channels calculation requires

the ground-state singlet and triplet potentials of $^7Li_2$ as input, as described previ-

ously [44, 45]. We have updated the potentials to be consistent with the new mea-

surements of B_∞ and B_0 reported here, as well as the previously measured binding

energy of the least bound triplet vibrational level [44, 46]. The updates involve ad-

justing the singlet and triplet dissociation energies to $D_e(X^1\Sigma_g^+) = 8516.68(10)\,\mathrm{cm}^{-1}$

and $D_e(a^3\Sigma_u^+) = 333.714(40)\,\mathrm{cm}^{-1}$, where the stated uncertainties account for un-

certainties in the remaining portions of the model potentials. These values agree

with previous determinations [45, 47]. The agreement between the calculated and

measured values of a, while not perfect over the entire range of fields, is reasonably

accurate over a range spanning $\sim$6 decades. Shown in Fig. 4.8 is a comparison of the

coupled channels prediction to the experimentally extracted values of a. The effects

---

[7]We should highlight the fact that due to the high inelastic losses at large scattering lengths, complicated dynamical issues become prevalent making the atomic density profiles hard to interpret. Not only are the majority of the atoms lost in the first few ms, making the signal weak, these clouds may not have had enough time to equilibrate. A more careful study of the dynamics of the condensate is necessary to prove whether or not these strongly interacting BECs can be useful to study beyond mean field effects.
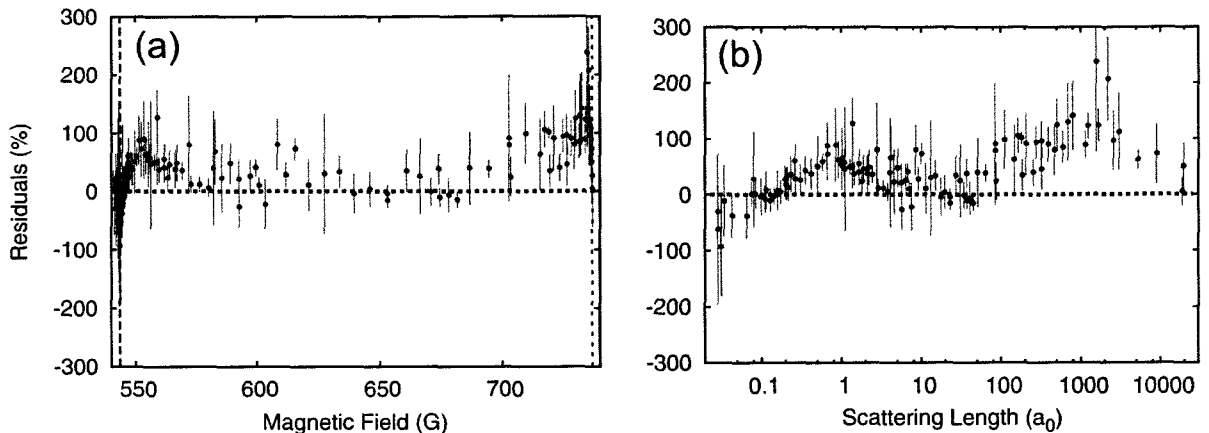
Figure 4.8 : (a) Plot of $100[(a_{exp} - a_{cch})/a_{cch}]$ versus B, where a_{exp} is the experimentally determined scattering length and a_{cch} the coupled channels result. Dashed lines located on the left and right right side of the plot denote the experimentally determined location of the zero-crossing and Feshbach resonance, respectively. (b) Same as (a) but plotted against a_{cch}.

of the MDI are strongly dependent on geometry. To better distinguish their role, we increased the axial trapping frequency from 3 Hz to 16 Hz by applying magnetic curvature. Figure 4.9 compares the extracted values of a for both trap geometries when the MDI is included or neglected in the mapping function. As expected, neglecting the MDI in the analysis systematically lowers the extracted values of a. This effect is most noticeable in the zero-crossing where a systematic geometry-dependent discrepancy appears in the derived values of a. Including the MDI results in a consistent value of a for a given magnetic field regardless of the trapping potential. The data show that the effect of the MDI is indeed discernible in ^{7}Li despite the weak atomic magnetic moment of only $\sim 1\,\mu_B$.
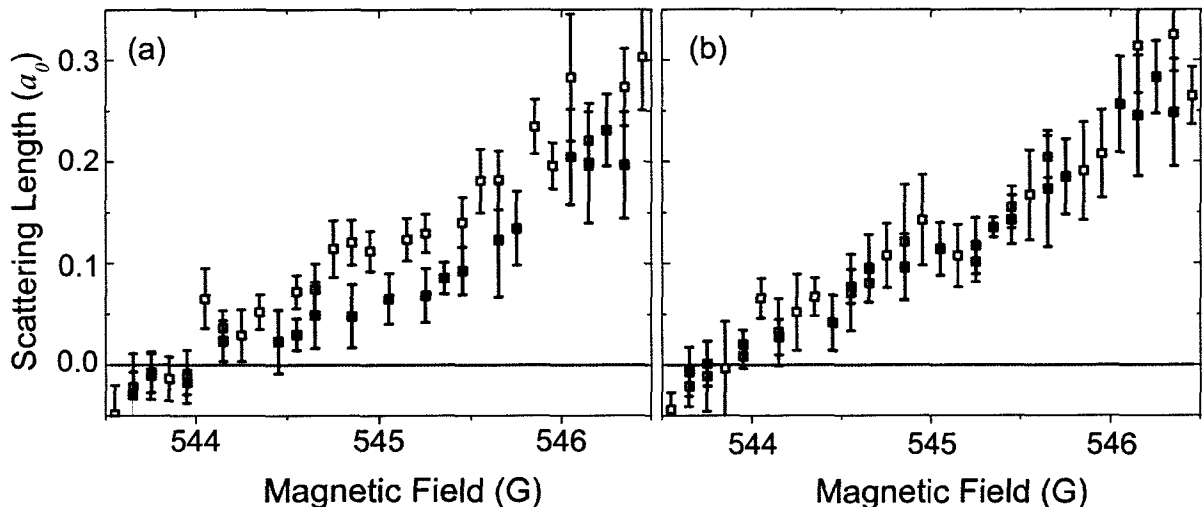
Figure 4.9 : Extracted values of a near the zero-crossing for trapping potentials with $\omega_z/2\pi = 3\,\text{Hz}$ (filled squares) or $\omega_z/2\pi = 16\,\text{Hz}$ (unfilled squares), when (a) neglecting or (b) including the MDI in the mapping function. The MDI has a negligible effect on the extracted values of a for the 16 Hz trap, but neglecting the MDI in analysis of the 3 Hz trap systematically lowers the mapped values of a, especially for $a \lesssim 0.15\,a_0$.

4.6 Dimensional Reduction by Tunable Interactions

Armed with the precise knowledge of the location of the zero-crossing at $B_0 = 543.6(1)\,\text{G}$, the interactions of the gas can be effectively turned off at will. For a small enough, the gas behaves as if it was one dimensional; a scenario that occurs because $\mu < \hbar\omega_r$ resulting in a "freezing out" of the radial dynamics. Figure 4.10 shows a plot of μ vs. a produced from a numerical solution to Eq. E.13 including the MDI, as described in Sec. 4.4 for typical experimental parameters. This calculation shows that $\mu = \hbar\omega_r$ at $a \sim 10\,a_0$. In addition, for attractive interactions the calculation shows that μ diverges when the scattering length becomes too negative, signaling a collapse of the BEC.

The phenomena of BEC collapse has been extensively studied in several atomic
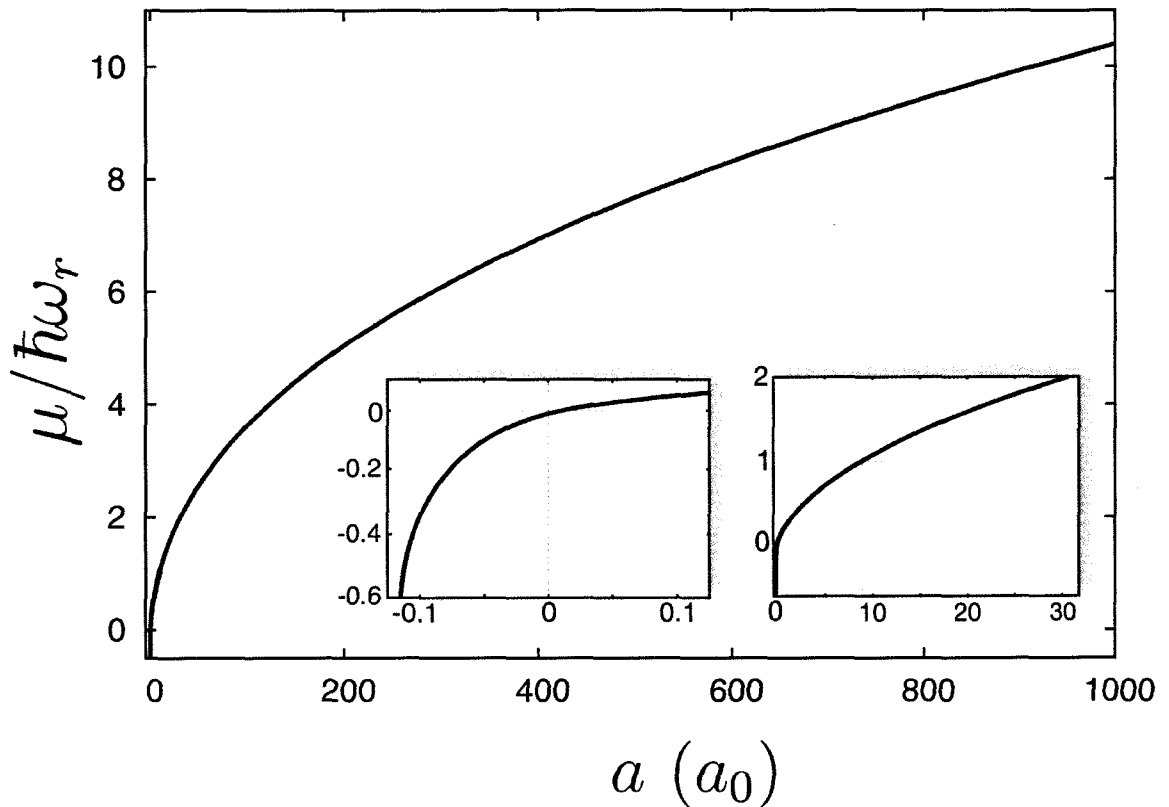
Figure 4.10 : Result of the numerical solution to the GP equation with the MDI included. Parameters used were $N = 3 \times 10^5$, $\omega_r = (2\pi)\,240\,\mathrm{Hz}$, and $\omega_z = (2\pi)\,5\,\mathrm{Hz}$. y-axis values are scaled to $\hbar\omega_r$. Insets show zoomed in ranges including the region where $\mu = \hbar\omega_r$ and the region near the zero crossing.

systems including bosons [48, 49, 50], Bose-Fermi mixtures [51, 52], and most recently dipolar BECs of Cr [36]. One of the most interesting consequences of this collapse is the formation of bright matter-wave solitons as collapse remnants [53, 54, 55]. As shown in Fig. 4.5, these structures can be created by slowly ramping the field through the zero crossing, but often with the result being a soliton train. We have found that by starting in a cross beam trap, more repeatable single solitons can be created. Figure 4.12 shows a comparison between a weakly repulsive BEC and a weakly attractive soliton that have been created in the cross beam trap. When the
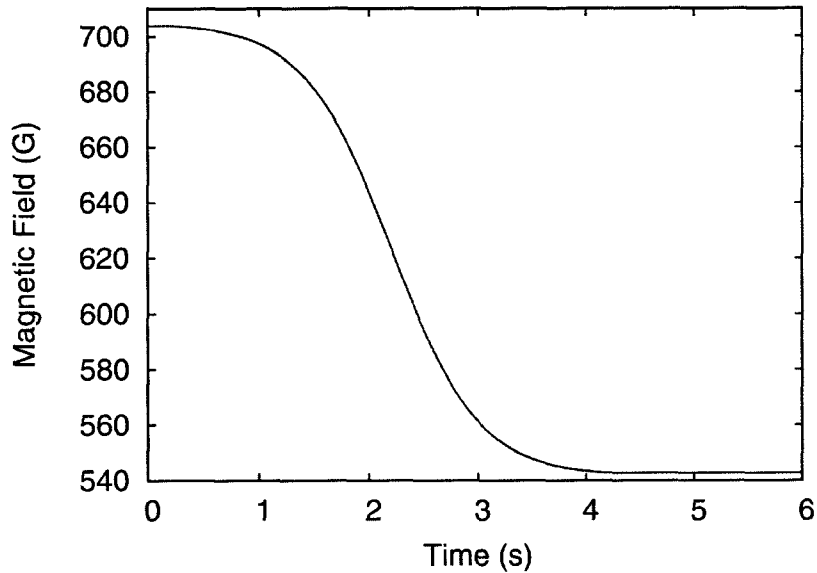
Figure 4.11 : Shown here is a typical magnetic field ramp used to create single solitons in the cross beam trap. This ramp is triggered immediately after the optical trap evaporation finishes. Images are typically taken soon after the ramp ends at $t \sim 4.25\,s$.

cross beam is turned off and the clouds allowed to expand in the weakly confining single beam trap, the repulsive BEC expands but the soliton does not; rather, it behaves like a self trapped BEC "droplet."

The formation process in the cross beam seems to be more repeatable than for the more elongated clouds in the single beam trap. Figure 4.6 shows a typical ramp used to create solitons in the cross beam trap. Immediately after the optical trap evaporation, the field is ramped down during $\sim$4 s according the the functional form

$$B(t) \propto \frac{-\tanh\left(2\pi\left(t - 1/2\right)\right)}{\tanh\left(\pi\right)} \tag{4.10}$$

We have found that once the field is ramped through the zero crossing, the number
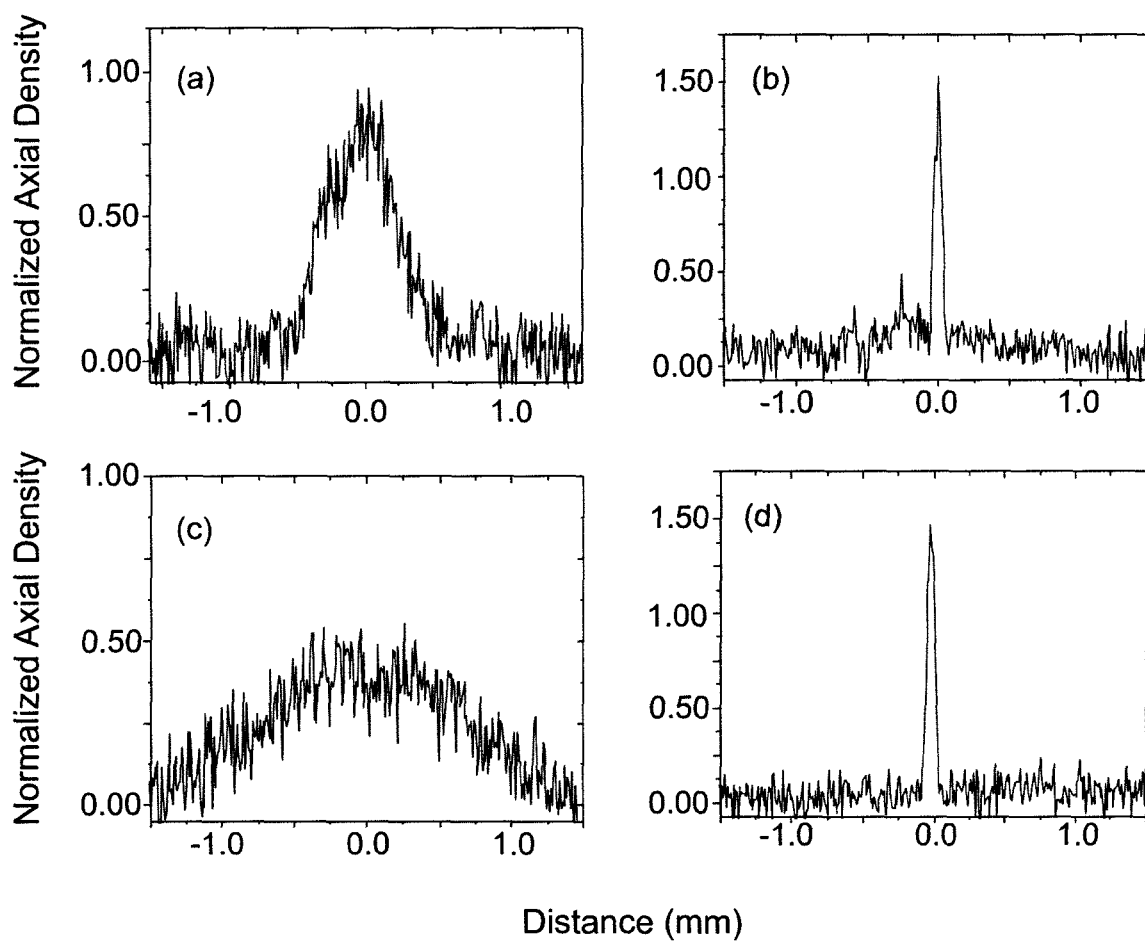
Figure 4.12 : (a) and (c): Expansion of a weakly repulsive BEC with $a \sim 0.1\,a_0$ after being released from the cross beam trap into the weakly trapping single beam trap. (a) and (c) are for 50 ms and 100 ms after the cross beam is switched off. (b) and (d): The identical procedure but with a weakly attractive BEC with $a \sim 0.5\,a_0$ showing absolutely no expansion, proving that this object is indeed a soliton.

stays roughly constant until the critical scattering length for collapse is reached. This occurs roughly where the attractive mean field energy overtakes the repulsion induced by the confinement due to the Heisenberg uncertainty principle. A more precise mathematical form for the critical number N_c has been derived for the case of cylindrically symmetric traps [56]

$$N_c = \frac{k l_z \lambda^{1/3}}{|a|}, \tag{4.11}$$

where k is a geometry dependent constant ~ 0.4 for elongated traps, and the aspect ratio $\lambda = \omega_z / \omega_r$.[8] When $N = N_c$, further reduction of a results in a loss of atoms with subsequent formation of a single soliton containing very nearly the critical number of atoms, as shown in Fig. 4.13.

The frequencies of collective oscillations are also affected by the dimensionality of the system. The full dynamical behavior of a weakly interacting BEC is captured in the time dependent GP equation

$$i\hbar \frac{\partial \psi}{\partial t} = -\frac{\hbar^2}{2m} \nabla^2 \psi + V(r)\psi + U_0 |\psi|^2 \psi. \tag{4.12}$$

The frequencies of the low energy collective modes of the trapped BEC can be found by solving Eq. 4.12 via a variational technique [57]. Of particular interest for our experiment is the frequency of the lowest lying (out of phase) quadrupole mode given

---

[8]An equivalent form for the critical number is $N_c = k l_r \lambda^{-1/6}/|a|$ which for our typical aspect ratios of $\lambda = 0.02$ reduces to $N_c \approx 0.7 \, l_r/|a|$.
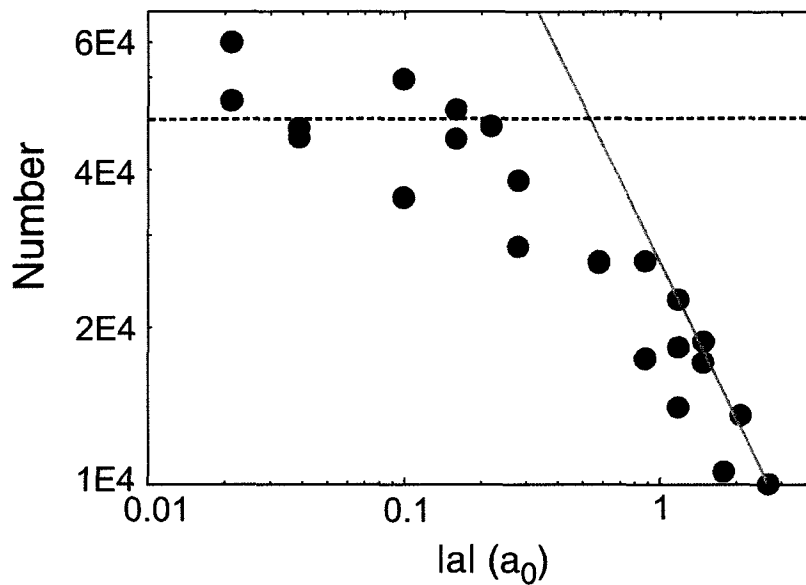
Figure 4.13 : Number of atoms remaining after a field ramp through the zero crossing that stops at a negative value of a (plotted as $|a|$ on the x-axis log scale). The condensate begins the ramp in the cross beam trap with $N \sim 5 \times 10^4$ (dashed horizontal line). As the scattering length becomes more negative, an abrupt decrease in the number occurs close to where the predicted critical number $N_c = 5 \times 10^4$. As the scattering length is increased further, $N \propto 1/|a|$ as expected. The green line is Eq. 4.11 using the measured parameters of $\omega_z = (2\pi)\, 9\,\mathrm{Hz}$ and $\omega_r = (2\pi)\, 360\,\mathrm{Hz}$, in addition to $k = 0.42$ calculated as described in [56].
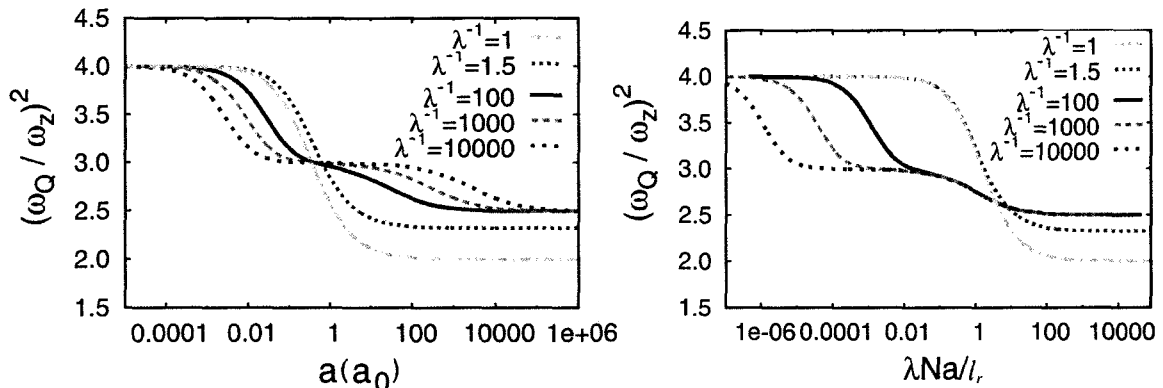
Figure 4.14 : Plotted here is the prediction of Eq. 4.13 for $N = 2 \times 10^5$ atoms and $\omega_r = (2\pi)\,235\,\text{Hz}$. The aspect ratios were varied by adjusting the axial trap frequency. (a) $(\omega_q/\omega_z)^2$ vs. a. The quasi-1D regimes (see text) are evident for traps with large aspect ratio. (b) $(\omega_q/\omega_z)^2$ vs. the dimensionless interaction parameter Na/l_r scaled by the aspect ratio λ. This particular scaling elucidates the universal behavior of highly elongated traps from the 1D mean field regime into the Thomas-Fermi regime. The highly elongated traps all begin going quasi-1D when $\lambda Na/l_r \sim 1$. As expected more highly elongated traps exhibit quasi-1D over a larger range of parameter space.

by

$$\left(\frac{\omega_Q}{\omega_z}\right)^2 = \frac{1}{\lambda^2}\left[2\left(1 + \lambda^2 - P_{2,3}\right) - 2\sqrt{\left(1 - \lambda^2 + P_{2,3}\right)^2 + 8P_{3,2}^2}\right] \qquad (4.13)$$

where $P_{i,j} = P/(4b_r^i b_z^j)$ and the dimensionless width parameters $w_r/l_r = b_r$ and $w_z/l_r = b_z$ are the $1/e$ sizes of the Gaussian variational solution to the time independent GPE as described above. The interaction parameter $P = \sqrt{2}Na/(\sqrt{\pi}l_r)$, where $l_r = \sqrt{\hbar/(m\omega_r)}$. Shown in Fig. 4.14 is a plot of Eq. 4.13 for a range of scattering lengths and trap aspect ratios. For traps with large anisotropy we observe three distinct regions. For large scattering lengths we see that $\omega_Q/\omega_z \to \sqrt{5/2}$ consistent with the prediction based on the Thomas-Fermi approximation[9] [58]. For

---

[9]This is somewhat surprising since Eq. 4.13 assumes a Gaussian wave function rather than the inverted parabola given by the Thomas-Fermi approximation.
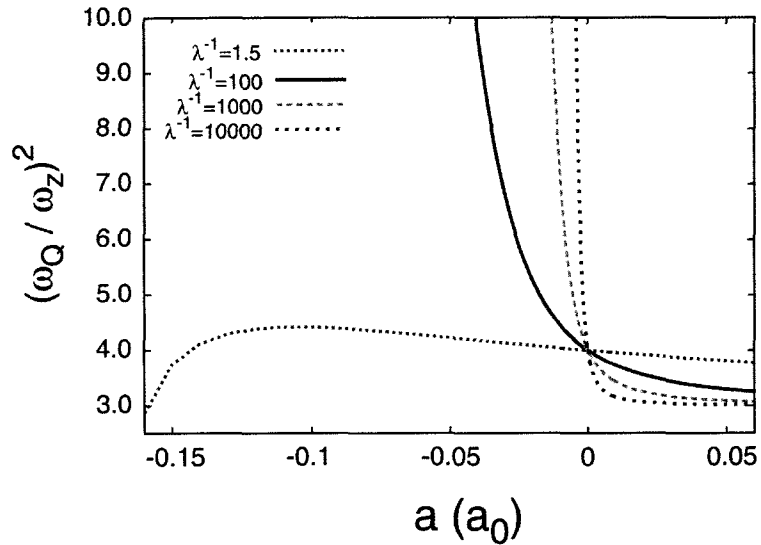
Figure 4.15 : Quadrupole frequency vs. a for $a < 0$ as predicted by Eq. 4.13.

$a \to 0$, $\omega_Q / \omega_z \to 2$ as predicted for the noninteracting gas. In the region between

the noninteracting and Thomas-Fermi regimes, a plateau at $\omega_Q / \omega_z = \sqrt{3}$ can be

seen, consistent with predictions based on 1D mean field theory [59] and the 1D

non-polynomial Schrödinger equation [60]. Equation 4.13 is also valid for $a < 0$. As

seen in Fig. 4.15, for all traps ω_Q rises before dramatically dropping to zero at the

point of collapse.

We have investigated the frequency of the low lying quadrupole mode as function

of a. To drive the oscillation, we take advantage of the Feshbach resonance and

oscillate the bias field (using the bias coils) sinusoidally in time. The drive frequency

is chosen to be close to the expected oscillation frequency, but we have found that

off resonant driving can also be used [61]. The condensate dynamics are shown

in Fig. 4.16 both during and after a modulation drive. Note that the oscillation
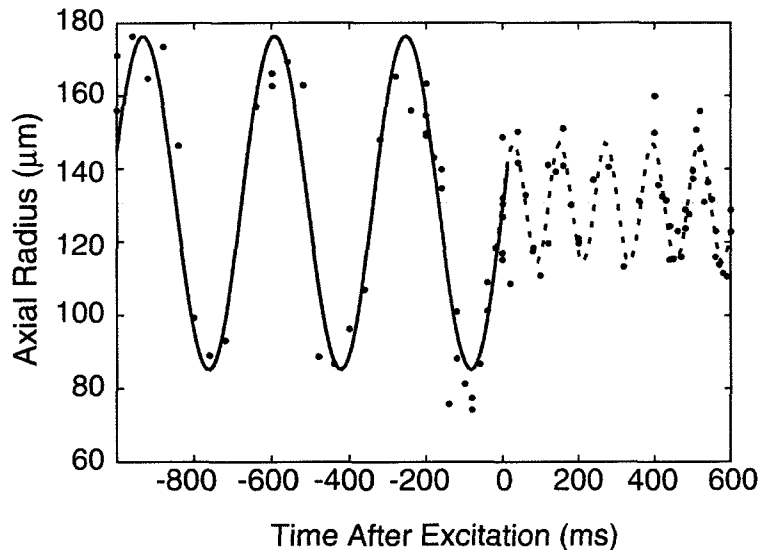
Figure 4.16 : We drive the quadrupole mode by sinusoidally oscillating the magnetic field and therefore a. Shown here is a short duration drive of 2.5 periods with $\omega = (2\pi)\, 3\,\text{Hz}$ and an amplitude of $2.3\, a_0$ applied to a BEC with $a = 3\, a_0$. After the drive is shut off ($t = 0$) the cloud begins its free undamped quadrupole oscillation. Both the drive and the free oscillation fit well to sinusoidal motion with the free oscillation frequency $\omega_Q = (2\pi)\, 8.2(2)\text{Hz}$. For this data $\omega_z = (2\pi)\, 4.7\,\text{Hz}$ and $\omega_r = (2\pi)\, 235\,\text{Hz}$

frequency is measured after the drive is turned off. We have found that, as expected, the drive frequency does not affect the free oscillation frequency. The drive simply serves to "stretch the spring" so to speak and send the cloud into free motion at the quadrupole frequency.

We extract the axial size of the cloud vs. time by fitting the axial densities obtained from *in situ* phase contrast images to Thomas-Fermi profiles. The measurement of $R(t)$ is then fit to the form

$$R(t) = R_{\text{TF}} + R_0 \cos(\omega_q t + \phi) \tag{4.14}$$
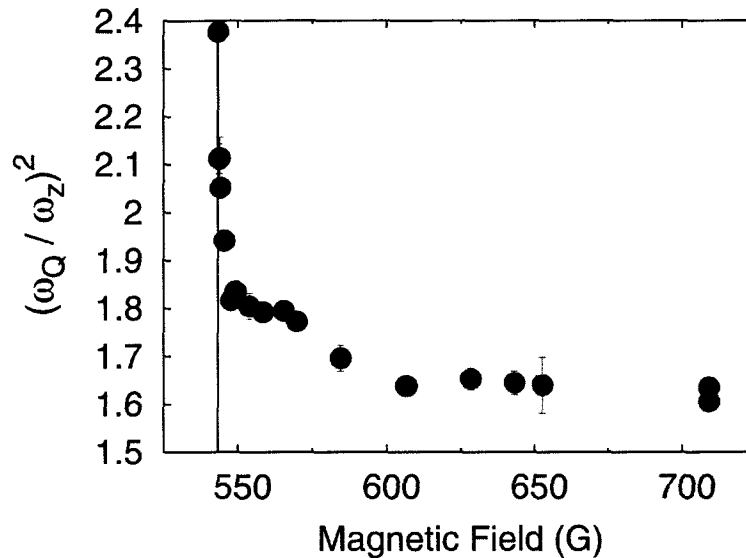
Figure 4.17 : ω_Q/ω_z vs. B near the Feshbach resonance at 737 G. The frequency of the mode appears to diverge near the zero crossing at 544 G (solid line). Error bars signify the uncertainty in fit parameter ω_Q in Eq. 4.14 and is determined by the deviation in ω_Q that produces $\Delta\chi^2 = 1$ in the fit to Eq. 4.14 letting all other parameters float. The uncertainty in B is 0.1 G as described in detail in Appendix E.1.

The result of several such measurements for different values of the magnetic field is shown in Fig. 4.17.

As expected, there is a dramatic rise in the frequency as B approaches the zero-crossing. In order to compare more directly to Eq. 4.13, we convert the magnetic field to scattering length using Eq. 4.9 for $B \geq 550$ G and $a(B) = 0.08\, a_0/\text{G}\, (B - 543.6)$ for $B < 550$ G. A plot of ω_Q/ω_z vs. $\lambda Na/l_r$ is shown in Fig. 4.18. Panel (a) shows a disturbing systematic shift in much of the data. This is likely a manifestation of the predicted nonlinear frequency shift in ω_Q vs. oscillation amplitude [62, 63]. In BEC systems, the nonlinear interaction can give rise to a weak coupling between collective modes, causing a shift in the mode frequency given by $\delta\omega/\omega \approx 0.1 A_z^2$

where $A_z = R_0/R_{\rm TF}$. In panel (b) the measured frequencies are corrected by this factor (of order 5% or less), resulting in much better agreement with the theoretical prediction. The remaining deviation at weak interactions is perhaps evidence of physics not encompassed by the theory. One immediately questions whether dipolar effects are playing a role in this deviation [64]. A more systematic study of this shift and in particular its dependence on trap geometry would help determine if the weak dipolar interaction is important. Extending the theoretical prediction to include this interaction would also prove illuminating.
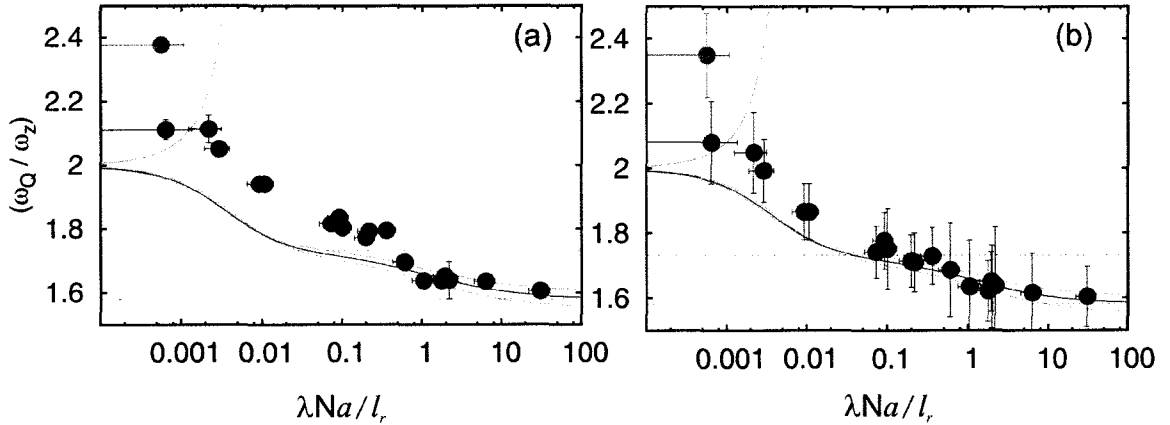
Figure 4.18 : (a) Comparison of measured ω_Q/ω_z with the theoretical prediction of Eq. 4.13 calculated using the measured parameters of $N = 3 \times 10^5$, $\omega_r = (2\pi)\,235 \pm 20\,$Hz, and $\omega_z = (2\pi)\,4.8\,$Hz as input. The red line is for $\omega_r = (2\pi)\,235\,$Hz and the cyan lines indicate 255 Hz and 215 Hz. The green line indicates ω_Q/ω_z for $a < 0$. Blue circles are for data above the zero crossing while the violet circle was taken just below the zero crossing with $B = 543.4(4)\,$G. Vertical error bars are as defined in Fig. 4.17. Horizontal error bars are dominated by the shot-to-shot fluctuations in N for the collection of shots making up each oscillation. A detailed accounting of all the uncertainties involved in this measurement is given in Appendix F. (b) Data in (a) corrected for the amplitude dependent nonlinear frequency shift. (see text.) The vertical error bars are determined from the errors in the fit parameters R_{TF} and R_0 determined using the $\Delta\chi^2 = 1$ method described in Fig. 4.17. Black dashed lines show expected frequencies for the 1D mean field $\omega_Q/\omega_z = \sqrt{3}$, and 3D elongated Thomas-Fermi $\omega_q/\omega_z = \sqrt{5/2}$ regimes. The non-interacting gas is predicted to oscillate at $\omega_Q/\omega_z = 2$.

Chapter 5

Dissipative Transport of a Bose-Einstein Condensate

5.1 Introduction

The observation of Bose-Einstein condensates (BECs) of ultracold atomic gases [65, 66, 67] has enabled investigations of some of the most fundamental concepts of condensed matter physics [68]. One of the most fruitful avenues of research has involved the use of BECs to probe the nature of superfluidity itself. Early studies led to observations of the critical velocity for the onset of dissipation [69, 70, 71] and quantized vortices [72, 73, 74, 75].

Recently, there has been much interest in using BECs to emulate disordered superfluids. Results from such experiments have wide ranging implications, from the transport of superfluid He in porous media [76] to the motion of atomic BECs in microchip traps or matter waveguides [77, 78, 79, 80]. Of particular interest is how disorder can disrupt, or even destroy, superfluidity. Due to their exquisite controllability, atomic BECs are ideal physical systems with which to systematically study the interplay between superfluidity, disorder, and interatomic interactions.

In this chapter, we report measurements of the dissipation of the superfluid flow of an elongated BEC subject to either a disordered potential or a single Gaussian defect. We characterize the superfluid nature of the harmonically trapped cloud

through detailed measurements of the velocity dependent damping of the collective dipole mode. We use a BEC of ^{7}Li in the $|F = 1, m_F = 1\rangle$ internal state, where the interactions may be tuned via a wide Feshbach resonance located at $737\,\text{G}$ [53, 1, 81]. This resonance includes a shallow zero-crossing that enables the s-wave scattering length a to be tuned over a range of nearly 7 decades, with a as small as $0.01\,a_0$, where a_0 is the Bohr radius [81]. The gas may be made nearly ideal with transport properties strikingly different from the more strongly interacting case. Furthermore, the healing length $\xi = 1/\sqrt{8\pi n_0 a}$, where n_0 is the peak density of the condensate, may be made as large as the condensate itself. In this regime, effects due to the fundamental wave nature of individual atoms become important. For example, if ξ is on the order of the disorder grain size or larger, a BEC can become an Anderson localized insulator [82, 83]. In addition, the chemical potential μ in this weakly interacting regime may be less than the radial harmonic oscillator ground state energy, effectively "freezing out" the radial dynamics and leading to quasi-one-dimensional behavior.

5.1.1 Superfluidity of a BEC

One of the seminal theoretical results originating from the theory of superfluid ^{4}He is Landau's criterion. According to this criterion, elementary excitations can be created

only if the fluid velocity v is greater than Landau's critical velocity v_L [84, 85]

$$v_L = \min \frac{\epsilon(p)}{p},$$

(5.1)

where $\epsilon(p)$ is the energy of an elementary excitation of momentum p. For the case of a weakly interacting BEC with uniform density n, Bogoliubov theory gives the excitation energy as [26]

$$\epsilon(p) = \sqrt{\left(\frac{p^2}{2m}\right)^2 + c^2 p^2},$$

(5.2)

where m is the atomic mass and c is the bulk speed of sound. For small p, this spectrum reduces to the well known relation $\epsilon(p) = c\,p$ describing phonon excitations with

$$c = \sqrt{\frac{nU}{m}},$$

(5.3)

where $U = 4\pi\hbar^2 a/m$. Application of Eq. 5.1 using $\epsilon(p) = c\,p$ gives $v_L = c$, implying that only supersonic flow can dissipate energy through the creation of elementary excitations; conversely, if the flow is subsonic, excitations are energetically forbidden, and the flow is superfluid. Application of Eq. 5.1 to the case of a non-interacting condensate implies that $v_L = 0$, suggesting that superfluidity cannot exist in an ideal gas.

The dynamics of highly elongated BECs can be accurately modeled using an effective one-dimensional (1D) nonlinear Schrödinger equation (NLSE) [86, 87, 88, 89]. In such a treatment, one starts from the 3D Gross-Pitaevskii equation (GPE),

and integrates out the radial dimension. The effect of this integration is a reduction in c relative to Eq. 5.3 due to the average over the nonuniform radial density. For the case of a harmonically trapped BEC in the Thomas-Fermi regime, the bulk density n is replaced with the average density $n_0/2$. Therefore, the speed of sound becomes

$$c_0 = \sqrt{\frac{n_0 U}{2m}}. \tag{5.4}$$

A theoretical description of an elongated BEC beyond the standard 1D NLSE leads to a reduction (on the order of 10%) to the speed of sound relative to Eq. 5.4 [90]. In addition, the spectrum of axially propagating excitations in a cylindrical BEC can differ dramatically from Eq. 5.2 when $\mu \gg \hbar \omega_r$, leading to an additional reduction in v_L [91]. The highest μ condensates created in our system have $\mu/\hbar \omega_r \sim 13$, resulting in a predicted 20% reduction [91].

When attempting to explain the onset of dissipation in any particular experimental situation, care must be taken to apply Landau's criterion *locally*, by using the local density $n(r = 0, z)$ instead of $n_0 \equiv n(r = 0, z = 0)$ in Eq. 5.4 [92]. For arbitrary trapping potentials, excitations will be nucleated first in regions of low density where the local speed of sound is small, and the critical velocity is reduced relative to the bulk. As a consequence of this effect, experimentally observed critical velocities are often much lower than the bulk speed of sound [69, 70, 71].

The remainder of this chapter is organized as follows: In Sec. 5.2 we describe our

experimental methods for creating a BEC in either a disordered harmonic potential or a harmonic potential with a single Gaussian defect; in Secs. 5.3 and 5.4 we discuss our results for the induced dissipation for these two scenarios, where both the 3D Thomas-Fermi and the quasi-1D weakly interacting regimes are discussed for each case.

5.2 Experimental Method

We create a BEC of ^{7}Li in a highly elongated, cylindrically symmetric, hybrid magnetic-optical dipole trap [93, 81] with radial and axial trapping frequencies in the ranges of $\omega_r/(2\pi) \sim 220\text{--}460\,\text{Hz}$ and $\omega_z/(2\pi) \sim 4\text{--}5.5\,\text{Hz}$, respectively. The radial confinement is dominated by the optical trapping potential formed by a single focused laser beam with wavelength 1030 nm and a $1/e^2$ Gaussian radius of $33\,\mu$m, while the axial confinement is dominated by an adjustable, harmonically confining magnetic field. A set of Helmholtz coils provides a uniform bias field along the long (z) axis of the trap, allowing for the tuning of a via a Feshbach resonance at 737 G [53, 1, 81]. The BEC is created at a field of 717 G where a is positive and large enough ($\sim$200 a_0) to allow for efficient evaporative cooling in the optical trap, but small enough to avoid substantial three-body losses. At this field, the trap lifetime is limited to $\sim$10 s due to three-body recombination with a loss coefficient of $L_3 \sim 10^{-26}\,\text{cm}^6/\text{s}$ [40]. After evaporation, the BEC has no discernible thermal component from which we estimate that the temperature $T < 0.5\,T_C$, where T_C is the

BEC transition temperature. The bias field is then ramped over a timescale on the order of seconds to achieve the desired value for a.

We excite the collective dipole mode of the condensate by pulsing on an axially oriented magnetic gradient, thereby abruptly shifting the center of the harmonic trap. After 1/4 of an oscillation period, the condensate is at the peak of an oscillation and we abruptly switch on either a disordered potential with an extent exceeding the oscillation amplitude of the condensate, or a single, narrow Gaussian defect located near the trap center. By varying the duration of the gradient pulse we precisely vary the amplitude A of the oscillation, and therefore the initial peak velocity v_0 of the condensate center of mass, where $v_0 = A\omega_z$. At various times thereafter we image the cloud to track the center of mass location as well as the shape of the density distribution. We investigate the dependence of the damped dipole motion on v_0, the strength of the disordered potential or single Gaussian defect, and on the value of a.

The disordered potential is an optical speckle pattern created by passing a laser beam through a diffuser plate in a manner similar to previous studies [93, 94, 95, 96]. This beam is directed perpendicular to the trap z-axis. Figure 5.1 shows a characteristic intensity slice of the disorder. The disorder speckle size σ_D is defined to be the $1/e^2$ radius of a Gaussian fit to the autocorrelation of the intensity pattern and is measured to be $\sigma_D = 5.5\,\mu$m. In the radial direction, the speckle size is much larger than the radial Thomas-Fermi radius $R_{TF} \sim 10\,\mu$m, making the disorder effectively 1D. We have verified that the intensity distribution of the disorder follows a decaying
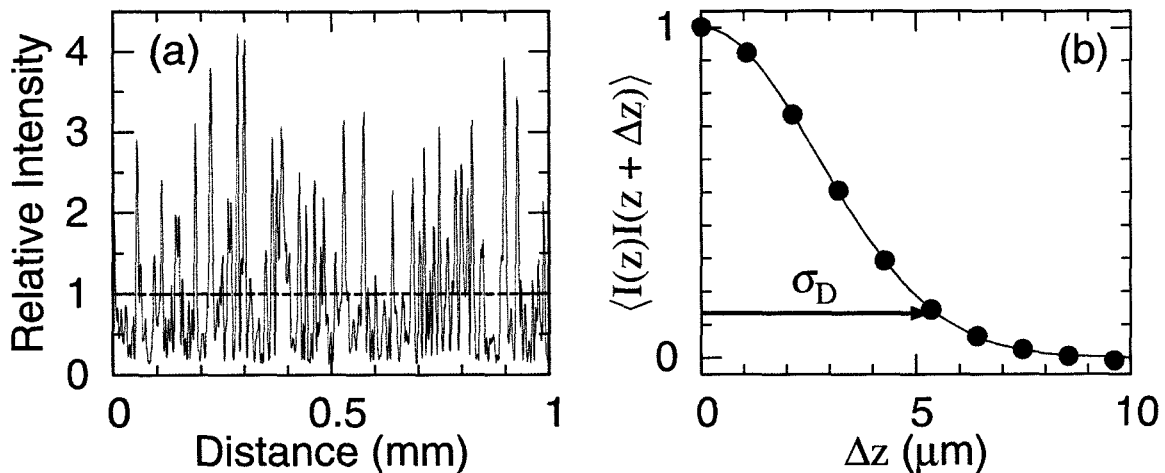
Figure 5.1 : Disordered potential created from laser speckle. (a) Cut through an image of the speckle potential. The disorder strength V_D is proportional to the average value of the intensity $\langle I \rangle$ (dashed line). (b) The autocorrelation of the intensity distribution is well fit by a Gaussian with $1/e^2$ radius $\sigma_D = 5.5\,\mu$m. For some of the data in this chapter (Figs. 5.6, 5.8, and 5.10) $\sigma_D = 3.4\,\mu$m.

exponential $P(I) = \langle I \rangle^{-1} e^{-I/\langle I \rangle}$, as expected for fully developed speckle [21]. The average value of the speckle intensity $\langle I \rangle$ determines the disorder strength through the relation $V_D = \hbar \Gamma^2 \langle I \rangle /(4 I_{sat} \Delta)$, where the transition linewidth $\Gamma = (2\pi)\,5.9\,$MHz and the saturation intensity $I_{sat} = 5.1\,$mW/cm^2. The detuning from the ^{7}Li $2S \to 2P$ transition $\Delta = (2\pi)\,300\,$GHz, producing a repulsive disorder potential. For the strongest disorder used in these studies, off-resonant scattering from the disorder occurs at a rate of $\sim 0.1\,$s^{-1}. The statistical properties of the speckle pattern are measured by direct imaging with a CCD camera before the optical system is installed onto the experimental apparatus.

A cylindrically focused laser beam is used for the studies involving a single Gaussian defect. This beam has a Gaussian intensity distribution $I(z,r) = I_0 e^{-2(r^2/w_r^2 + z^2/w_z^2)}$, with beam waists $w_r = 5\,$mm and $w_z = 12\,\mu$m. The radial size of the defect w_r is

much larger than R_{TF}, ensuring that flow around the defect is suppressed. We conduct experiments using both a repulsive (blue detuned) and an attractive (red detuned) defect with $|\Delta| = 300\,\text{GHz}$.

We adjust the healing length through an approximate range $0.5\,\mu\text{m} < \xi < 20\,\mu\text{m}$ by tuning a. Thus, a wide range of values are achievable for the relevant dimensionless quantities, $0.1 < \xi/\sigma_{\text{D}} < 3.6$ and $0.04 < \xi/w_z < 1.7$.

5.3 Disorder Induced Dissipation

5.3.1 Thomas-Fermi Regime

Figure 5.2 shows the position of the center of a condensate at various times during a dipole oscillation in a disordered potential. The dipole oscillation is initiated by a kick that produces an initial peak velocity of $v_0 = 20\,\text{mm/s}$ when the condensate passes through the center of the trap. For this data, the condensate begins its motion well into the supersonic regime with $v_0 \sim 4\,c_0$. The resulting oscillation is characterized by a time-dependent damping, suggesting that the damping depends on v_0. The damping begins relatively weak, goes through a maximum after about 3.8 s, and then diminishes at later times. We fit 4-period sections of the data in Fig. 5.2 to the form of a damped harmonic oscillator:

$$z(t) = Ae^{-\beta t}\cos\left(\omega' t + \phi\right), \tag{5.5}$$
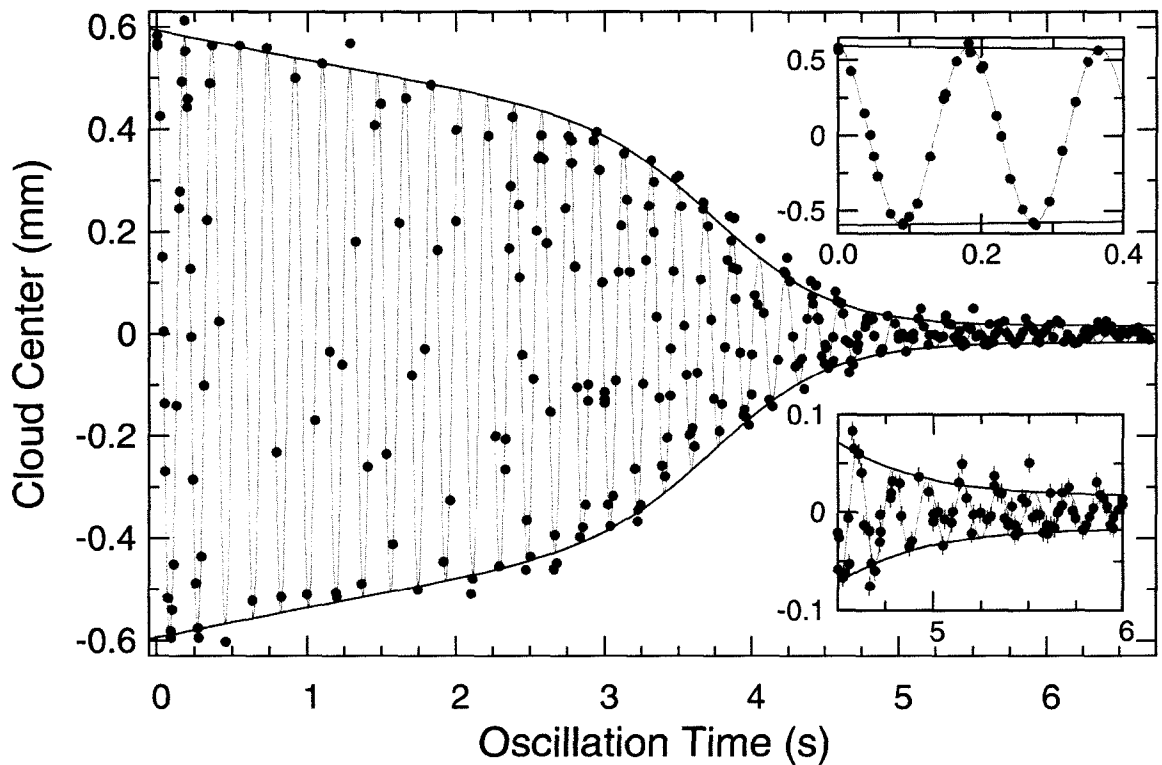
Figure 5.2 : Damping of a condensate initially traveling supersonically through a disordered potential with $V_D/h = 280\,\mathrm{Hz}$. The center of the BEC (circles) is extracted from a Thomas-Fermi fit to the radially integrated column density (the "axial density"). The thick lines tracing the amplitude are phenomenological guides to the eye. The initial amplitude is $A = 0.6\,\mathrm{mm}$ yielding an initial peak velocity of $v_0 = 20\,\mathrm{mm/s}$. For this data, $\omega_z = (2\pi)\,5.5\,\mathrm{Hz}$, $\omega_r = (2\pi)\,260\,\mathrm{Hz}$, $a = 25\,a_0$, and $\mu = \frac{1}{2}m\omega_z^2 R_{\mathrm{TF}}^2 = h\,(1.1\,\mathrm{kHz})$. In addition, $c_0 = 5.6\,\mathrm{mm/s}$, $\xi = 0.8\,\mu\mathrm{m}$, and $\xi/\sigma_D = 0.2$. The insets show details of the oscillation at early and late times.
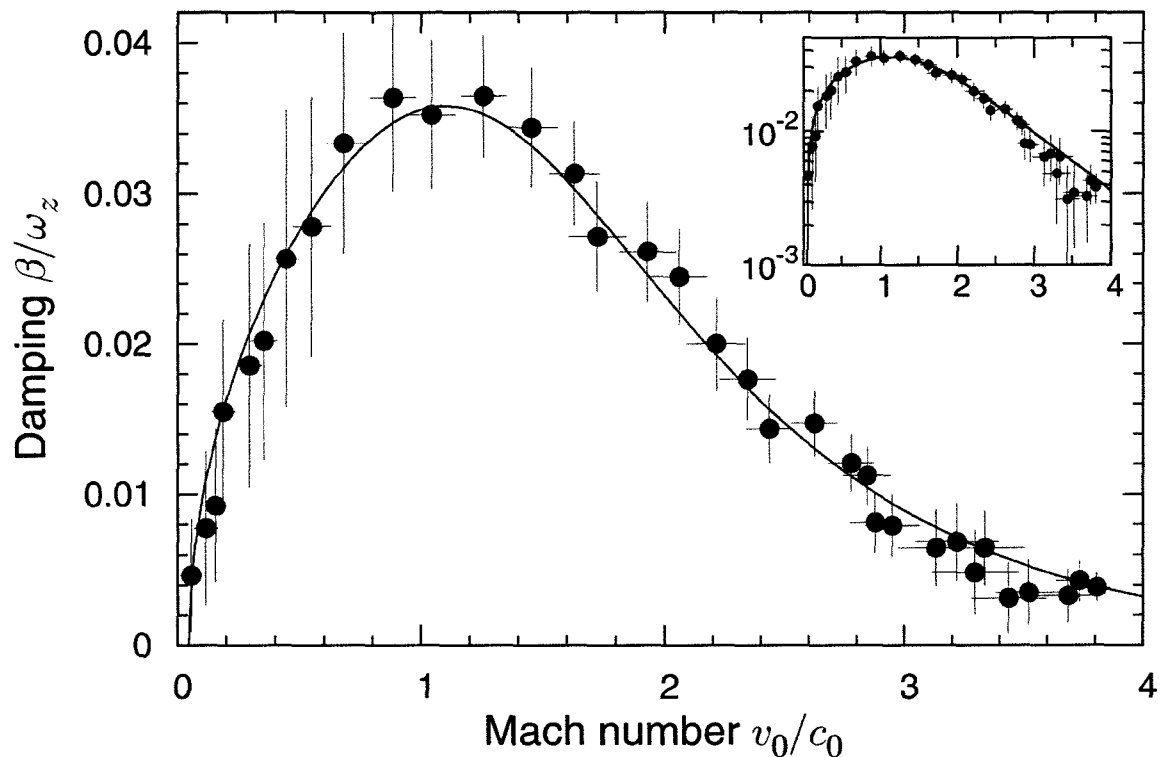
Figure 5.3 : Velocity dependent damping. Results of fitting the data of Fig. 5.2 to Eq. 5.5 using a traveling 4-period window. The peak velocity v_0 is obtained from $v_0 = A\omega_z$. The solid line is a square-root function convolved with an exponential decay and is meant as a guide to the eye. The inset shows the same data on a semi-log plot, emphasizing the nearly exponential decay of β/ω_z for large v_0/c_0. Vertical error bars correspond to the range in β for which $\Delta\chi^2 = 1$ for the fit to Eq. 5.5 while simultaneously adjusting all other parameters to minimize χ^2. Horizontal error bars are determined using an identical process for A in Eq. 5.5 and are typically ~15%.

where $\omega' = (\omega_z^2 - \beta^2)^{1/2}$. The peak velocity v_0 is then computed from the fitted A for each data subset to obtain the damping coefficient β as a function of v_0, with the results shown in Fig. 5.3. The damping monotonically increases for small v_0, peaking near $v_0 \sim 1.1 \, c_0$, followed by a nearly exponential decay of β for $v_0 > c_0$.

A perturbative theoretical treatment has produced a closed form solution for the velocity-dependent damping, resulting in good quantitative agreement with our measurements [97]. For weak disorder the qualitative behavior shown in Fig. 5.3 can be understood through a local Landau critical velocity argument. At low velocities, Bogoliubov quasiparticles are only created within a thin shell at the surface of the condensate, where the low density leads to a low local speed of sound, and therefore a low local v_L. As the velocity of the condensate increases, a larger condensate volume can support excitations because a larger fraction of the atoms violate the local Landau criterion. The maximum damping occurs near the point where the velocity of the BEC reaches the peak speed of sound c_0 in the condensate. At even larger velocities the excitation volume cannot increase further, but the Bogoliubov density of states decreases, resulting in the observed exponential decrease of the damping.

Except for the absence of a critical velocity, the qualitative behavior of the velocity dependent damping shown in Fig. 5.3 is remarkably similar to that predicted by 1D NLSE simulations of a uniform, repulsive BEC in the presence of an oscillating Gaussian obstacle [98, 99]. In these simulations, above a certain impurity strength-

dependent critical velocity, the impurity moving at a velocity v deposits energy into the BEC in the form of density fluctuations. The average rate of condensate energy growth $\langle dE/dt \rangle$ increases nearly linearly with v, to a peak at $v \sim c$ as the defect excites dark solitons and linear sound waves. As the velocity of the defect is increased further, the density fluctuations decrease significantly, accompanied by an exponential decrease of $\langle dE/dt \rangle$, similar to our experimental observations. In contrast to a single impurity in a uniform condensate, a defect is always present in a low density region of a condensate in a disordered harmonic trap. Consequently, v_0 is always greater than the local speed of sound at the edge of the condensate and excitations are always present. Previous experimental [94, 100, 93] and numerical [101] studies of the damping of collective modes and the damping of Bloch oscillations in a disordered lattice potential [102, 103] have found qualitatively similar results.

Figure 5.4 shows *in situ* polarization phase-contrast images [104] of the BEC at various times in the oscillation shown in Fig. 5.2. The damping clearly does not result from a loss of collectivity as predicted by 1D NLSE numerical simulations [101]. Rather, the BEC nearly maintains its original shape throughout the oscillation. Close inspection of the density distributions in Fig. 5.4 reveals a "tail" of non-condensed atoms that appears to oscillate slightly out-of-phase with the central Thomas-Fermi distribution. At early times, these non-condensed atoms appear to lag behind the BEC, while at later times they oscillate in-phase with it. This two-component out-of-phase oscillation is reminiscent of the second sound-like oscillation reported in
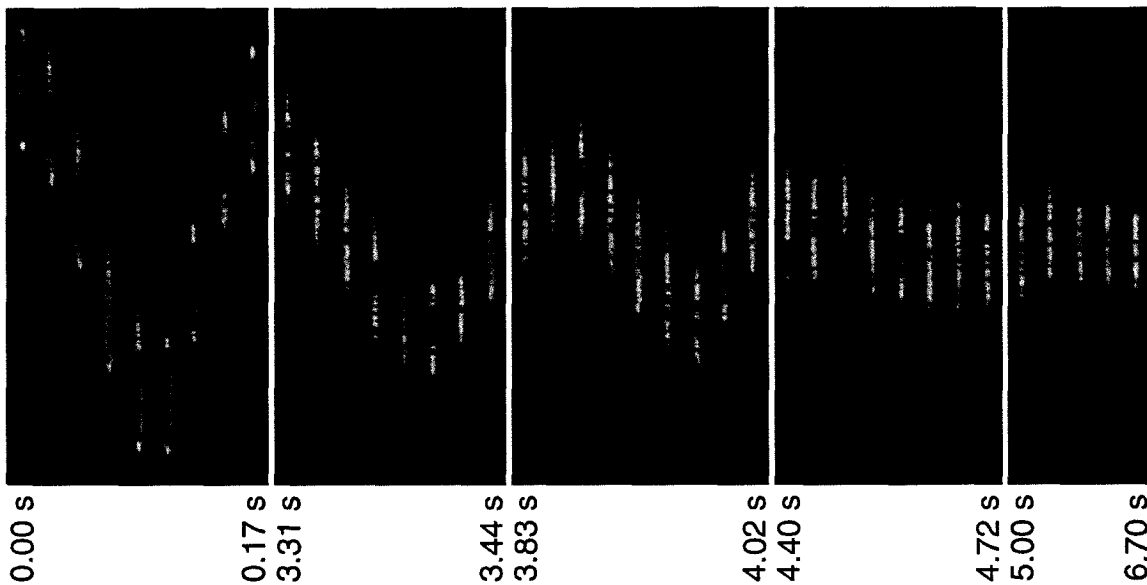
Figure 5.4 : Characteristic *in situ* polarization phase-contrast images of the data shown in Fig. 5.2 at various times. The images are nearly equally spaced in time between the time labels.

Ref. [105]. In that work, the initial temperature was high enough that damping occurred due to the interaction between a BEC and a thermal component. In contrast to those results, we observe that the dipole oscillation is undamped in the absence of the disordered potential. Furthermore, there is no observable heating due to the quick switch on of the disorder. In our experiment, therefore, the presence of the non-condensed component seems to be linked to the motion of the BEC in the disordered potential. A recent numerical simulation using a truncated Wigner method predicts the emission of incoherent atoms from a BEC moving supersonically through a disordered potential [106], consistent with our observations.

We have investigated this effect in further detail using *in situ* absorption imaging, which allows for determination of the low density non-condensed wings of the
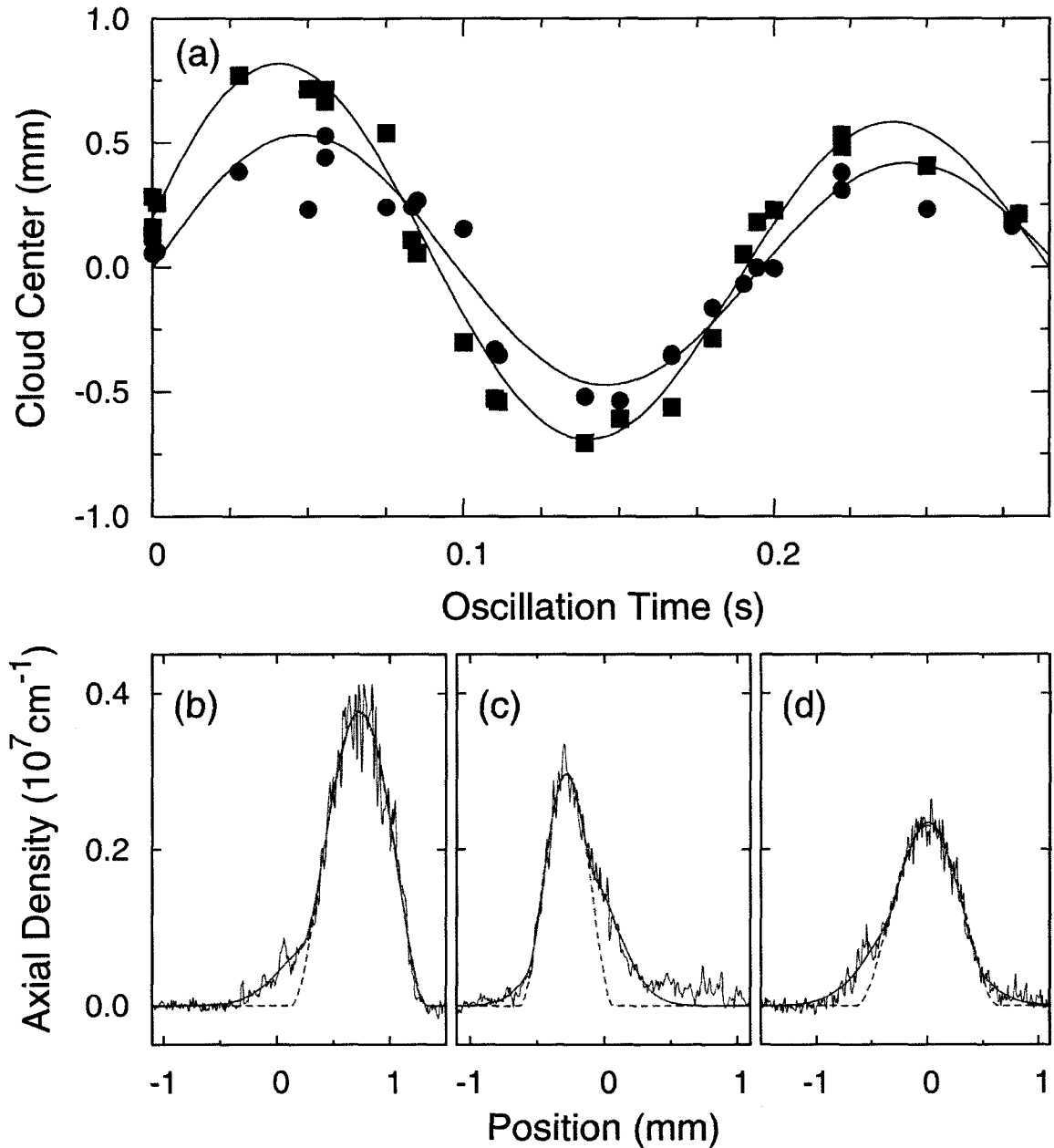
Figure 5.5 : Generation of a non-condensed component. (a) Squares show the center of the Thomas-Fermi (condensed) component and circles show the center of the Gaussian (non-condensed) component. The Gaussian center trails behind the Thomas-Fermi center and has a lower amplitude of oscillation. Within experimental uncertainty, $\omega_z = (2\pi)\,5.1(2)\,\mathrm{Hz}$ for both components. For this data, $a = 200\,a_0$, $N = 3 \times 10^5$, $\mu/h = 1.8\,\mathrm{kHz}$, $V_\mathrm{D}/\mu = 0.22$, $v_0 = 28\,\mathrm{mm/s}$, $c_0 = 7.2\,\mathrm{mm/s}$, and $\omega_r = (2\pi)\,220\,\mathrm{Hz}$. (b–d) Axial density distributions with bimodal fits (solid lines) and a single component Thomas-Fermi fit (dashed lines) at various times during the oscillation: (b) 28 ms, (c) 100 ms, (d) 190 ms. The condensates in (b) and (d) are traveling in the positive direction whereas the condensate in (c) is traveling in the negative direction.

distributions. Figure 5.5 shows that by fitting the cloud to a bimodal Thomas-Fermi plus Gaussian profile, a phase difference of $\Delta\varphi = 0.23$ between the condensed and non-condensed cloud centers is found. Note that the interaction strength is different for this data than that shown in Figs. 5.2–5.4.

We have systematically investigated the dependence of β on the disorder strength V_D. Figure 5.6 shows the normalized damping parameter β/ω_z plotted against the normalized disorder strength V_D/μ, where μ is the chemical potential of the condensate prior to the kick and before the disorder is switched on. We find the data fits well to a power law

$$\frac{\beta}{\omega_z} \propto \left(\frac{V_D}{\mu}\right)^p, \tag{5.6}$$

for all measured velocities. The precise value of p, however, depends weakly on v_0 across the range of velocities $0 < v_0/c_0 < 5$, with a mean value of $p = 2.1(5)$ (see Fig. 5.6 inset).

Figure 5.7 presents the measured values of β as a function of both V_D and v_0. As expected, a vertical trace through this plot shows a qualitative similarity to Fig. 5.3. We observe two distinct regimes of reduced damping: one where $v_0/c_0 \ll 1$ and the other when $v_0/c_0 \gg 1$, with the damping reaching a maximum at $v_0 \sim c_0$. A numerical simulation using an effective 1D NLSE has produced qualitatively similar results [101].
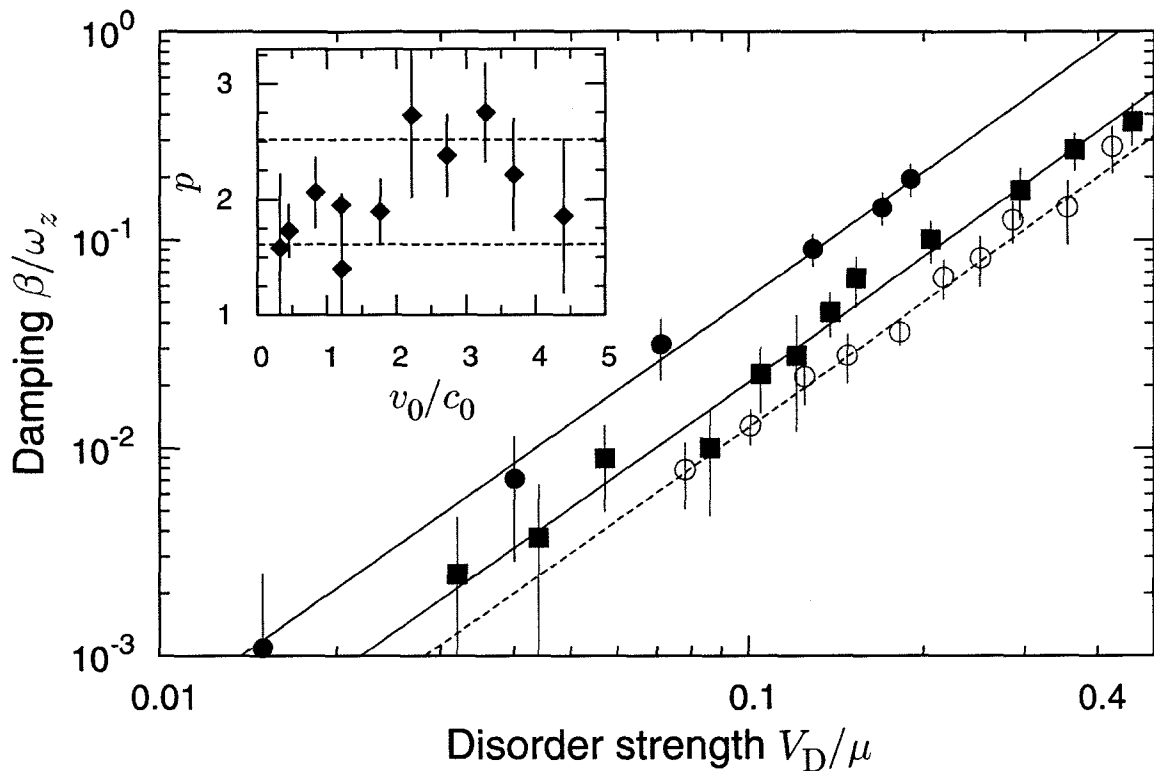
Figure 5.6 : Damping vs. V_D. Open circles correspond to the data shown in Fig. 5.7 $(a = 200\,a_0)$ in the range $0.7 < v_0/c_0 < 0.9$; filled circles correspond to $a = 200\,a_0$, $v_0/c_0 = 1.2$, $\mu/h = 2.2\,\mathrm{kHz}$; squares correspond to $a = 25\,a_0$, $v_0/c_0 = 1.2$, $\mu/h = 750\,\mathrm{Hz}$. The damping parameter β follows a power law with $p \sim 2$ (solid and dashed lines), independent of μ or a. To minimize systematic effects associated with the velocity dependence of β (e.g., Figs. 5.2 and 5.3), we fit a 4-period window for which the data is described well by Eq. 5.5. Vertical error bars are as defined in Fig. 5.3. The inset shows the fit values of p as a function of v_0/c_0 for a collection of data sets at $a = 200\,a_0$. The dashed lines indicate the plus-and-minus one standard deviation extent for the collection of measured velocities. Vertical error bars for p are determined as in Fig. 5.3 using a fit to Eq. 5.6 for each oscillation at a given v_0/c_0. Data corresponding to filled circles and squares was taken using an optical trap setup different from that described in Sec. 5.2 with $\lambda = 1064\,\mathrm{nm}$ and a beam waist of $24\,\mu\mathrm{m}$ resulting in $\omega_z = (2\pi)\,4.9\,\mathrm{Hz}$, $\omega_r = (2\pi)\,460\,\mathrm{Hz}$, and $N = 3 \times 10^5$. Also, for these data sets $\sigma_D = 3.4\,\mu\mathrm{m}$.
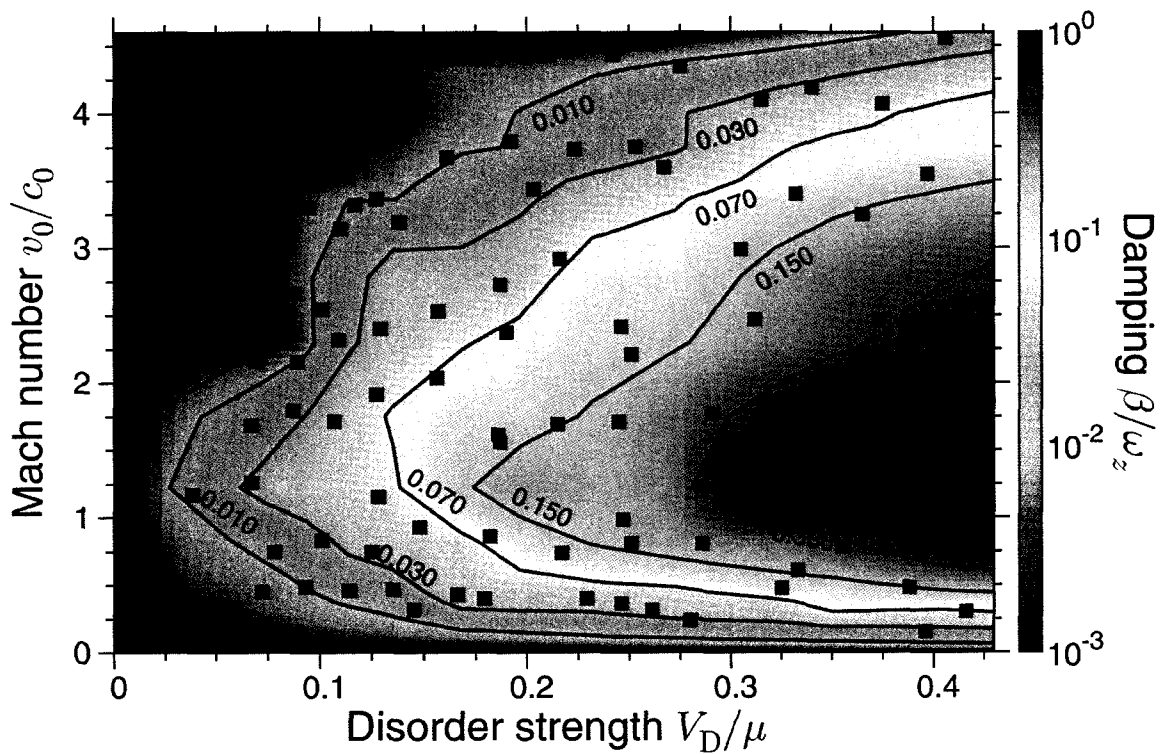
Figure 5.7 : Transport regimes of a BEC traveling through a disordered harmonic potential. Black squares show the values of disorder strength V_D/μ and initial peak center of mass velocity v_0/c_0 for the data used to extract β from a fit to Eq. 5.5 using 4-6 periods of oscillation. The interpolated color map (and contour lines) for β/ω_z is derived from the measured results. These measurements have $a = 200\,a_0$, $N = 2 \times 10^5$ atoms, $\mu/h = 1.5\,\text{kHz}$, $c_0 = 6.5\,\text{mm/s}$, $\omega_r = (2\pi)\,260\,\text{Hz}$, and $\omega_z = (2\pi)\,5.5\,\text{Hz}$. Due to small shot-to-shot fluctuations in the position of the center of mass of the cloud, measurements with $v_0 < 0.2\,c_0$ are not reliable. Data with $\beta \leq 2 \times 10^{-3}$ is consistent with undamped motion.

5.3.2 Variation with Interaction Strength

We observe nearly universal behavior for β as a function of both V_D/μ, and v_0/c_0 for BECs in the Thomas-Fermi regime. As already shown in Fig. 5.6, $\beta \propto (V_D/\mu)^2$ for condensates with μ differing by a factor of 2 (corresponding to a factor of 8 in a). Shown in Fig. 5.8 is a comparison between the damping at interaction strengths $a = 200\,a_0$ and $a = 28\,a_0$, with constant V_D/μ. Although the respective values of c_0 differ by nearly a factor of 2 between the two data sets, the peak damping occurs at $v_0/c_0 \sim 1$ for both, demonstrating the nearly universal behavior of β vs. v_0/c_0. On the other hand, the peak damping rate between the two data sets differs by nearly a factor of 5, showing that while the general shape of the damping curve is universal, the magnitude of the damping is not.

An investigation of the effect of interatomic interactions on the peak damping $(v_0/c_0 \sim 1)$ at fixed V_D/μ is shown in Fig. 5.9. We find that β scales linearly with a, going to zero with decreasing interactions, consistent with the disappearance of the low energy phonon portion of the excitation spectrum as $U \to 0$.

The elongated confinement geometry in our system facilitates the investigation of the dimensional crossover from the 3D to the quasi-1D regime where $\mu \ll \hbar\omega_r$ [107, 108]. Shown in Fig. 5.10 are measurements of β vs. μ at constant V_D and v_0. When $\mu > \hbar\omega_r$ and v_0 is comparable to c_0, we find $\beta \propto \mu^{-p}$ with $p \sim 1.4$. By reference to Fig. 5.7, one can gain a qualitative understanding of this behavior going from high to low μ: starting subsonically (open and filled circles), the system travels along a
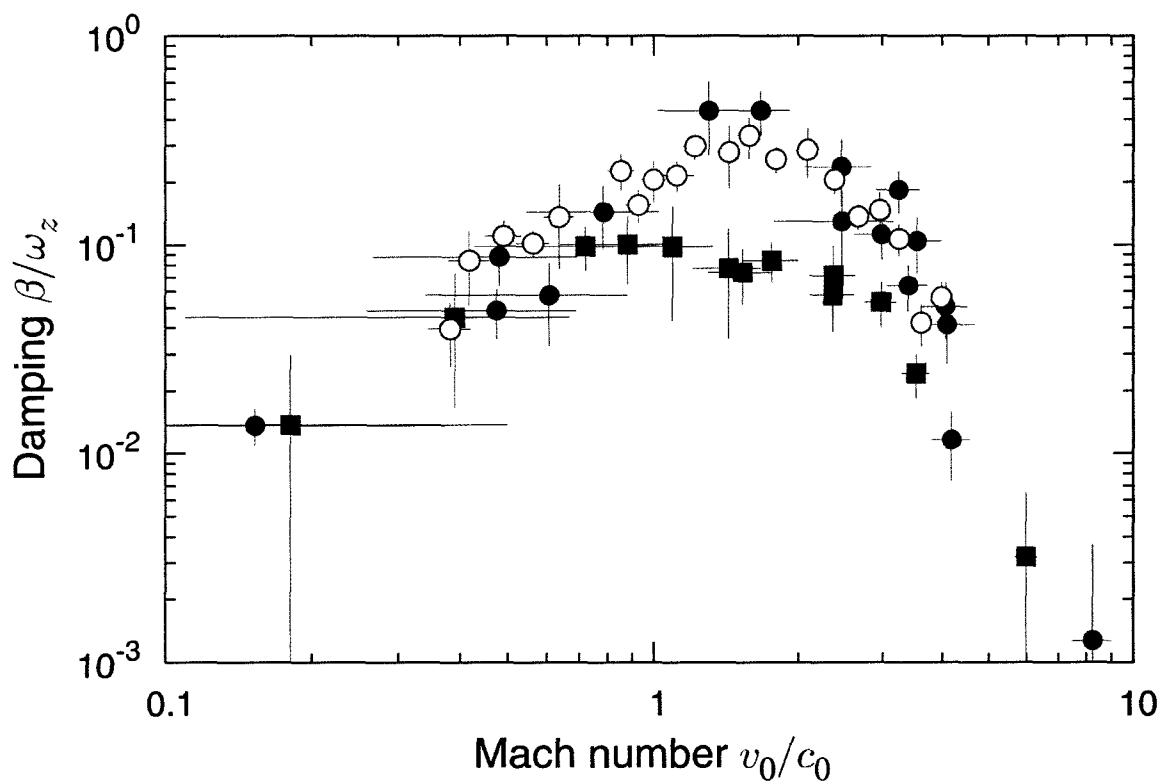
Figure 5.8 : Universal damping vs. v_0/c_0. The disorder strength was adjusted to keep $0.30 < V_D/\mu < 0.35$ for all of the data. Squares correspond to $a = 28\,a_0$, $N = 2.5 \times 10^5$, $\mu/h = 550\,\mathrm{Hz}$, $c_0 = 4.0\,\mathrm{mm/s}$, $\omega_z = (2\pi)\,5.5\,\mathrm{Hz}$, and $\omega_r = (2\pi)\,260\,\mathrm{Hz}$; open circles correspond to $a = 200\,a_0$, $N = 3 \times 10^5$, $\mu/h = 2.4\,\mathrm{kHz}$, $c_0 = 8.3\,\mathrm{mm/s}$, $\omega_z = (2\pi)\,4.5\,\mathrm{Hz}$, and $\omega_r = (2\pi)\,460\,\mathrm{Hz}$; filled circles correspond to the same parameters as Fig. 5.7. Error bars are as defined in Fig. 5.3.
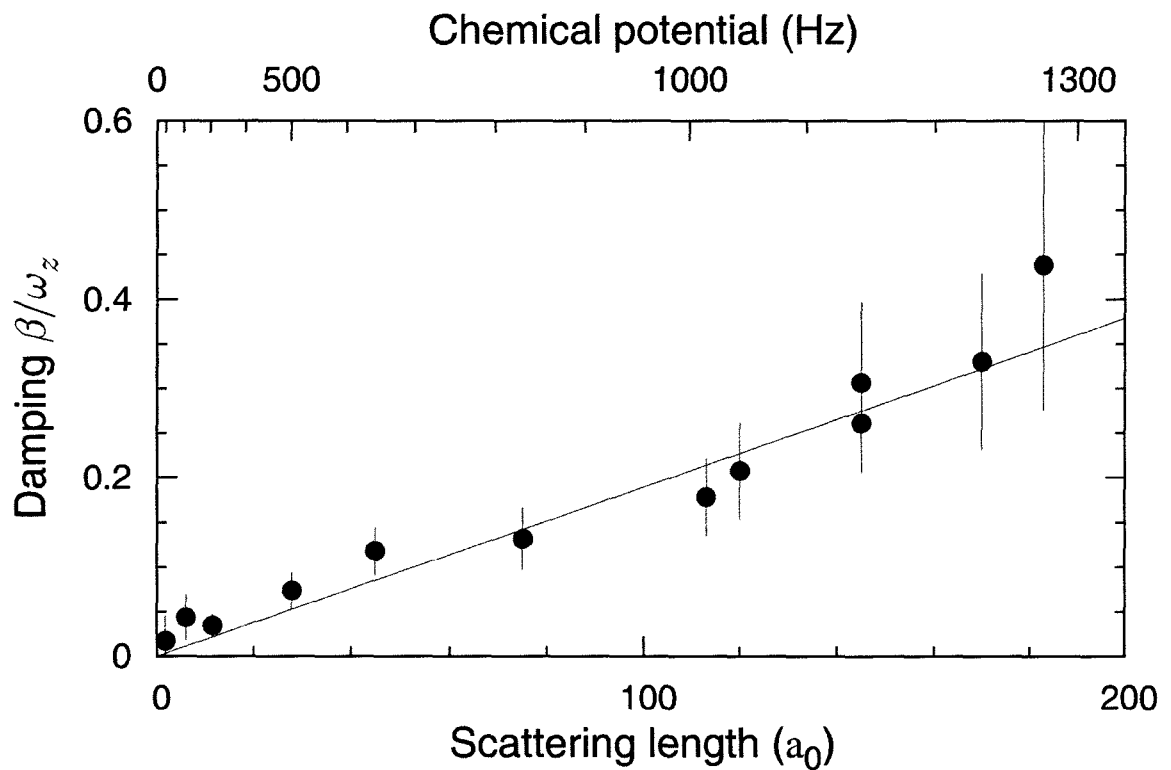
Figure 5.9 : Peak damping vs. a with fixed V_D/μ and v_0/c_0. For this data, V_D and v_0 were adjusted to keep $0.3 < V_D/\mu < 0.4$ and $0.6 < v_0/c_0 < 1.4$ with all other parameters as in Fig. 5.7. The upper horizontal axis shows values for μ obtained from a variational solution of the GPE [81]; note that the upper tick marks are not strictly logarithmically spaced. The linear fit has a slope $0.002\,a_0^{-1}$. Vertical error bars are as defined in Fig. 5.3.
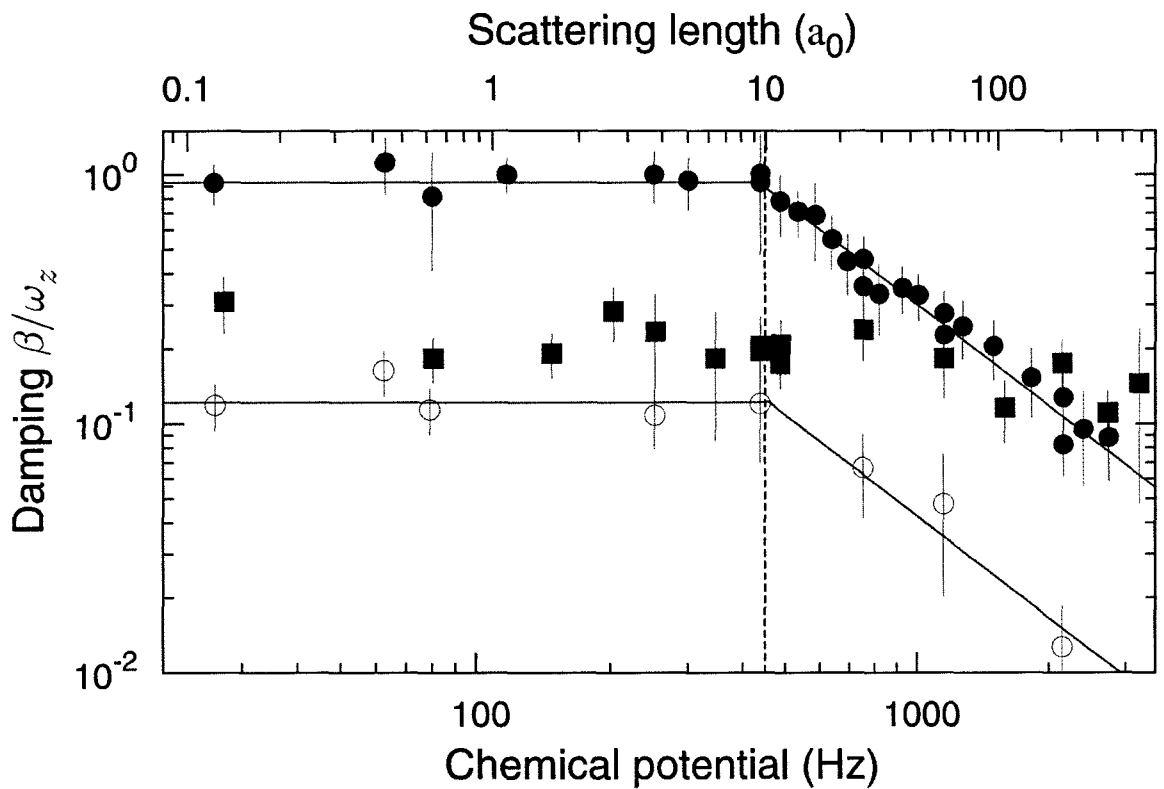
Figure 5.10 : Damping vs. μ with fixed V_D and v_0. Squares and filled circles correspond to $V_D/h = 370\,\text{Hz}$ with $v_0 = 11\,\text{mm/s}$ and $6\,\text{mm/s}$, respectively. Open circles correspond to $V_D/h = 140\,\text{Hz}$ and $v_0 = 6\,\text{mm/s}$. The vertical dashed line denotes $\mu = \hbar\omega_r$. We varied μ by adjusting a, shown on the upper horizontal axis; note that the upper tick marks are not strictly logarithmically spaced. Values for μ are obtained from a variational solution of the GPE [81] using the following measured experimental parameters: $\omega_r = (2\pi)\,460\,\text{Hz}$, $\omega_z = (2\pi)\,4.5\,\text{Hz}$, and $N = 4 \times 10^5$ atoms. For this data $\sigma_D = 3.4\,\mu\text{m}$. Vertical error bars are as defined in Fig. 5.3.

trajectory from the weakly damped regime (lower left corner of Fig. 5.7) towards the

regime of strong damping (middle right region). However, starting supersonically

(squares) allows the BEC to roughly trace a contour of constant β as μ is reduced,

resulting in only a weak dependence of β on μ. When $\mu < \hbar\omega_r$, and consequentially

$v_0 \gg c_0$, we also observe a weak dependence of β on μ. In this quasi-1D regime, β

is affected only by changing V_D or v_0, consistent with the behavior expected for a

nearly ideal, classical fluid. This may be understood by reference to Eq. 5.2 where

for $v \gg c$, the first term in the Bogoliubov excitation spectrum dominates making

the system "quasi-ideal" with $\epsilon(p)$ independent of μ.

Figure 5.11 shows damping of a weakly interacting gas with $a = 0.4\,a_0$, deep into

the quasi-1D regime, where $\mu/\hbar\omega_r \sim 0.1$. We find that $V_D = 4\,\mu$ produces the same

damping ($\beta/\omega_z = 0.07$) as that for a BEC with $a = 200\,a_0$ and $V_D = 0.25\,\mu$. The na-

ture of the damped motion of a weakly interacting gas in strong disorder is strikingly

different from the damped motion of a strongly interacting gas in weak disorder, even

though the timescale of the damping in both cases is comparable. Figure 5.11 shows

that the damping in the weakly interacting regime is caused by the loss of coher-

ence of the collective dipole mode brought on by extensive fragmentation. Because

$V_D > \mu$, it is perhaps not surprising that the condensate quickly fragments. While

the center of mass of the cloud damps after about 5 oscillation periods, examina-

tion of shot-to-shot differences in the damped density distributions reveal that the

position of the fragments are highly non-repeatable, suggesting that some fragments
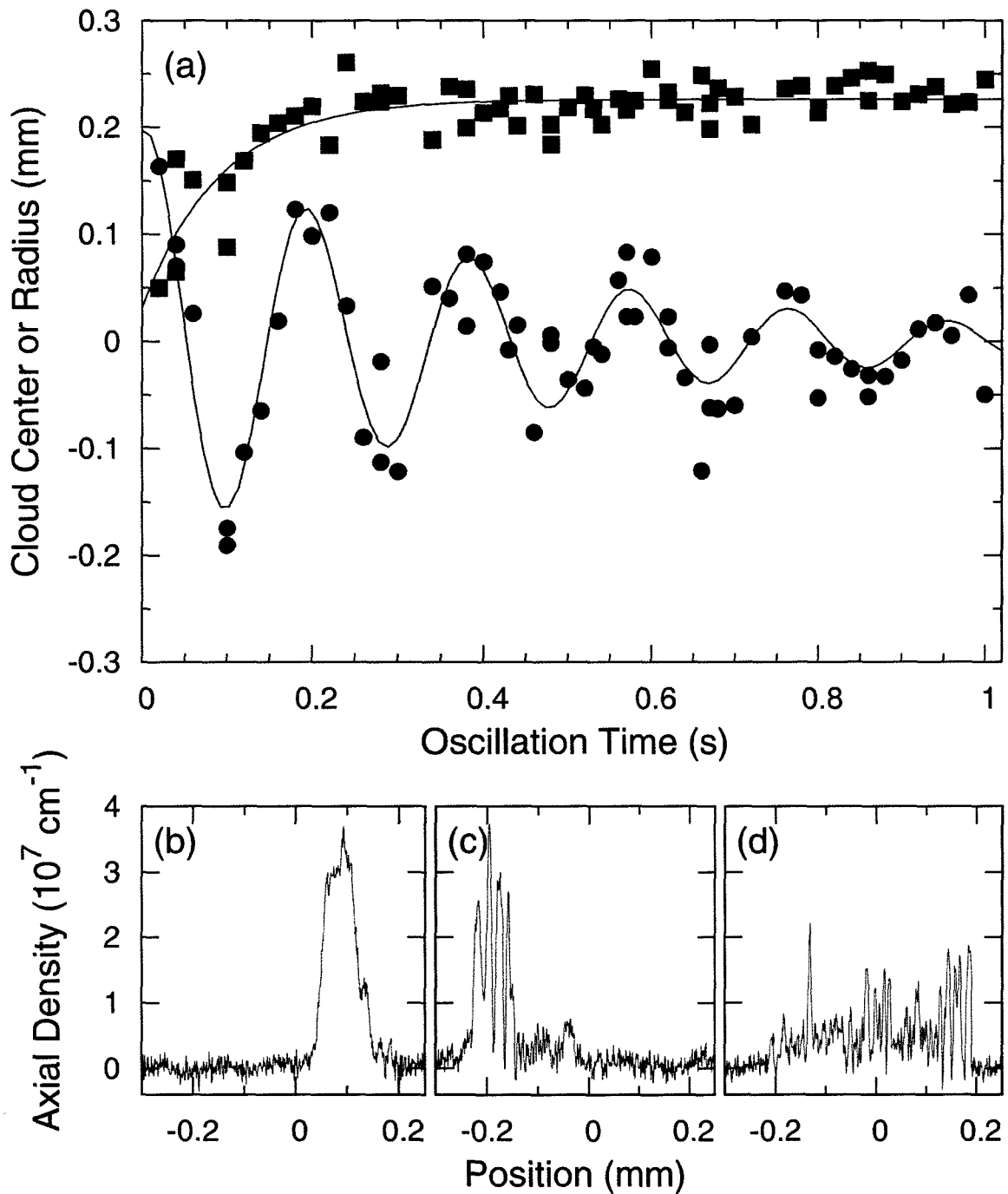
Figure 5.11 : Damping of a nearly non-interacting gas. For this data $a = 0.4\,a_0$, $N = 2 \times 10^5$, $\mu/h = 26\,\mathrm{Hz}$, $c = 1.2\,\mathrm{mm/s}$, $V_D = 4\,\mu$, $\omega_r = (2\pi)\,240\,\mathrm{Hz}$, and $\omega_z = (2\pi)\,5.3\,\mathrm{Hz}$. (a) Center of mass position (circles) and radius (squares) of the condensate as a function of time. Here we use statistically determined values for the center of mass $z_{\mathrm{cm}} = \int z\,n(z)dz/N$ and radius R, given by $R^2 = 4\int(z - z_{\mathrm{cm}})^2\,n(z)dz/N$. (b-d) Axial density traces at various times in the oscillation: (b) 40 ms (c) 100 ms, (d) 960 ms. After two full oscillations, the cloud has fragmented and spread to a size comparable with the initial oscillation amplitude.

remain in motion. This residual motion is consistent with the long thermalization time expected from weak two-body interactions. It is interesting to note that the maximum single particle kinetic energy, $E_K = \frac{1}{2}m\omega_z^2 A^2 = h\,(295\,\text{Hz})$, is 2.8 times larger than the average height of the disordered potential. The observed dephasing is therefore consistent with the expected behavior of a gas of non-interacting particles interacting with a disordered potential where the disorder strength is smaller than the kinetic energy of the individual particles.

5.3.3 Dipole Oscillations of Bright Solitons in Disorder

As alluded to in the introduction, our system can be used to create bright matter-wave solitons. Figure 5.12(a) and (b) shows a comparison between BECs with $a = 0.4\,a_0$ and a single soliton at $a = -0.4\,a_0$ both undergoing dipole oscillation without disorder. For both BECs the $E_{\text{KIN}}/h = 300\,\text{Hz}$. As expected, the attractive interactions modify the shape of the soliton such that it is axially much smaller than the slightly repulsive BEC but the axial oscillation frequency remains unchanged. Figure 5.12(c) shows the result of turning on the disorder to $V_D = 500\,\text{Hz}$ right at the peak of the oscillation. In this scenario, the soliton becomes pinned as expected for a classical single particle in strong disorder. However, the disorder appears to induce fragmentation of the soliton. For weaker disorder, we observe damped oscillation of the soliton with a time scale identical to that found for the weakly attractive gas. As for the weakly repulsive case, the damping results from a fragmentation

and dephasing of the dipole mode. Shown in Fig. 5.13 is a comparison between $a = 0.4\,a_0$ and $a = -0.4\,a_0$ under identical oscillation conditions as Fig. 5.12 except with a weaker disorder of $V_D = 103\,\mathrm{Hz}$. As the strength of the disorder is much weaker than E_{KIN} pinning of the cloud is avoided.

5.4   Dissipation Induced by a Single Gaussian Defect

5.4.1   Thomas-Fermi Regime

In an effort to better understand the mechanisms responsible for the damping in our disorder experiments, we have investigated the dissipation induced by a *single* Gaussian defect. The defect potential is described by $V(z) = V_D e^{-2z^2/w_z^2}$, where $w_z = 12\,\mu\mathrm{m}$. The static effect of either an attractive or repulsive defect on a repulsively interacting BEC in the Thomas-Fermi regime is shown in Fig. 5.14. As expected, the attractive defect leads to an increase of the density in the region of the defect, accompanied by a small decrease of the density in the wings of the distribution, while the opposite is true for the case of a repulsive defect.

The dynamical distributions can differ dramatically from the static case, as shown in Fig. 5.15 where *in situ* axial densities are displayed for various times throughout the dipole oscillation. In the following discussion we refer to the upstream side of the condensate as the portion of the BEC that reaches the barrier after the leading or downstream portion. The interaction of the BEC with the repulsive defect, shown in Fig. 5.15(b), produces a deep downstream density rarefication as well as a large

(a)

(b)

(c)

t=0ms

$\Delta t = 30\,ms$
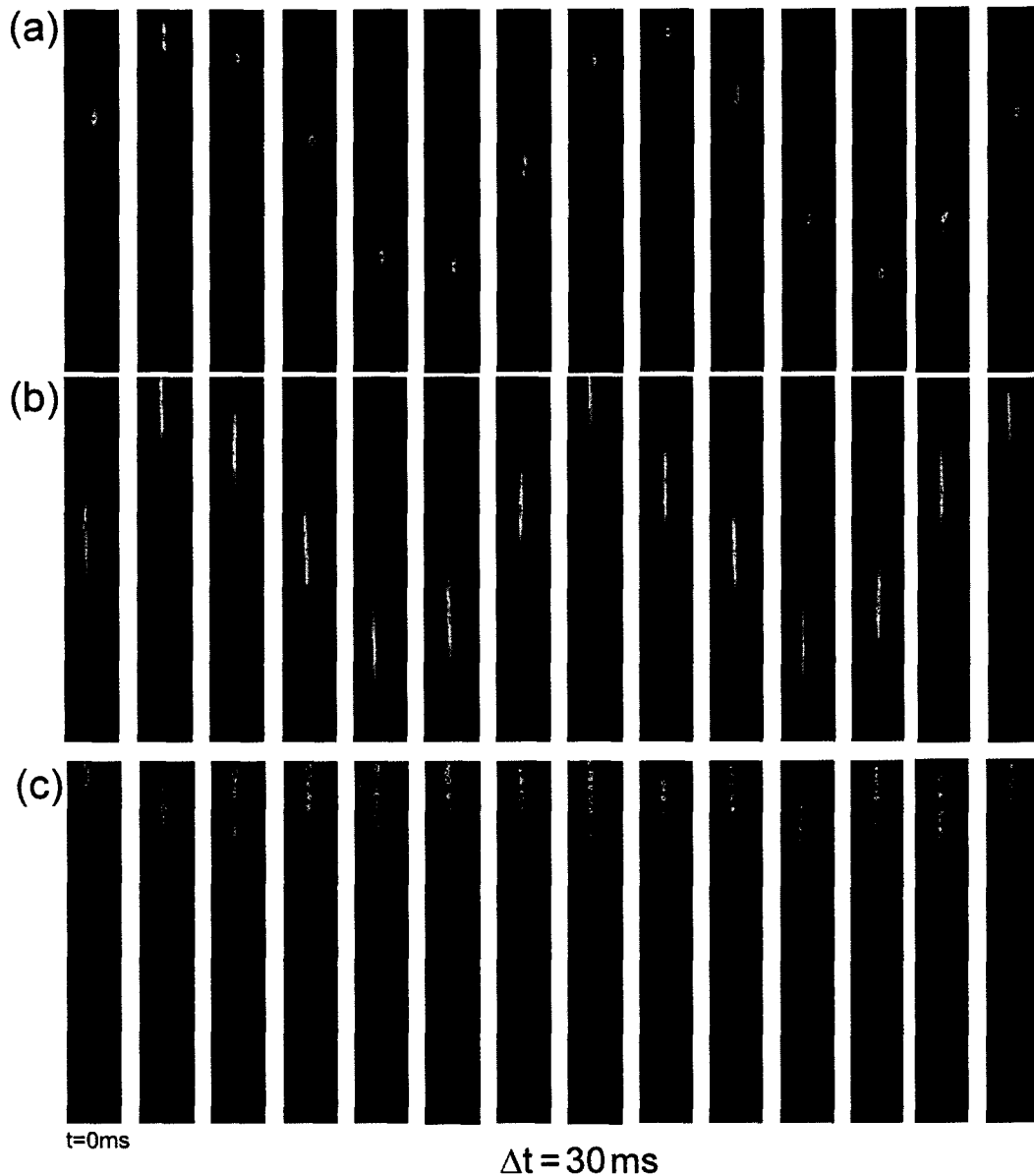
Figure 5.12 : (a) Dipole oscillation of a bright matter wave soliton with $N \sim 70 \times 10^3$ and $a = -0.42\, a_0$. Note N is very close to the critical number for collapse of $N_c = 80 \times 10^3$ given by $N_c = 0.35 l_z \lambda^{1/3}/a$ where $\lambda = \omega_z/\omega_r$ and $l_z = \sqrt{\hbar/(m\omega_z)}$[56]. Therefore, occasional shots with slightly larger numbers will produce two solitons, as in the second frame. (b) Free dipole oscillation of a weakly repulsive BEC with parameters as described in Fig. 5.11. (c) Pinning and fragmentation of the soliton in (a) but under the influence of a disorder potential of strength $V_D = 500\,Hz$. Trap parameters are the same as in Fig. 5.11.
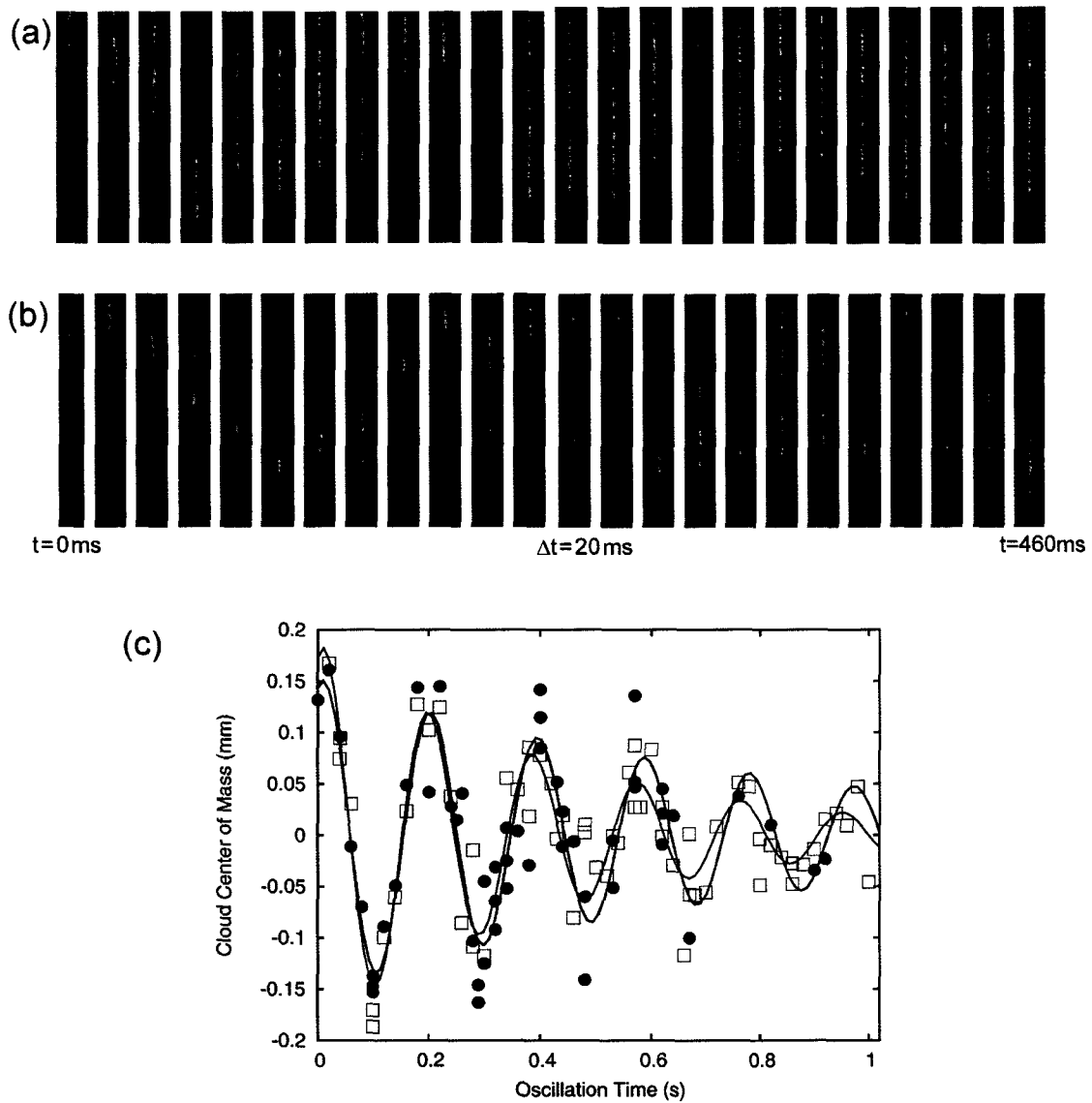
Figure 5.13 : (a) 2D images of the weakly repulsive gas shown in Fig. 5.11. (b) Damping of a soliton with identical parameters to Fig. 5.12(a) but with $V_D = 100\,\text{Hz}$. (c) Cloud center of mass (as defined in Fig. 5.11) as a function of time for the soliton (solid circles) and weakly repulsive gas (open squares) with $V_D = 100\,\text{Hz}$ and trap parameters as in Fig. 5.11. Solid lines show fits to data of corresponding color.
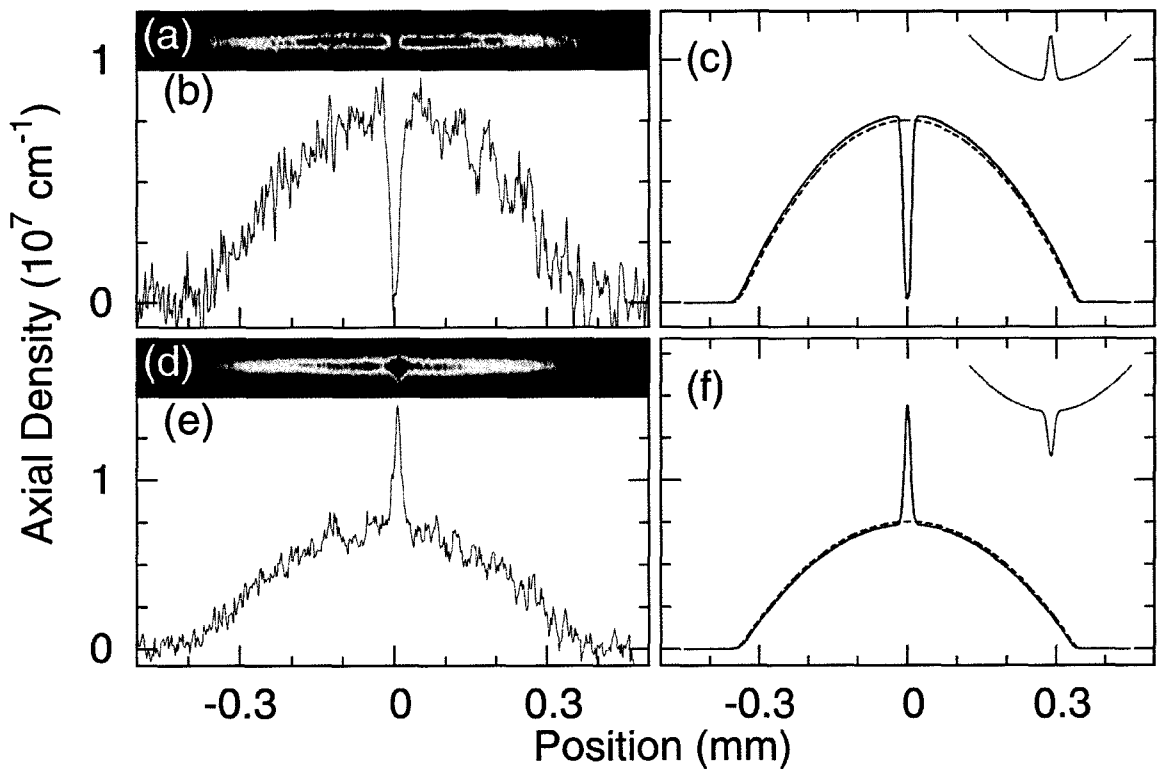
Figure 5.14 : BEC in a harmonic trap with a single Gaussian defect. (a–c) correspond to a repulsive defect, while (d–f) to an attractive one. (a) and (d) *in situ* polarization phase-contrast images, (b) and (e) axial densities corresponding to the images, and (c) and (f) numerical solutions to the GPE with the dashed lines showing the solution in absence of a defect. The inset trace shows the characteristic shape of the potential. For all panels, $a = 200\,a_0$, $N = 4 \times 10^5$, $\omega_z = (2\pi)\,5.0\,\text{Hz}$, and $\omega_r = (2\pi)\,360\,\text{Hz}$.
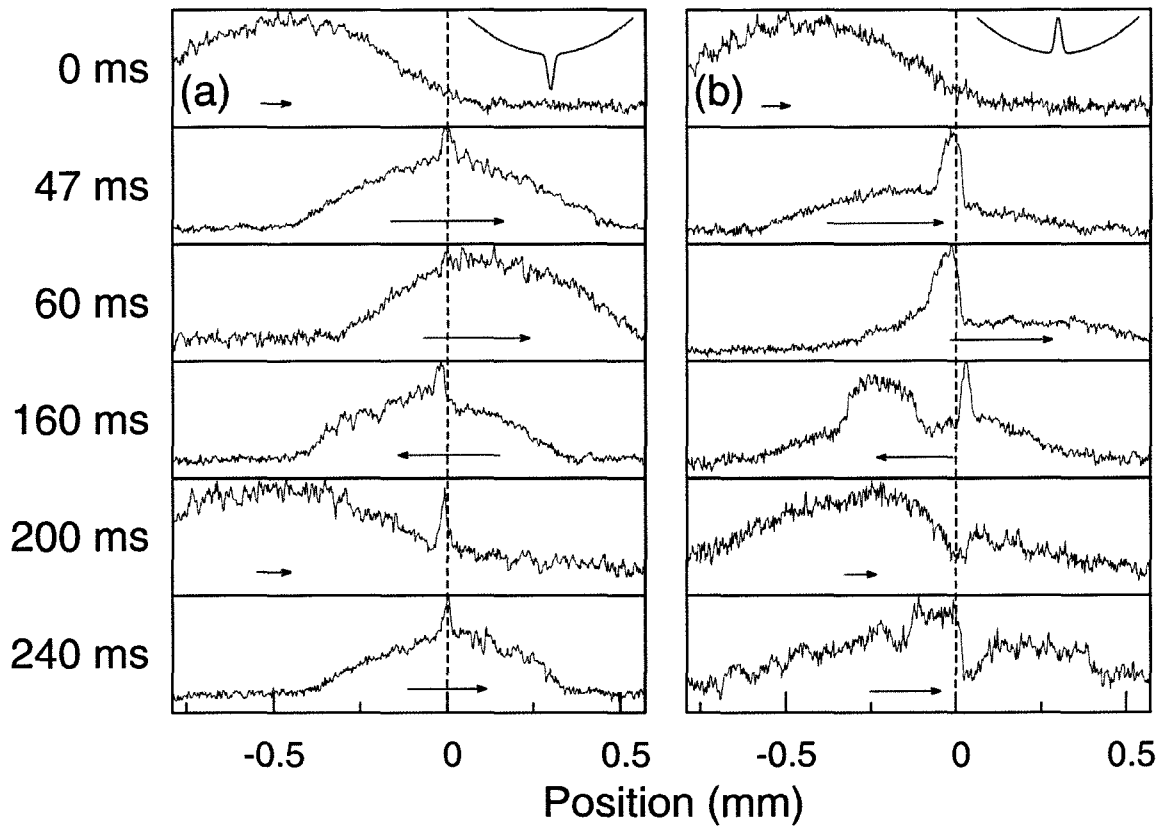
Figure 5.15 : Axial densities at various times during a supersonic oscillation in the presence of an (a) attractive or (b) repulsive defect. The arrows are proportional to the instantaneous velocity of the condensate. The vertical dashed lines denote location of the defect. For this data, $a = 200\,a_0$ and $v_0 = 13\,\text{mm/s}$; (a) corresponds to $N = 4 \times 10^5$, $\mu = 1.5\,\text{kHz}$, $v_0/c_0 = 2$, $V_D = -0.8\,\mu$, $\omega_z = (2\pi)\,4.7\,\text{Hz}$, and $\omega_r = (2\pi)\,360\,\text{Hz}$; (b) corresponds to $N = 1 \times 10^6$, $\mu = 3\,\text{kHz}$, $v_0/c_0 = 1.4$, $V_D = 0.4\,\mu$, $\omega_z = (2\pi)\,5.0\,\text{Hz}$, and $\omega_z = (2\pi)\,360\,\text{Hz}$.
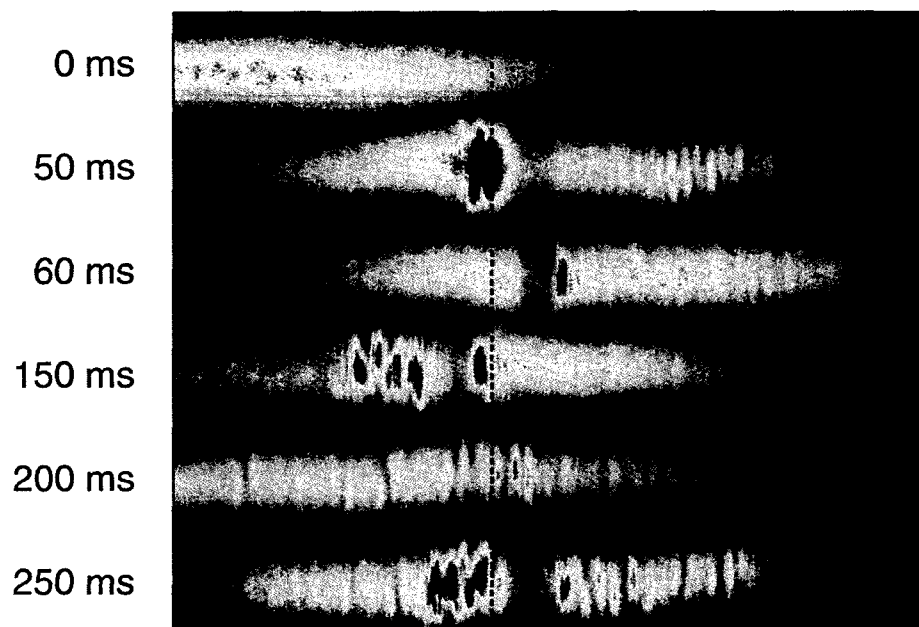
Figure 5.16 : Density fluctuations produced crossing a repulsive defect. Absorption images after 4 ms time-of-flight. The vertical dashed line denotes the location of the defect. For this data, parameters are as stated in Fig. 5.15(b).

upstream density compression bearing a qualitative similarity to a *dispersive* shock wave. Such shocks have been theoretically studied in the context of BEC with repulsive interactions in one [89, 109, 110], two [90, 111], and three dimensions [112], and have been experimentally observed in both BEC systems [113, 114, 112, 115, 105] and in nonlinear optical media [116]. Rather than dissipating energy through interparticle collisions, as in classical fluids, the dynamical behavior of shocks in superfluids is dominated by dispersion. This "quantum pressure" is a direct result of the governing dynamics of the quantum analog of the hydrodynamic equations for

a perfect fluid [26].[1]

In contrast, the the interaction of the BEC with the attractive defect, shown in Fig. 5.15(a), produces no such shock waves. However, the cloud is slightly compressed near the defect simply due to the attractive defect potential. Because $v_0 > c_0$, phonon excitations cannot be emitted in the upstream direction as they would have to propagate faster than the speed of sound. Close inspection of Fig. 5.15(a) reveals minimal density modulation of the upstream side, while more modulation is evident on the downstream side.

Several 1D theoretical studies predict the formation of downstream propagating dark solitons in addition to upstream propagating phonons as a repulsive or attractive defect is swept through a condensate [118, 119, 99, 120, 121, 101], which is consistent with the density fluctuations visible in Fig. 5.15. However, the size of the dark solitons will be on the order of the healing length, $\xi = 0.5\,\mu$m for these condensates, which is a factor of 6 smaller than our imaging resolution.

Figure 5.16 shows time-of-flight images of the BEC oscillating in the presence of a single repulsive defect. In contrast to the *in situ* images of Fig. 5.15(b), after time-of-flight additional short length scale structures emerge which were not previously visible. These structures are consistent with dark solitons that form from short

---

[1]The fact that BEC dynamics is described well by hydrodynamics is quite remarkable given the fact that for typical ultra-cold samples, densities are low enough and interactions are weak enough that the system is far from what one normally considers to be hydrodynamic [117]. In the macroscopically occupied groud state, however, the dynamics are described nearly perfectly by the hydrodynamic theory found by recasting the Gross-Pitaevskii equation in terms of the superfluid density $|\psi(r)|^2$ and supefluid velocity $v = \hbar/m\nabla\phi$. This fact is one of the many fascinating implications of the phase coherence of BEC.
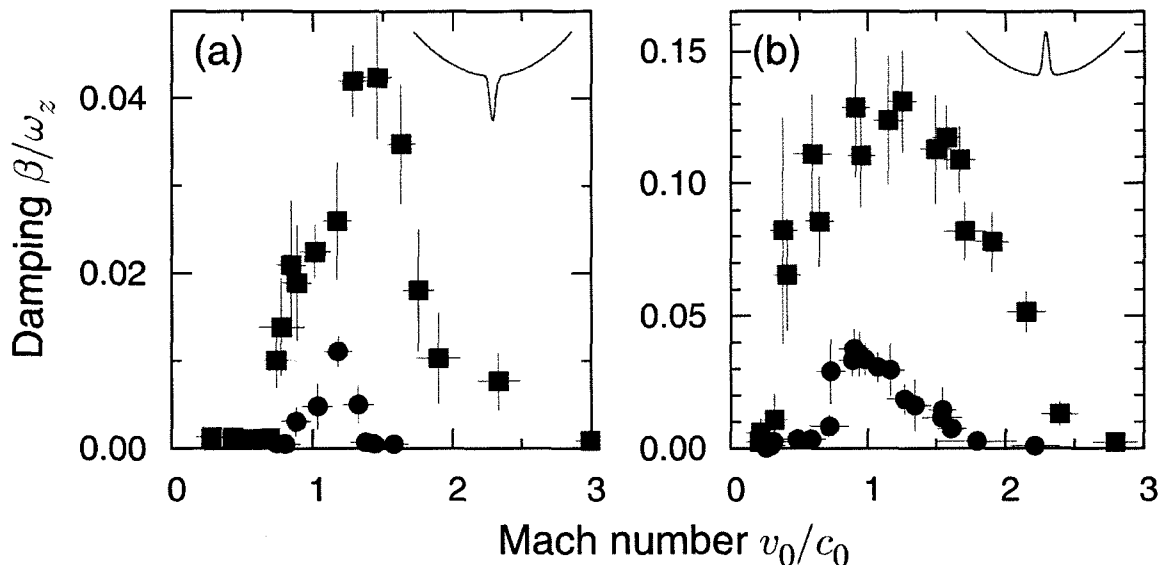
Figure 5.17 : Velocity dependence of β induced by a single Gaussian defect. (a) Attractive defect with (squares) $V_D/\mu = -0.8$ or (circles) $V_D/\mu = -0.3$ and other parameters as stated in Fig. 5.15(a) except with $N = 8 \times 10^5$ and $\mu/h = 2\,\mathrm{kHz}$. (b) Repulsive defect wth (squares) $V_D/\mu = 0.4$ or (circles) $V_D/\mu = 0.2$ and other parameters as stated in Fig. 5.15(b). Both types of impurities show critical behavior at low velocities as well as undamped motion at large v_0/c_0. Note the difference in scale between damping induced by an attractive versus a repulsive impurity. Vertical and horizontal error bars are as described in Fig. 5.3.

length scale *in situ* phase fluctuations that map onto larger scale density modulations after time-of-flight. However, *in situ* phase fluctuations may also arise from thermal excitations in highly elongated BECs, and these can also manifest as density fluctuations after time-of-flight [122]. Close inspection of Fig. 5.16 reveals that deep density modulations are present only in the downstream portion of the BEC (after the first pass through the defect), consistent with the dark soliton interpretation. Similar density fluctuations have been interpreted as dark solitons in an experiment using a moving defect and a stationary BEC [123].

We have measured β as a function of both V_D and v_0, with characteristic results
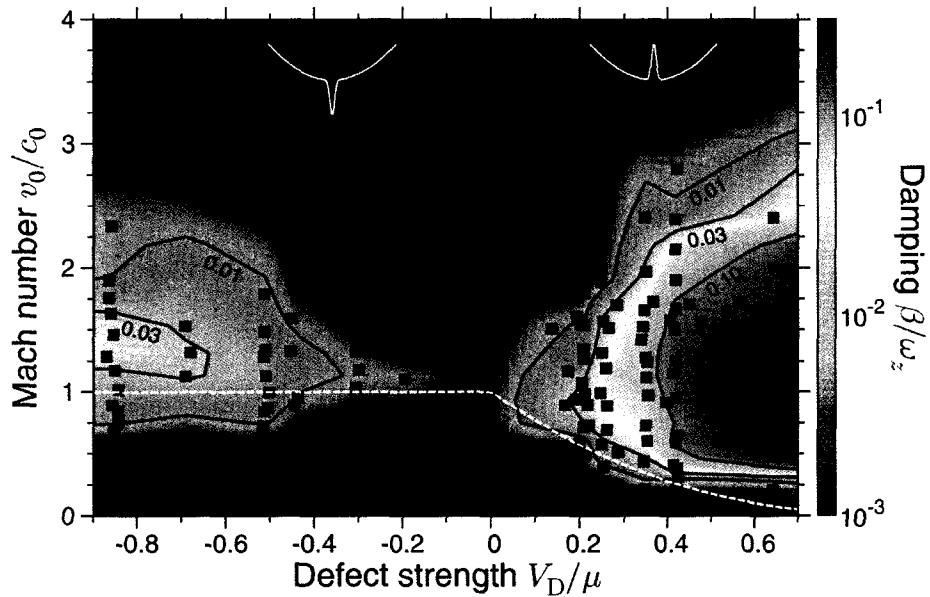
Figure 5.18 : Transport regimes of a BEC traveling through a harmonic potential with a central Gaussian defect. Coordinates of the black squares are the values of V_D/μ and v_0/c_0 for the data sets used to extract β/ω_z from a fit to Eq. 5.5. The color map (and contour lines) for β/ω_z is derived from an interpolation using the measured results. Dashed white lines show the local Landau critical velocity as given by Eqs. 5.7 and 5.9. The attractive and repulsive cases are qualitatively similar: superfluidity for $v_0/c_0 \ll 1$, increased damping as $v_0/c_0 \rightarrow 1$, and reduced damping for $v_0/c_0 \gg 1$. Damping induced by an attractive impurity is an order of magnitude weaker than for a repulsive one. Data with $V_D < 0$ and $V_D > 0$ correspond to parameters in Figs. 5.15(a) and (b), respectively.

presented in Fig. 5.17. Contrary to what was observed for a disordered potential, we observe a critical velocity v_c below which the motion is undamped, for both the attractive and repulsive defects. We find that the peak damping for an attractive defect is significantly weaker than for a repulsive one. The results of a thorough study of β as a function of both V_D and v_0 are presented in Fig. 5.18. For an attractive defect, we find that $v_c/c_0 \sim 0.6$ with v_c depending only weakly on V_D. However, for a moderately strong repulsive defect, v_c/c_0 occurs significantly below 1 and depends strongly on V_D. For both attractive and repulsive defects, however, v_c tends to c_0 as $|V_D/\mu|$ is reduced to zero.

Once again, a model based on a local Landau criterion is sufficient to explain the dependence of v_c on V_D. For simplicity, consider a uniform density flow impinging on either a repulsive or attractive Gaussian potential [119]. With the assumption that the superfluid flow pattern is stationary, the local density of the condensate near the defect must be modified in a similar way to that shown in Fig. 5.14 for a static defect. For the repulsive (attractive) case, the local density is reduced (increased) near the defect, resulting in a lower (higher) local speed of sound. In addition, flux conservation requires that the local condensate velocity increase (decrease) in the low (high) density region near the repulsive (attractive) impurity to preserve the stationary flow pattern. These effects serve to increase the local value of $v(z)/c(z)$ near a repulsive defect and decrease it for an attractive one. As a result, excitations can be created near the peak of the repulsive defect in a BEC with a center of mass

velocity that is significantly lower than the bulk speed of sound. For the case of an attractive impurity, on the other hand, one expects excitations to occur in the bulk condensate first, rather than near the impurity, and therefore at a flow velocity near the bulk speed of sound, as observed.

We quantify this picture, in the case of a repulsive defect, by applying the local Landau criterion at the instant the center of the BEC crosses the defect. Using an effective 1D NLSE in the high density regime, the locus of points where the local condensate velocity $v(z)$ is equal to the local speed of sound $c(z)$ defines the curve [101]

$$\frac{v_c}{c_0} = \left(1 - \frac{V_D}{\mu}\right)^{5/2}, \quad V_D > 0, \tag{5.7}$$

where $V_D/\mu \equiv \delta n_0/n_0$ is the fractional change in the peak density at the peak of the repulsive defect. When $v_0/c_0 < 1$, we can ignore effects of the axial Thomas-Fermi profile of the condensate because $A \ll R_{TF}$ for our trap, where R_{TF} is the axial Thomas-Fermi radius. Equation 5.7 is plotted in Fig. 5.18 when $V_D > 0$ and is found to agree with the measured v_c for the range of V_D used in this experiment. Therefore, the observed reduction of the critical velocity below c_0 is consistent with the *local* Landau critical velocity without invoking more exotic mechanisms, such as vortex nucleation. This is in contrast with several experiments involving BECs in less elongated configurations [70, 71], as well as in superfluid ^{4}He where nucleation of vortex lines and rings can result in $v_c < v_L$ [85].

In the case of the attractive defect, the density, and therefore $c(z)$, is enhanced at the location of the defect and reduced only slightly elsewhere. We find that the reduction in density in the bulk due to the enhancement at the defect is less than 1% for the strongest barriers used, leading to an essentially unperturbed speed of sound in the bulk. The ratio of the local fluid velocity to the local speed of sound can then be found by considering only the bare Thomas-Fermi profile, and is given by

$$\frac{v(z)}{c(z)} = \frac{v_0}{c_0} \left(\frac{1 - z^2/A^2}{1 - z^2/R_{\mathrm{TF}}^2} \right)^{1/2}, \tag{5.8}$$

where, using Eq. 5.4, $v_0/c_0 = 2A/R_{\mathrm{TF}}$. Therefore, if $2A < R_{\mathrm{TF}}$ then $v_0/c_0 < 1$ and the local Landau criterion is satisfied everywhere inside the condensate. This model predicts

$$\frac{v_c}{c_0} = 1, \quad V_{\mathrm{D}} < 0, \tag{5.9}$$

implying that v_c is independent of V_{D}. Our measurements, however, show a weak dependence on V_{D} with $v_c/c_0 = 1$ only for very weak impurities. Our experimental results are consistent with numerical simulations using a 1D NLSE [101] for which the local Landau criterion accurately describes the repulsive impurity case, but slightly overestimates v_c in the attractive case.

Figures 5.17 and 5.18 demonstrate that the damping is significantly suppressed deep into the supersonic regime. We observe undamped motion when v_0 is greater

than a V_D-dependent upper critical velocity v_+. Numerical simulations [124, 99, 101] have shown that for "wide and smooth" barriers ($\xi \ll w_z$) the emission of radiation from the defect in the form of phonons and solitons can be very small for supersonic velocities. In fact, it has been shown analytically that the radiation emission rate resulting from a defect moving supersonically through a condensate decreases exponentially with the ratio ξ/w_z [125]. Without emission of radiation, energy dissipation is inhibited and the flow persists, even though Landau's criterion is violated. For the data presented in Figs. 5.14–5.19, $\xi/w_z \sim 0.04$, well within the regime where supersonic non-dissipative flow is predicted. Experiments similar to ours have also shown a reduction in soliton emission from a barrier moving through a condensate in the supersonic regime [123].

We therefore observe three distinct regimes of flow in the single defect system: subsonic superfluid ($v_0/c_0 < 1$), dissipative ($v_0/c_0 \sim 1$), and supersonic non-dissipative ($v_0/c_0 > v_+$). Figure 5.19 shows axial densities from *in situ* polarization phase-contrast images at the instant the defect passes through the peak of the condensate for the three different velocity regimes. As expected, for the superfluid flow regime the axial density profiles look very much like the equilibrium profiles of Fig. 5.14: there is an increase (decrease) in the density at the location of the attractive (repulsive) defect. In the dissipative flow regime, on the other hand, the flow patterns for $V_D > 0$ show significant distortion, while for $V_D < 0$ there is little distortion, as discussed in detail above. Finally, in the supersonic non-dissipative
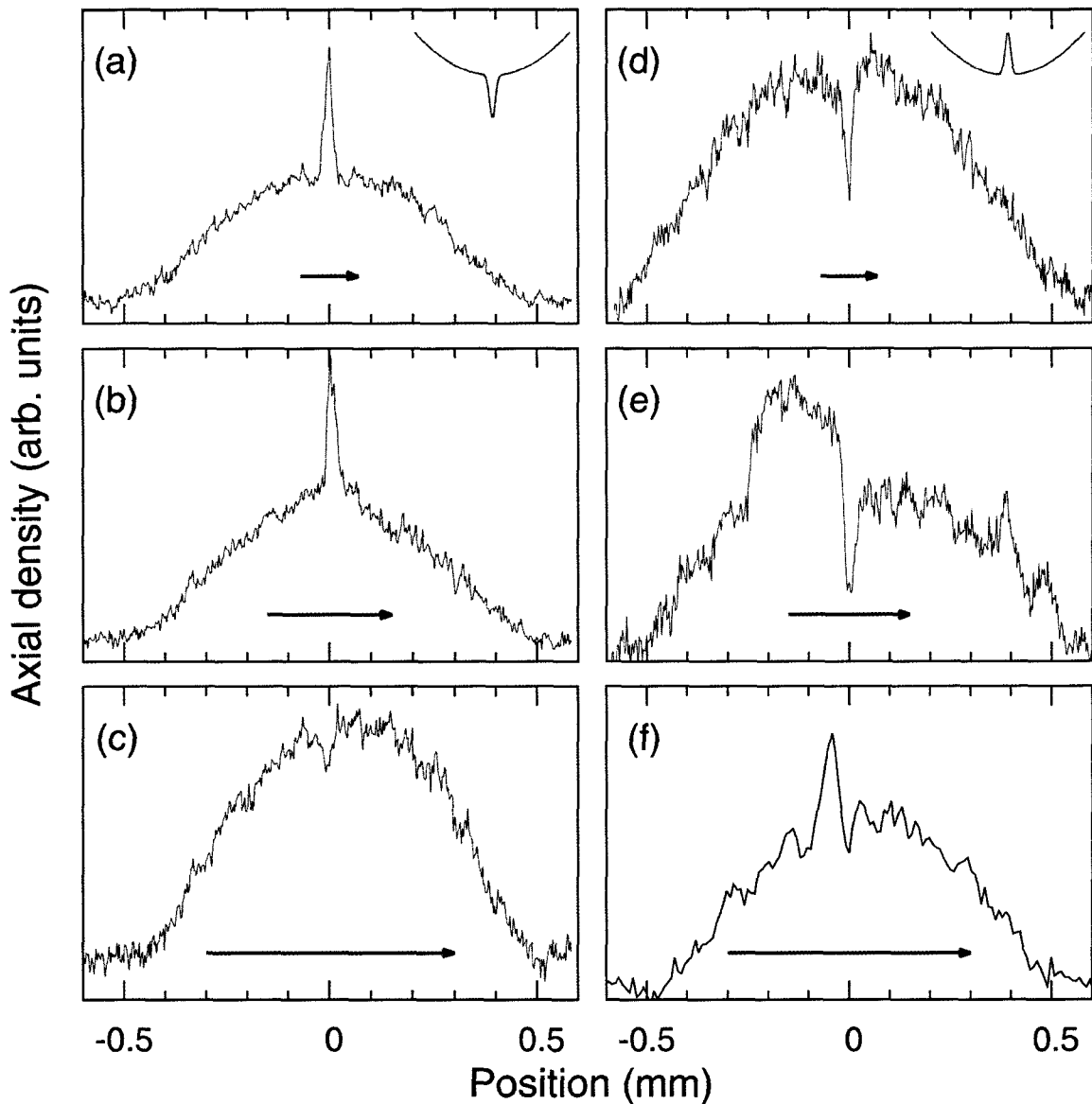
Figure 5.19 : *In situ* density distributions of a condensate passing through a Gaussian defect. These images were taken at the instant the center of the BEC first crossed the defect. Rows correspond to the three flow regimes: subsonic superfluid ($v_0/c_0 < 1$), dissipative ($v_0/c_0 \sim 1$), and supersonic non-dissipative ($v_0/c_0 > 1$). (a–c) Attractive defect with $V_D/\mu = -0.85$ and $v_0/c_0 = 0.31$, $v_0/c_0 = 1.0$, and $v_0/c_0 = 3.0$, respectively. (d–f) Repulsive defect with $V_D/\mu = 0.65$ and $v_0/c_0 = 0.15$, $v_0/c_0 = 0.90$, and $v_0/c_0 = 2.0$, respectively. The arrows indicate the direction and relative speed of the condensate. For this data, all other parameters are as described in Fig. 5.15.

flow regime, we observe a counter-intuitive density *inversion* with respect to the $v_0/c_0 < 1$ superfluid flow, where the attractive defect produces a density depression while the repulsive defect causes a density peak.

The physical origin of this counter-intuitive density inversion can be understood by considering the behavior of the gas at large v_0. In this regime, as in the disordered case, the Bogoliubov excitation spectrum, given by Eq. 5.2, is dominated by the $p^2/2m$ term. For this "quasi-ideal" gas, the drag should be determined by the scattering of linear waves off of the defect [119]. Accordingly, one expects vanishing dissipation at high velocities because these waves will not reflect from the barrier. If we extend this argument further and consider the atoms to be classical particles, one expects the atoms to slow down in the presence of the repulsive defect, resulting in a density increase near the defect, while the opposite is expected for an attractive defect.

Density inversions similar to the ones presented here have also been discussed in the context of dissipationless stationary states at supersonic velocities [126, 125, 127, 118] as well as sonic black holes [128]. Under our experimental conditions, when $v_0/c_0 \sim 1$ the edge of the barrier can serve as a sonic event horizon. Such systems have been proposed as possible candidates with which to study "table top" astrophysics, where exotic effects, such as Hawking radiation, should be observable. Interestingly, in this system the experimenter plays the role of the so-called super-observer, having access to the regions both outside and *inside* the event horizon [129, 130, 131, 128].

5.4.2 Weakly Interacting Regime

Figure 5.20 shows the result of a weakly interacting condensate ($a = 0.6\,a_0$) oscillating in a trap with a repulsive defect. Under these conditions the condensate is in the quasi-1D regime with $\mu/\hbar\omega_r = 0.15$. We find that the axial density profile of the condensate becomes increasingly modulated during the damped oscillation [99, 120].

Results of measurements of the velocity-dependence of the damping by a repulsive defect with $a = 0.6\,a_0$ are shown in Fig. 5.21. As was the case with disordered potentials, we find that the timescale for damping in the quasi-1D regime with a strong impurity strength is much longer than that observed in the Thomas-Fermi regime with a weak impurity strength.

5.4.3 Dark Soliton Production in the Weakly Interacting Regime

Of particular interest in the quasi-1D regime is the ability to create and observe long-lived dark solitons. These nonlinear excitations have been previously created in BECs with repulsive interatomic interactions through a variety of means, including direct phase imprinting [132, 133], spatially selective microwave transfer [134], slow light [113], two condensate interference [135, 115], and, similar to the work presented here, as a result of a BEC crossing a semi-permeable defect [123].

In general, the decay of dark solitons occurs as a result of dynamical instability or as a result of dissipative dynamics associated with the interaction of the soliton with quasiparticle excitations of the BEC. However, it is known that dark solitons
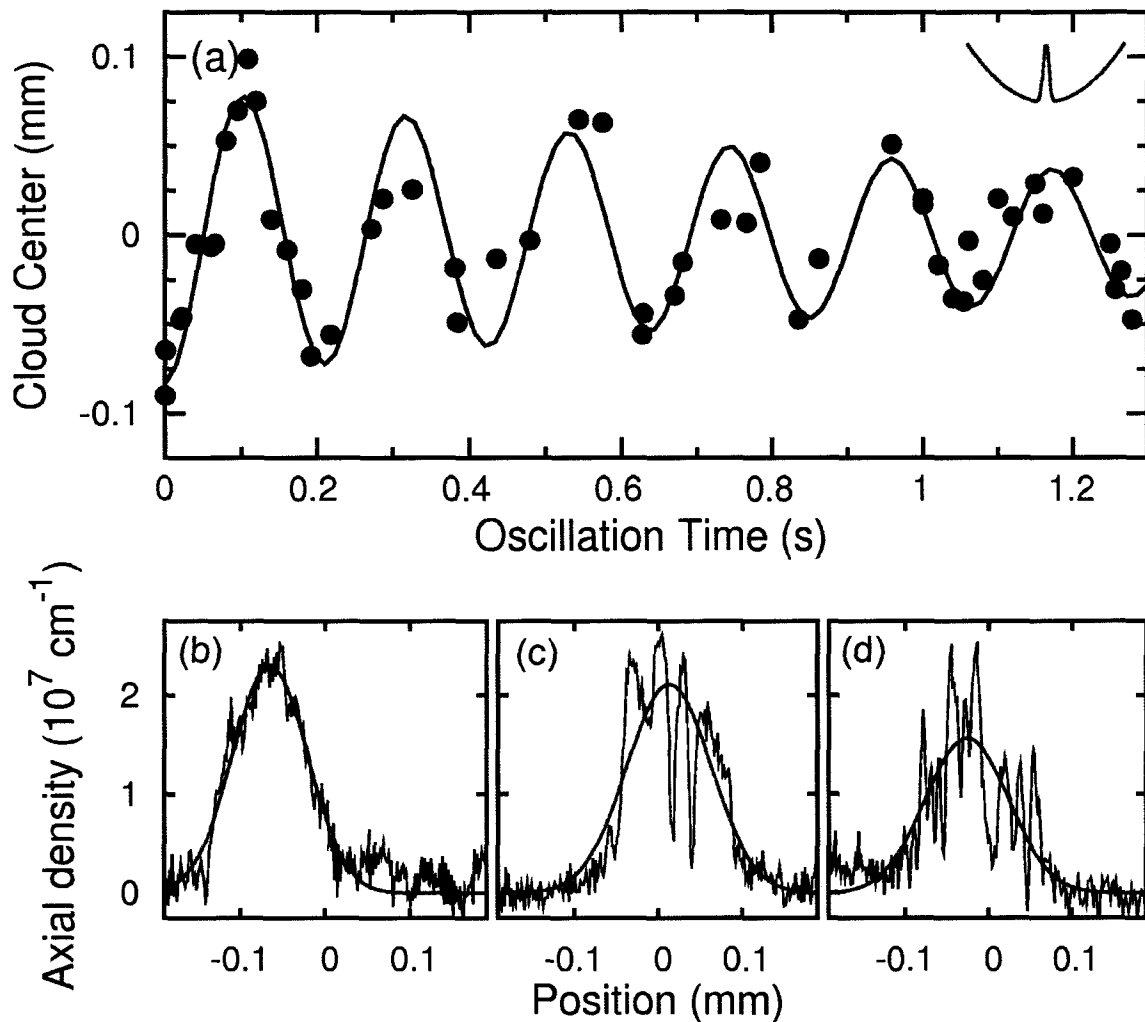
Figure 5.20 : Oscillation of a weakly interacting BEC in the presence of a repulsive defect, with $a = 0.6\,a_0$, $N = 2.5 \times 10^5$, $\mu/h = 44\,\mathrm{Hz}$, $V_D/\mu = 0.8$, $\omega_z = (2\pi)\,4.7\,\mathrm{Hz}$, $\omega_r = (2\pi)\,300\,\mathrm{Hz}$, $v_0/c_0 = 1.6$ and $\beta/\omega_z = 0.03$. (a) Center of mass position as a function of time (computed as in Fig. 5.11); (b-d) *In situ* axial density traces at various oscillation times: (b) 0 ms; (c) 140 ms, at the second crossing of the defect; and (d) 1260 ms, after several crossings of the defect. At large times we find that the large density modulations are accompanied by only a slight increase of the axial size of the condensate.
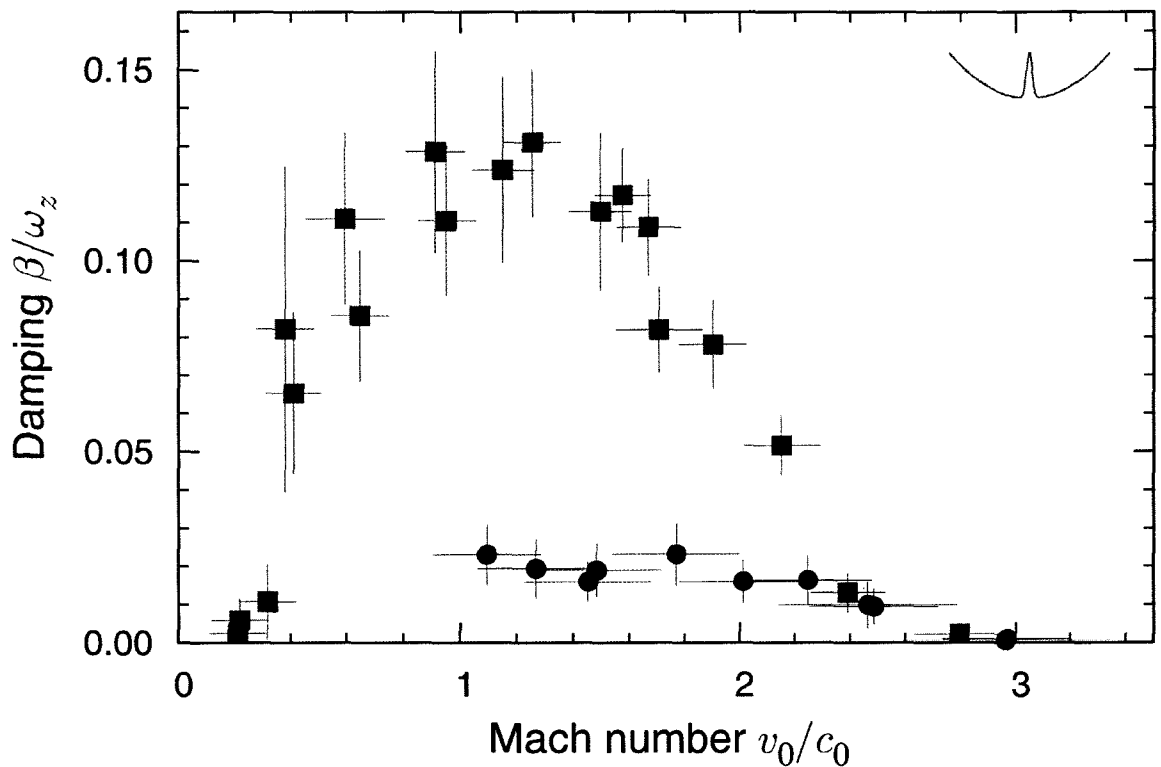
Figure 5.21 : Velocity dependence of damping with a repulsive defect. Circles correspond to a nearly non-interacting BEC with $a = 0.6\,a_0$, $\mu/h = 31\,\text{Hz}$, $c_0 = 0.9\,\text{mm/s}$, and $V_D = 0.9\,\mu$. Shot-to-shot variations in the position of the cloud limit the extraction of β to $v_0 > 1\,\text{mm/s}$, corresponding to $v_0/c_0 > 1.1$. Squares correspond to data from Fig. 5.17(b) for comparison, $a = 200\,a_0$, $\mu/h = 3\,\text{kHz}$, $c_0 = 9.2\,\text{mm/s}$, and $V_D = 0.4\,\mu$. Error bars are as defined in Fig. 5.3.

can have very long lifetimes in the quasi-1D regime [136]. For the most weakly interacting BECs presented here, $\mu/\hbar\omega_r = 0.13$, making our system ideally suited to study long-lived dark solitons.

We have studied the formation of deep *in situ* density modulations in BECs for different values of a, with the results shown in Fig. 5.22. Dipole motion is initiated after the field is slowly ramped to a desired value near the scattering length zero-crossing at 544 G. Panels (a–e) of Fig. 5.22 show the cloud after 3/4 of a complete oscillation. The defect is switched off after the first pass of the cloud, and the cloud is imaged after it returns to the center of the trap after half a period. Therefore $\sim$100 ms elapses between the initial interaction of the cloud with the defect, where the soliton is created, and imaging. Deep density modulations, consistent with the formation of stable dark solitons, are observed. For comparison, panels (e–h) of Fig. 5.22 show the cloud after passing through the defect 4 times. The density modulations in this case appear less monochromatic than in the single pass case, suggesting the presence of both linear (phonons) and nonlinear (solitons) excitations. We extract the healing length ξ_s the data in Fig. 5.22 by independently fitting each individual soliton to [137]

$$n(z) = A e^{-z^2/\sigma^2} \left[1 - D \operatorname{sech}^2 \left(\frac{z - z_0}{\xi_s \sqrt{2}} \right) \right] . \tag{5.10}$$

where A is the background density, σ is the size of the atomic cloud, D is the depth of the soliton, z_0 is the location of the soliton, and ξ_s is the healing length. Through a variational solution of the GPE, we can independently estimate the healing length
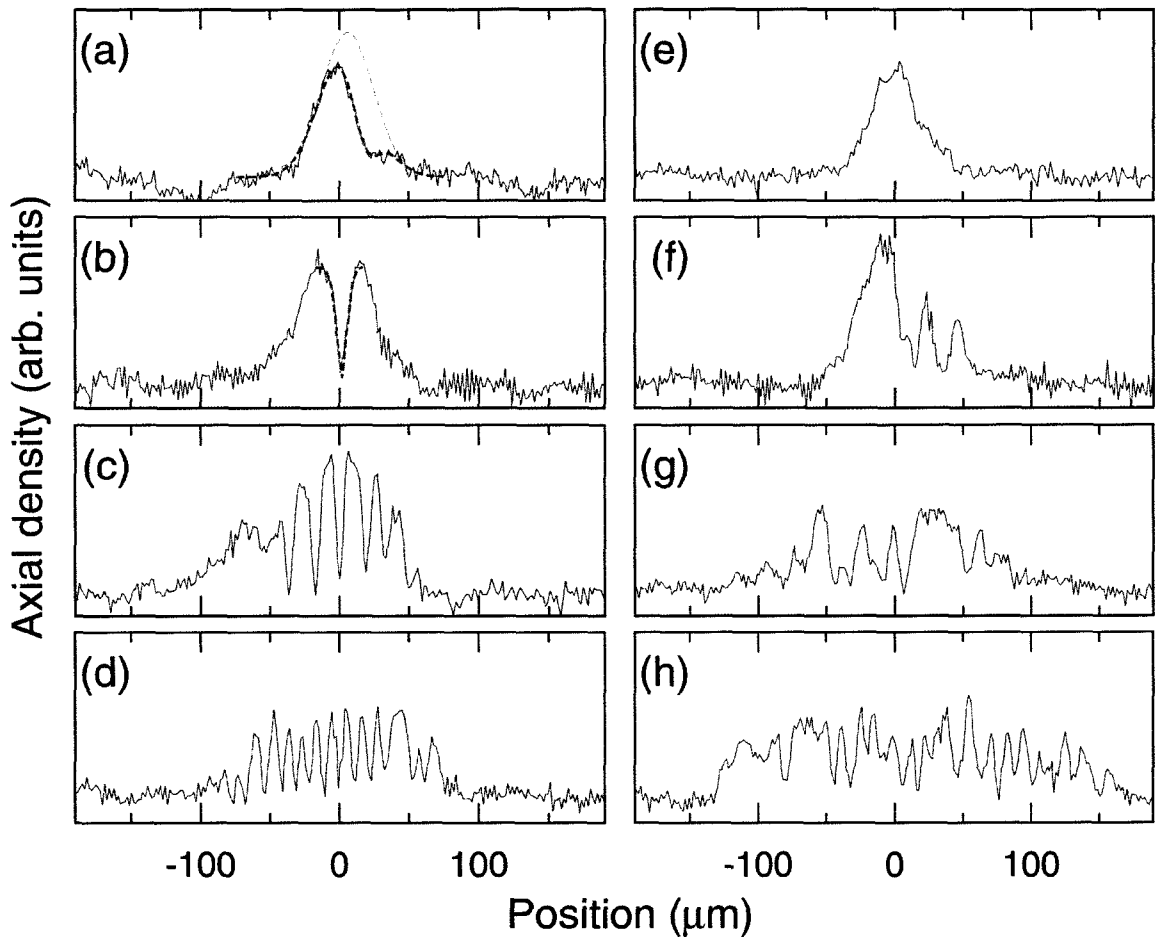
Figure 5.22 : Dark soliton formation. *In situ* axial densities of BECs during the first (a–d) and fourth (e–h) passes through a semi-permeable defect. The defect is located at $z = 0$, and its strength was adjusted to keep $V_D/\mu \sim 0.7$. Oscillation amplitudes were adjusted to keep $v_0 \sim c_0$. (a), (e): $a = 0.1 a_0$, $N = 1.0 \times 10^5$, $\mu/h = 5\,\mathrm{Hz}$, $\xi = 12.5\,\mu\mathrm{m}$, $\xi_s = 16(6)\,\mu\mathrm{m}$; (b), (f): $a = 0.5 a_0$, $N = 2.2 \times 10^5$, $\mu/h = 30\,\mathrm{Hz}$, $\xi = 4.9\,\mu\mathrm{m}$, $\xi_s = 6.6(2)\,\mu\mathrm{m}$; (c), (g): $a = 1.7 a_0$, $N = 2.6 \times 10^5$, $\mu/h = 77\,\mathrm{Hz}$, $\xi = 3.06\,\mu\mathrm{m}$, $\xi_s = 2.8(4)\,\mu\mathrm{m}$; (d), (h): $a = 5.4 a_0$, $N = 2.2 \times 10^5$, $\mu/h = 144\,\mathrm{Hz}$, $\xi = 2.24\,\mu\mathrm{m}$, $\xi_s = 2.5(3)\,\mu\mathrm{m}$. The trap frequencies for this data are $\omega_r = (2\pi)\,240\,\mathrm{Hz}$ and $\omega_z = (2\pi)\,4.75\,\mathrm{Hz}$. The thick dashed line in (a) and (b) show the fit to Eq. 5.10. For comparison, the thin dashed line in (a) is only the Gaussian portion of the fit. Error bars for ξ_s are given by the standard deviation of a collection of images.

ξ using the measured values of N, a, ω_z, and ω_r. The results of this analysis are reported in Fig. 5.22. As expected $\xi_s \sim \xi$ providing further evidence that the deep density modulations are indeed dark solitons.

5.5 Transmission and Reflection of a Bose-Einstein Condensate Through a Single Gaussian Defect

We have investigated the transmission and reflection properties of a weakly interacting Bose-Einstein condensate impinging on a repulsive Gaussian defect. In the regime where c and μ are both small, ξ/w_z can be of order 1 or larger. As described above, we expect the dynamics to be governed mainly by the ratio $E_{\mathrm{KIN}} < V_{\mathrm{D}}$ with internal excitations of the BEC suppressed due to the superfluid motion. Classically, one would expect complete reflection for $E_{\mathrm{KIN}} < V_{\mathrm{D}}$ or complete transmission for $E_{\mathrm{KIN}} > V_{\mathrm{D}}$. However, we observe a very different result. As shown in Figs. 5.23–5.25, even for barriers as strong as $V_{\mathrm{D}}/E_{\mathrm{KIN}} \sim 3$ we observe that a significant fraction of the BEC tunnels through the barrier. For $V_{\mathrm{D}}/E_{\mathrm{KIN}} \sim 1$ we observe nearly complete transmission while for $V_{\mathrm{D}}/E_{\mathrm{KIN}} \sim 17$ we observe perfect reflection.

130

$\Delta t = 5\,\mathrm{ms}$
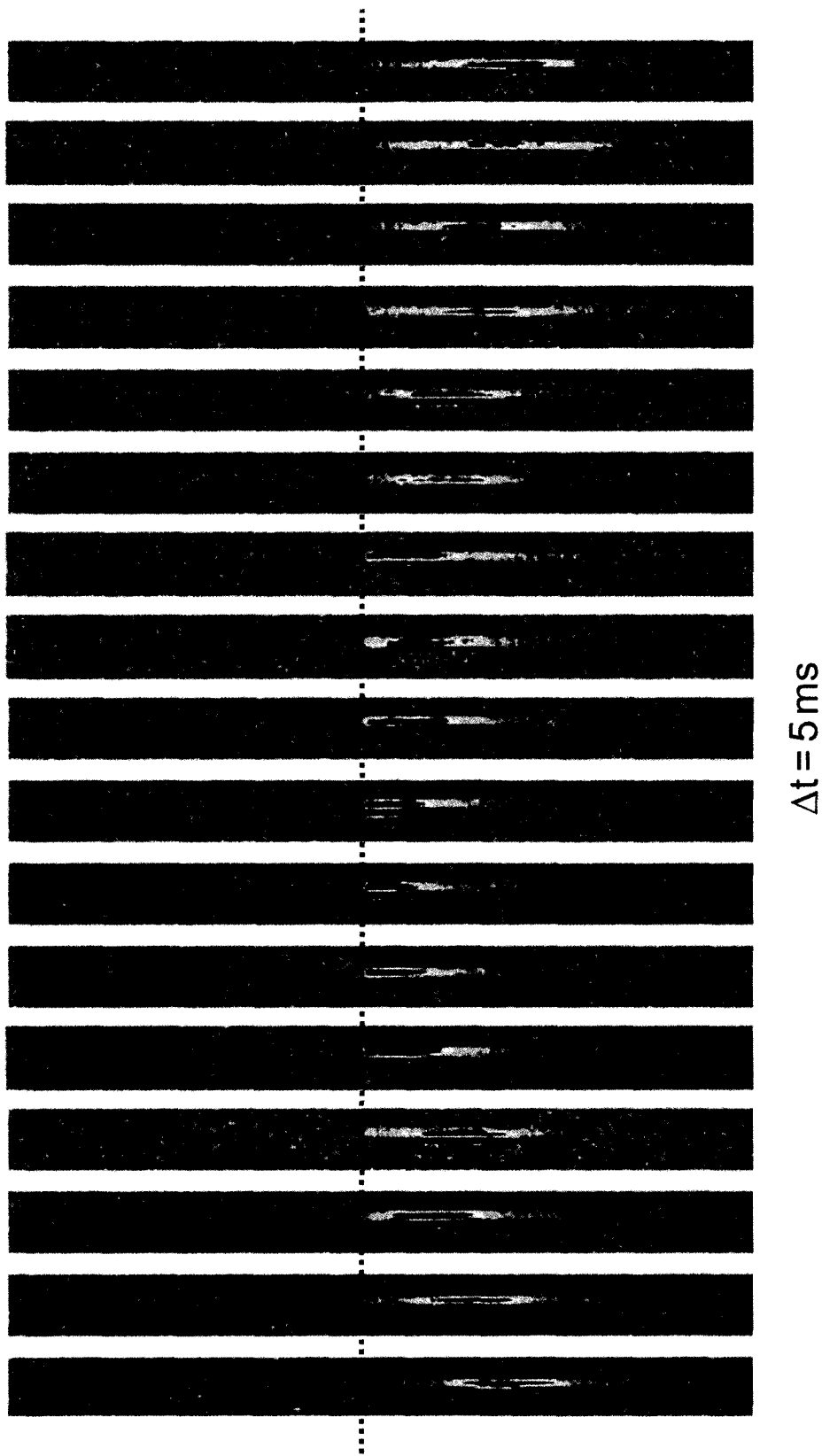
Figure 5.23 : Shown here is a time sequence showing *in situ* column densities of a BEC interacting with a strong potential barrier (dashed line) of $V_\mathrm{D}/E_\mathrm{KIN} \sim 17$. For this data, $a = 0.6\,a_0$, $N = 2 \times 10^5$, $\mu/h = 100\,\mathrm{Hz}$, $v/c = 2.3$, and $V_\mathrm{D}/\mu = 20$ with trap parameters are as described in Fig. 5.22. Perfect reflection of the BEC is observed.

$\Delta t = 20\,\text{ms}$
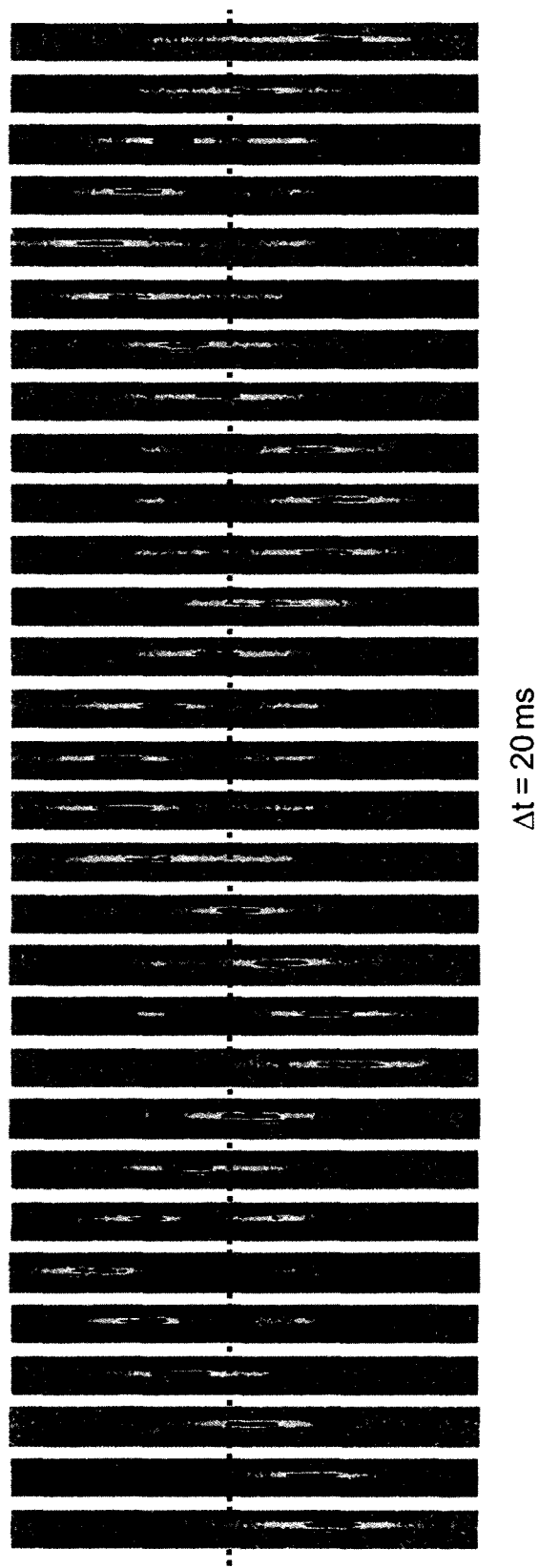
Figure 5.24 : Shown here is a time sequence showing *in situ* column densities of a BEC interacting with a potential barrier (dashed line) of $V_\text{D}/E_\text{KIN} \sim 1$. For this data, $a = 0.6\,a_0$, $N = 2 \times 10^5$, $\mu/h = 100\,\text{Hz}$, $v/c = 4.2$, and $V_\text{D}/\mu = 3.8$ with trap parameters are as described in Fig. 5.22. Nearly perfect transmission of the BEC is observed.

$\Delta t = 20\,\text{ms}$
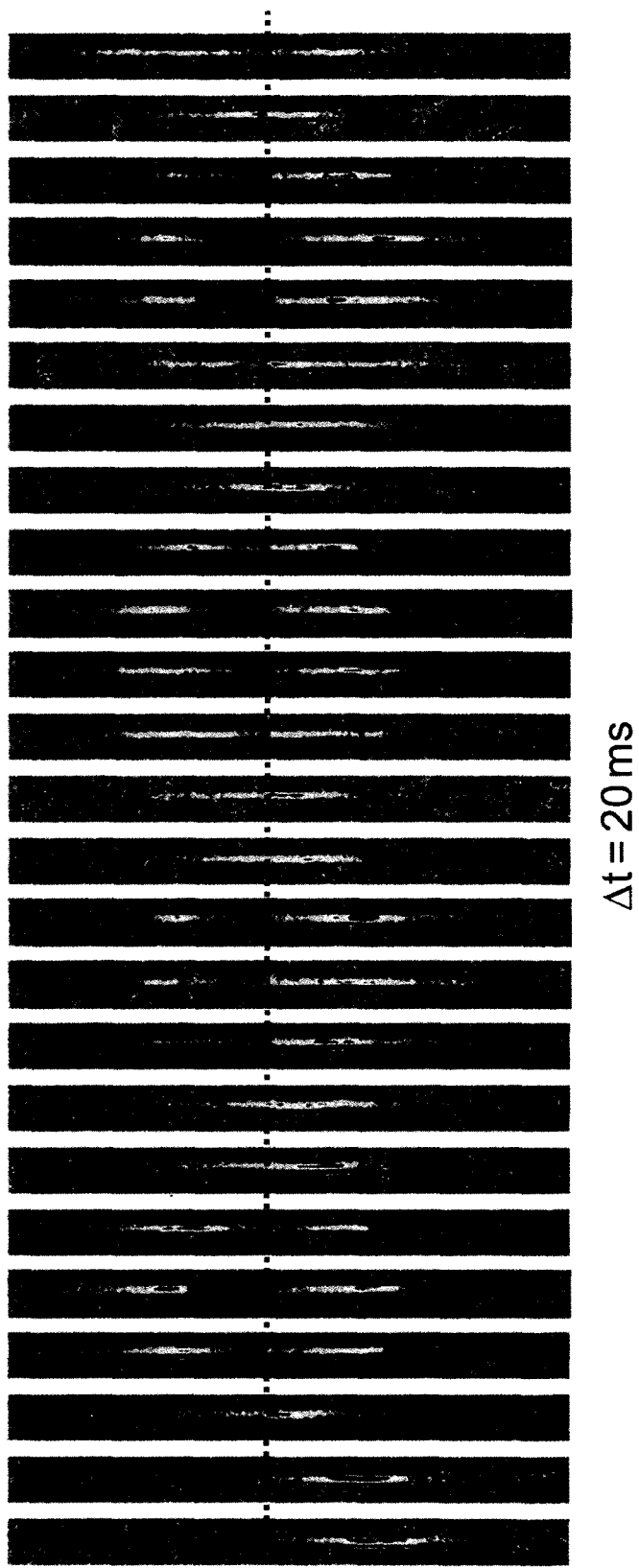
Figure 5.25 : Shown here is a time sequence showing *in situ* column densities of a BEC interacting with a potential barrier (dashed line) of $V_D/E_{KIN} \sim 3$. For this data, $a = 0.6\,a_0$, $N = 3.5 \times 10^5$, $\mu/h = 120\,\text{Hz}$, $v/c = 2.3$, and $V_D/\mu = 4$ with trap parameters are as described in Fig. 5.22. A significant fraction of the BEC is observed to tunnel through the barrier.

We have also investigated the transmission properties of a matter wave soliton interacting with the potential barrier. For this study, we create a single soliton by a slow field ramp to $a = -0.3\, a_0$. This soliton is very near collapse, with $N \sim N_c$, where $N_c = 100,000$. Unlike the repulsive condensate, Fig. 5.26(a) shows that $V_D/E_{KIN} \sim 3$ leads to a complete classical reflection of the soliton. Figure 5.26(b) shows that for $V_D/E_{KIN} \sim 1$ nearly complete transmission through the barrier occurs, with a potential fragmentation of the soliton occurring as it crosses the barrier.

Finally, Fig. 5.27 shows the almost equal splitting of a soliton when $V_D/E_{KIN} \sim 1.8$. Half the soliton appears to tunnel through the barrier with the two fragments *recombining* after a second pass through the barrier. Unfortunately we had to dismantle the barrier setup soon after this data was taken to pursue the Anderson localization experiment. However, current efforts are underway to repeat this measurement with the prospect of making a soliton matter wave interferometer.
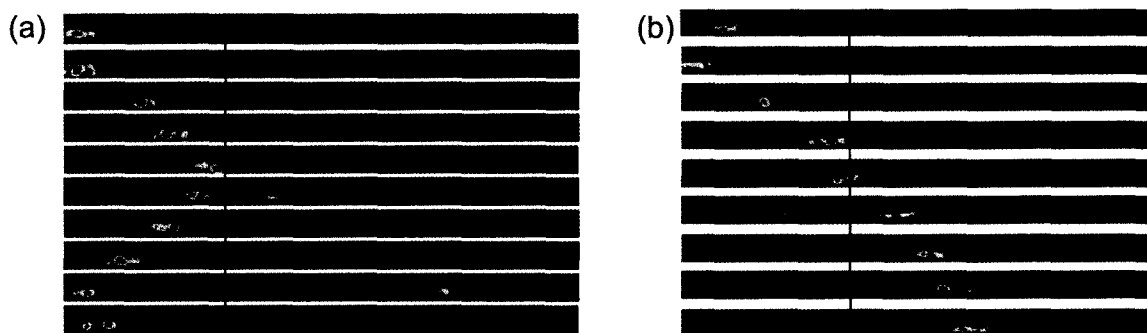
Figure 5.26 : A time sequence with $\Delta t = 10\,ms$ showing *in situ* axial densities of a soliton interacting with a potential barrier (red line) of $V_{\mathrm{D}}/E_{\mathrm{KIN}} \sim 3$(a) and $V_{\mathrm{D}}/E_{\mathrm{KIN}} \sim 1$(b). For this data, $a = -0.3\,a_0$ and $N \sim 1.0 \times 10^5$ with $N_c \sim 1 \times 10^5$. The $1/e$ radius of this soliton is $\sim 10\,\mu$m with trap parameters are as described in Fig. 5.22. The soliton appears to show a reduced tendency to tunnel through the barrier as compared to the repulsive case with $V_{\mathrm{D}}/E_{\mathrm{KIN}} \sim 3$ shown above. Close inspection of (a) reveals that in two of the shots a small fraction of the atoms appear to have tunneled through the barrier. The non-repeatability of this weak transmission also suggests an experimental fluctuation in $V_{\mathrm{D}}/E_{\mathrm{KIN}}$ as a possible explanation. The fluctuations in E_{KIN} can be see in (a) and (b) as small, random shot-to-shot deviations in the trajectory of the cloud. (b) Nearly perfect transmission of the soliton through the barrier.

t=0   Δt= 5 ms
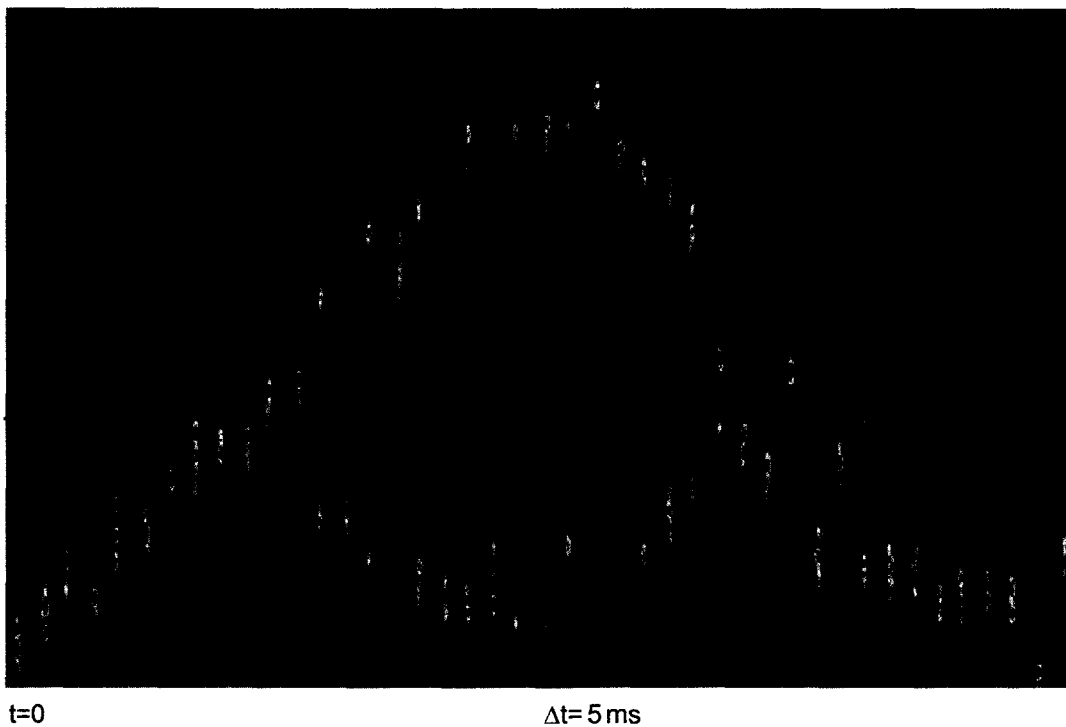
Figure 5.27 : Preliminary data showing a time sequence with $\Delta t = 5\,ms$ showing *in situ* axial densities of a soliton interacting with a potential barrier (dashed line) of $V_D/E_{KIN} \sim 1.8$. Parameters are identical to that described in Fig. 5.26. The soliton appears to split in two with half reflecting and half tunneling through the barrier. Remarkably, the fragments appear to recombine after the second pass through the barrier suggesting phase coherence between the fragments.

Chapter 6

1D Anderson Localization in a BEC of ^{7}Li

6.1 Introduction

One of the most useful aspects of ultra-cold atomic systems is the high degree of controllability over many of the system parameters. The case of disordered BEC is no different. All real condensed matter systems have disorder. A crystal lattice may have point defects, or edge defects in the form of dislocations. These defects often vary from sample to sample in uncontrolled ways. In atomic systems we begin with a perfectly clean sample in the sense that the external trapping potential is well defined and free of any form of disorder. For example, atoms trapped in an optical or magnetic dipole trap will experience a smooth harmonic potential. Once the initial trap geometry is chosen, fully characterized disorder can then be added in a controlled way to the system.

To date, optical speckle, bi-chromatic lattices, atomic mixtures and spatially inhomogeneous magnetic fields have been proposed and used to create disorder in atomic systems [138]. Of particular interest recently has been the use of atomic systems to simulate some of the basic foundational models of condensed matter physics, in particular the metal insulator transition proposed by Anderson [139]. Even though the idea of Anderson localization was proposed now over 50 years ago, it has proven
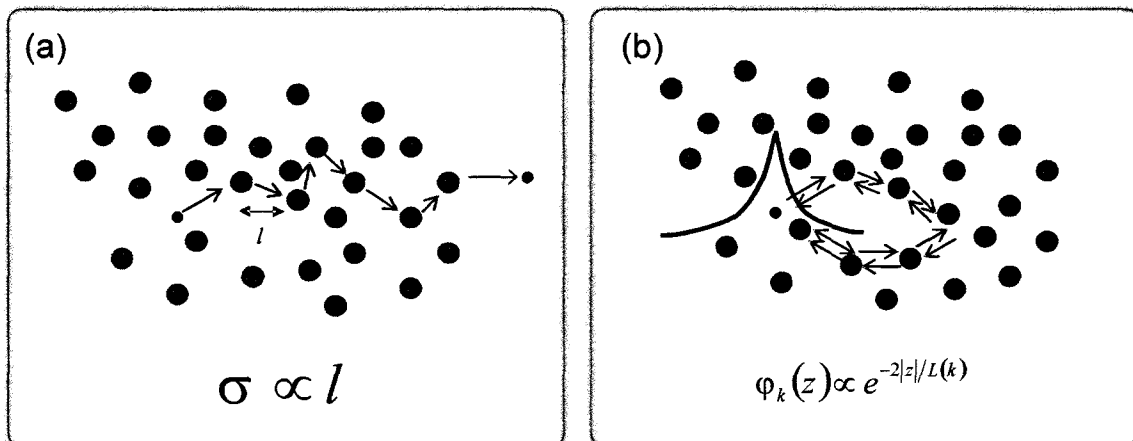
Figure 6.1 : (a) In the simplest classical model of conductivity, the so-called Drude model, the conductivity σ of a sample is directly proportional to the mean free path l, which is in turn inversely proportional to the density of scatters. (b) When dealing with quantum particles (or classical waves) undergoing multiple scattering in disordered media, one has to be careful to consider the coherence properties of the system. If the wavelength of the wave is on the order of the average distance between scattering centers, then one must consider the coherent superposition of all possible paths that the particle can take. Anderson was the first to show that such a process will result in the formation exponentially localized eigenstates. If the system size is much larger than L, then $\sigma = 0$, even if conduction is expected classically.

elusive and conclusive observation of this phenomena in any traditional condensed matter system remains an open challenge. Since the recognition of the effect as fundamentally a wave phenomena [140, 141], experimentalists have over the years observed the localization in many classical wave systems. Evidence of localization has been made for scattered elastic waves in lucite blocks [142]. Localization has also been observed with light in disordered bulk materials [143, 144] and photonic lattices [145, 146, 147]. In addition, localization has been observed in ultrasound [148, 149] and microwaves [150, 151, 152].

Matter waves have also provided useful systems with which to study localization.

First observations were in the field of dynamical localization [153, 154] and recent experiments have shown localization in correlated [82] and quasi-periodic disorder [83]. Our experiments are designed to investigate localization in a 1D expansion of a BEC in correlated disorder created from laser speckle, similar to Ref. [82].

6.2   1D Transport in a BEC

We have studied the phenomena of Anderson localization in a BEC of ^{7}Li in the $|F = 1, m_F = 1\rangle$ internal state, in a 1D disordered optical guide. A set of Helmholtz coils provides a uniform bias field along the long (z) axis of the guide, allowing for the tuning of a via the Feshbach resonance at 737 G [53, 1, 81]. The BEC is created through evaporative cooling at a field of 704.3 G ($a = 119\, a_0$), precisely where there exists a minimum in the three body loss rate coefficient L_3 associated with merging of an Efimov trimer state with the atom-dimer continuum [40]. This evaporation is conducted in a cross beam "dimple" trap, where, at high trap depths, the confinement is dominated by the guide beam constructed from a single focused laser beam, while near the end of the evaporation the atoms are funneled into the center of the trap where a weak cross beam overlaps the guide beam resulting in a final trap with a radial trap frequency of $\omega_r = (2\pi)\, 460\, \mathrm{Hz}$ and an axial trap frequency ranging from $\omega_z = (2\pi)\, 2\, \mathrm{Hz}$ up to $\omega_z = (2\pi)\, 28\, \mathrm{Hz}$, depending on the power in the cross beam.

The overall bias field is then ramped to achieve the desired a and the cross beam is quickly switched off. The expansion dynamics of the condensate are then monitored
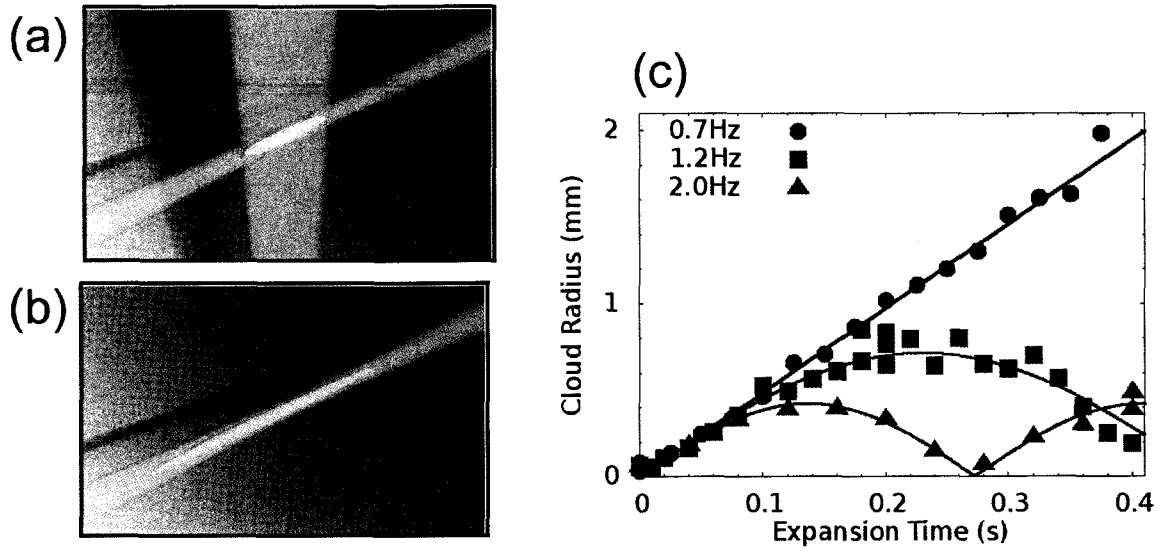
Figure 6.2 : (a) BEC is created in a cross beam trap. (b)To initiate the experiment, the cross beam is switched off and the cloud is allowed to expand freely in the weakly trapping single beam. (c)We use a tunable magnetic curvature to null out the axial confinement from the single beam optical trap. To measure the residual trap frequency of the nulled "guide," we measure the resulting quadrupole oscillations for different values of the residual curvature. Due to residual quartic confinement from the bias coils, we are limited to $\omega_z > (2\pi)\, 1\, \text{Hz}$.

for a variety of atomic expansion momenta and disorder strengths V_D.

The details of the "flat trap" are in fact very important for interpretation of any observed localization phenomena. A calculation showing the details of the axial potential of the 1D guide is illustrated in Fig. 6.3. For the optical trap, we use the typical form for the optical dipole potential of

$$U_{\text{opt}} = \frac{\hbar\Gamma^2 P}{2\pi\Delta w(z)^2 I_{\text{sat}}} \tag{6.1}$$

and

$$w(z) = w_0\sqrt{1 + \left(\frac{z}{R_{\text{L}}}\right)^2}, \tag{6.2}$$

where $w_0 = 33\,\mu\text{m}$, $I_{\text{sat}} = 5.1\,\text{mW/cm}^2$, $\Gamma = (2\pi)\,5.9\,\text{MHz}, \Delta = 2\pi c\,(1/1030\,\text{nm} -$

$1/670.8\,\text{nm})$, and $R_{\text{L}} = \pi w_0^2/\lambda$, with $\lambda = 1030\,\text{nm}$. The magnetic potentials orig-

inate from two independent sets of coils. The bias coils are in nearly Helmholtz

configuration and are described by

$$B_{\text{bias}}(z) = \frac{\mu_0 N I 2\pi R_{\text{bias}}^2}{4\pi} \left(\frac{1}{\left(z_1^2 + R_{\text{bias}}^2\right)^{3/2}} + \frac{1}{\left(z_2^2 + R_{\text{bias}}^2\right)^{3/2}} \right) \tag{6.3}$$

with $R_{\text{bias}} = 43\,\text{mm}$, $z_1 = z - \frac{R_{\text{bias}} + \delta z}{2}$, $z_1 = z + \frac{R_{\text{bias}} + \delta z}{2}$ and $N = 30$. The field from

the curvature coils, which are significantly smaller than the bias follow a similar form

$$B_{\text{curve}}(z) = \frac{\mu_0 N I 2\pi R_{\text{curve}}^2}{4\pi} \left(\frac{1}{\left(z_1^2 + R_{\text{curve}}^2\right)^{3/2}} + \frac{1}{\left(z_2^2 + R_{\text{curve}}^2\right)^{3/2}} \right) \tag{6.4}$$

with $R_{\text{curve}} = 18.3\,\text{mm}$ and a separation equal to that of the bias coils: $z_1 = z -$

$\frac{R_{\text{bias}} + \delta z}{2}$ and $z_1 = z + \frac{R_{\text{bias}} + \delta z}{2}$ and $N = 35$.

Of course the atoms experience a combined potential from the optical dipole trap

and the magnetic potentials $U = -\vec{\mu} \cdot \vec{B}$. To accurately model the system for various

curve coil currents, we use a typical bias current of 100 A, optical trap power of 13 mW

and deviation from Helmholtz of $\delta z = 45\,\mu\text{m}$. We model the potentials for ^{7}Li atoms

in the $|F = 1, m_F = 1\rangle$ state with $|\vec{\mu}| = \mu_B$. The slight deviation from Helmholtz

is a typical experimental situation resulting from small manufacturing errors (or

sometimes even a shim or two). In this scenario, the separation between the bias

is slightly larger than in the standard Helmholtz configuration. The result for the
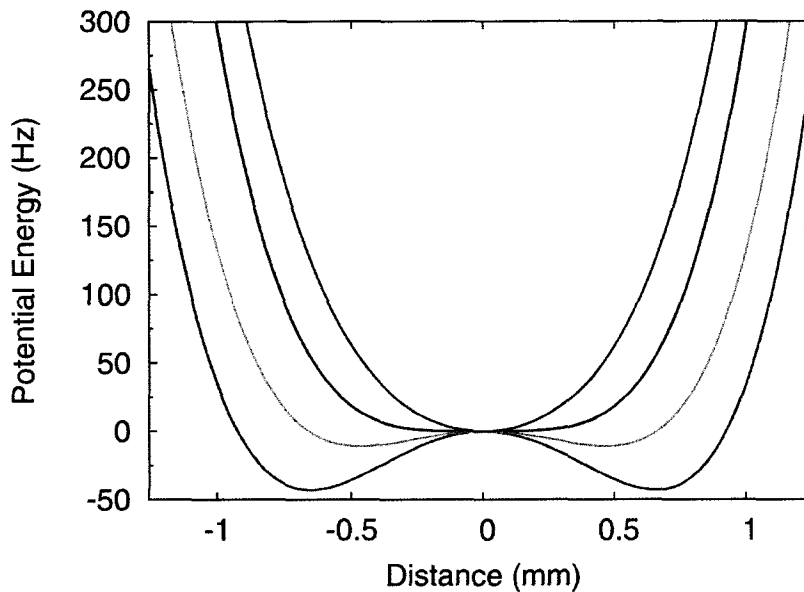
Figure 6.3 : Shown here is a calculation including the effects of the optical trap, bias and curvature coils. The black line is the quartic term from the bias coils alone (i.e. what results from complete nulling of the optical trap). Starting with no current in the curve coils produces a potential of the combined optical and bias coils shown in red. Adding current to the curve coils progressively flattens the trap until one is left with only the quartic term from the bias. Adding more curvature current creates a nice harmonic trap. This added flexibility in choosing the overall curvature of the combined potential is very handy for optimizing evaporation trajectories.

combined optical and bias potential is the double well structure shown as the red line in Fig. 6.3. While evaporation in this potential alone is impossible, addition of the trapping curvature coil potential allows us to tune the full range from a totally nulled optical trap (black line) to strong axial confinement (blue line). Note that the flat region of the trap in the "nulled" configuration is limited by the quartic potential from the bias coils. The field from this component in the simulation shown in Fig. 6.3 is $B_{quartic}(z) = 300\,\mathrm{G/mm}^4\,z^4$. Therefore, care must be taken in interpreting expansion measurements in such a trap as clouds will always undergo quadrupole oscillations.

The key for successfully observing localization due to disorder is to assure that the localization length is much shorter than the amplitude of the quadrupole oscillation.

The presence of the wide Feshbach resonance at 737 G allows for precise tuning of the cutoff in the atomic momentum distribution k_{max}. We measure k_{max} directly by measuring the expansion rate of the cloud in the guide without disorder. The slope of the linear portion of a Thomas-Fermi radius R_{TF} vs. t plot then yields an accurate measure of k_{max} as shown in Fig. 6.2. The presence of the shallow ($\sim 0.1\,a_0/G$) zero crossing in a near 544 G facilitates the tuning of a over nearly a range of 7 decades which, coupled with the tunability in the initial confinement by varying the intensity of cross beam, allows for a wide range of expansion momenta with $0.1\,\mu m^{-1} < k_{max} < 2\,\mu m^{-1}$. Thus, we have the convenient ability to tune k_{max} two independent ways: through a change in a or through a change in ω_z at $a \sim 0$. A plot of k_{max} vs. a is shown in Fig 6.4.

6.3 Correlated Disorder from Laser Speckle

The disordered potential used in our experiment is an optical speckle pattern created by passing a laser beam through a diffuser plate in a manner similar to previous studies [93, 94, 95, 96]. Our particular implementation is described in detail in Chapter 3.6.1, so the following description will be brief. The disorder laser beam propagates perpendicular to the z-axis of the 1D optical guide. We use the average intensity of the speckle pattern as a convenient measure of the disorder strength V_D
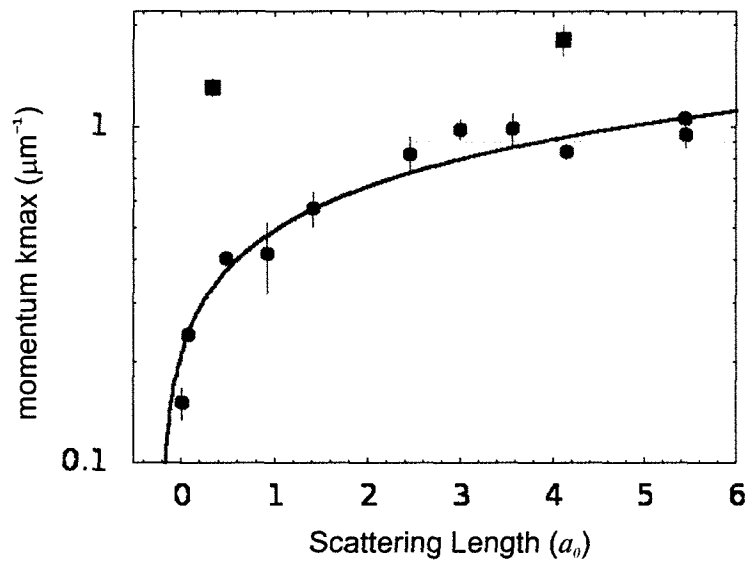
Figure 6.4 : Tunability of k_{max} vs. a and ω_z. Shown here is k_{max} extracted from the slope of the linear portion of plots of R_{TF} vs. t for various values of the scattering length. Red circles are for an initial confinement of $\omega_z = (2\pi)\,11\,\mathrm{Hz}$ and the green squares are for $\omega_z = (2\pi)\,30\,\mathrm{Hz}$. The dashed line indicates $1/l_c \sim 0.8\,\mu\mathrm{m}^{-1}$, the location of the effective mobility edge for localization. See Sec. 6.5 below.
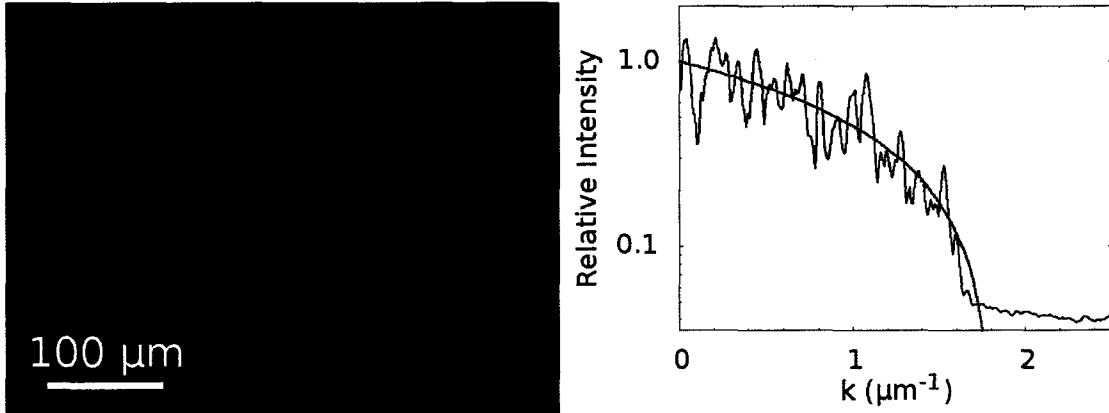
Figure 6.5 : Optical disorder produced from laser speckle. (a) false color CCD image of the elongated disorder potential. (b) Plot of the average of several power spectra for single pixel axial cuts through the data in (a). This average power spectrum shows a cutoff of $2k_D \sim 1.7\mu m^{-1}$, a consequence of the diffraction limit of the optical system used to create the speckle potential. See Chap. 3.6.1 for more technical detail on the setup used to create the disorder.

[155, 21]. The correlation length of the disorder in the direction along the long axis of the guide is $l_c = 1.3(2)\,\mu m$. In the orthogonal direction, the correlation length is much larger than the size of the trap and therefore this highly elongated speckle pattern approximates a 1D correlated disorder potential.

6.4   Disorder Induced Trapping Scenario

Localization, or more precisely the inhibition of expansion of the BEC due to a disorder potential does not always imply Anderson localization. In fact, a phenomena known as disorder induced trapping can occur for systems where the healing length $\xi << l_c$. In this situation, fast atoms expand freely while slow atoms classically reflect from the occasional, strong disorder site eventually resulting in a halting of the expansion [156, 95]. Shown in Fig. 6.6 is exactly this situation for a BEC

in a repulsive disorder potential. While the expansion clearly halts as shown in Fig. 6.6(d) we see that this is not due to Anderson localization. The localized cloud is not described well by an exponential distribution. Rather, it has sharp edges, indicative of the disorder induced trapping scenario. We see how the cloud evolves into this trapped state in Fig. 6.6(a)–(c). Initially the cloud is trapped in the cross beam (a). A short time after release from the cross beam we begin to see two lobes of fast atoms expanding out to either side (b). This is the direct result of the BEC fragmenting into two portions: one portion is a trapped BEC with a chemical potential that is less than two spatially separated strong disorder sites; the other portion is the small fraction of atoms that have enough energy to expand freely in the + and - z-directions. These atoms may eventually reflect as well but only after a much longer excursion. At $t = 150\,\mathrm{ms}$, we are only left with the trapped BEC and since $\xi/l_c \sim 0.1$, tunneling is greatly suppressed and this state does not evolve further.

6.5 Anderson Localization in Expanding BEC

In the regime where $\xi \sim l_c$ the phenomena becomes much richer. In this regime, the finite extent of the power spectrum for the disorder has dramatic consequences for the localization properties of the BEC. In the case of the 1D Bose condensate expanding in the presence of a disorder potential, the ground state wave function for

an atom with wave-number k is predicted to be a decaying exponential

$$\phi_k(z) \propto e^{-|z|/L_{\text{loc}}(k)}.$$ (6.5)

The localization lengths $L_{\text{loc}}(k)$ has been calculated in the Born approximation [25],

$$L_{\text{loc}}(k_{max}) = \frac{\hbar^2 k_{max}^2 k_{\text{D}}}{\pi m^2 V_{\text{D}}^2 \left(1 - \frac{k_{\text{max}}}{k_{\text{D}}}\right)}$$ (6.6)

This result implies that $L_{\text{loc}}(k) \to \infty$ for $k > k_{\text{D}}$ where $k_D = 1/l_c$. Thus, the Born

approximation implies that correlated disorder produced by laser speckle possesses

an *effective* mobility edge (EME) in 1D: atoms with $k < k_{\text{D}}$ will be localized while

atoms with $k > k_{\text{D}}$ will not. For accurate descriptions of the gas above the EME,

a perturbative treatment beyond the Born approximation is necessary [24]. Such

an analysis reveals a series of EME's at integer values of k_{max} joined by regions of

decreasing exponential localization. The amount the localization length changes at

each mobility edge is highly dependent on the strength of the disorder, but for weak

disorder[1] the Born approximation result is expected to be valid [24]. One can then

assume that the zeroth order ground state density distribution $n(z)$ of a collection

of noninteracting particles described by the momentum distribution $D(k)$ is simply

the superposition of many localized states $\phi_k(z)$, each with a L_{loc} given by Eq. 6.6

---

[1]Defined as $\epsilon \ll 1$ where $\epsilon = 2ml_c^2 V_{\text{D}}/\hbar^2 = V_{\text{D}}/430\,\text{Hz}$ for our system.

$$n(z) \equiv \langle |\Psi(z)|^2 \rangle \propto \int_0^\infty dk D(k) \langle |\phi_k(z)|^2 \rangle. \qquad (6.7)$$

Shown in Fig. 6.7 is the expansion behavior of a BEC under the influence of a weak disorder potential for $k_{max}/k_D = 0.4$. One can see that the expansion of the gas is strongly inhibited by the presence of the disorder. Also clear from the images of the axial density distributions is the presence of exponential wings, the hallmark of Anderson localization.

We have examined the dependence of L_{loc} on V_D for clouds with $k_{max}/k_D = 0.45$, with the results presented in Fig 6.8. The clouds are all exponentially localized thus allowing the wings to be fit to the functional form $n(z) = Ae^{-2z/L_{loc}}$.

We have also investigated the nature of the localization across the EME, fully exploiting the tunability of k_{max}. These results are shown in Fig. 6.9. We find that the cloud fits reasonably well to a generalized exponential function of the form [83]

$$n(z) = n_0 e^{-2(|z|/L)^\alpha} \qquad (6.8)$$

for all expansion velocities. We observe a smooth crossover in the shape of the cloud from exponential to Gaussian as we cross the EME. We believe the flattening of the L vs. k_{max} curve to be due primarily to the residual trapping frequency of the 1D guide of $\sim 2\,\text{Hz}$. Invoking conservation of energy and setting $\hbar^2 k^2/(2m) = (1/2)m\omega_z^2 z^2$ and solving for z for $k_{max} = 1\,\mu\text{m}^{-1}$, gives the maximum classical excursion of such a

particle to be ~0.7 μm, very close to the observed plateau.
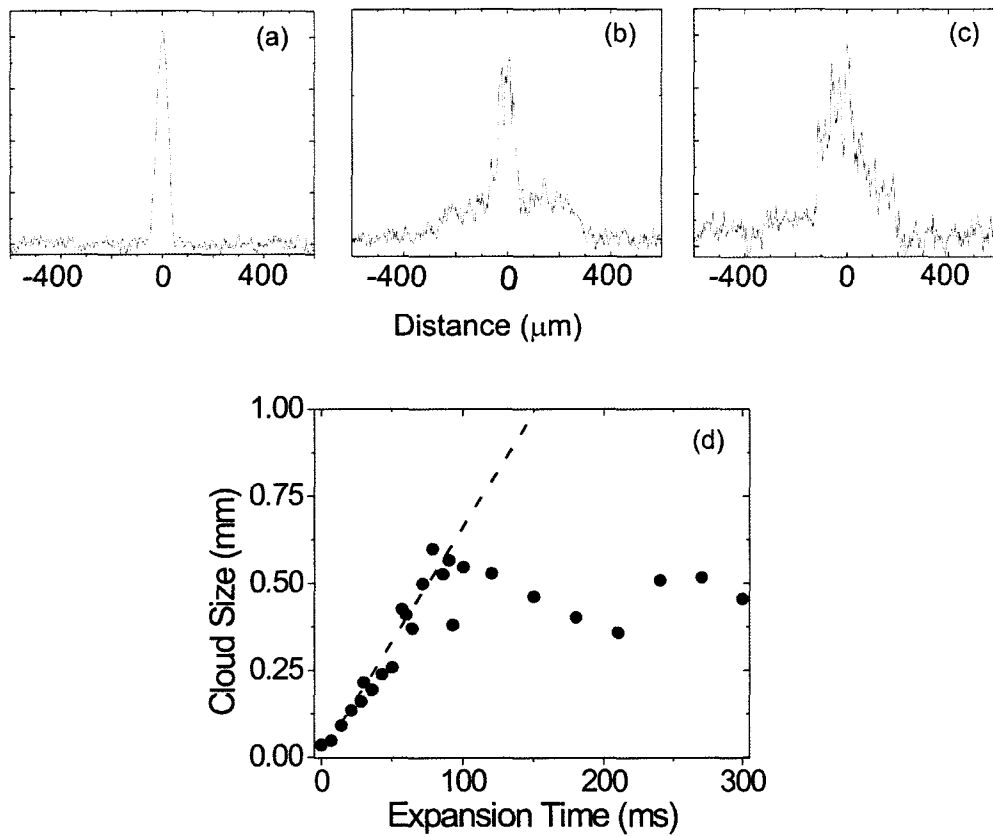
Figure 6.6 : Panels (a)-(c) axial densities showing the fast expansion of a BEC with $k_{max}l_c = 2.2$ expanding in the 1D guide with $V_D = 0.2\,\mu$ where $\mu/h = 3.5\,\mathrm{kHz}$ is the chemical potential in the cross beam trap. (a) $t = 0$ (In the cross beam). (b) after $t = 50\,\mathrm{ms}$ of expansion in the disordered guide. (c) $150\,\mathrm{ms}$ of expansion. (d) Shows the statistical width of the cloud as defined in Fig. 5.11. In this regime, $\xi \sim 0.5\,\mu\mathrm{m}$, much smaller that the speckle size of $\pi l_c \sim 4\,\mu\mathrm{m}$ and the gas behaves "classically."
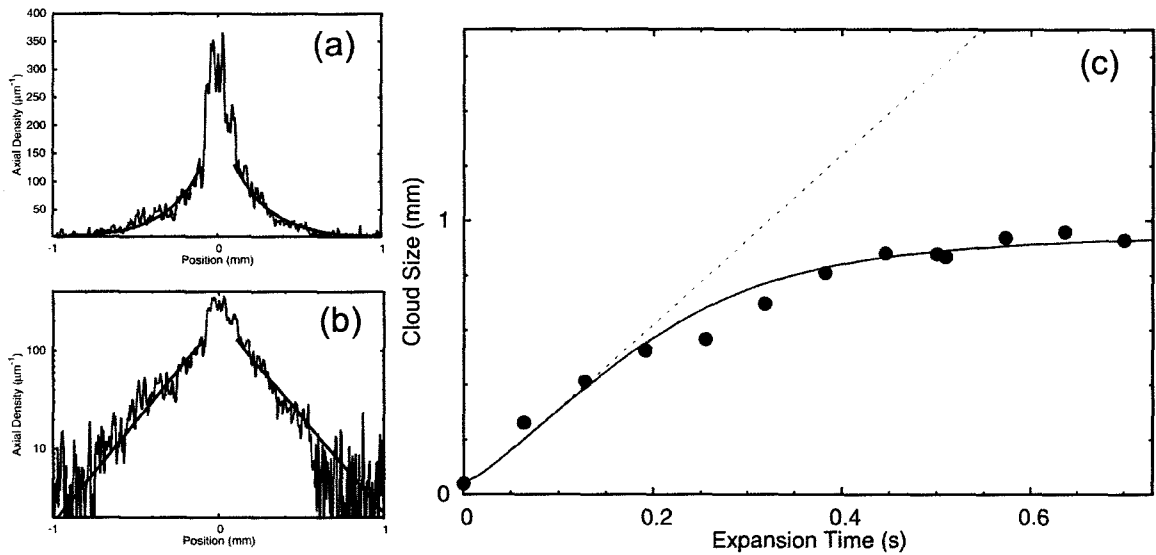
Figure 6.7 : Anderson localization for a BEC with $k_{max}/k_D = 0.4$. As shown in (c), transport is strongly inhibited, even for the weak disorder of $V_D = 15\,\text{Hz}$. (a) and (b) show the axial densities obtained from absorption imaging on a linear and log scale, respectively. Solid lines show fits to the exponential tails.
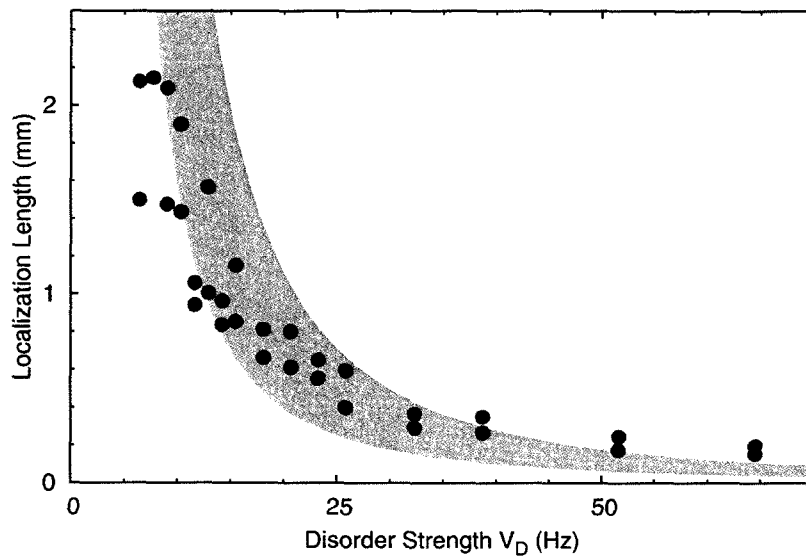
Figure 6.8 : L_{loc} vs. V_D for atoms below the EME with $k_{max}/k_D = 0.45$. Shaded area is the prediction of Eqn. 6.6 reflecting our uncertainty in k_D and k_{max}. The residual trapping potential in the 1D guide was $\omega_z \sim 1\,\text{Hz}$ for this data.
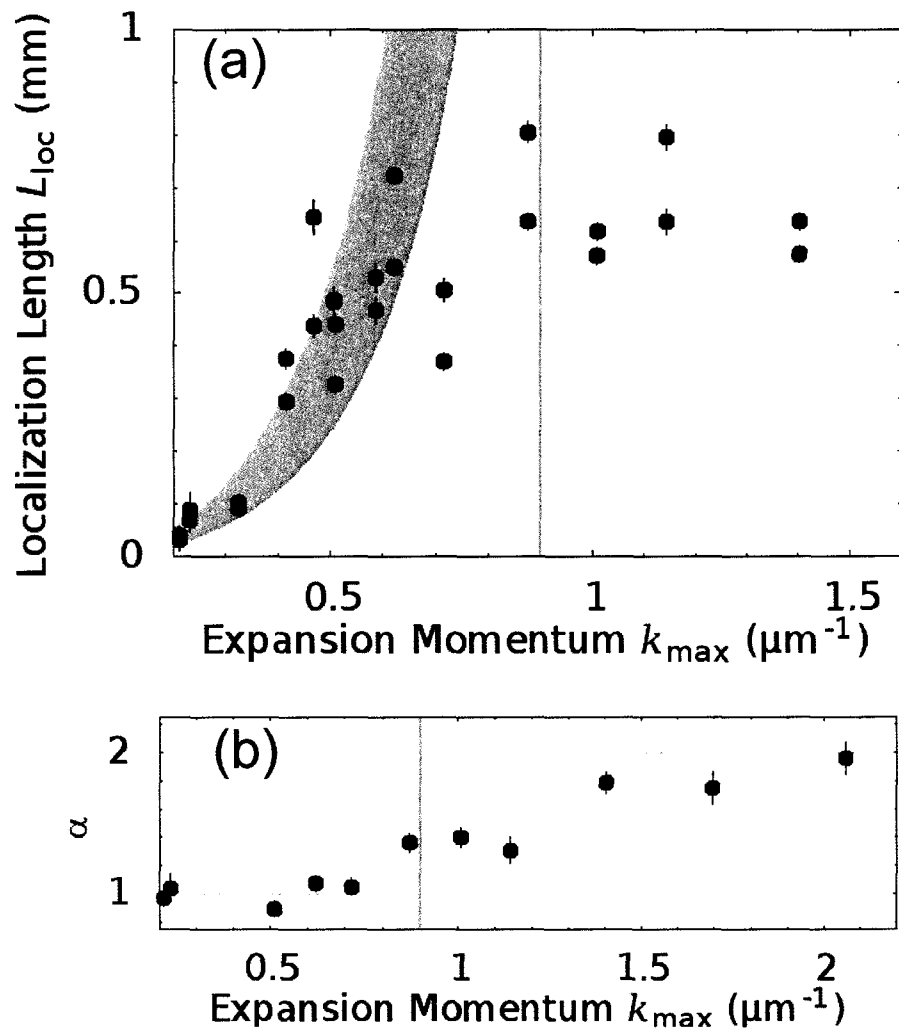
Figure 6.9 : (a) L_{loc} vs. k_{max} for $V_D = 40\,\text{Hz}$. For $k_{max} < k_D$ the atoms appear exponentially localized while for large k the cloud takes a Gaussian shape. Note that data for $L_{loc} \geq 0.5\,\mu m$ the shape of the cloud is heavily influenced by the residual harmonic trap. Shown in (b) is the power for the generalized exponential fitting function described in the text. For this data, the residual trapping frequency was $\omega_z = (2\pi)\,2\,\text{Hz}$.

Chapter 7

Conclusion and Future Directions

This project has been both immensely challenging and extremely gratifying. We set out to build a versatile apparatus for trapping and cooling ^{7}Li and to that end we have certainly succeeded. I am proud to say that I have been a part of it from the first day of building, when we decommissioned the legendary permanent magnet trap, leaving a 10'×4' slab of empty floor for us to fill. This quest is now fully chronicled in [2],[157],[6],[158], and finally this document. The system we have implemented fully exploits the tunability of the effective interatomic interaction in ^{7}Li, allowing the experimenter to tune a over nearly 7 decades. In addition, we have implemented a versatile optical trapping scheme that allows for a seamless transition from single beam to cross beam configurations, even within a single run. We have also implemented a cheme with which to add or subtract an additional harmonic trapping potential through the use of the curve coils in the high field. This allows for traps with a wide range of aspect ratio to be implemented almost trivially. Our apparatus allows for detailed diagnostics of the trapped atom cloud at any stage in the cooling cycle, from MOT to BEC. For the purposes of imaging, we have implemented a system that can use fluorescence, phase contrast, or absorption imaging over a large range of magnetic fields. Through a frame transfer technique called fast kinetics, we have implemented non-destructive phase contrast imaging, allowing

more than a dozen consecutive images to be taken in quick succession of the same trapped cloud.

In has not, however, been all "nuts and bolts." We have fully characterized the s-wave interactions in the $|1,1\rangle$ state of ^{7}Li. By tuning the magnetic field to near the zero crossing at 544 G, we were able to conclusively demonstrate the effects of the weak magnetic dipole interaction (MDI) in ^{7}Li. We also characterized the frequency shift of the collective quadrupole oscillation, showing a shift consistent with the a quasi-1D description of the dynamics of the gas. Near the zero crossing, we observed an anomalously high quadrupole frequency. More work is needed to deduce the cause of this shift, but a prime candidate is the MDI. Tuning the interactions slightly negative has allowed us to repeatably and controllably create single or multiple matter wave solitons.

Through the design and implementation of an optical system that creates fine grained laser speckle or a single Gaussian defect, we have studied the effects of impurities on the transport properties of a BEC. We revisited perhaps the first phenomena where BEC was used to study a concept traditionally thought of as living solely in the realm of condensed matter: superfluid transport. Our data largely support the validity of the Landau criterion for a critical velocity above which the superfluid motion is damped, as long as the criterion is applied *locally*. The local criterion accounts for the inherent inhomogeneity of trapped gases, as well as density modifications produced by large defects. The only exception is for attractive defects

of relatively large strength, where we find that v_c decreases to $v_c \sim 0.6\,c_0$ for $V_D/\mu <$ -0.5. Dissipation is also found to diminish for velocities greater than v_+, which we associate with reduced excitation of dark solitons and phonons.

Throughout the 3D Thomas-Fermi regime, the damping is found to be well described by a universal relation depending on the *dimensionless* defect strength V_D/μ and velocity v_0/c_0. The universal damping peaks at $v_0/c_0 \sim 1$ for any V_D/μ and scales as $(V_D/\mu)^2$ for all μ. As μ decreases, the peak damping rate decreases as well, consistent with the disappearance of the phonon portion of the excitation spectrum as $c_0 \to 0$. Damping in the quasi-1D regime is qualitatively different. In this case, we find for fixed *absolute* V_D and v_0 that β is independent of μ. In this regime, damping is accompanied by fragmentation and spreading of the cloud, with the damping monotonically increasing with V_D/E_K.

While we have exhaustively mapped out the dynamical properties of the system, the equilibrium properties of the disordered BEC are still a "low hanging fruit." Through the tunability in the interactions, future work should be able to characterize the equilibrium phase diagram of a disordered Bose gas, perhaps shedding light in the nature of the elusive Bose-glass state [138, 159].

For the case of a weakly interacting condensate expanding in a 1D guide, we have verified that this system can undergo Anderson localization. Further study of this phenomena provides a golden opportunity for the study of the effect of interactions on the Anderson localized state, a long standing open question in the field of condensed

matter physics. Experiments in higher dimensions could also provide measurements of the critical exponents describing the superfluid to insulator transition [160, 161].

Exciting opportunities also abound for extending the work on soliton scattering. We have to date observed tunneling, splitting and recombination of solitons that have scattered off of a single barrier and also have observed destruction of a soltion due to a disordered potential. In the case of a disordered potential there exists the opportunity to study the transport properties of bright matter-wave solitons [162] with the prospect of observing Anderson localization in such systems [163, 164]. For a single defect, there is also a possibility for the creation of coherently split solitons or solitonic Schrödinger's cat states [165, 166, 167].

The future looks bright!

Appendix A

Acousto-optic Modulator Stabilization Circuit
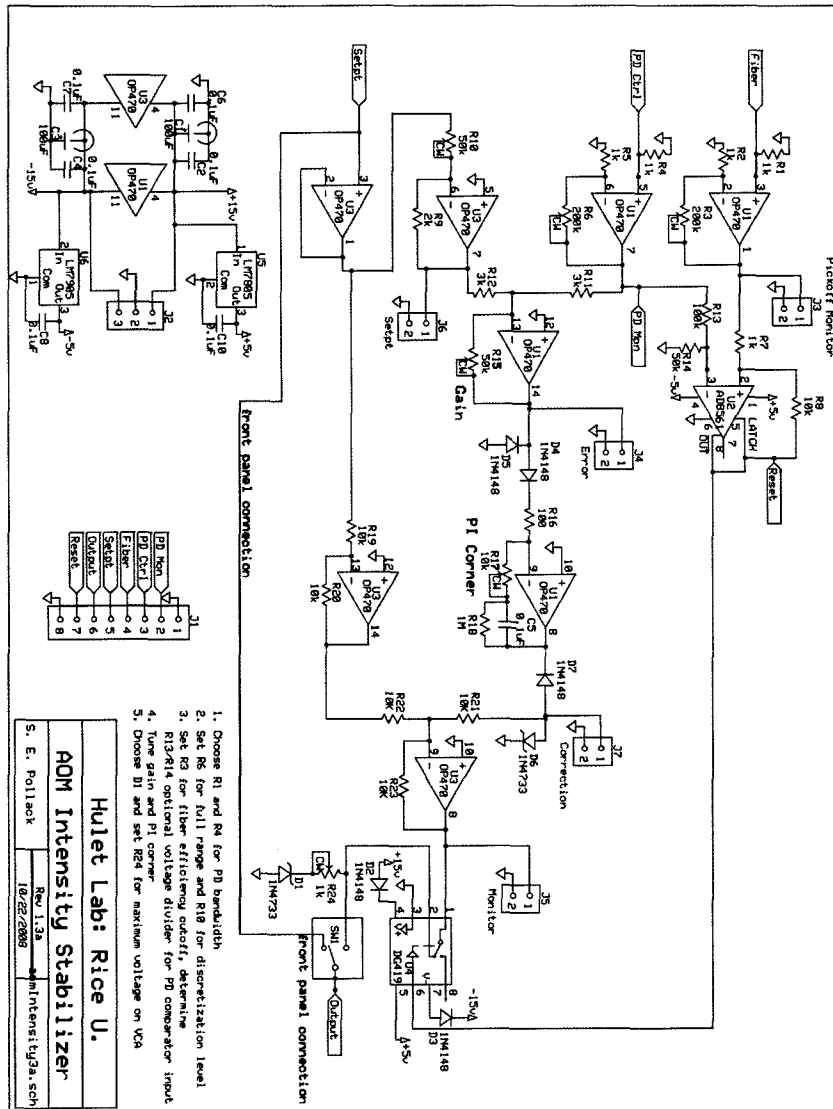
Figure A.1

Appendix B
Side-of-Filter Lock
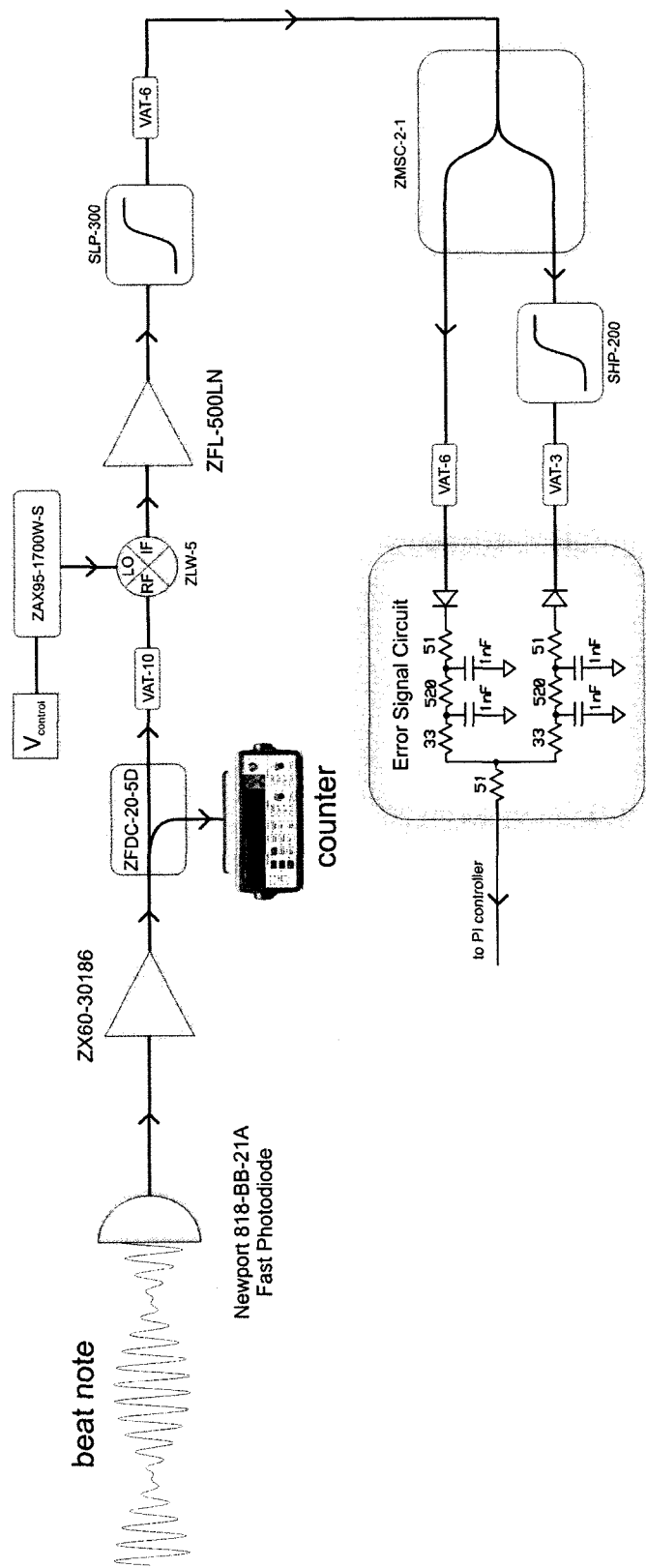
Figure B.1 : Schematic diagram of the SOFT lock. All RF components are manufactured by Minicircuits. The error signal circuit is made from all surface mount components soldered onto a home-etched circuit board. Resistors were manufactured by Vishay and purchased from Newark Electronics PN: 95C2564 (51Ω), 95C2568 520Ω), and 95C2539 33Ω). Diodes are surface mount RF Schottky barrier diodes manufactured by Avago Technologies and purchased from Newark Electronics PN: 63J9546. The system is based off of the design reported in [14]
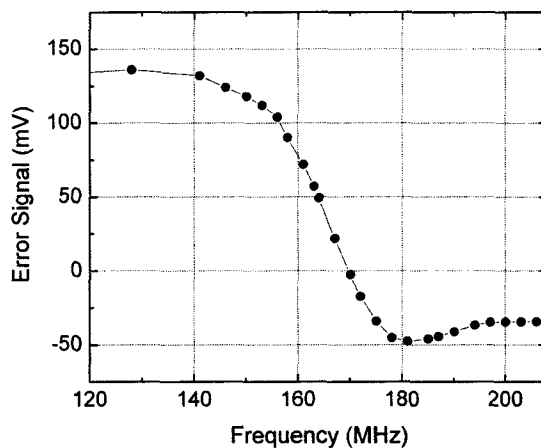
Figure B.2 : Output of the error signal circuit for a power of 4 dBm a the input to the splitter ZMSC-2-1. This signal is sent to a PI controller that feeds back to both the current and the grating of the probe ECDL.
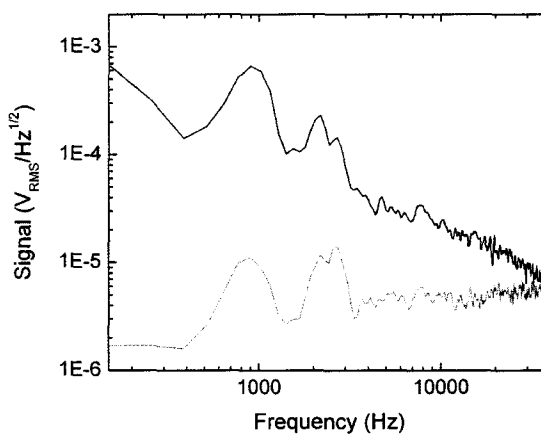
Figure B.3 : Power spectrum of the error signal locked (green) vs. unlocked (red).

Appendix C

Magnetic Field Control Circuit Diagrams
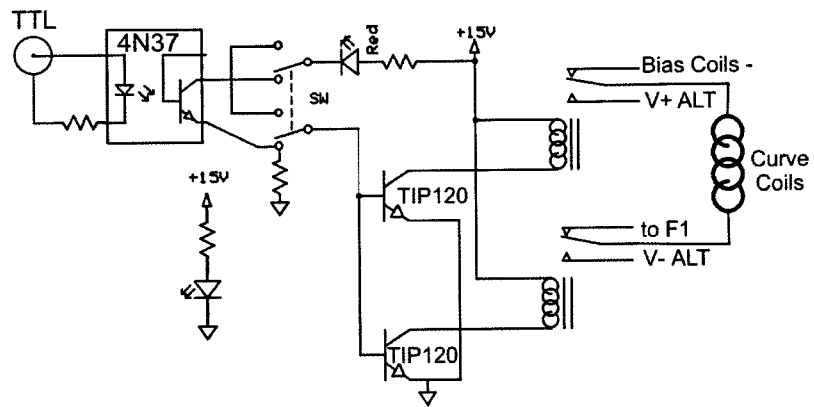
Figure C.1 : TTL buffer for alt. supply curve control. Relays are KEST KAR1260, 12V, 60A rated automotive relays purchased from EPO.
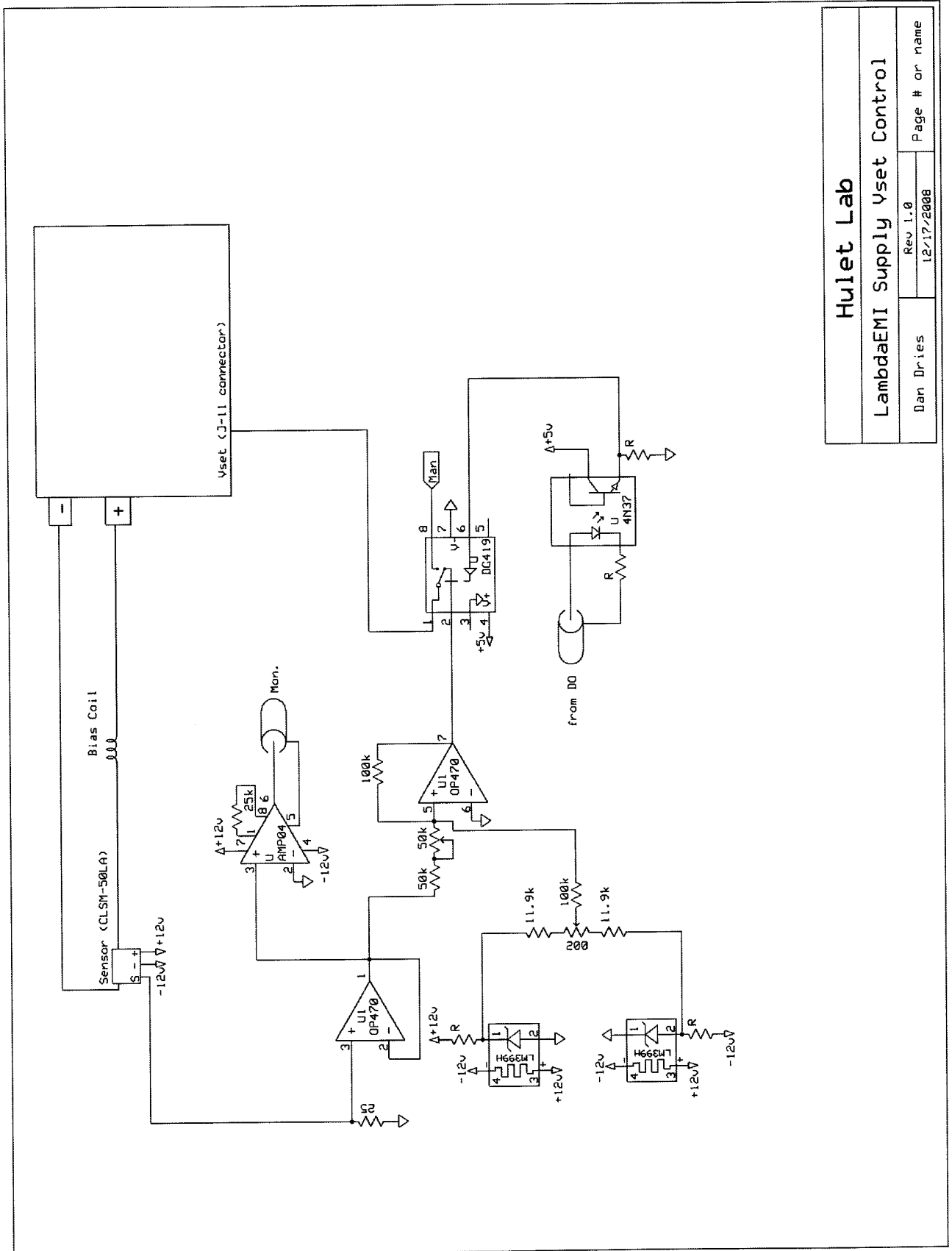
Figure C.2 : Control circuit for power supply voltage set point.
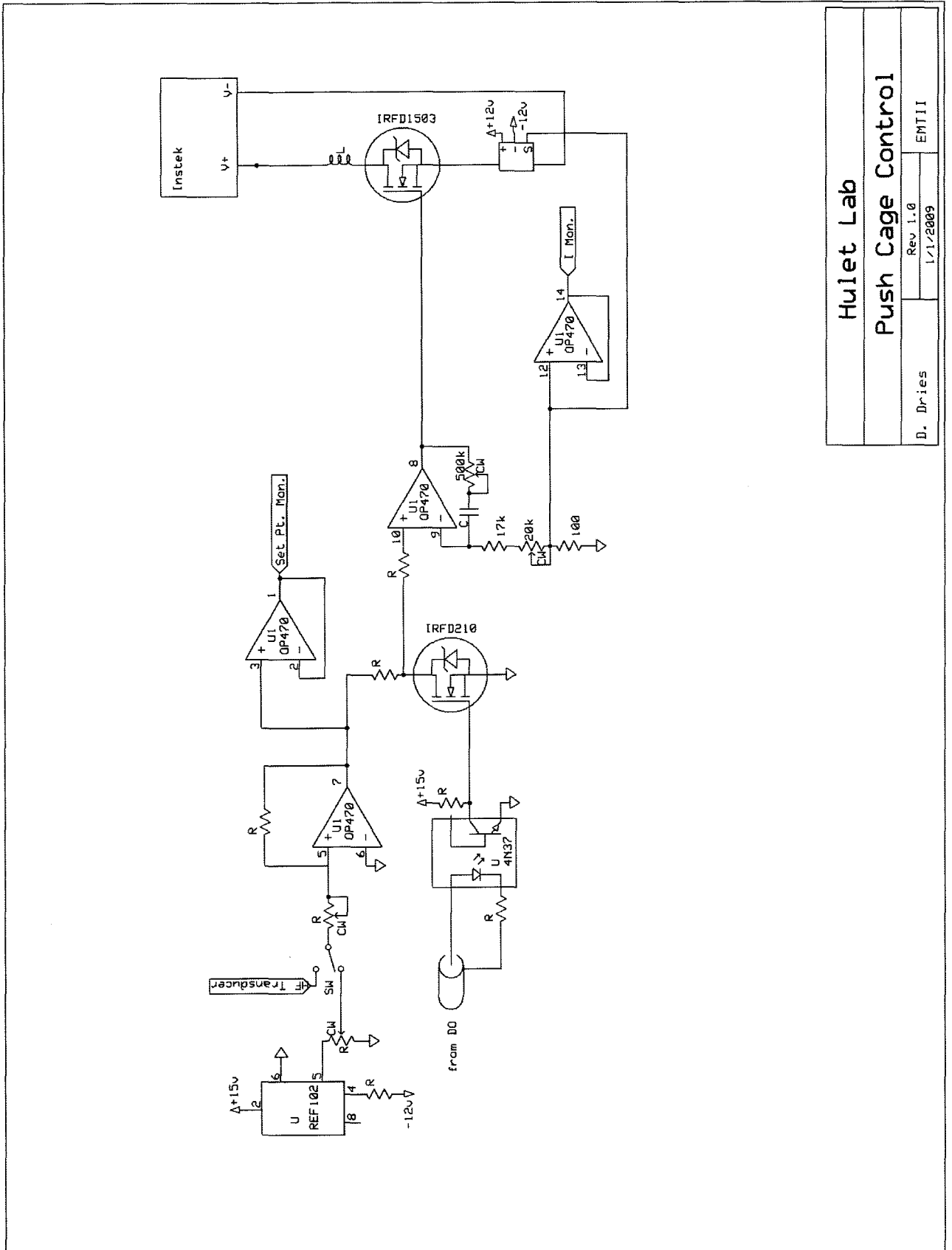
Figure C.3 : Circuit for transducer control of push coil.

Appendix D

Andor Multi-Pic Script

```
//rem   Auto Data Strip
rem   For 6Li and 7Li this script:
rem   subtracts a reference,
rem   normalizes atoms and no atoms with a user defined patch,
rem   displays normalized, subtracted signal,
rem   saves atoms and noatoms for 6 and 7 (.fit) !ref is already subtracted...mi
rem   optionally saves a log file of parameters
rem   optionally logs summed patch values

rem Fast Kinetics Mode Settings: trigger= external; rows=170 (currently);
rem exposure t=100 us; number in series=2; shift speed=4us;

rem Optional User input.  they are strings...so words ok.
 logfile$="log2.txt";
 atom$="13 "
 sixdet$="cmot "
 sevendet$ = "0.6 "
 opt$ = "1 "
 dop$ = "100ms "
 rf3dbm$ = "0.0 "

rem output log? (1 or 0)
 out = 0

 w1=activeWindow()
rem  7atoms minus ref

//rem CloseWindow (#1)
//load(#1, "L:\data\emt2\2008\jul\atomsbgnd.fit")
//MoveWindow(#1,300,420,500,200)


     run$="\\10.97.67.106\\data\\.runNumber";
```

```
    read(run$,folder$)
    read(run$,date$)
    read(run$,f$)
    read(run$,new_npic$)
    nnpic=val(new_npic$)
    error=close ()
    if (error<0) then print "Error closing .runNumber"
    run$="C:\data\emt2\junk.txt";
    read(run$,junk$)

    npic = nnpic
    npix = 512 / (npic + 1) - mod(512, (npic+1)) / (npic+1)
    expTime=100
    print ("Now ",npic," pictures of ",npix," pixels")
    SetFastKinetics(expTime, npic, npix)

counter=0
while (counter<100)

    Run()

    run$="\\10.97.67.106\\data\\.runNumber";
    read(run$,folder$)
    read(run$,date$)
    read(run$,f$)
    read(run$,new_npic$)
    nnpic=val(new_npic$)
    error=close ()
    if (error<0) then print "Error closing .runNumber"
    run$="C:\data\emt2\junk.txt";
    read(run$,junk$)
    print (folder$,date$,f$,new_npic$)

    dfolder$="C:\data\emt2"+date$;
    folder$=folder$+date$;

    for pic=1 to npic step 1
        #pic=#0_sig{1}[1<<2,1<<2]
        TopWindow(#pic)
        CloseWindow(#pic)
        #pic=#0_sig{pic}[1<<512,1<<npix]
```

```
            filename$="\atoms"+f$+"_"+str$(pic)
            if (npic == 2) then filename$="\atoms"+f$
            if (pic == npic) then filename$="\noatoms"+f$
            print (f$, filename$, folder$, dfolder$)

            saveFITS(#pic,dfolder$+filename$+".fit")
            saveFITS(#pic,folder$+filename$+".fit")

            TopWindow(#pic)
            MoveWindow(#pic,260,380,1000,500)
        next
        for pic=npic-1 to 1 step -1
            // Save noatoms shots
            filename$="\noatoms"+f$+"_"+str$(pic)
            saveFITS(#npic,dfolder$+filename$+".fit")
            saveFITS(#npic,folder$+filename$+".fit")
            //print filename$

            ps = npic + pic
            #ps=#0_sig{1}[1<<2,1<<2]
            TopWindow(#ps)
            CloseWindow(#ps)
            #ps = (#npic - #pic) / (#npic - 705.5)
            TopWindow(#ps)
            MoveWindow(#ps,260,0,1000,500)
            ScaleData(#ps,-.2,.2)
        next

        if (nnpic != npic) then
            npic = nnpic
            npix = 512 / (npic + 1) - mod(512, (npic+1)) / (npic+1)
            print ("Now ",npic," pictures of ",npix," pixels")
            SetFastKinetics(expTime, npic, npix)
        endif
wend

rem  End of Program
```

Appendix E

Discussion of Experimental Uncertainty in Measurement of a

E.1 Discussion Relating to measurments in PRL 102 090402 (2009)

The following is adapted from an internal manuscript written by S.E. Pollack in May of 2009. I have corrected some errors and changed certain notations for consistency with this thesis, however large portions of the text remain unchanged.

For the meaurements found in Ch. 4.5 of this thesis and in Ref. [81], we used polarization phase-contrast imaging (PPCI) to extract the *in situ* density and size of the BEC. See Ch. 3.5.1 of this thesis, Bradley et al., Phys. Rev. Lett. **78** 985 (1997) and Curtis Bradley's thesis for more information on this imaging technique.

Starting from Eq. 3.13,

$$I_{\text{sig}} = E_0^2 a_1^2 \sin^2(\theta) e^{-\alpha} + E_0^2 (1 - a_1^2) \cos^2(\theta) + 2E_0^2 a_1 \sin(\theta) \sqrt{1 - a_1^2} \cos(\theta) e^{-\alpha/2} \cos(\phi + \gamma)$$

(E.1)

We take circularly polarized light with $a_1 = 1/\sqrt{2}$ and $\gamma = \pi/2$. Maximal sensitivity occurs when the output polarizer angle is $\theta = \pi/2$ (See Fig. 3.18). In practice, to improve signal to noise, we take two pictures: one with atoms and one without, then subtract the two and divide by the no atoms shot. We also subtract a dark image

from each shot, resulting in

$$S = \frac{I_{\text{atoms}} - I_{\text{noatoms}}}{I_{\text{noatoms}} - I_{\text{dark}}} \tag{E.2}$$

For the purposes of this discussion we set $\gamma = \gamma' - \pi/2$ and keep the first order corrections to S for small γ'

$$S = \frac{1}{2} \left(e^{-\alpha} - 1\right) - \frac{\gamma'}{2} \left(1 + e^{-\alpha}\right) + e^{-\alpha/2} \left[\sin\left(\phi\right)\left(1 - \gamma'\right) + \gamma' \cos\left(\phi\right)\right], \tag{E.3}$$

with ϕ and α given by

$$\phi = -\frac{\Delta}{\Gamma}\alpha \tag{E.4}$$

$$\alpha = \frac{\sigma_0 n_x(y, z)}{1 + 4\left(\frac{\Delta}{\Gamma}\right)^2 + 2\frac{I}{I_{\text{sat}}}} \tag{E.5}$$

In practice Eq. (E.3) is numerically inverted to determine α for a given value of S. With a solution for α we determine the column density by inverting Eq. (E.5).

Errors in Determination of α

The systematic parameters involved in α determination are a_1, θ, γ, and Δ/Γ. These will yield some systematic uncertainty in the final number of atoms. Systematic uncertainty in the camera magnification m ($\sim 1\%$) and efficiency $\eta = 1.29(10) \times 10^{-15}$ mJ/count come into the determination of the measured intensity of light. Statistical camera noise δC is a combination of read noise and dark current noise, which

have been measured to be less than 5 and 30 counts respectively. Photon counting also contributes to the error in I:

$$\delta I^2 = I + \delta C^2 + I^2 \left[\left(\frac{\delta \eta}{\eta} \right)^2 + 4 \left(\frac{\delta m}{m} \right)^2 \right]. \tag{E.6}$$

For completeness, the error in the signal is

$$\delta S^2 = \left(\frac{\delta I_{\text{atoms}}}{I_{\text{noatoms}}} \right)^2 + \left(\frac{I_{\text{atoms}} \delta I_{\text{noatoms}}}{I_{\text{noatoms}}^2} \right)^2. \tag{E.7}$$

The first order corrections in S due to the light field angles can be directly determined by variation of Eq. (E.1). The first order correction in γ was found to be relatively large ($\delta S \approx S \, \delta \gamma$), which is why it is directly included in Eq. (E.3). The first order corrections to S in θ and a_1 are:

$$\frac{\delta S}{\delta \theta} \approx -1 + e^{-\alpha} \tag{E.8}$$

$$\frac{\delta S}{\delta a_1} \approx -\sqrt{2}(-1 + e^{-\alpha}) \tag{E.9}$$

For small values of α these effects are 1% or less. The error in detuning is fractionally small ($\Delta/\Gamma \sim 10$—100 with $\delta(\Delta/\Gamma) \sim O(1)$) and does not contribute much in the determination of α from S. For example, for small α we find from Eq. (E.3)

$$\alpha = \frac{S}{-\frac{1}{2} + \frac{\Delta}{\Gamma}}, \qquad \delta \alpha^2 = \frac{\delta S^2 + \alpha^2 \, \delta \left(\frac{\Delta}{\Gamma} \right)^2}{-\frac{1}{2} + \frac{\Delta}{\Gamma}}. \tag{E.10}$$

A maximal value of δS is 0.1 (in general we keep $S < 0.4$ by adjusting Δ); for $\Delta/\Gamma = 10$ we determine $\alpha \approx 0.06$ reducing the contribution from the error in detuning by a considerable amount below the error in the signal. Although errors in detuning are not important in determination of α, they are in the determination of column density n_y from α.

Errors in Determination of n_y

The error in n_y is given by the variation of Eq. (E.5)

$$\delta n_y^2 = \left[\frac{n_y}{\alpha}\,\delta\alpha\right]^2 + \left[\frac{8\alpha}{\sigma_0}\frac{\Delta}{\Gamma}\,\delta\left(\frac{\Delta}{\Gamma}\right)\right]^2 + \left[\frac{2\alpha}{\sigma_0}\frac{\delta I}{I_{\text{sat}}}\right]^2. \tag{E.11}$$

Note that the error in the density is computed for each pixel. We typically measure the detuning with an accuracy as large as $0.5\,\text{MHz}$. Typically $\delta I/I_{\text{sat}} \approx 0.1$ so that the last term is negligible for large detunings. In general the resulting fractional error $\delta n/n$ is less than 5%, with the error growing towards the edge of the condensate.

Determination of N

N is found by integrating over the condensate. Therefore the error in N is

$$\delta N^2 = m^4 \sum \delta n_y^2 + \left(2N\frac{\delta m}{m}\right)^2 \tag{E.12}$$

where the sum spans the condensate. For the contribution from the first term we almost always find $\delta N/N < 10^{-2}$ and typically $\delta N/N \approx 2 \times 10^{-3}$. Therefore the second term dominates and $\delta N/N \sim 2\%$.

Determination of Axial Size

We fit the integrated axial density profile $n_{xy}(z) = \sum_x m n_y(x, z)$ to a Gaussian function and determine the $1/e$ width, which is used as the axial size of the condensate R. The fit is weighted (i.e., we use δn_{xy} in the fitting routine) and the resulting parameter uncertainty is determined from the correlation matrix of the data set. Given the large numbers of data points, and the typical noise level in n_{xy}, the fit value contributes a fractional error of $\sim 0.1\%$. Therefore the systematic error in m dominates: $\delta R/R \approx 1\%$.

Temperature Effects

There is some uncertainty of the axial size due to being at non-zero temperature. We have estimated this effect by simulating clouds with non-zero temperature and fitting to a single distribution. The results of this calculation are shown in Fig. E.1. We measure accurate values for T/T_c when there is a good thermal component in the cloud (i.e., for $T/T_c > 0.5$), below this the measurement error becomes large due to the small thermal contribution making it difficult to estimate T. After measuring T/T_c as a function trap power we extrapolate and determine that T/T_c is typically 0.3 or smaller.
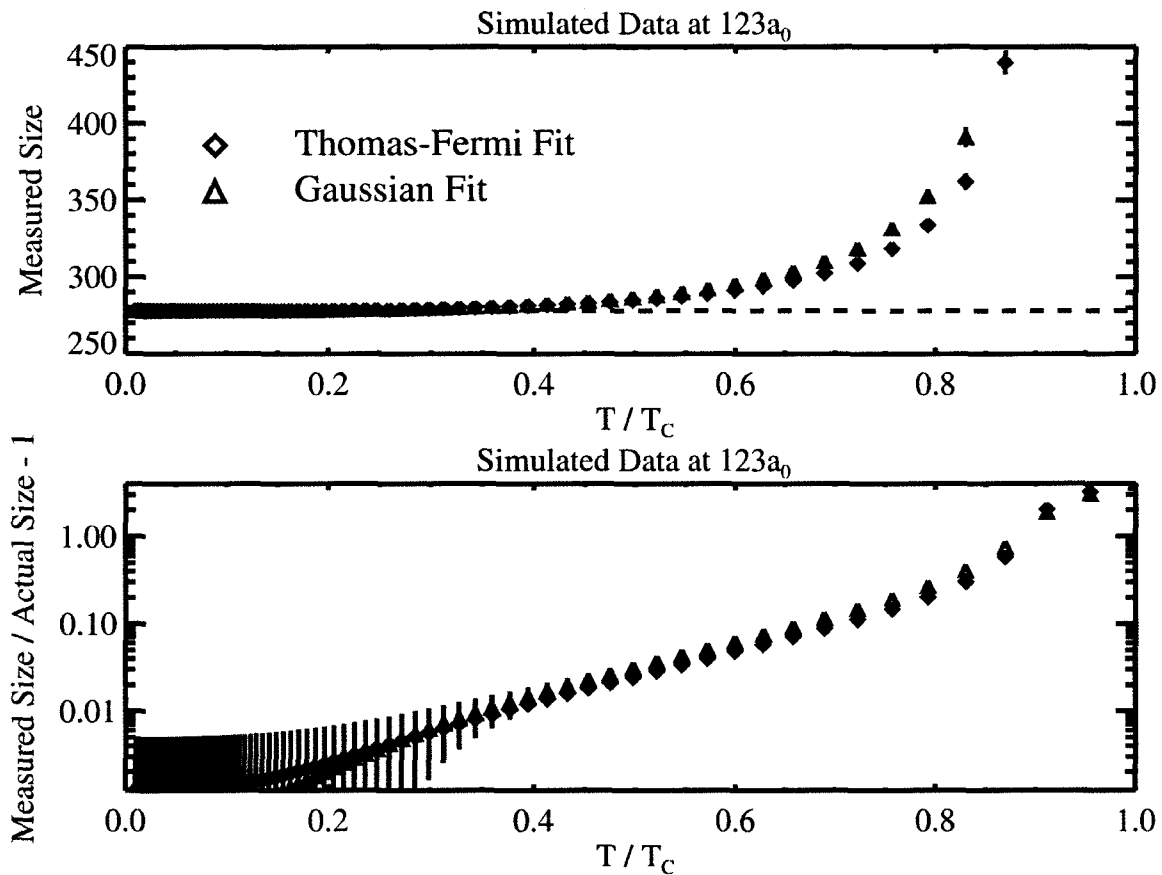
Figure E.1 : Simulated data at $a = 123\,a_0$ with non-zero temperature fit with either a Thomas-Fermi or a Gaussian distribution. Top: Measured sizes using either fit, the horizontal line is the equivalent Thomas-Fermi radius in axial size. Bottom: The fractional deviation of the measured size from the actual size. We typically operate at $T/T_c \sim 0.3$ and in practice fit with a Gaussian distribution.

Determination of a for a Condensate

We model the system using the Gross-Pitaevskii equation

$$\mu\psi = -\frac{\hbar^2}{2m}\nabla^2\psi + V\psi + \frac{4\pi\hbar^2 a}{m}|\psi|^2\psi$$
$$+\frac{\mu_0\mu_m^2}{4\pi}\int\frac{1-3\cos^2\theta}{|\mathbf{r}-\mathbf{r}'|^3}|\psi(\mathbf{r}')|^2 d\mathbf{r}'\psi, \tag{E.13}$$

where we have included the magnetic dipole interaction (MDI). A variational method is used with a 3D cylindrically symmetric Gaussian wavefunction as a trial. We obtain coupled equations for the radial and axial sizes of the Gaussian as functions of N and a. These equations are inverted to find a numerical function with N and R (and trap frequencies) as inputs and a as output.

Thomas-Fermi Limit

A closed form equation for a is available in the Thomas-Fermi regime [26].

$$a = \frac{m^2 \omega_z^4 R_{TF}^5}{15\hbar^2 \omega_r^2 N} \tag{E.14}$$

Here the Thomas-Fermi radius $R_{TF} \propto (Na)^{1/5}$. The error in a in the large interacting regime is

$$\left(\frac{\delta a}{a}\right)^2 = \left(5\frac{\delta R}{R}\right)^2 + \left(\frac{\delta N}{N}\right)^2 + \left(2\frac{\delta f_r}{f_r}\right)^2 + \left(4\frac{\delta f_z}{f_z}\right)^2. \tag{E.15}$$

The radial frequency is measured by oscillating the power in the optical trap after a condensate has been formed. Loss in the trap is maximal at the radial trapping frequency and harmonics. We fit the center of the loss to better than 5% precision. The axial frequency is measured with dipole oscillations by displacing the condensate using a magnetic field gradient. The asymptotic standard errors in the axial frequency measurement are typically 0.5% or less. However, realistically the actual error in the determination of these frequencies is much larger since there is some variation in

the position for each image and timing jitter. A more reasonable estimation for the uncertainty might be 1/(the total oscillation time), which yields ~1% for the best axial measurements and 3% as a more typical value. Collecting the fractional errors it is clear that uncertainty in the axial trap frequency provides the largest source of error in determination of a. For these values $\delta a/a \approx 0.20$.

Numerical Estimation of Error

There is no closed-form solution in the weakly interacting regime for a. However, we can numerically estimate the contributions of uncertainties in the various parameters by numerical error propagation. The form of the uncertainty in a is similar to that expressed in Eq. (E.15) however the prefactors will be functions of N, R, and the trap frequencies. What is relatively easy to present is the response of a to the inputs at particular values of the inputs. For example, for $f_r = 200\,\text{Hz}$, $f_z = 3\,\text{Hz}$, $R = 50\,\text{um}$, and $N = 3 \times 10^5$ we find

$$\frac{\delta a}{a} \sim \frac{\delta N}{N}, \qquad \frac{\delta a}{a} \sim \frac{\delta f_r}{f_r}, \qquad \frac{\delta a}{a} \sim 2\frac{\delta f_z}{f_z} \qquad \text{(E.16)}$$

The remaining quantity is a strong function of R, but the prefactor remains below 5 for $a > 0.02$ (and outside the TF regime) as shown in Fig. E.2. Again, using the values above we find typically find $\delta a/a \approx 0.1$ or better.
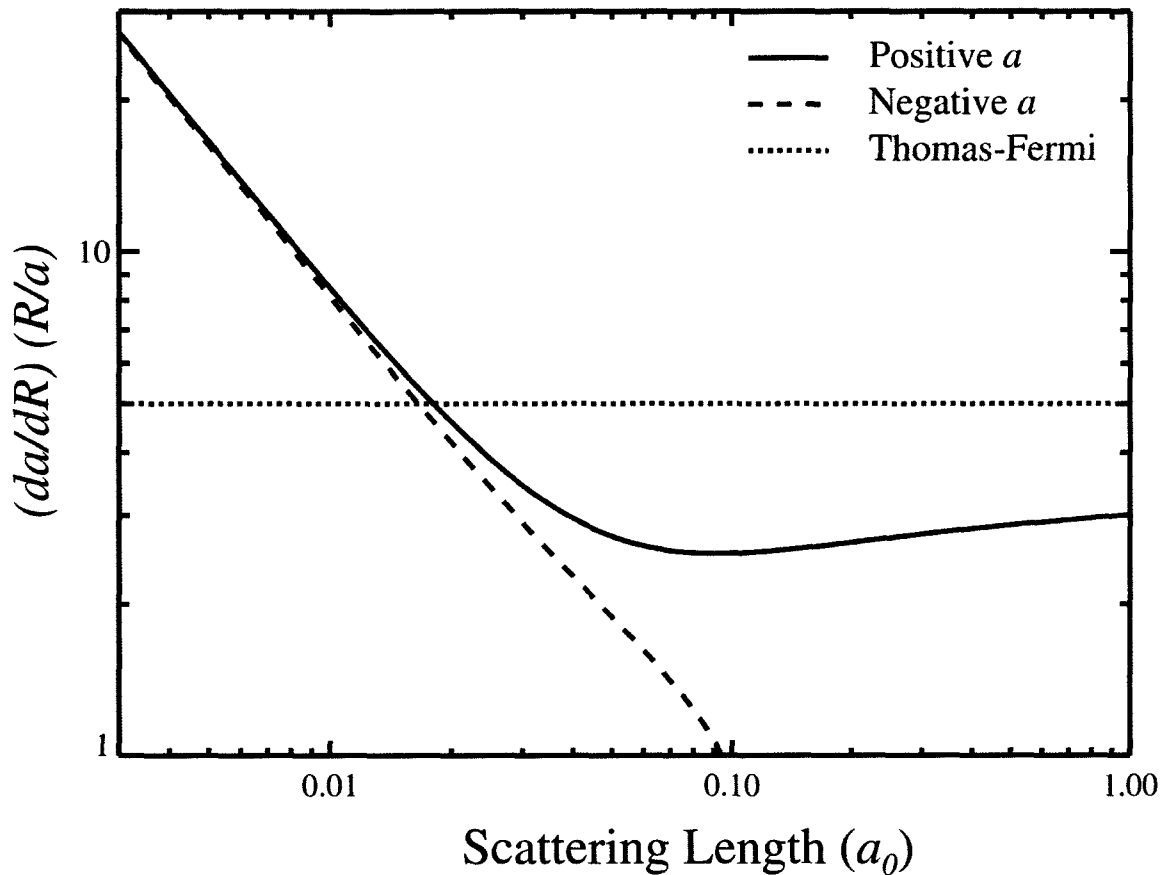
Figure E.2 : Numerically computed coefficient in front of $\delta R/R$ in Eq. (E.15) using the variational approach. We have chosen to plot against a rather than R for convenience. Parameters: $f_r = 200\,\text{Hz}$, $f_z = 3\,\text{Hz}$, and $N = 3 \times 10^5$.

Magnetic Field Uncertainty

We use radio frequency transitions between the $|2,2\rangle$ and $|1,1\rangle$ states along with the Breit-Rabbi formula to determine the magnetic field for a particular current, measured by a voltage drop across a shunt resistor V, running through the bias magnetic field coils. The location of the RF transfer (and therefore the magnetic field) is determined with a width of typically $0.3\,\text{MHz}$ which corresponds to $0.1\,\text{G}$. Note that the uncertainty in the location is by far smaller than this and we could

use a smaller error here. A collection of field values are measured and a straight line fit is formed. As an example with typical errors,

$$B \approx -5.00(8) + 25.000(2)V/\text{mV} \tag{E.17}$$

$$\delta B^2 = (0.08)^2 + (0.002\ V)^2 + (25\ \delta V)^2 \tag{E.18}$$

We measure $\delta V < 0.001\,\text{mV}$ within a shot, making this contribution small. Using an average value of $V = 28\,\text{mV}$ we find $\delta B \approx 0.1\,\text{G}$, with an additional systematic uncertainty of $0.1\,\text{G}$.

Scattering Length vs. Magnetic Field

For each value of B we take on order 10 shots. Values of a and B are recorded for each shot along with the errors in these values as describe above. The weighted mean and standard deviation of each collection is used as the value and 1σ error for each data point we plot in Fig. E.3. In general, $\delta a/a$ for an individual collection is between 10% and 30%.

E.2   Discussion from Pollack et al. Science (2009)

This following is an excerpt from the SOM in Pollack et. al [40]. It is reprinted here for the sake of completeness. It should be noted that the field calibration in Ref. [81] was limited to $\sim 0.100\,G$, fundamentally by the arbitrary waveform generator we
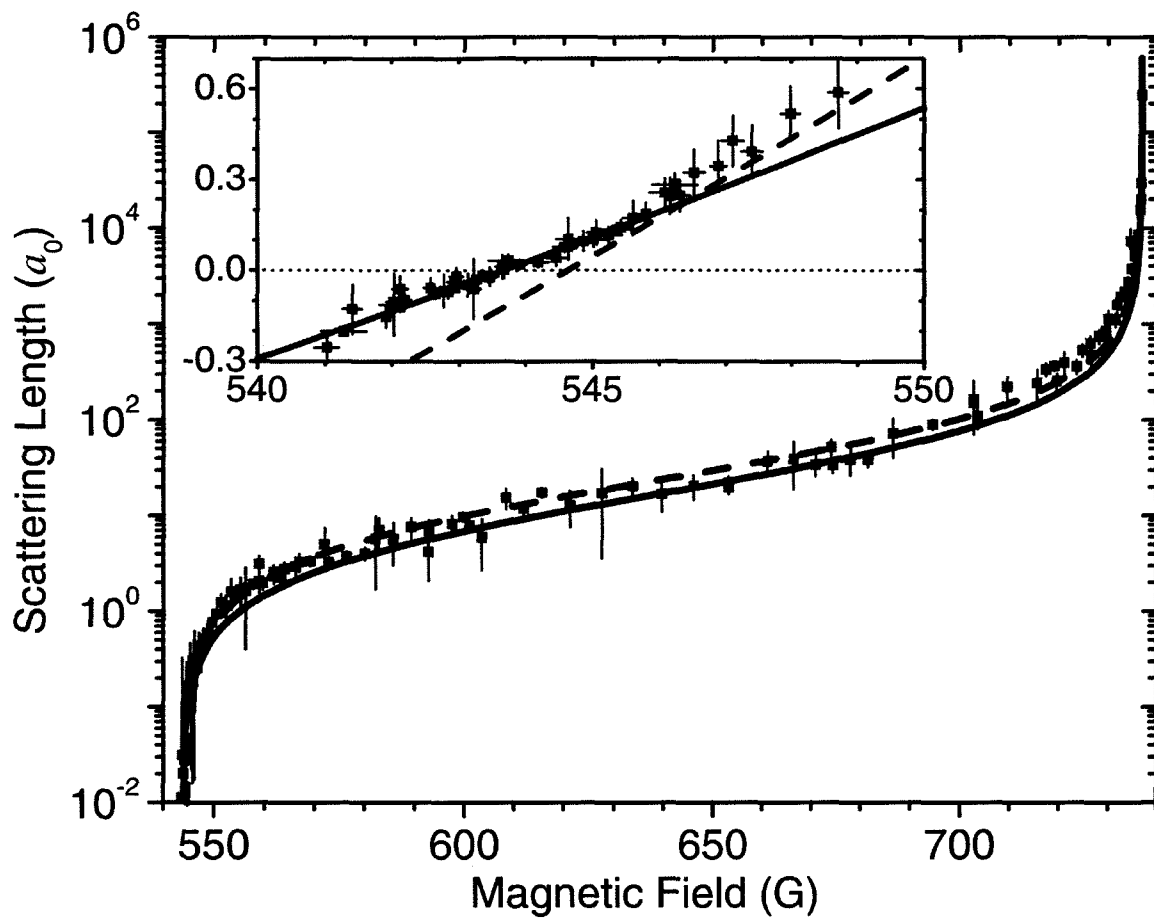
Figure E.3 :   Axial size data mapped onto a. Results of a coupled-channels calculation are shown by the solid line, and a Feshbach resonance fit by the dashed line. The inset shows the extracted values of a near the zero-crossing. A linear fit in this regime matches the coupled-channels calculation.

used to program the current. For the data near resonance, in Ref. [40], a stable voltage reference was used that provided $\sim 0.020\,G$ as discussed below.

E.3 Comparison of Measured a with Coupled Channels Calculation

The s-wave scattering length a is controlled via a magnetic Feshbach resonance. We extract a (for $a > 0$) as a function of magnetic field B from the axial size of a Bose-Einstein condensate ($S7$). The measured functional form of a vs. B is well described by a Feshbach resonance fit $a(B) = a_{BG}[1+\Delta/(B-B_\infty)]$, where the values $a_{BG} = -24.5^{+3.0}_{-0.2}\, a_0$, $\Delta = 192.3(3)$ G, and $B_\infty = 736.8(2)$ G were previously reported ($S7$). We find that axial size measurements agree with the Feshbach resonance fit to within 25% over the interval $10 < a/a_0 < 10^3$, and $< 50\%$ for $a > 10^3\, a_0$, as shown in Fig. S1.

To repeatably achieve very large values of a it is necessary to have both high field stability and accurate knowledge of the location of B_∞. We determine the shot-to-shot stability of the magnetic field from radio frequency spectroscopy on the $|2,2\rangle \rightarrow |1,1\rangle$ transition. We have improved the control of the current in the coils that provide the magnetic bias field in our experiment such that a Lorentzian characterizing the shot-to-shot field stability has a full width at half maximum of $115\,$kHz, corresponding to $21\,$mG instability at a bias field of $717\,$G, shown in Fig. S2C. With this improved field stability we have increased the precision in the determination of the resonance location to $B_\infty = 736.97(7)$ G. In addition, we can use the measured values of $L_3(B)$ to determine the location of the resonance. This method is consistent with our determination of B_∞ from the $a(B)$ fit. The uncertainty in the determina-

tion of a is given by $\delta a = a_{BG}\Delta(\delta B^2 + \delta B_\infty^2)^{1/2}(B - B_\infty)^{-2} \approx 2 \times 10^{-5}\, a^2/a_0$, where δB is the shot-to-shot field stability and δB_∞ is the uncertainty in the resonance location.

Since we have only measured a for $a > 0$, we have no direct knowledge of $a < 0$. However, a coupled-channels calculation ($S8$) agrees with the Feshbach resonance fit to within 10% over the range of $10 < a/a_0 < 3 \times 10^4$, shown in Fig. S2, which gives us confidence that the Feshbach resonance fit is equally reliable on the $a < 0$ side of the resonance.
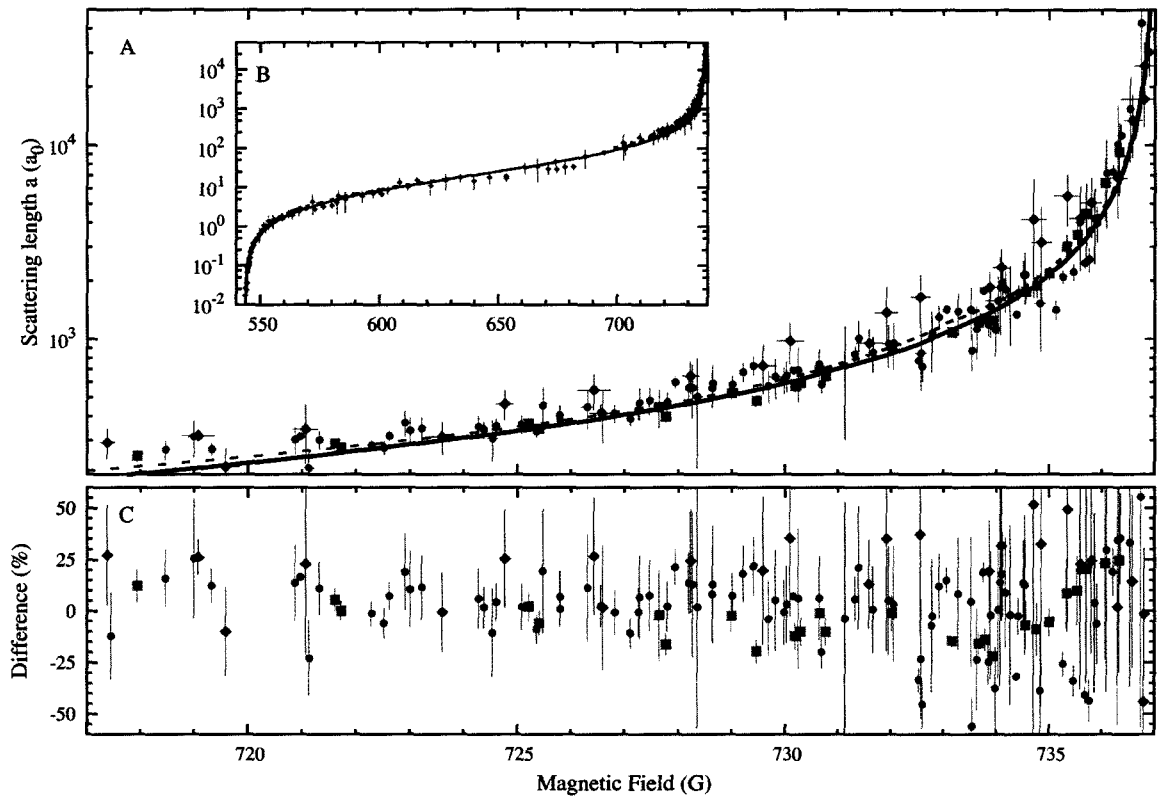
Figure E.4 : (**A**) a extracted from the axial size of Bose-Einstein condensates as a function of magnetic field. Results of a coupled-channels calculation are shown by the solid red line. The dashed black line is the Feshbach resonance fit. (◆) Data previously reported with trapping frequencies $\omega_r = (2\pi)\,193\,\text{Hz}$ and $\omega_z = (2\pi)\,3\,\text{Hz}$ (*S7*). Data with $\omega_r = (2\pi)\,236\,\text{Hz}$ and $\omega_z = (2\pi)\,4.6\,\text{Hz}$ (●) or $\omega_z = (2\pi)\,16\,\text{Hz}$ (■). (**B**) Full range of data spanning nearly 7 decades in a. (**C**) Fractional difference between the extracted values of a and the Feshbach resonance fit.
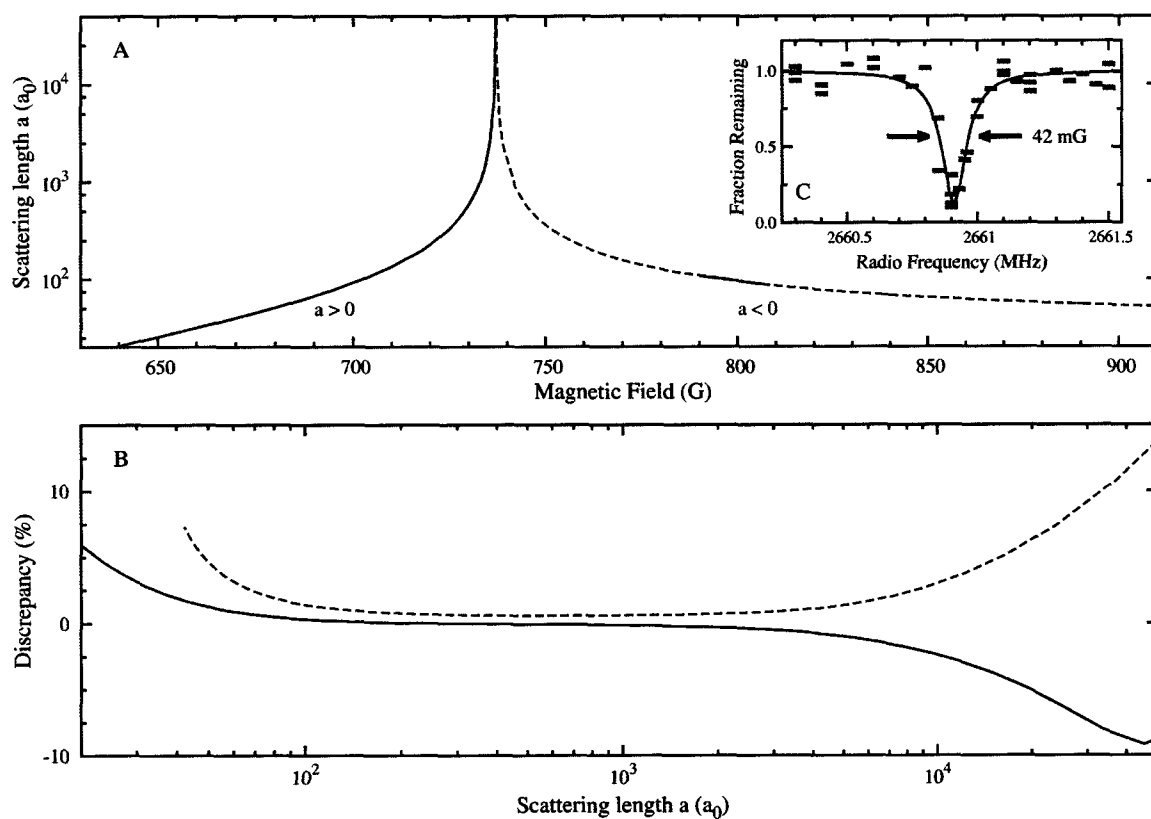
Figure E.5 : (**A**) a versus magnetic field from a coupled channels calculation. (**B**) Discrepancy between the coupled channels calculation and the Feshbach resonance fit used to determine a. (**C**) Radio frequency spectroscopy signal at 717 G showing a full width at half maximum of 115 kHz.

Appendix F

Discussion of Uncertainty for Quadrupole Oscillations

The uncertainty in the scaled interaction parameter

$$P' = \frac{\lambda N a}{l_r} \tag{F.1}$$

is given by

$$\frac{\delta P'}{P'} = \sqrt{\left(\frac{\delta \lambda}{\lambda}\right)^2 + \left(\frac{\delta N}{N}\right)^2 + \left(\frac{\delta a}{a}\right)^2 + \left(\frac{\delta l_r}{l_r}\right)^2} \tag{F.2}$$

with

$$\frac{\delta \lambda}{\lambda} = \sqrt{\left(\frac{\delta \omega_z}{\omega_z}\right)^2 + \left(\frac{\delta \omega_r}{\omega_r}\right)^2} \tag{F.3}$$

and

$$\frac{\delta l_r}{l_r} = \frac{1}{2} \frac{\delta \omega_r}{\omega_r} \tag{F.4}$$

The uncertainties in ω_z and ω_r are typically 3% and 5%, respectively as discussed above in Appendix E.1. This then yeilds $\frac{\delta \lambda}{\lambda} = 6\%$. $\frac{\delta N}{N}$ is dominated by shot to shot fluctuations in N and is typically 20%. (As discussed above in Appendix E.1, for PPCI the single shot uncertainty in N is comparatively small at $\delta N/N \sim 2\%$.) Near the zero crossing, we must account for the uncertainty caused by both the field error and our error in the calibration of $a(B)$. Near the zero crossing, we fit the measured

a to the form

$$a(B) = m(B - B_0) \tag{F.5}$$

with $m = 0.08(1)$ and $B_0 = 543.6(1)\,\mathrm{G}$ (see chapter 4.5). The uncertainty in a is therefore

$$\delta a/a_0 = \sqrt{(\delta m)^2 (B - B_0)^2 + m^2 \left[(\delta B)^2 + (\delta B_0)^2\right]} \tag{F.6}$$

As described in Appendix E.1, $\delta B = 0.1\,\mathrm{G}$. This then implies

$$\delta a = \sqrt{\left(\frac{0.01}{0.08}\right)^2 a^2 + (0.08)^2 \left[2(0.1)^2\right] a_0^2} \tag{F.7}$$

$$\delta a = \sqrt{(0.125a)^2 + (0.01\,a_0)^2} \tag{F.8}$$

When calculating the error bars, for consistency accross all fields, we replace the prefactor in the first term Eq. F.8 of with 0.2 which is a more accurate estimate of the uncertainty in a for fields away from the zero crossing, as described above in Appendix. E.1. This will however, slightly overestimate the error near the zero crossing with a deminishing effect as $a \to 0$. Combining the errors in λ, N, and the trap frequencies gives $\sim$20% error. Including the error from the scattering length gives for the final uncertainty in P'

$$\delta P' = \sqrt{(.20P')^2 + (\lambda N \delta a/l_r)^2} \tag{F.9}$$

$$\delta P' = \sqrt{2(.20)\,P'^2 + (\lambda N 0.01\,a_0/l_r)^2} \tag{F.10}$$

Bibliography

[1] M. Junker, D. Dries, C. Welford, J. Hitchcock, Y. P. Chen, and R. G. Hulet. "Photoassociation of a Bose-Einstein condensate near a Feshbach resonance." *Phys. Rev. Lett.* **101**(6) 060406 (2008).

[2] M. Junker. "Single Photon Photoassociation in a ^{7}Li BEC near a Feshbach Resonance." Ph.D. Thesis, Rice University (2008).

[3] K. E. Strecker. "Sympathetic cooling of a Bose/Fermi mixture of lithium to quantum degeneracy." M.S. Thesis, Rice University (2002).

[4] W. D. Phillips. "Nobel lecture: Laser cooling and trapping of neutral atoms." *Rev. Mod. Phys.* **70** 721 (1998).

[5] S. Chu. "Nobel lecture: The manipulation of neutral particles." *Rev. Mod. Phys.* **70** 685 (1998).

[6] C. J. Welford. "Systems for the Radiative Trapping of Lithium and the Tuning of its Interactions via Magnetic Field Control." M.S. Thesis, Rice University (2007).

[7] M.-O. Mewes, M. R. Andrews, N. J. van Druten, D. M. Kurn, D. S. Durfee, and W. Ketterle. "Bose-Einstein condensation in a tightly confining dc magnetic trap." *Phys. Rev. Lett.* **77** 416 (1996).

[8] K. E. Strecker. "Tunable interaction in quantum degenerate lithium." Ph.D. Thesis, Rice University (2004).

[9] C. A. Sackett, C. C. Bradley, and R. G. Hulet. "Optimization of evaporative cooling." *Phys. Rev. A* **55**(5) 3797 (1997).

[10] R. W. P. Drever, J. L. Hall, F. V. Kowalski, J. Hough, G. M. Ford, A. J. Munley, and H. Ward. "Laser phase and frequency stabilization using an optical resonator." *Applied Phys. B* **31** 97 (1983).

[11] E. D. Black. "An introduction to Pound–Drever–Hall laser frequency stabilization." *American Journal of Physics* **69** 79 (2001).

[12] C. A. Sackett. "Dynamics of Bose-Einstein Condensation in ^{7}Li." Ph.D., Rice University (1999).

[13] J. D. Lyons and T. P. Das. "Theoretical analysis of level crossing in a ^2P atomic state." *Phys. Rev. A* **2** 2250 (1970).

[14] G. Ritt, G. Cennini, C. Geckeler, and M. Weitz. "Laser frequency offset locking using a side of filter technique." *Applied Phys. B* **79** 363 (2004).

[15] D. Comparat, A. Fioretti, G. Stern, E. Dimova, B. Laburthe Tolra, and P. Pillet. "Optimized production of large Bose-Einstein condensates." *Phys. Rev. A* **73** 043410 (2006).

[16] Y.-J. Lin, A. R. Perry, R. L. Compton, I. B. Spielman, and J. V. Porto. "Rapid production of ^{87}Rb Bose-Einstein condensates in a combined magnetic and optical potential." *Phys. Rev. A* **79** 063631 (2009).

[17] C. C. Bradley. "Bose-Einstein Condensation of Lithium." PhD thesis.

[18] R. I. Kamar. "Measurement of the Interactions in a Paired Zero Temperature ^{6}Li Gas Throughout the BEC-BSC Crossover." M.S. Thesis, Rice University (2006).

[19] W. Ketterle, D. S. Durfee, and D. M. Stamper-Kurn. "Bose-Einstein condensation in atomic gases." . In *Proceedings of the International School of Physics, Enrico Fermi, course CXL*, page 67 (1999).

[20] Rodney Loudon. "The Quantum Theory of Light." Oxford Science Publications (2000).

[21] Joseph W. Goodman. "Speckle phenomena in optics." Roberts and Company (2007).

[22] R. Hanbury Brown and R. Q. Twiss. "A test of a new type of stellar interferomter on Sirius." *Nature* **178** 1046 (1956).

[23] J. M. Hitchcock. "Transport and Phase Coherence Studies of a Quantum Gas in a Disordered Potential." M.S. Thesis, Rice University (2008).

[24] P. Lugan, A. Aspect, L. Sanchez-Palencia, D. Delande, B. Grémaud, C. A. Müller, and C. Miniatura. "One-dimensional Anderson localization in certain correlated random potentials." *Phys. Rev. A* **80** 023605 (2009).

[25] L. Sanchez-Palencia, D. Clément, P. Lugan, P. Bouyer, G. V. Shlyapnikov, and A. Aspect. "Anderson localization of expanding Bose-Einstein condensates in random potentials." *Phys. Rev. Lett.* **98** 210401 (2007).

[26] C. J. Pethick and H. Smith. "Bose-Einstein Condensation in Dilute Gases." Cambridge University Press (2002).

[27] K. Burnett, P. S. Julienne, P. D. Lett, E. Tiesinga, and C. J. Williams. "Quantum encouters of the cold kind." *Nature* **416** 225 (2002).

[28] E. R. I. Abraham, W. I. McAlexander, J. M. Gerton, R. G. Hulet, R. Côté, and A. Dalgarno. "Triplet s-wave resonance in ^{6}Li collisions and scattering lengths of ^{6}Li and ^{7}Li." *Phys. Rev. A* **55**(5) R3299 (1997).

[29] J. Weiner, V. S. Bagnato, S. Zilio, and P. S. Julienne. "Experiments and theory in cold and ultracold collisions." *Rev. Mod. Phys.* **71** 1 (1999).

[30] K. M. Jones, E. Tiesinga, P. D. Lett, and P. S. Julienne. "Ultracold photoassociation spectroscopy: Long-range molecules and atomic scattering." *Rev. Mod. Phys.* **78** 483 (2006).

[31] C. Chin, R. Grimm, P. Julienne, and E. Tiesinga, e-print arXiv:0812.1496.

[32] W. I. McAlexander. "Collisional interactions in an ultracold lithium gas." Ph.D., Rice University (2000).

[33] T. Koch, T. Lahaye, J. Metz, B. Frohlich, A. Griesmaier, and T. Pfau. "Stabilization of a purely dipolar quantum gas against collapse." *Nature Phys.* 4(3) 218 (2008).

[34] J. Stuhler, A. Griesmaier, T. Koch, M. Fattori, T. Pfau, S. Giovanazzi, P.Pedri, and L. Santos, Phys. Rev. Lett. **95**, 150406 (2005); T. Koch, T. Lahaye, J. Metz, B. Fröhlich, A. Griesmaier, and T. Pfau, Nat. Phys. **4**, 218 (2008); T. Lahaye, *et. al.*, Phys. Rev. Lett. **101**, 080401 (2008).

[35] S. Yi and L. You. "Trapped condensates of atoms with dipole interactions." *Phys. Rev. A* **63** 053607 (Apr 2001).

[36] T. Lahaye, J. Metz, B. Fröhlich, T. Koch, M. Meister, A. Griesmaier, T. Pfau, H. Saito, Y. Kawaguchi, and M. Ueda. "d-wave collapse and explosion of a dipolar Bose-Einstein condensate." *Phys. Rev. Lett.* **101**(8) 080401 (2008).

[37] C. C. Bradley, C. A. Sackett, and R. G. Hulet. "Bose-Einstein condensation of lithium: Observation of limited condensate number." *Phys. Rev. Lett.* **78**(6) 985 (1997).

[38] There is a typo in the caption of Fig. 3 of Ref. [53]: the field value of 547 G should read 540 G [K. E. Strecker, Ph.D. thesis, Rice University (2004)]. At this field we calculate $a \approx -0.3\,a_0$.

[39] P. O. Fedichev, M. W. Reynolds, and G. V. Shlyapnikov. "Three-body recombination of ultracold atoms to a weakly bound s level." *Phys. Rev. Lett.* **77**(14) 2921 (1996).

[40] Scott E. Pollack, Daniel Dries, and Randall G. Hulet. "Universality in Three- and Four-Body Bound States of Ultracold Atoms." *Science* **326** 1683 (2009).

[41] K. Huang and C. N. Yang, Phys. Rev. **105**, 767 (1957); T. D. Lee and C. N. Yang, Phys. Rev. **105**, 1119 (1957); T. D. Lee, K. Huang, and C. N. Yang, Phys. Rev. **106**, 1135 (1957).

[42] D. Blume and Chris H. Greene. "Quantum corrections to the ground-state energy of a trapped Bose-Einstein condensate: A diffusion monte carlo calculation." *Phys. Rev. A* **63**(6) 063601 (2001).

[43] S. B. Papp, J. M. Pino, R. J. Wild, S. Ronen, C. E. Wieman, D. S. Jin, and E. A. Cornell. "Bragg spectroscopy of a strongly interacting [85]rb Bose-Einstein condensate." *Phys. Rev. Lett.* **101** 135301 (2008).

[44] E. R. I. Abraham, W. I. McAlexander, C. A. Sackett, and Randall G. Hulet. "Spectroscopic determination of the s-wave scattering length of lithium." *Phys. Rev. Lett.* **74**(8) 1315 (1995).

[45] E. R. I. Abraham, W. I. McAlexander, J. M. Gerton, R. G. Hulet, R. Côté, and A. Dalgarno. "Triplet s-wave resonance in [6]Li collisions and scattering lengths of [6]Li and [7]Li." *Phys. Rev. A* **55**(5) R3299 (1997).

[46] We use a new value for the binding energy of the least-bound triplet vibrational level of 12420.17028(16) MHz [J. M. Gerton, Ph.D. thesis, Rice University (2001)] that is consistent with, but more precise than, the previous measurement [44].

[47] C. Linton, F. Martin, A. J. Ross, I. Russier, P. Crozet, A. Yiannopoulou, L. Li, and A. M. Lyyra, J. Mol. Spect. **196**, 20 (1999); F. D. Colavecchia, J. J. P. Burke, W. J. Stevens, M. R. Salazar, G. A. Parker, and R. T. Pack, J. of Chem. Phys. **118**, 5484 (2003).

[48] C. A. Sackett, J. M. Gerton, M. Welling, and R. G. Hulet. "Measurements of collective collapse in a Bose-Einstein condensate with attractive interactions." *Phys. Rev. Lett.* **82** 876 (1999).

[49] J. M. Gerton, D. Strekalov, I. Prodan, and R. G. Hulet. "Direct observation of growth and collapse of a Bose-Einstein condensate with attractive interactions." *Nature* **408** 692 (2000).

[50] J. L. Roberts, N. R. Claussen, S. L. Cornish, E. A. Donley, E. A. Cornell, and C. E. Wieman. "Controlled collapse of a Bose-Einstein Condensate." *Phys. Rev. Lett.* **86** 4211 (2001).

[51] G. Modugno, G. Roati, F. Riboli, F. Ferlaino, R. J. Brecha, and M. Inguscio. "Collapse of a Degenerate Fermi Gas." *Science* **297** 2240 (2002).

[52] C. Ospelkaus, S. Ospelkaus, K. Sengstock, and K. Bongs. "Interaction-driven dynamics of ^{40}K-^{87}Rb fermion-boson gas mixtures in the large-particle-number limit." *Phys. Rev. Lett.* **96** 020401 (2006).

[53] K. E. Strecker, G. B. Partridge, A. G. Truscott, and R. G. Hulet. "Formation and propagation of matter-wave soliton trains." *Nature* **417** 150 (May 2002).

[54] L. Khaykovich, F. Schreck, G. Ferrari, T. Bourdel, J. Cubizolles, L. D. Carr, Y. Castin, and C. Salomon. "Formation of a Matter-Wave Bright Soliton." *Science* **296**(5571) 1290–1293 (2002).

[55] Simon L. Cornish, Sarah T. Thompson, and Carl E. Wieman. "Formation of bright matter-wave solitons during the collapse of attractive Bose-Einstein condensates." *Phys. Rev. Lett.* **96**(17) 170401 (2006).

[56] A. Gammal, T. Frederico, and Lauro Tomio. "Critical number of atoms for attractive Bose-Einstein condensates with cylindrically symmetrical traps." *Phys. Rev. A* **64** 055602 (2001).

[57] Víctor M. Pérez-García, H. Michinel, J. I. Cirac, M. Lewenstein, and P. Zoller. "Low energy excitations of a Bose-Einstein condensate: A time-dependent variational analysis." *Phys. Rev. Lett.* **77** 5320 (1996).

[58] S. Stringari. "Collective excitations of a trapped bose-condensed gas." *Phys. Rev. Lett.* **77** 2360 (1996).

[59] Cc Menotti and S. Stringari. "Collective oscillations of a one-dimensional trapped Bose-Einstein gas." *Phys. Rev. A* **66** 043610 (2002).

[60] L. Salasnich, A. Parola, and L. Reatto. "Dimensional reduction in Bose-Einstein-condensed alkali-metal vapors." *Phys. Rev. A* **69** 045601 (2004).

[61] S.E. Pollack et al., to be published in PRA.

[62] F. Dalfovo, C. Minniti, and L. P. Pitaevskii. "Frequency shift and mode coupling in the nonlinear dynamics of a bose-condensed gas." *Phys. Rev. A* **56** 4855 (1997).

[63] L. P. Pitaevskii. "Phenomenological theory of mode collapse-revival in a confined bose gas." *Phys. Lett. A* **229** 406 (1997).

[64] S. Giovanazzi, L. Santos, and T. Pfau. "Collective oscillations of dipolar Bose-Einstein condensates and accurate comparison between contact and dipolar interactions." *Phys. Rev. A* **75** 015604 (2007).

[65] M. H. Anderson, J. R. Ensher, M. R. Matthews, C. E. Wieman, and E. A. Cornell. "Observation of Bose-Einstein Condensation in a Dilute Atomic Vapor." *Science* **269** 198 (1995).

[66] C. C. Bradley, C. A. Sackett, J. J. Tollett, and R. G. Hulet. "Evidence of Bose-Einstein condensation in an atomic gas with attractive interactions." *Phys. Rev. Lett.* **75**(9) 1687 (1995).

[67] K. B. Davis, M. O. Mewes, M. R. Andrews, N. J. van Druten, D. S. Durfee, D. M. Kurn, and W. Ketterle. "Bose-Einstein condensation in a gas of sodium atoms." *Phys. Rev. Lett.* **75** 3969 (1995).

[68] I. Bloch, J. Dalibard, and W. Zwerger. "Many-body physics with ultracold gases." *Rev. Mod. Phys.* **80** 885 (2008).

[69] C. Raman, M. Köhl, R. Onofrio, D. S. Durfee, C. E. Kuklewicz, Z. Hadzibabic, and W. Ketterle. "Evidence for a critical velocity in a Bose-Einstein condensed gas." *Phys. Rev. Lett.* **83** 2505 (1999).

[70] R. Onofrio, C. Raman, J. M. Vogels, J. R. Abo-Shaeer, A. P. Chikkatur, and W. Ketterle. "Observation of superfluid flow in a Bose-Einstein condensed gas." *Phys. Rev. Lett.* **85** 2228 (2000).

[71] C. Raman, R. Onofrio, J. M. Vogels, J. R. Abo-Shaeer, and W. Ketterle. "Dissipationelss flow and superfluidity in gaseous Bose-Einstein condensates." *J. Low Temp. Phys.* **122**(1/2) 99 (2001).

[72] K. W. Madison, F. Chevy, W. Wohlleben, and J. Dalibard. "Vortex formation in a stirred Bose-Einstein condensate." *Phys. Rev. Lett.* **84** 806 (2000).

[73] J. R. Abo-Shaeer, C. Raman, J. M. Vogels, and W. Ketterle. "Observation of Vortex Lattices in Bose-Einstein Condensates." *Science* **292** 476 (2001).

[74] P. C. Haljan, I. Coddington, P. Engels, and E. A. Cornell. "Driving Bose-

Einstein-condensate vorticity with a rotating normal cloud." *Phys. Rev. Lett.* **87** 210403 (2001).

[75] E. Hodby, G. Hechenblaikner, S. A. Hopkins, O. M. Maragò, and C. J. Foot. "Vortex nucleation in Bose-Einstein condensates in an oblate, purely magnetic potential." *Phys. Rev. Lett.* **88** 010405 (2001).

[76] D. Reppy, J.*J. Low Temp. Phys.* **87** 205 (1992).

[77] J. Fortágh, H. Ott, S. Kraft, A. Günther, and C. Zimmermann. "Surface effects in magnetic microtraps." *Phys. Rev. A* **66** 041604 (2002).

[78] A. E. Leanhardt, A. P. Shin, Y. and, D. Kielpinski, W. Ketterle, and D. E. Pritchard. "Bose-Einstein condensates near a microfabricated surface." *Phys. Rev. Lett.* **90** 100404 (2003).

[79] M. P. A. Jones, C. J. Vale, D. Sahagun, B. V. Hall, and E. A. Hinds. "Spin coupling between cold atoms and the thermal fluctuations of a metal surface." *Phys. Rev. Lett.* **91** 080401 (2003).

[80] J. Estève, C. Aussibal, T. Schumm, C. Figl, D. Mailly, I. Bouchoule, C. I. Westbrook, and A. Aspect. "Role of wire imperfections in micromagnetic traps for atoms." *Phys. Rev. A* **70** 043629 (2004).

[81] S. E. Pollack, D. Dries, M. Junker, Y. P. Chen, T. A. Corcovilos, and R. G. Hulet. "Extreme tunability of interactions in a ^{7}Li Bose-Einstein condensate."

Phys. Rev. Lett. **102** 090402 (2009).

[82] J. Billy, V. Josse, Z. Zuo, A. Bernard, B. Hambrecht, P. Lugan, D. Clément, L. Sanchez-Palencia, P. Bouyer, and A. Aspect. "Direct observation of Anderson localization of matter waves in a controlled disorder." *Nature* **453** 891–894 (June 2008).

[83] G. Roati, C. D'Errico, L. Fallani, M. Fattori, C. Fort, M. Zaccanti, G. Modugno, M. Modugno, and M. Inguscio. "Anderson localization of a non-interacting Bose-Einstein condensate." *Nature* **453** 895 (2008).

[84] L. Landau. "The Theory of Superfluidity of He II." *J. Phys. (USSR)* **5** 51 (1941).

[85] D. R. Tilley and J. Tilley. "Superfluidity and superconductivity." IOP Publishing (1990).

[86] E. Zaremba. "Sound propagation in a cylindrical bose-condensed gas." *Phys. Rev. A* **57** 518–521 (1998).

[87] G. M. Kavoulakis and C. J. Pethick. "Quasi-one-dimensional character of sound propagation in elongated Bose-Einstein condensed clouds." *Phys. Rev. A* **58** 1563 (1998).

[88] S. Stringari. "Dynamics of Bose-Einstein condensed gases in highly deformed traps." *Phys. Rev. A* **58** 2385 (1998).

[89] L. Salasnich, A. Parola, and L. Reatto. "Effective wave equations for the dynamics of cigar-shaped and disk-shaped bose condensates." *Phys. Rev. A* **65** 043614 (2002).

[90] A. M. Kamchatnov, A. Gammal, and R. A. Kraenkel. "Dissipationless shock waves in bose-einstein condensates with repulsive interaction between atoms." *Phys. Rev. A* **69** 063605 (2004).

[91] P. O. Fedichev and G. V. Shlyapnikov. "Critical velocity in cylindrical Bose-Einstein condensates." *Phys. Rev. A* **63** 045601 (2001).

[92] T. Frisch, Y. Pomeau, and S. Rica. "Transition to dissipation in a model of superflow." *Phys. Rev. Lett.* **69** 1644 (1992).

[93] Yong P. Chen, J. Hitchcock, D. Dries, M. Junker, C. Welford, and R. G. Hulet. "Phase coherence and superfluid-insulator transition in a disordered Bose-Einstein condensate." *Phys. Rev. A* **77**(3) 033632 (2008).

[94] J. E. Lye, L. Fallani, M. Modugno, D. S. Wiersma, C. Fort, and M. Inguscio. "Bose-Einstein condensate in a random potential." *Phys. Rev. Lett.* **95** 070401 (2005).

[95] D. Clément, A. F. Varón, M. Hugbart, J. A. Retter, P. Bouyer, L. Sanchez-Palencia, D. M. Gangardt, G. V. Shlyapnikov, and A. Aspect. "Suppression of transport of an interacting elongated Bose-Einstein condensate in a random potential." *Phys. Rev. Lett.* **95**(17) 170409 (2005).

[96] T. Schulte, S. Drenkelforth, J. Kruse, W. Ertmer, J. Arlt, K. Sacha, J. Za-krzewski, and M. Lewenstein. "Routes towards Anderson-like localization of Bose-Einstein condensates in disordered optical lattices." *Phys. Rev. Lett.* **95** 170411 (2005).

[97] S. G. Bhongale, P. Kakashvili, C. J. Bolech, and H. Pu, e-print arXiv:1003.2608.

[98] A. Radouani. "Gray solitons and phonons in repulsive Bose-Einstein conden-sates confined in one-dimensional nonharmonic traps." *Phys. Rev. A* **68**(4) 043620 (Oct 2003).

[99] Abdelaziz Radouani. "Soliton and phonon production by an oscillating obstacle in a quasi-one-dimensional trapped repulsive Bose-Einstein condensate." *Phys. Rev. A* **70**(1) 013602 (2004).

[100] M. Modugno. "Collective dynamics and expansion of a Bose-Einstein conden-sate in a random potential." *Phys. Rev. A* **73** 013606 (2006).

[101] M. Albert, T. Paul, N. Pavloff, and P. Leboeuf. "Dipole oscillations of a Bose-Einstein condensate in the presence of defects and disorder." *Phys. Rev. Lett.* **100**(25) 250405 (2008).

[102] T. Schulte, S. Drenkelforth, G. Kleine Büning, W. Ertmer, J. Arlt, M. Lewen-stein, and L. Santos. "Dynamics of Bloch oscillations in disordered lattice potentials." *Phys. Rev. A* **77** 023610 (2008).

[103] S Drenkelforth, G Kleine Buning, J Will, T Schulte, N Murray, W Ertmer, L Santos, and J J Arlt. "Damped Bloch oscillations of Bose-Einstein condensates in disordered potential gradients." *New Journal of Physics* **10** 045027 (2008).

[104] C. C. Bradley, C. A. Sackett, and R. G. Hulet. "Bose-Einstein condensation of lithium: Observation of limited condensate number." *Phys. Rev. Lett.* **78** 989 (1997).

[105] R. Meppelink, S. B. Koller, J. M. Vogels, H. T. C. Stoof, and P. van der Straten. "Damping of superfluid flow by a thermal cloud." *Phys. Rev. Lett.* **103** 265301 (2009).

[106] R. G. Scott and D. A. W. Hutchinson. "Incoherence of Bose-Einstein condensates at supersonic speeds due to quantum noise." *Phys. Rev. A* **78** 063614 (2008).

[107] A. Görlitz, J. M. Vogels, A. E. Leanhardt, C. Raman, T. L. Gustavson, J. R. Abo-Shaeer, A. P. Chikkatur, S. Gupta, S. Inouye, T. Rosenband, and W. Ketterle. "Realization of Bose-Einstein condensates in lower dimensions." *Phys. Rev. Lett.* **87** 130402 (2001).

[108] F. Schreck, L. Khaykovich, K. L. Corwin, G. Ferrari, T. Bourdel, J. Cubizolles, and C. Salomon. "Quasipure Bose-Einstein condensate immersed in a Fermi sea." *Phys. Rev. Lett.* **87** 080403 (2001).

[109] Bogdan Damski. "Formation of shock waves in a bose-einstein condensate." *Phys. Rev. A* **69** 043610 (2004).

[110] A. M. Leszczyszyn, G. A. El, Yu. G. Gladush, and A. M. Kamchatnov. "Transcritical flow of a Bose-Einstein condensate through a penetrable barrier." *Phys. Rev. A* **79** 063608 (2009).

[111] G. A. El, A. M. Kamchatnov, V. V. Khodorovskii, E. S. Annibale, and A. Gammal. "Two-dimensional supersonic nonlinear schrödinger flow past an extended obstacle." *Phys. Rev. E* **80** 046317 (2009).

[112] M. A. Hoefer, M. J. Ablowitz, I. Coddington, E. A. Cornell, P. Engels, and V. Schweikhard. "Dispersive and classical shock waves in bose-einstein condensates and gas dynamics." *Phys. Rev. A* **74** 023623 (2006).

[113] Z. Dutton, M. Budde, C. Slowe, and L. V. Hau. "Observation of quantum shock waves created with ultra- compressed slow light pulses in a Bose-Einstein condensate." *Science* **293** 663 (2001).

[114] T. P. Simula, P. Engels, I. Coddington, V. Schweikhard, E. A. Cornell, and R. J. Ballagh. "Observations on sound propagation in rapidly rotating bose-einstein condensates." *Phys. Rev. Lett.* **94** 080404 (2005).

[115] J. J. Chang, P. Engels, and M. A. Hoefer. "Formation of dispersive shock waves by merging and splitting bose-einstein condensates." *Phys. Rev. Lett.* **101** 170404 (2008).

[116] Wenjie Wan, Shu Jia, and Jason W. Fleischer. "Dispersive superfluid-like shock waves in nonlinear optics." *Nature Phys.* **3** 46 (2007).

[117] K. M. R. van der Stam, R. Meppelink, J. M. Vogels, and P. van der Straten. "Reaching the hydrodynamic regime in a bose-einstein condensate by suppression of avalanches." *Phys. Rev. A* **75** 031602 (2007).

[118] P. Leboeuf and N. Pavloff. "Bose-Einstein beams: Coherent propagation through a guide." *Phys. Rev. A* **64**(3) 033602 (2001).

[119] Nicolas Pavloff. "Breakdown of superfluidity of an atom laser past an obstacle." *Phys. Rev. A* **66**(1) 013610 (2002).

[120] G. Theocharis, P.G. Kevrekidis, H.E. Nistazakis, D.J. Frantzeskakis, and A.R. Bishop. "Generation of dark solitons in oscillating Bose-Einstein condensates." *Phys.Lett. A* **337** 441 (2005).

[121] R. Carretero-Gonzlez, P.G. Kevrekidis, D.J. Frantzeskakis, B.A. Malomed, S. Nandi, and A.R. Bishop. "Soliton trains and vortex streets as a form of Cerenkov radiation in trapped Bose-Einstein condensates." *Mathematics and Computers in Simulation* **74** 361 (2007).

[122] S. Dettmer, D. Hellweg, P. Ryytty, J. J. Arlt, W. Ertmer, K. Sengstock, D. S. Petrov, G. V. Shlyapnikov, H. Kreutzmann, L. Santos, and M. Lewenstein. "Observation of phase fluctuations in elongated Bose-Einstein condensates." *Phys. Rev. Lett.* **87** 160406 (2001).

[123] P. Engels and C. Atherton. "Stationary and nonstationary fluid flow of a Bose-Einstein condensate through a penetrable barrier." *Phys. Rev. Lett.* **99** 160405 (2007).

[124] Vincent Hakim. "Nonlinear Schrödinger flow past an obstacle in one dimension." *Phys. Rev. E* **55**(3) 2835 (1997).

[125] M. Haddad and V. Hakim. "Superfluidity at supersonic speed?" *Phys. Rev. Lett.* **87**(21) 218901 (2001).

[126] C. K. Law, C. M. Chan, P. T. Leung, and M.-C. Chu. "Motional dressed states in a Bose-Einstein condensate: Superfluidity at supersonic speed." *Phys. Rev. Lett.* **85**(8) 1598–1601 (2000).

[127] C. K. Law, C. M. Chan, P. T. Leung, and M. C. Chu. "Law et al. reply:." *Phys. Rev. Lett.* **87** 218902 (2001).

[128] O. Lahav, A. Blumkin, C. Gordon, and J. Steinhauer, e-print arXiv:0906.1337.

[129] L. J. Garay, J. R. Anglin, J. I. Cirac, and P. Zoller. "Sonic analog of gravitational black holes in Bose-Einstein condensates." *Phys. Rev. Lett.* **85** 4643 (2000).

[130] R. Balbinot, A. Fabbri, S. Fagnocchi, A. Recati, and I. Carusotto. "Nonlocal density correlations as a signature of Hawking radiation from acoustic black holes." *Phys. Rev. A* **78** 021603 (2008).

[131] I. Carusotto, S. Fagnocchi, A. Recati, R. Balbinot, and A. Fabbri. "Numerical observation of Hawking radiation from acoustic black holes in atomic bose einstein condensates." *New Journal of Physics* **10** 103001 (2008).

[132] S. Burger, K. Bongs, S. Dettmer, W. Ertmer, K. Sengstock, A. Sanpera, G. V. Shlyapnikov, and M. Lewenstein. "Dark solitons in Bose-Einstein condensates." *Phys. Rev. Lett.* **83** 5198 (1999).

[133] J. Denschlag, J. E. Simsarian, D. L. Feder, Charles W. Clark, L. A. Collins, J. Cubizolles, L. Deng, E. W. Hagley, K. Helmerson, W. P. Reinhardt, S. L. Rolston, B. I. Schneider, and W. D. Phillips. "Generating solitons by phase engineering of a Bose-Einstein condensate." *Science* **287** 97 (2000).

[134] B. P. Anderson, P. C. Haljan, C. A. Regal, D. L. Feder, L. A. Collins, C. W. Clark, and E. A. Cornell. "Watching dark solitons decay into vortex rings in a Bose-Einstein condensate." *Phys. Rev. Lett.* **86** 2926 (2001).

[135] A. Weller, J. P. Ronzheimer, C. Gross, J. Esteve, M. K. Oberthaler, D. J. Frantzeskakis, G. Theocharis, and P. G. Kevrekidis. "Experimental observation of oscillating and interacting matter wave dark solitons." *Phys. Rev. Lett.* **101** 130401 (2008).

[136] A. Muryshev, G. V. Shlyapnikov, W. Ertmer, K. Sengstock, and M. Lewenstein. "Dynamics of dark solitons in elongated Bose-Einstein condensates." *Phys. Rev. Lett.* **89** 110401 (2002).

[137] T. Tsuzuki *J. Low Temp. Phys.* **4** 441 (1971).

[138] L. Fallani, C. Fort, and M. Inguscio. "Bose-Einstein condensates in disordered potentials." *Adv. At. Mol. Opt. Phys.* **56** 119 (2008).

[139] P. W. Anderson. "Absence of diffusion in certain random lattices." *Phys. Rev.* **109** 1492 (1958).

[140] S. John. "Electromagnetic absorption in a disordered medium near a photon mobility edge." *Phys. Rev. Lett.* **53** 2169 (1984).

[141] P. W. Anderson. "The question of classical localization. a theory of white paint?" *Phil. Mag. B* **52** 505 (1985).

[142] L. Ye, G. Cody, M. Zhou, P. Sheng, and Andrew N. Norris. "Observation of bending wave localization and quasi mobility edge in two dimensions." *Phys. Rev. Lett.* **69** 3080 (1992).

[143] D. Wiersma, P. Bartolini, A. Lagendijk, and R. Righini. "Localization of Light in a Disordered Medium." *Nature* **390** 671 (1997).

[144] Martin Störzer, Peter Gross, Christof M. Aegerter, and Georg Maret. "Observation of the critical regime near Anderson localization of light." *Phys. Rev. Lett.* **96** 063904 (2006).

[145] T. Schwartz, G. Bartal, S. Fishman, and M. Segev. "Transport and Anderson localization in disordered two-dimensional photonic lattices." *Nature* **446** 52

(2007).

[146] J. Topolancik, B. Ilic, and F. Vollmer. "Experimental observation of strong photon localization in disordered photonic crystal waveguides." *Phys. Rev. Lett.* **99** 253901 (2007).

[147] Y. Lahini, A. Avidan, F. Pozzi, M. Sorel, R. Morandotti, D. N. Christodoulides, and Y. Silberberg. "Anderson localization and nonlinearity in one-dimensional disordered photonic lattices." *Phys. Rev. Lett.* **100** 013906 (2008).

[148] R. L. Weaver. "Anderson localization of ultrasound." *Wave Motion* **12** 129 (1990).

[149] H. Hu, A. Strybulevych, J. H. Page, E. Skipetrov, and B. A. van Tiggelen. "Localization of ultrasound in a three diminsional elastic network." *Nature Phys.* **4** 945 (2008).

[150] R. Dalichaouch, J. P. Armstrong, S. Schultz, P. M. Platzman, and S. L. McCall. "Microwave localization by two-dimensional random scattering." *Nature* **354** 53 (1991).

[151] A. A. Chabanov, M. Stoytchev, and A. Z. Genack. "Statistical singatures of photon localization." *Nature* **404** 850 (2000).

[152] A. A. Chabanov and A. Z. Genack. "Photon localization in resonant media." *Phys. Rev. Lett.* **87** 153901 (2001).

[153] F. L. Moore, J. C. Robinson, C. F. Bharucha, Bala Sundaram, and M. G. Raizen. "Atom optics realization of the quantum δ-kicked rotor." *Phys. Rev. Lett.* **75** 4598 (1995).

[154] J. Chabé, G. Lemarié, B. Grémaud, D. Delande, P. Szriftgiser, and J. C. Garreau. "Experimental observation of the Anderson metal-insulator transition with atomic matter waves." *Phys. Rev. Lett.* **101** 255702 (2008).

[155] D Clement, A F Varon, J A Retter, L Sanchez-Palencia, A Aspect, and P Bouyer. "Experimental study of the transport of coherent interacting matter-waves in a 1d random potential induced by laser speckle." *New J. Phys.* **8**(8) (2006).

[156] C. Fort, L. Fallani, V. Guarrera, J. E. Lye, M. Modugno, D. S. Wiersma, and M. Inguscio. "Effect of optical disorder and single defects on the expansion of a Bose-Einstein condensate in a one-dimensional waveguide." *Phys. Rev. Lett.* **95** 170410 (2005).

[157] M. Junker. "Photoassociation in a quantum degenerate gas of [7]Li." M.s. Thesis, Rice University (2004).

[158] D. Dries. "Fabrication of a high resolution relay lens for use in imaging ultracold quantum gases." M.s. Thesis, Rice University (2005).

[159] P. Lugan, D. Clément, P. Bouyer, A. Aspect, M. Lewenstein, and L. Sanchez-

Palencia. "Ultracold bose gases in 1d disorder: From lifshits glass to bose-einstein condensate." *Phys. Rev. Lett.* **98** 170403 (2007).

[160] S. Flach, D. O. Krimer, and Ch. Skokos. "Universal spreading of wave packets in disordered nonlinear systems." *Phys. Rev. Lett.* **102** 024101 (2009).

[161] Ch. Skokos, D. O. Krimer, S. Komineas, and S. Flach. "Delocalization of wave packets in disordered nonlinear chains." *Phys. Rev. E* **79** 056211 (2009).

[162] E. Akkermans, S. Ghosh, and Z. H. Musslimani. "Numerical study of one-dimensional and interacting Bose-Einstein condensates in a random potential." *Journal of Physics B: Atomic, Molecular and Optical Physics* **41** 045302 (2008).

[163] Y. V. Kartashov and V. A. Vysloukh. "Anderson localization of solitons in optical lattices with random frequency modulation." *Phys. Rev. E* **72** 026606 (2005).

[164] K. Sacha, C. A. Müller, D. Delande, and J. Zakrzewski. "Anderson localization of solitons." *Phys. Rev. Lett.* **103** 210402 (2009).

[165] A. I. Streltsov, O. E. Alon, and L. S. Cederbaum. "Formation and dynamics of many-boson fragmented states in one-dimensional attractive ultracold gases." *Phys. Rev. Lett.* **100** 130401 (2008).

[166] C. Weiss and Y. Castin. "Creation and detection of a mesoscopic gas in a nonlocal quantum superposition." *Phys. Rev. Lett.* **102** 010403 (2009).

[167] A. I. Streltsov, O. E. Alon, and L. S. Cederbaum. "Scattering of an attractive Bose-Einstein condensate from a barrier: Formation of quantum superposition states." *Phys. Rev. A* **80** 043616 (2009).